STUDIES ON DEFORMATION OF MATERIALS VIA RATE TREATMENT OF COMPRESSION TEST

[1]A.G. Olugbenga, [2]Bala. Saliu Alhaji, and [3]M. U. Garba

[1]Department of Chemical Engineering, Federal University of Technology Minna,
[2]Department of Telecommunication Engineering, Federal University of Technology Minna,
[3]Department of Chemical Engineering, Federal University of Technology Minna, and
[3]University of Leeds, Leeds LS2 9JT, United Kingdom
Corresponding Author: grace.adeola@futminna.edu.ng

Abstract

Fractures in sandstone formations are responsible for well instabilities. The micro properties of sandstone grains are crucial to their deformation. However, little attention has been given to the study of these properties because it is challenging to determine the said properties. Advances in the data acquisition systems attached to the compression test on rock materials have been employed. Here we obtain a procedure which has made it possible to explore the role played by micro-parameters of sandstone in understanding mechanisms of well fractures experimentally. The macroscopic deformation of rock model samples used in experiment coupled with data acquisition confirmed the deformation of bonded grains structure starts with a single grain distortion, which is where micro-parameters are obtained as calibrations. It was observed that the grain and bond stiffness can be related to the elastic modulus while the bond strength can be related to the tensile strength of the bonds within the grains. The synergetic effect of the grain distortion due to bond softening, grain stiffness and bond strength controlled the mode of deformation along the crack path, which occurred along the highly stressed points. Core sample examination was observed to re-define mechanical stress or loading magnitude to enhance operational safety. Obtaining micro-properties of core samples prior to drilling program will provide reliability of macroscopic elastic properties of handling rock structures under engineering project. The initial data of the micro-properties representing the physical rock under mechanical stress can be enhanced if a simulation is required to plan drilling operations.
Keywords: Micro-measurements, fracture, micro-properties, stiffness, sandstone.

10   INTRODUCTION

Deformations as planar surface are represented by one particle sliding past another particle in discrete assembly of particles as shown in figure 1. In most desecrate element modelling, the development of models was to solve the problem of empirical dependence of existing constitutive model which accommodate the asperities effect and the deformation during shearing. (Stephen, 2013). A new contact model based on the description of solid granular materials were represented in Stephan (2013) work where actual surface morphology was used as input in DEM simulation of rock. Rock is seen as bonded particles. The simulated model reliably shows a behaviour of its exacts physical rock and can be used to understand rock's behaviour and account for three dimensionality at the surface. His work was a step to understanding the discontinuous heterogeneities in rock which is complex to understand. For further understanding of this complexity in rock behaviour, a further step to the work of Hasanpour and Choupani, (2008) will be to reliably provide micro measurements for the natural rock mass by experiments, since their models did not use micro parameters of the grains and bonds binding the grains. Hence additional information to understand the processes that leads to rock deformation and macro mechanical behaviour were provided by the experimental Sharpe and William (2008).

The particle flow code has obtained the macro-parameters of rock by first defining calibration as micro parameters. Micro properties of sandstone can be made to interact to produce corresponding macro properties of the material. Further the macro properties are then synthesized to understand the material

behaviour under stress. The works of Potyondy and Cundall (2004) have shown that choice of appropriate micro parameters depends largely on the material behaviour. The particles are simulated as bonded together with cement called parallel bond where they closely interact by contact forces occurring in every particle to particle contact point. The degree of closeness of the particles makes the packing properties cohesive but bonded particles connected by parallel bond. The bond is a finite dimensionally compared to the particle diameter (James and James, 1989). It possesses both tensile and shears strength, stiffness of both normal and tangential strength. During loading, when either of the strength are exceeded, the parallel bond breaks and forms micro-cracks inside the rock mass between the particles. Coalescence of the micro-cracks occurs as the loading weight increases which are seen as cracks which divide the rock mass into separate clusters. The location of this failure point can be tracked by accurate evaluation of both contact and parallel bond existing in the microstructure of the material.

In this work the micro-mechanical properties are studied and simulated and are presented for the evaluation and determination of deformability of rock material.

2.0   METHODOLOGY

The complete set of micro-parameters that characterize a parallel-bonded material is given by the radius multiplier used to set the parallel-bond radii via equations, the particle friction coefficient (μ) The normal and shear strengths respectively, of the cement-like material represented by a parallel bond within the material. When either of these exceeded their original strength deformation occurs. The three micro-parameters for particle-particle contact were specified.

The deformation test was done using the conventional test for rock test. During this test, the core sample was compressed. The stress causing the fractures was recorded. The curve obtained were rate treated and the resulting curve was used to obtain the stiffness parameter and the bond parameter. The overall modulus at a parallel-bonded contact (at which the two bonded particles have a nonzero overlap) is the sum of micro modulus. When a parallel bond breaks, the overall modulus at the contact is reduced by modulus One was evaluated as the a modulus-damage index such that the local measure of the damage, in terms of modulus reduction, that occurs when a parallel bond breaks. It was estimated that the relation between the deformability micro-parameters and the macroscopic modulus of a complete assembly using the relation in which the ratios of micro-modulus to macro-modulus contribution for the particle-particle contacts and the parallel bonds, respectively, and modulus is the macroscopic modulus. These ratios can be estimated for a given particle system in which the majority of particles possess two or more contacts to inhibit rolling of contact-bonded particle pairs, as follows. (Cundall et al, 2011)

3.0   RESULTS AND DISCUSSIONS

An increase in the normal and shear stiffness at the bond reduces the initial elastic slope, thus micro-parameter play a key role in the determination of the material's Young's modulus. If there is a low value of the bond strength it delays attaining peak strength and slightly reduces the peak strength. However in Figure, 1 the bond stiffness has little or no effect on the peak strength since it is not in ratio with the shear bond. This is an indication that the bond under observation is just a point bond which was captured by strain gauge.
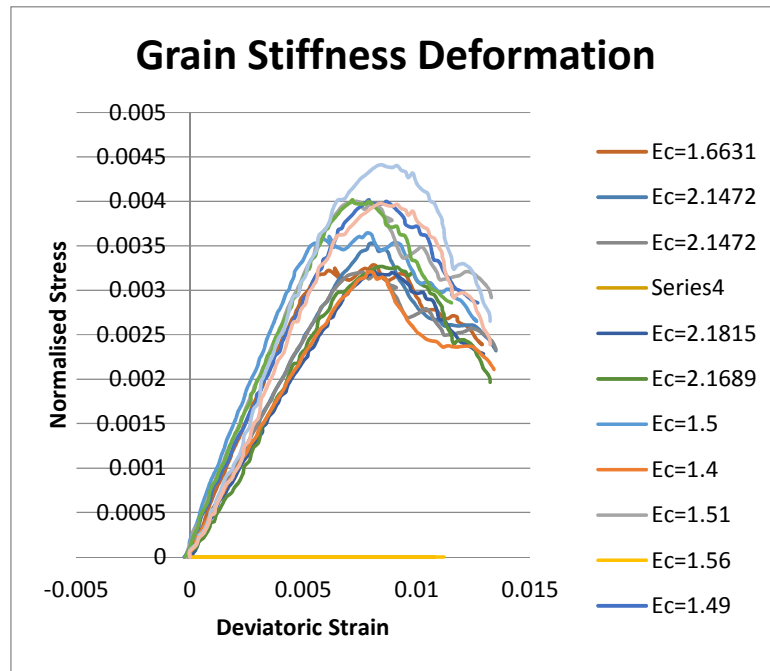
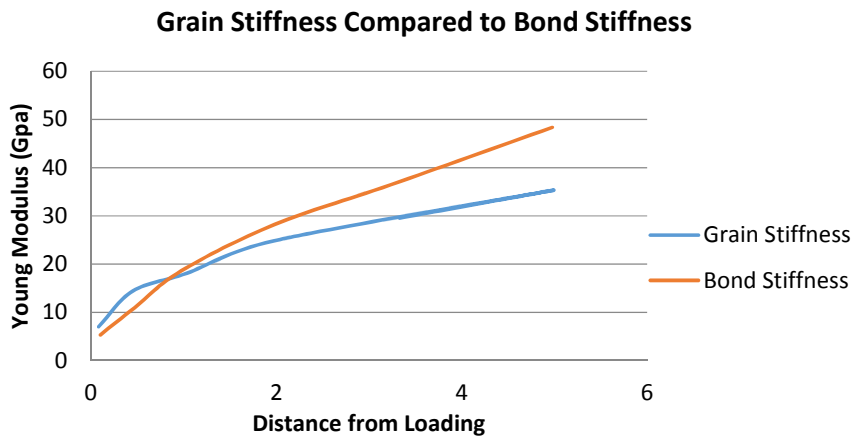Figure 1: Iteration of bond stiffness as point Young Modulus in sample

Figure 2: The effect of grain and bond stiffness change on Young's modulus

The stiffness was determined using data from compression test to obtain point young modulus. Next the material stiffness was obtained, this gave the particle stiffness. With stiffer grains and bond, the Young modulus increased. This should be so because the two parameters constitute properties of the linkage particles in the rock material.

In Figure 2. It is then easy to state that both grain and bond stiffness's are major factors that determines the magnitude of the Young's modulus. As such the grain stiffness and bond stiffness were micro parameter used as calibration suitable to obtain macro parameters since it is obvious that Young's modulus increased with increase in radius multiplier with bond stiffness having higher effect.

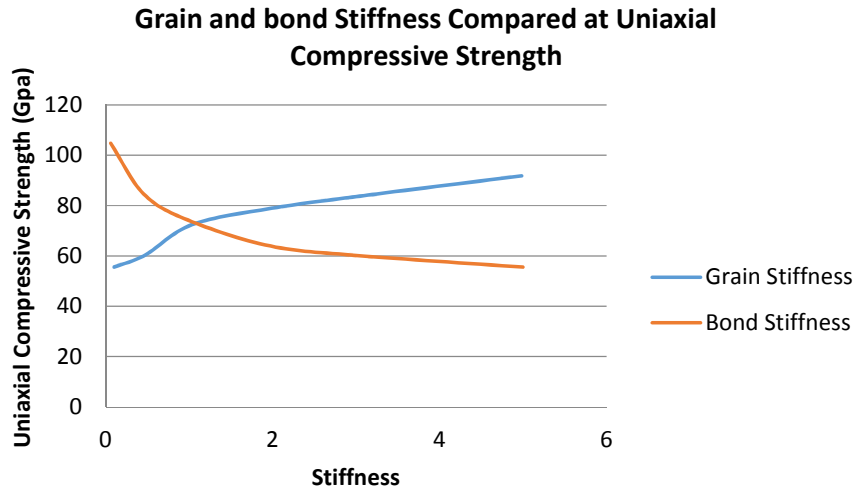**Grain and bond Stiffness Compared at Uniaxial Compressive Strength**

Figure 3: The effect of stiffness change of grain and bond on uniaxial compressive strength.

In Figure 3, the uniaxial compressive strength increases in the curve for grain stiffness whereas a decrease was observed for bond stiffness. It is true of stress-strain behaviour in materials which are composite. Thus it is seen that as the bond stiffness increases, higher stress was needed to compress bond for the same given strain observed at the point of taking the micro measurements finally drops the uniaxial compressive strength
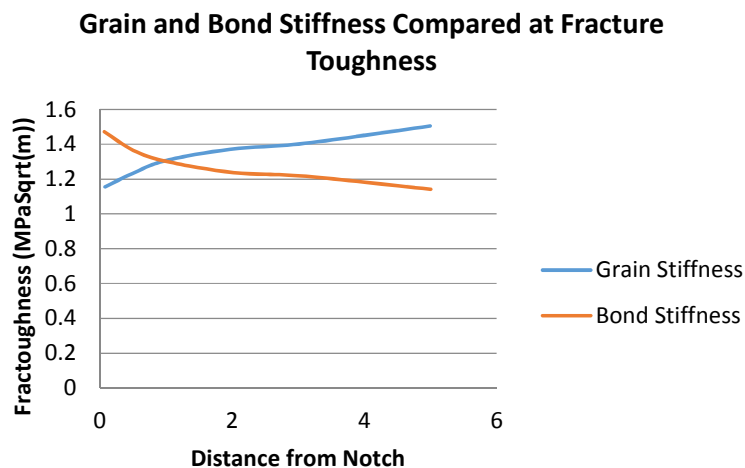
Grain and Bond Stiffness Compared at Fracture Toughness

Figure 4: The effect of stiffness change of grain and bond on fracture toughness.

Fracture toughness can be explained the same way as uniaxial compressive strength. The same effect was observed for the grains and bond responses to the tensile and compressive failure test. The stress strain curve shows that for this composite material, at a particular given strain under observation, as the bond stiffness increases, the stress acting on it increases and then this stress weakens the bond strength that is weakens the uniaxial compressive strength initially possesses by the original material. Figure 9 and also weakens the fracture toughness at that same point under investigation. The material therefore becomes are elastic up till peak strength. The material's behaviour is generally controlled by the cement/ bond strength. In Figure 9 the higher the stiffness of grains, the higher the magnitude of the uniaxial compressive strength, whereas as the bond stiffness increases, the uniaxial compressive

strength decreases. This is properly illustrated in Figure 10 the higher the stiffness of grains the higher the magnitude of the fracture toughness whereas as the bond stiffness increases, the fracture toughness decreases. Analytical explanation also provides proves for the reliability of this fact. Bruno et al. (1990) did simulation and arrived at similar explanation.

In addition to the deformability and strength investigated by micro-parameters, Micro-parameter Specification in particle flow code has relevant and direct correlations. Parallel bonds are direct representation of bond stiffness and strength obtained from photo stress micro measurements in the particle flow code. The parallel bond in particle flow code is characterized by its bond radius, As the bond radius is reduced, the parallel bond experiences a reduction in stiffness Thus, reducing bond radius mimics the effect of reducing the amount of cement-like material joining the two bonded particles. The micro-properties obtained can be used in a way to build a simple discrete model of the sandstone. Thus the angle of deformation gave a close values of smooth joint displacement of 55^0. The stress strain curves was in agreement with the conventional rock fracture test when the peak stress at deformation was 74MPa.

4.0   Conclusion

Micro measurements from the rate treatment test techniques have been successful in providing micro parameter of sandstone sample. The grain toughness, grain stiffness, bond stiffness, ratio of normal to shear bond stiffness are real micro parameters obtained from a real bonded grains of sandstone under uniaxial compressive stress.

The initial guess for micro-parameter for PFC simulation can be more accurate from the results obtained from photo stress analysis. In fact, a true representation of rock behaviour can be inferred from the result if data from rate treament are used for obtaining micro-mechanical behaviour of rock or cemented granular materials.

The grain toughness, grain stiffness, bonds strength, ratio of grain's normal to shear bond stiffness were micro parameter used to investigate the strength characteristics of the micro-cracks in the rock sample. Uniaxial compressive test and rate treatment of the compressive strength data analysis was a synergetic research route that revealed that sandstone toughness dependence largely on the bond strength of the grains it contains.

The values obtained from uniaxial compressive test are real time data inputs for simulations to access the crack strength and rock behaviour. Thus the application of experimental technique to concrete structures composed of bonded grains can give reliable results when plain strain is achievable in the experimental specimen (Zang and Stephensson, 2010).

More bond spacing is an indication of bigger porosity within the grains that constitute rock or cemented granular materials; simulations will result into larger micro-cracks. A sensitivity analysis of the effect of porosity will enhance understanding micro-crack strength. Simulation results are applicable for use as toughness value to show locations of cracks for relevant compares with crack locations revealed by the experimental toughness data (Cho, et. al., 2004)

References

Zang, A., & Stephansson, O. (2008). Stress Field of the Earth's Crust. Dordrecht: Springer
Akhtar S. Khan and Xinwei Wang (2000), Strain Measurements and Stress Analysis. Imprint/Publisher : upper saddle River, N.J.Prentic e Hall, c2001. ISBN 0130800767 ISBN-13: 9780130800763. Page 150-172.

Arno Zang and Ove Stephensson (2010) Stress Field of the Earth's Crust, Publication Date: 24 Feb 2010 | ISBN-10: 1402084439 | ISBN-13: 978-1402084430 Edition: 2010, Publisher: Springer; 2010 edition (24 Feb 2010) Language: English ISBN-10: 1402084439 ISBN-13: 978-1402084430. Page 144 -150

Hasanpour, R. and Choupani, N., (2008) Mixed-Mode Study of Rock Fracture Mechanics by using the Modified Arcan Specimen Test, World Academy of Science, Engineering and Technology 17 2008

Sharpe, Jr., William N. (Ed.) (2008) Springer Handbook of Experimental Solid Mechanics ISBN 978-0-387-30877-7 XXX, 1098 p. 874 illus., 58 in color, http://link.springer.com/referencework/10.1007/978-0-387-30877-7/page/1

James F. Doyle, James W. Phillips, (1989), Experimental Stress Analysis Bethel, Conn. : Society for Experimental Mechanics, ©1989. http://www.worldcat.org/title/manual-on-experimental-stress-analysis/oclc/19873535 Society for Experimental Mechanics, - Technology & Engineering
Hudson, J. A. (1989): Rock Mechanics Principles in Engineering Practice, CIRIA, Butterworths

Bruno, M.S., 1994, Micromechanics of Stress-Induced Permeability Anisotropy and Damage in Sedimentary Rock, Mechanics of Material, Vol. 18, pp. 31-48.

Bruno, M.S., Bovberg, C.A., and Nakagawa, F.M., 1991, Anisotropic Stress Influences on the Permeability of Weakly-Cemented Sandstones, Proceedings of 32nd U.S. Symposium on Rock Mechanics, pp. 375-383.

Bruno, M.S., Dorfmann, A., Lao, K., and Honeger, C., 2001, Coupled Particle and Fluid Flow Modeling of Fracture and Slurry Injection in Weakly Consolidated Granular Media, Proceedings of 38th U.S. Symposium on Rock Mechanics: Rock Mechanics in the National Interest, 7 – 10, July, Washington D.C., Vol. 1, pp. 173-180.

Cho, N. Martin, C.D. Sego, D.C. and Christiansson, R. (2004), Modelling Dilation in Brittle Rocks. American Rock Mechanics Association ARMA/ narMS 04-483, Dept. of Civil and Environmental Engineering, University of Alberta, Canada

DETERMINATION OF THE EFFECT OF COLLECTOR CONFIGURATION ON THE THERMAL PERFORMANCE OF A SOLAR WATER HEATING SYSTEM

Zwalnan, S. Johnson[1], Caleb N. Nimmyel[2] Bongdap, Nanbol Keza[3]

1, Department of Metallurgical Engineering, Plateau State Polytechnic, Barkin-Ladi
2 Department of Computer l Engineering, Plateau State Polytechnic, Barkin-Ladi
3 Department of Mechanical Engineering, Nigerian Defence Academy, Nigeria

ABSTRACT

The use of solar water heating system to heat water for domestic and industrial application improves environmental impact and reduces greenhouse gas emissions through reduced dependence on fossil fuel for energy. However, the use of this technology is not commonly adopted due its initial high cost and lower thermal efficiency when compare to the conversional energy system. In this research, the effect of flat plate solar collector configuration on the thermal performance of an active solar water heating system was investigated. Two models of the active solar water heating system were developed in TRNSYS 16 software. The first system was modelled using a serpentine flat [plate solar collector as the heating unit. The second system was modelled using the riser-header flat plate solar collector. The two systems have the same design parameters and characteristic as shown in table 1. The performance of the system was then simulated under the same solar and weather data condition for two days in the month of November. The inlet temperature of the solar collector of the two systems were recorded simultaneously at an interval of 1 hour from 8.00 am to 5.00pm. To validate the predicted behavior of the modeled system, the performance of the two systems were experimentally measured on the same day as the simulated. The result of this investigation lead to the conclusion that the flat plate solar collector configuration has significant effect on the thermal performance of a solar water heating system and the computed values of Nash-Sutcliff coefficient of 0.82 between the modeled collector inlet temperature and the observed tank inlet temperature for the two days test confirm that the model formulation using TRNSYS software proposed here for the performance simulation of the system is valid, realistic and is a representative of the real system and can be used to estimate the dynamic behavior of the real system owning to the good quality of fit between experimental results and the simulated results

Key words: Simulation, TRNSYS Software, Riser-header flat plate, Serpentine flat plate,

Numeclature

T_{sim}-	Simulated temperature
T_{expt}-	Experimental temperature
T_{expt_ave}-	Average of experimental temperature

1.0 INTRODUCTION

The solar water heating system (SWHS) is one of the technologies used for the conversion of solar energy into heat for both domestic and industrial application[1] [2] . [3] reported that solar water heating system is an economical means of heating water especially for domestic application when compare to conventional water heating systems.. The energy saved from using a solar water heating system helps to reduce domestic energy demand from power utilities. The use of a solar water heating system improves environmental impact and reduces greenhouse gas emissions through reduced use of electricity [4]. However, the use of this technology is not commonly adopted due its initial high cost and lower thermal efficiency when compare to the conversional energy system. Most customers would

want to know their monthly saving if they were to convert to solar powered systems Different researches have been conducted by many researchers to determine the economics of adopting solar water heating systems for both domestic and industrial applications[5],[6]. In their conclusion all have agreed that the system has long term economic and environmental benefits when compare to the conventional energy systems[7],[8]. It is therefore very important to improve on the energy conversion efficiency of a solar water heating system so as to improve on the energy saving of the system. One way to improve the performance of solar water heating system is through proper sizing and arrangement of collector components, in such a way to maintain the temperature of the solar collector at temperature almost equal to the inlet fluid temperature[9]. Generally, poor collector performance is an indication of an inherently low poor sizing and geometric configuration [9] .

Many studies have been conducted to enhance the thermal performance of solar water heating systems, A study to investigate the effect of collector configurations on the thermal performance of photovoltaic thermal energy system (PVT) was carried by [10]. In this study the effect of collector configuration was studied along with the building implication for which the system was installed. The performance of four different PVT configurations was measured during an experiment. The result revealed that the four configuration investigated have different thermal and electrical performances. [11], [12], conducted an extensive review and investigation on various studies conducted in the area of enhancing the thermal performance of solar collectors by use of Nano fluid as working fluid in collectors' tubes. Various properties of the fluid were investigated to determine the sensitivity of the performance of the system to change in Nano fluid properties. The results of this research shows that the particle size, base fluid material, additives, particle shape, temperature, Ph value, particle volume concentration and Nano fluid stability have significant effect on the thermal performance of the system.

A numerical solution to determine the optimal design parameters of a solar flat plat collector designed to supply hot water was developed by [13] . Matlab software was used to model the time dependent behavior of flat plat collector. The sensitivity study shows that water output temperature and the overall heat loss coefficient decreases with increase in water flow rate, The output water temperature augments with the input temperature. Water flow rate of the system also a strong determinant the optimum number of solar collector tubes requires to give the maximum collector outlet water temperature.

Analytical solution based on the energy balance of a solar air heater flat plat using the climatic solar and weather data variables of Jeddah (lat. 21_ 420 N, long. 39_ 110 E) was modeled by [14] to study the thermal performance of a collector . The computer model was used to investigate the effect of the length and breadth of the collector on the collector air output temperature. The developed model was also used to study the performance of the air heater to determine the effect of selective coating materials on the solar air heater output temperature.

The result of the simulation shows that the solar air collector that was coated with   nickel–tin has better performance than collector coated with Galvanized Iron Copper oxide or nickel rhodium black or galvanized Iron Cobalt oxide and iron coated with nickel. The simulated result of the model was then compare with the result measured experimental using a collector that was coated with a black pant. An error of 7.7% between the modeled performance and the experimental performance of the system indicates a good agreement. This therefore validates the model used. It was also inferred that the annual average performance of with a nickel–tin selectively coated absorber is higher than that with a black painted absorber by 29.23%.

In this research, a simulation base approach was used to design simulate, construct and test an active solar water heating system under the weather data of Jos, Nigeria. The simulation model developed

using TRNSYS software was also used to determine the effect of flat plat collector configuration on the water output temperature an active solar water heating system designed,

The system was then constructed and tested based on the simulated system parameters and sizes The performance of the system was determined experimentally under the weather and solar condition of Jos. During the experiment, the collector inlet and outlet temperatures were measured.

2.0 MATERIALS AND METHODS.

2.1 System Description

The system consists of two active solar water heating systems integrated as a single system with a total collector area of $1.5m^2$. The first system consists of a flat plate solar collector tilted at 17° from horizontal with 8 copper tubes which convey the circulating fluid separated at equal distance to each held on the flat plate absorber constructed inside the collector casing in a serpentine fashion. The collector is interconnected to a vertical water storage tank of volume $0.03m^3$ to form a close cycle. Water is circulated through the system by means of a solar powered pump driven by 20 watts' solar panel. The second system is identical to the first system in all dimensions. The main difference is that the copper tubes constructed inside the collector casing is constructed in the 'Riser-header' fashion. The riser consist of 8 risers tubes whose total length is equal to the total length of the serpentine tube used in the first system. Figure1 below is the photograph of the constructed system used as the experimental grid during the experiment.
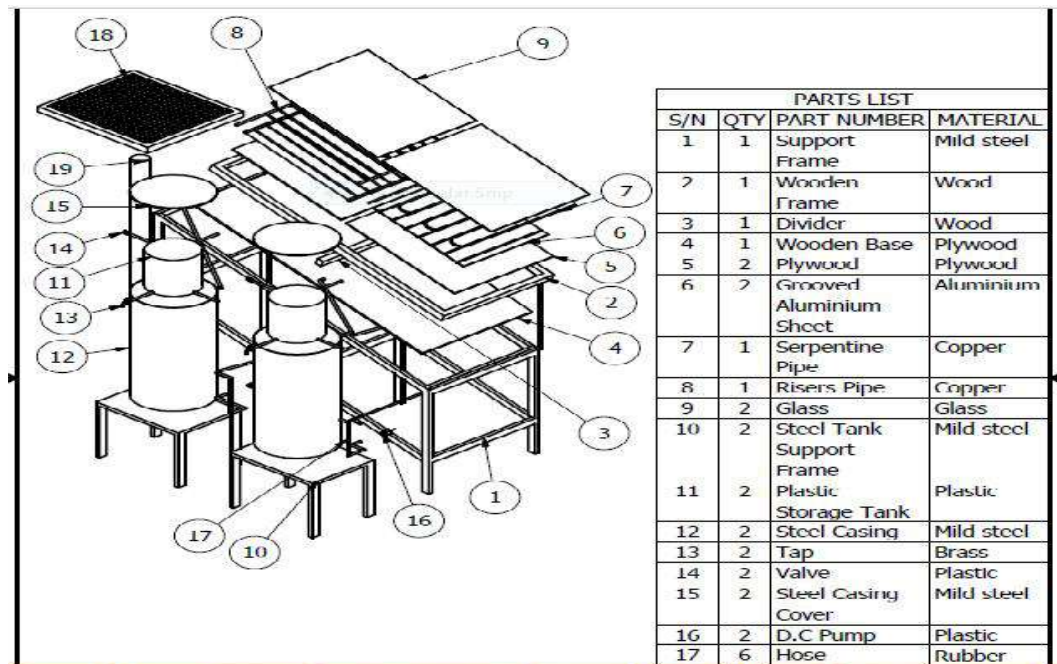

S/N	QTY	PART NUMBER	MATERIAL
1	1	Support Frame	Mild steel
2	1	Wooden Frame	Wood
3	1	Divider	Wood
4	1	Wooden Base	Plywood
5	2	Plywood	Plywood
6	2	Grooved Aluminium Sheet	Aluminium
7	1	Serpentine Pipe	Copper
8	1	Risers Pipe	Copper
9	2	Glass	Glass
10	2	Steel Tank Support Frame	Mild steel
11	2	Plastic Storage Tank	Plastic
12	2	Steel Casing	Mild steel
13	2	Tap	Brass
14	2	Valve	Plastic
15	2	Steel Casing Cover	Mild steel
16	2	D.C Pump	Plastic
17	6	Hose	Rubber

Figure 1: Exploded view of the experimental setup of an active solar water heating system.

2.2   Working Principle

When solar radiation from the atmosphere falls on the collectors, it heats the absorber surface within the solar collector. A heat-transfer fluid (water) flowing through the copper tubes attached to the

absorber plate picks up the heat from it and moves to the top of the storage tank by aid of a solar powered pumps. The pump again draws the water from the bottom of the tank and pumps it back into the collector and the cycle is continued until the sun goes down [15]. The process is self-controlled because it continues until there is no radiation from the sun since the pumps are powered by a solar panel. The heated water can be reheated by other forms of conventional heaters when the solar system fails to meet up the water temperature requirement.

2.3   System Design and Simulation

A simulation base approach using TRNSYS software was adopted for the design of the system. Two models of the solar water heating system were developed in TRNSY simulation studio (figure 2). In the first model, a serpentine flat plat solar collector was used as the heating unit while the second system adopts the riser-header flat solar collector as the heating unit. All other system parameters and characteristics are the same for both systems (Table 1). The two systems were simulated under the same weather condition and time. Figure 2 below show the model of the two systems developed in the TRNSY simulation studio. The system model was used to simulate the performance of the system on the 18th and 19th in the month of November 2017. The simulated performance of the two systems is shown in figure 3 and figure 4 for the 18th and 19th day of November 2017 respectively.
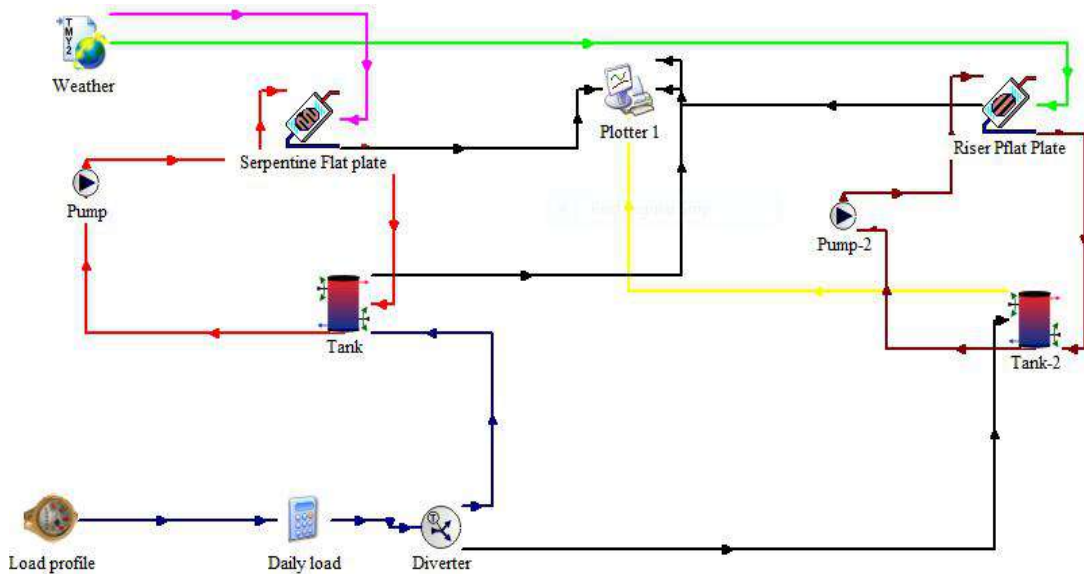

Figure 2: System model of the active solar water heating system in the simulation studio [16]

Table 1: System parameters and characteristics.

Sn	Parameters	Serpentine Flat Plate	Riser Flat Plate	Unit
1	Collector length	1.0	1.0	M
2	Collector width	0.8	0.8	M
3	Absorber plate thickness	5	5	Mm

4	Conductivity of absorber material	400	400	W/m.K
5	Number of serpentine bends/no of Risers	8	8	-
6	tube spacing	8	8	Cm
7	Serpentine/riser length	0.75	0.75	M
8	Inner tube diameter	1.5	1.5	mm
9	Outer tube diameter	2.0	2.0	cm
10	Fluid specific heat	4.190	4.190	kJ/kg.K
11	Absorptance of the absorber plate	0.9	0.9	Fraction
12	Emissivity of the absorber plate	0.9	0.9	Fraction
13	Number of identical covers	1	1	-
14	Index of refraction of cover material	1.526	1.526	-

2.4 Description of the Experimental Set-Up and Procedure

The constructed solar water heating system whose characteristics and configurations are as described in Figure 2 and Tables 1 was installed at Plateau State Polytechnic Clinic and was used to carry out the experiment. K-type Digital thermometers were mounted at the collector inlet and outlet of the two systems to measure the outlet and inlet temperatures of the collectors simultaneously at a time interval of 1 hour starting from 8.00 am to 5.00 p.m. for two days.

Figure 3: System experimental set-up

Each day within this test period, 0.03 m^3 of water was poured into the storage tank before 7.00 am. The inlet and outlet temperatures of the collectors were then recorded at an interval of 1.00 hour from 8.00 am to 5.00pm. To accomplish the above, a digital thermocouple was used to take the temperature reading by creating a hole in the inlet and outlet pipes of the collector and then inserting the sensor of the thermocouple into the holes to gain direct access to the water. Also, each day's experiment was

started by recording the temperature of the water in the storage tank, emptying the water tank and charging it with fresh water. During the experiment, no water was drawn off from the system. Temperature of 0.03 m³ (same volume as contain in the system) of water kept in a tank left in the open air was also measured and recorded at the same interval of time. This was used as a control to compare the effect of the heating system to open air heating.

3.0   Result and Discussion

3.1   Simulated System Performance

Figure 4 and figure 5 below shows the simulated collector inlet temperature variation from 8.00 am to 5.00 pm for 18th and 19th of November 2017 for the two systems respectively. Temperature of the two system rises steadily reaching its peak between 2.00 pm and 3.00 pm. This is because the variation of the water temperature of both systems is a direct response of the system to the available solar radiation of the location. Solar radiation from this location rises from morning and reaching its peak between 2.00 and 3.00 pm as shown in figure 8 below.

The performance of the systems was simulated for two days. This is to ensure repeatability of the pattern of performance shown at the first day during the test. The results recorded for the two days in figures 4 and 5 show very similar pattern in performance. The serpentine flat plate collector shows better performance than the riser-header flat plate in the morning as the solar radiation increases from morning to its peak at about 2.00 pm and 3.00pm, however, the performance of the serpentine system is lower than the riser flat plate solar collector when the solar radiation starts dropping. The riser-header system shows better performance at a period that the solar radiation is dropping after the peak period. The implication of the pattern of behavior exhibited by the two systems is that the serpentine flat plat collector system loses its water temperature faster than the riser-header flat plate solar collector when the solar radiation drops from a higher value to a lower value especially in the evening. This then implies that the riser-header system can maintain higher water temperature in the evening than the serpentine flat plate system. On the other hand, the serpentine system gives higher water temperature from morning till when the radiation is peak. The implication is that this system is better in meeting hot water demand of facilities whose hot water demand lies between the period of 8.00 am to 2.00 for the said location.
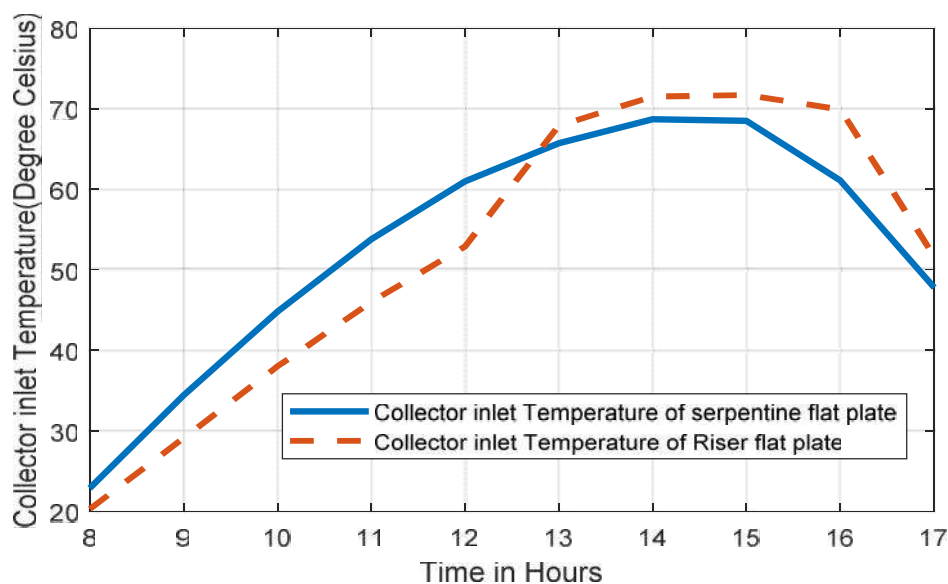

Figure 4: Comparison of the simulated thermal performance of the serpentine and Riser-Header
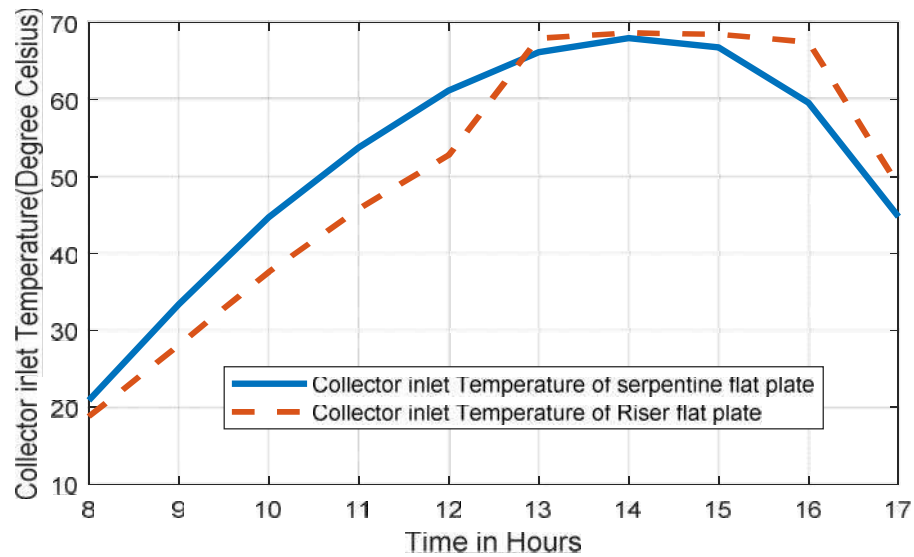
flat plate solar collector. (18th November 2017)

Figure 5: Comparison of the simulated thermal performance of the serpentine and Riser-Header flat plate solar collector. (19th November 2017)

3.2 Experimental System Performance

figure 6 and 7 shows the experimental performance of the systems recorded during the 2 the day's test performed on the 18 and 19th of November 2017. These test days are the same as the days used for the simulation of the systems using TRNSYS software under the weather data of Jos, Nigeria. The thermal behavior of the system shows very similar trend in the collector inlet temperature recorded from 8.00am to 5.00 pm. The measured thermal performance of the system shows good agreement with the simulated performance with a Nash-Sutcliffe Coefficient of Efficiency (NSE) of 82% (Table 2) which means that the model formulated using TRNSYS software is valid and can predict the thermal performance of the real system with an accuracy of 82%. The result obtained also shows that solar water heating system have big advantage over open air heating as there is a huge difference between the temperature of water heated by the open air solar radiation and the water heated by the solar system.
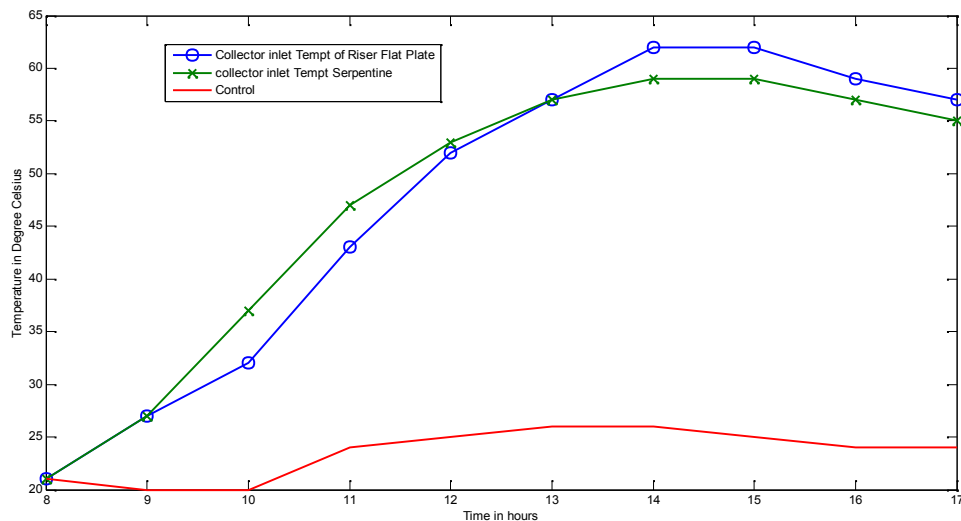
Figure 6: Comparison of the experimental thermal performance of the serpentine and Riser-Header flat plate solar collector. (18th November 2017)
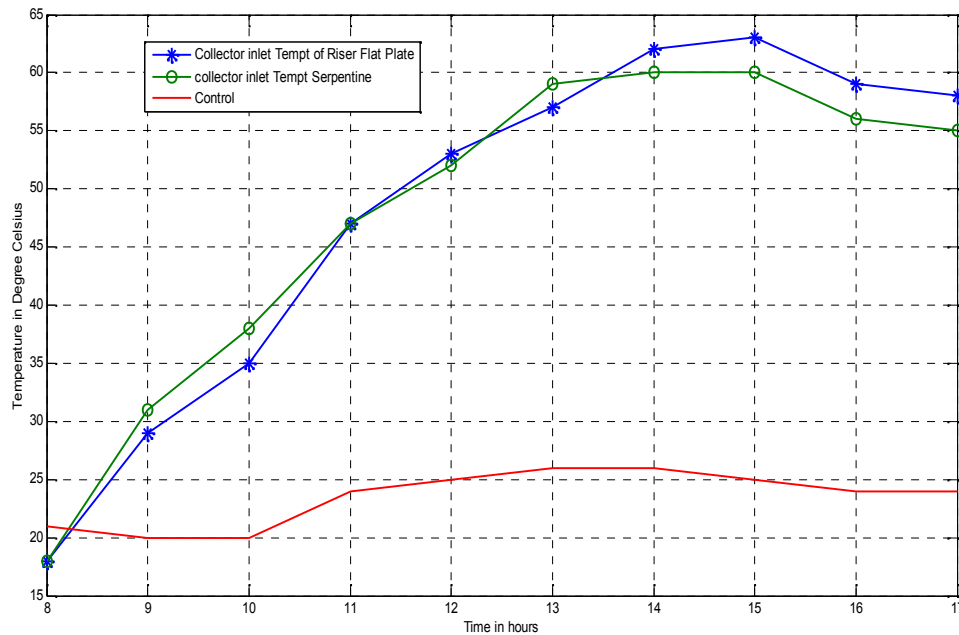

Figure 7: Comparison of the experimental thermal performance of the serpentine and Riser-Header flat plate solar collector. (19th November 2017)

3.3 Validation of Simulation Model

The Nash-Sutcliffe Coefficient of Efficiency (NSE) was employed to compare the simulated and experimental results in order to validate the simulated model.
The Nash-Sutcliffe Coefficient of Efficiency (NSE) is defined as:

$$\text{NSE} = 1 - \frac{\sum_{i=1}^{n}(X_{obs,i} - X_{model,i})^2}{\sum_{i=1}^{n}(X_{obs,i} - \overline{X}_{obs})^2} \tag{1} [17]$$

where:

X_{obs} is the observed value

X_{model} is the modelled value at time/place i.

$\overline{X}_{obs}$ is the mean of the observed value.

The value of the NSE ranges from $-\infty$ to 1. A computed NSE value 1 indicates a perfect match between model and experimental values. The closer the NSE value is to 1 the better the predictive power of the model used to simulate the real performance of the system.
Table 2 and 3 show the calculation of the NSE between the experimental and the simulated performance of the two systems.

Table 2: Calculation of NSE between the simulated and experimental performance of the serpentine system.

Time	Tsim (ºC)	Texpt (ºC)	(Tsim - Texpt) (ºC)	(Tsim - Texpt)^2 (ºC)	(Texpt-Texpt_ave)^2 (ºC)
8	2.03E+01	1.90E+01	1.3	1.7	607.0

9	2.91E+01	2.90E+01	0.1	0.0	214.2
10	3.80E+01	3.50E+01	3.0	9.0	74.6
11	4.60E+01	4.60E+01	0.0	0.0	5.6
12	5.29E+01	5.20E+01	0.9	0.8	70.0
13	6.79E+01	5.60E+01	11.9	141.5	152.9
14	7.15E+01	6.30E+01	8.5	72.0	375.0
15	7.17E+01	6.40E+01	7.7	59.6	414.7
16	6.99E+01	5.90E+01	10.9	118.1	236.0
17	5.17E+01	5.70E+01	-5.3	27.6	178.6
Total	**5.19E+02**	**4.80E+02**	**39.08**	**430.36**	**2328.41**
Ave	**47.18915**	**4.36E+01**			
RSME			**6.25%**		
NSE			**0.82**		

Table2 : Calculation of NSE between the simulated and experimental performance of the Riser-header system**.**

Time	Tsim (ºC)	Texpt (ºC)	(Tsim - Texpt) (ºC)	(Tsim - Texpt)^2 (ºC)	(Texpt-Texpt_ave)^2 (ºC)
8	1.88E+01	2.30E+01	-4.2	17.5	392.8
9	2.81E+01	2.60E+01	2.1	4.6	282.9
10	3.76E+01	2.80E+01	9.6	92.7	219.6
11	4.58E+01	4.40E+01	1.8	3.4	1.4
12	5.28E+01	5.00E+01	2.8	7.8	51.6
13	6.80E+01	5.50E+01	13.0	168.5	148.4
14	6.87E+01	6.40E+01	4.7	21.8	448.7
15	6.85E+01	6.40E+01	4.5	20.0	448.7
16	6.75E+01	6.00E+01	7.5	56.2	295.2
17	4.88E+01	5.70E+01	-8.2	66.5	201.1
Total	**5.05E+02**	**4.71E+02**	**33.68414528**	**459.055381**	**2490.24**
Ave	**45.88038**	**4.28E+01**			
RSME			**6.46%**		
NSE			**0.82**		

The analysis gives a Nash-Sutcliff coefficient (NSE) value of 0.82. between the modeled collector inlet temperature and the observed collector inlet temperature for the two systems. This then means that the model formulation using TRNSYS software proposed here for the performance simulation of the system is valid, realistic and is a representative of the real system and can be used confidently to estimate the dynamic behavior of the real system owning to the good quality of fit between experimental results and the simulated results. This means that the model used for the predicting the thermal is 82% accurate in predicting the actual performance of the system base on the weather data used for the simulation.

4.0 Conclusion

This research is aimed at investigating the effect of solar flat plate configuration on the thermal performance of an active solar water heating system. To achieve this aim, an active solar water heating system was simulated using TRNSYS software. The system was also constructed and tested for two days. The result of this investigation lead to the following conclusion

1 The flat plate solar collector configuration has effect on the thermal performance of a solar water heating system.
2 The serpentine flat plat solar collector performs better than the riser flat plat solar collector from the early hours of the morning to hours where the radiation is maximum. This makes it best suitable for facilities whose hot water demand lies within morning and noon.
3 The serpentine flat plat solar collector loses its temperatures faster than the riser flat plat solar collector when solar radiation starts dropping after attaining its peak value. This again suggest that for facilities whose hot water demand lies in the evening, the riser plat solar collector is more suitable than the serpentine solar system.
4 The computed values of Nash-Sutcliff coefficient of 0.82 between the modeled collector inlet temperature and the observed tank inlet temperature for the two days test confirm that the model formulation using TRNSYS software proposed here for the performance simulation of the system is valid, realistic and is a representative of the real system and can be used to estimate the dynamic behavior of the real system owning to the good quality of fit between experimental results and the simulated results.

References

[1] S. Gautam, A., Chamoli, S., Kumar, A., & Singh, "A review on technical improvements, economic feasibility and world scenario of solar water heating system.," Renew. Sustain. Energy Rev., vol. 68, pp. 541–562, 2017.
[2] A. Gautam, S. Chamoli, A. Kumar, and S. Singh, "crossmark," Renew. Sustain. Energy Rev., vol. 68, no. August 2016, pp. 541–562, 2017.
[3] S. Hussain and S. J. Harrison, "Evaluation of thermal characteristics of a flat plate solar collector with a back mounted air channel," Appl. Therm. Eng., vol. 123, pp. 940–952, 2017.
[4] L. Romero et al., "Analysis of the economic feasibility and reduction of a building ' s energy consumption and emissions when integrating hybrid solar thermal / PV / micro-CHP systems," vol. 165, pp. 828–838, 2016.
[5] M. Ã. Smyth, P. C. Eames, and B. Norton, "Techno-economic appraisal of an integrated collector / storage solar water heater," vol. 29, pp. 1503–1514, 2004.
[6] T. Lang, D. Ammann, and B. Girod, "Pro fi tability in absence of subsidies : A techno-economic analysis of rooftop photovoltaic self-consumption in residential and commercial buildings," Renew. Energy, vol. 87, pp. 77–87, 2016.
[7] C. J. Koroneos and E. A. Nanaki, "Life cycle environmental impact assessment of a solar water heater," J. Clean. Prod., vol. 37, pp. 154–161, 2012.
[8] A. Abdon, X. Zhang, D. Parra, M. K. Patel, and C. Bauer, "Techno-economic and environmental assessment of stationary electricity storage technologies for different time scales," vol. 139, 2017.
[9] J. A. D. Deceased and W. A. Beckman, of Thermal Processes Solar Engineering. 2006.
[10] V. Tomar, B. Norton, and G. N. Tiwari, "A novel approach towards investigating the performance of different PVT con fi gurations integrated on test cells : An experimental study," Renew. Energy, 2017.
[11] P. Raj and S. Subudhi, "A review of studies using nano fl uids in fl at-plate and direct absorption

solar collectors," Renew. Sustain. Energy Rev., vol. 84, no. January, pp. 54–74, 2018.

[12] F. Kiliç, T. Menlik, and A. Sözen, "E ff ect of titanium dioxide / water nano fl uid use on thermal performance of the fl at plate solar collector," Sol. Energy, vol. 164, no. February, pp. 101–108, 2018.

[13] M. Hamed, A. Fellah, and A. Ben Brahim, "Parametric sensitivity studies on the performance of a flat plate solar collector in transient behavior," Energy Convers. Manag., vol. 78, pp. 938–947, 2014.

[14] A. . El-Sebaii, "Effect of selective coating on thermal performance of flat plate solar air heaters," Energy, vol. 35, pp. 1820–1828.

[15] A. . & C. P. Soteris, "Modelling of a Thermosyphon Solar Water Heating System and Simple Model," Renew. Energy, vol. 21, pp. 471–493, 2000.

[16] R. L. Shrivastava, V. Kumar, and S. P. Untawale, "Modeling and simulation of solar water heater : A TRNSYS perspective," Renew. Sustain. Energy Rev., vol. 67, pp. 126–143, 2017.

[17] A. S. Julien, G. A, Emmanuel, L., Clément, A., Rufin, O. A., and Brice, "Modeling solar energy transfer through roof material in Africa Sub-Saharan Regions," ISRN Renew. Energy, vol. 34(, no. 7, 2013.

EXPERIMENTAL DETERMINATION OF THE EFFECT OF ENGINE SPEED AND RUN TIME OF THE TIMING BELT GEOMETRY OF PEUGEOT 307

Y. Tanimu[1], A. B. Hassan[2]and B. Alkali[2], M.M Mohammed[1] and Clifford O. Ogheneme[3].

[1]Department of Mechanical Engineering, Federal Polytechnic, Bida, Niger State.
[2]Department of Mechanical Engineering, Federal University of Technology, Minna.
[3]Department of Mechatronics Engineering, Federal University of Technology, Minna.
[4]Department of Mechanical Engineering, Waziri Umaru Federal Polytechnic, Birnin Kebbi, Kebbi State.
*Corresponding Email: tanson3006@yahoo.com

ABSTRACT

The operation of the timing belt is very critical to the performance of an automobile engine and the behavioural function is largely unpredictable especially on a poor road pavement and poor maintenance services. During operation timing belt are subjected to excessive elongation and wear. These detonation properties contribute to the timing belt running life and quality. The failure of the timing belt for some engine especially 307 means that apart from replacing the time belt, some part of the engines can be damage that is bent valves. In this Paper, the effect of the engine speed, run times on the timing belt geometry were investigated. The results obtained shows that the Pitch and groove thickness of the belt were more affected than the width and the total height and also that the engine speed has a positive correlation with the Pitch while the groove thickness has a negative correlation with the engine speed and that means failure will occur from these factors.

Keywords: Timing belt, Engine speed, Run time, Pitch, Groove thickness

1.0   INTRODUCTION

 The auto-industry is one of the important sector of any economy. From past two decades optimum vehicle design is a prime concern in front of automobile industry. The timing drive system of an automobile is one of the most important system of an engine. The function of a timing drive is to transfer the rotation of crankshaft to camshaft and fuel Injection Pump (FIP) and other connected accessories so as to achieve proper timing at valves and the timing for fuel injection. Timing drive consisting of timing belts, timing belt/chains and timing gear drives.(Aniket and mulik, 2016) . A timing belt is located on the front side of the vehicle's engine and behind the plastic cam belt covers. It is designed to reduce the friction as well as generate more horsepower in an engine. The belt helps to keep the engine in check, preventing the valves from reaching and hitting the pistons.

Older belt have trapezoid shaped teeth leading to high rates of tooth wear. Newer manufacturing techniques allow for curved teeth that are quieter and last longer. Aftermarket timing belts may be used to alter engine performance. Original equipment manufacturer (OEM) timing belts may stretch at high revolution per minute, retarding the cam and therefore the ignition. (Simmens, 2009). Stronger, aftermarket belts, will not stretch and timing was preserved (Goodyear, 2010). In terms of engine design, 'shortening the width of the timing belt reduces weight and friction' (Mitsubishi, 2005).

Timing belts are typically covered by metal or polymer timing belt covers which require removal for inspection or replacement. Engine manufacturers recommend replacement at specific intervals (Gates, 2010). The manufacturer may also recommend the replacement of other parts, such as the water pump, when the timing belt is replaced because additional cost to replace the water pump is negligible

compared to the cost of accessing the timing belt. Indicators that the timing chain may need to be replaced include rattling noise from the front of the engine. (Siegel, 2007).
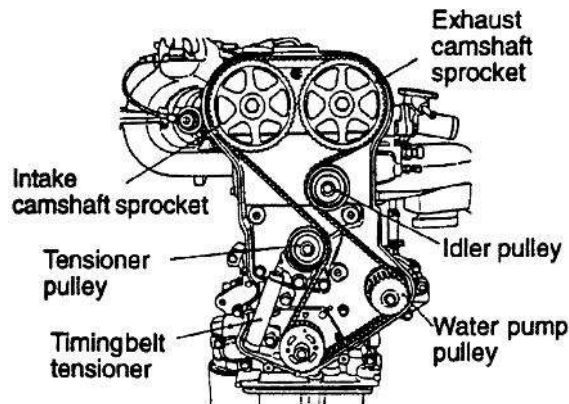

Figure 1: Engine timing system parts identification (www.autozone.com).

2.0 MATERIALS AND METHODS

2.1 Materials

Engine timing systems utilize the following components: idler or pulley, tensioner, hydraulic damper pivot arm and water pump as shown in Figure 2 below

Figure 2: Timing components (www.autozone.com)

2.2 Experimentation

The experimental setup comprises of a Peugeot 307 vehicle, a timing belt and a digital veneer calliper. It is desire to measure the timing belt wear as it run over a time period. Therefore, the table used to conduct the experiment were presented in the table 1. The Vanier calliper was used to record the geometric defects on the timing belts as it run over the time period, the speedometer on the dash board were used to record and set the engine speed of the at 1000rpm, 1500 rpm and 2000rpm for a period of four (4) hrs each. The images taken during the experimentation are presented in figure 3.

The timing belt used in this study has 140 teeth with a width of 24.76 mm and a pitch of 13.46 mm. Crank shaft pulley with 20 teeth drives two cam shaft pulleys with 40 teeth each through the timing belt.
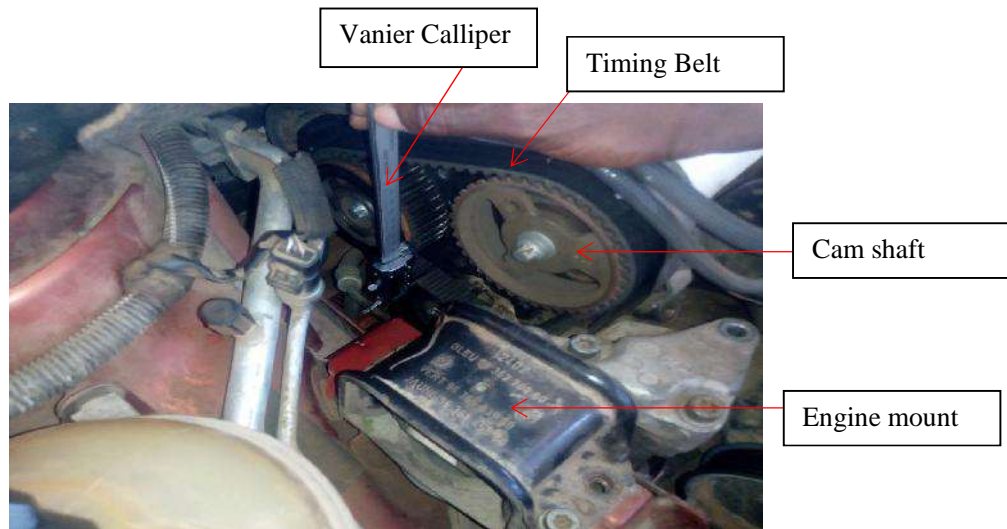
Figure 3: Image of experiment

2.3 Digital Vanier Calliper

The digital calliper used for measuring the variation in belt geometry is shown in Figure 4 below; it is portable and has up to four (4) decimal digits.

Figure 4: The Vanier Calliper.

3.0   Results and Discussion

The variation of the Timing belt Geometry obtained from the result of Experimental analysis was tabulated as shown in the table 1.

Table 1: Experimental results of analysis of timing belt geometry of Peugeot 307

ENGINE SPEED (RPM)	OPERATION TIME (Hrs)	PITCH (mm)	WIDTH (mm)	GROOVE THICK.(mm)	TOTAL HEIGHT (mm)
0	0	13.46	24.76	2.56	5.92
1000	0.5	13.475	24.76	2.480	5.92
	1	13.480	24.76	2.440	5.91
	2	13.488	24.76	2.390	5.91
	4	13.490	24.76	2.340	5.90
1500	0.5	13.477	24.76	2.475	5.90
	1	13.482	24.76	2.430	5.90
	2	13.492	24.76	2.370	5.90
	4	13.495	24.76	2.310	5.90
2000	0.5	13.479	24.76	2.470	5.90
	1	13.485	24.76	2.400	5.90
	2	13.494	24.76	2.340	5.90
	4	13.496	24.76	2.290	5.90

The graph of timing belt Pitch wear against run time was plotted as shown in Figure 5 below. (P = Pitch)
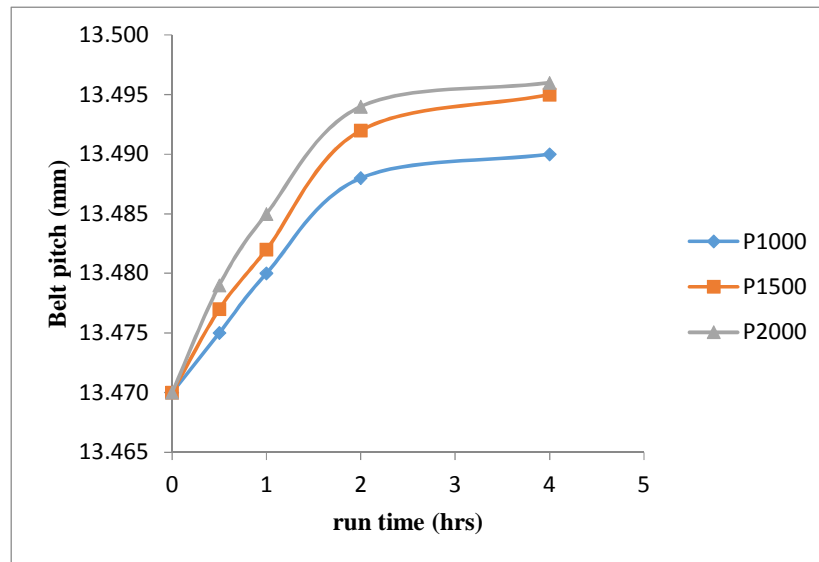

Figure 5: Effect of pitch against run time

The Figure 6 below represents the plotted graph showing the effect of belt Pitch against Engine speed.
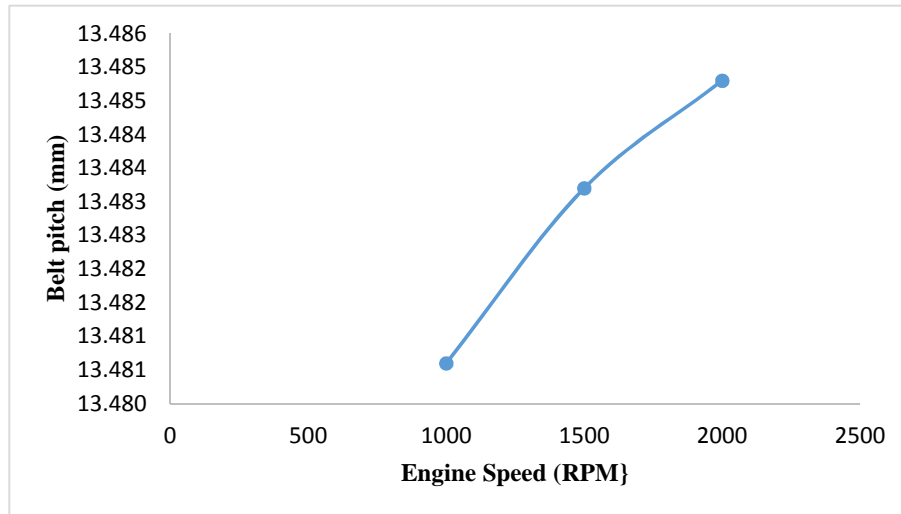
Figure 6: Effect of belt Pitch against Engine speed

The graph showing the relationship between belt groove thickness and run time was plotted as shown in figure 7 below. (T= Groove thickness)
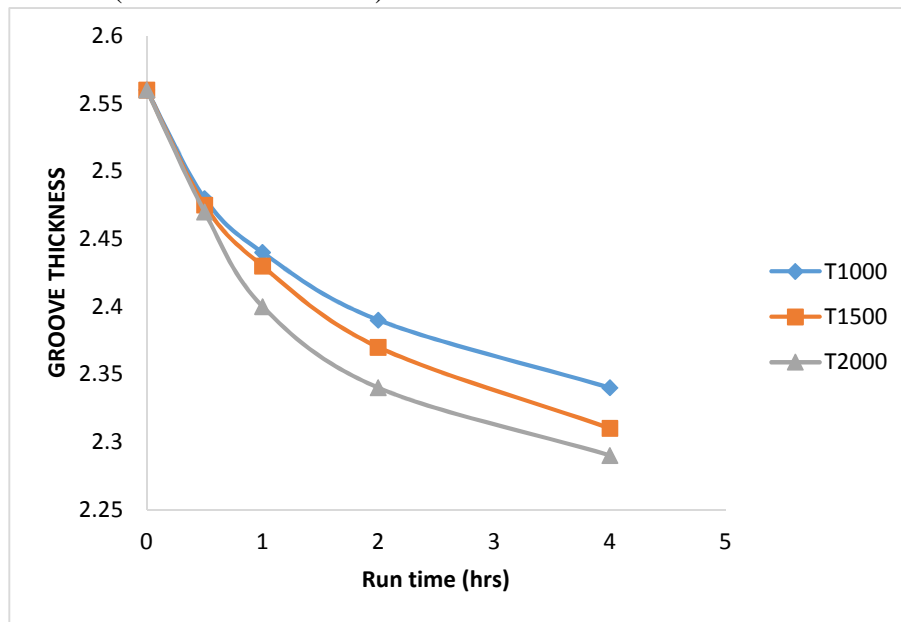

Figure 7: Effect of belt groove thickness against run time

The figure 8 below represents the plotted graph showing the effect of belt groove thickness against Engine speed
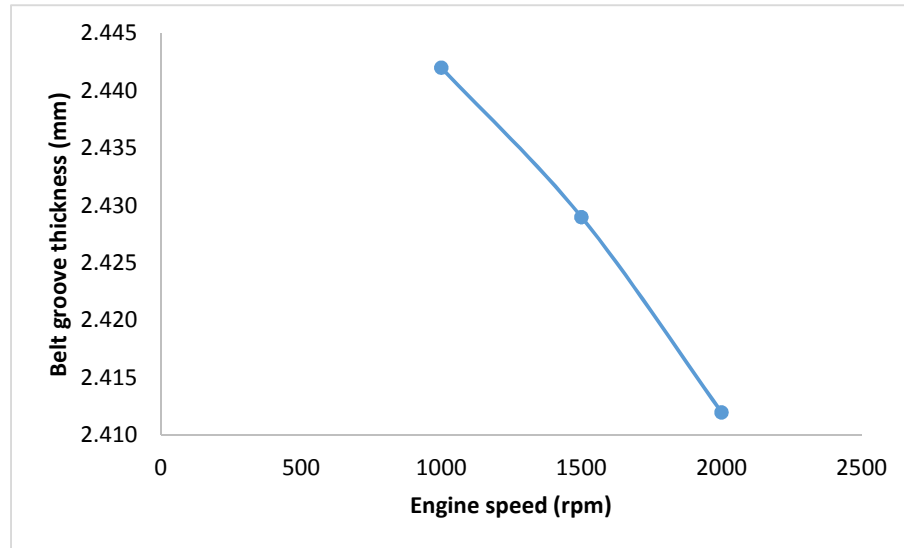
Figure 8: The effect of belt groove thickness against Engine speed

By monitoring the parameters in the period of working out, Figure 5 and 6 shows that the pitch and the thickness wear were more pronounced between 0-2 hours of operation after which they becomes approximately linear. It was also observed from Figure 7 that there is a linear relationship between the Engine speed and the belt pitch. Increase in speed will cause the pitch wear to increase accordingly, whereas from Figure 8 increasing the speed reduces the groove thickness.

4.0 Conclusions

The research studied the effects of run time and speed on the timing belt geometry. The result reveals that the run time and engine speed affects the belt pitch and the groove thickness, but the pitch is more affected than the belt width and the total height of the belt. Therefore all the common culprits of failure in timing belt analysis deeply focused on the variable effects performed under all the common culprits. Also with this paper it can be conclude that the lifetime dependency and influenced factors of timing belt drives will help us to provide guidance while occurring on those damages of belts and also the study of various effects on failure analysis steps of common study resulting on a decreasing performance that further lead to help for saving our money and valuable time of maintenance.

References
Aniket, V., & Gujar, A. (2016). Literature review on simulation and analysis of timing belt of an automotive engine. International journal of Engineering research and application, Vol 6, Issue 8, (part 1) pp.17-21.
Dolan, J. A. (1971). Motor vehicle technology and practical work: parts 1 and 2. Heinemann Educational Publishers.
Gates. (2010, may 12). Gates 2010 Timing belt installation manual. Retrieved may 16, 2018, from www.autoserviceworld.com
Goodyear. (2010). Good year introduces Timing belt tools. Retrieved from www.autoserviceworld.com
Krumi, R. S., & Gupta, J. K. (2008). A Textbook of Machine Design . New Delhi: Euroshia.
Norbye, J. p. (1984). Expanding on Excellence. The 5-Series and 3-Series". BMW - Bavaria's Driving Machines. Skokie, IL, USA: Publications International, p. 192. ISBN 0-517-42464-9.

Ritch, O. (2014). Small bore big pull. Retrieved from https:web.archive.org

Siegel, i. (2007, April 5). Rattling noise could be from worn timing belt. Retrieved from Chicago sun times: https://web.archive.org

Simmons, K. (2009, February). Timing to win ignition timing for maximum performance. Retrieved from Circle track magazine: www.hotrod.com

Steven H. (2012), Safety Considerations in Optimal Automotive Vehicle Design, A phd Thesis, The University of Michigan.

Stojanovic, B., Ivanovic, L., & Blagojevic, M. (2011). Failure Analysis of the timing belt drives. International Conference on Tribology in Serbian Tribology Society, Vol. 21 pp.210-215.

Stojanovic, B., Tanasijevic, N., & Miloradovic, N. (2009). Trobomechanical systems in Timing belt drives. Journal of balkan tribological association, Vol 15, No. 4 465-473.

Temple, S. (2004). Behold your timing belt: keeping the camshaft and crankshaft in sync. Retrieved from Know how advance auto parts: https://web.archive.org

Kost F. (2014). Basic principles of vehicle dynamics. In: Reif K. (eds) Fundamentals of Automotive and Engine Technology. Bosch Professional Automotive Information. Springer Vieweg,

Wiesbaden. Retrieved from https://link.springer.com/chapter/10.1007%2F978-3-658-03972-1_10#citeas

EFFECT OF PLASMA ARC CUTTING PROCESS PARAMETERS ON THE SURFACE ROUGHNESS AND KERF WIDTH OF MILD STEEL USING DESIGN OF EXPERIMENT

Agbonoga, E. A[1], Lawal, S. A[1].
Department of Mechanical Engineering, Federal University of Technology, P.M.B 65 Minna, Niger State, Nigeria.
*Corresponding author email: agbonogaanderson@gmail.com, +243 803 8640 348.

Abstract

The desire to achieve cuts which are cost effective with lower material wastage, superior surface finish and high dimensional accuracy has opened an avenue to improve the plasma cutting process. The plasma arc cutting (PAC) process is used in the manufacturing industries as a result of the possibilities to cut various types of electrically conductible materials. This study investigated the effects of process parameters of PAC of low carbon steel. Three process parameters, cutting speed, cutting current and gas pressure were considered and experiments were conducted based on response surface methodology (RSM) via the box-Behnken approach. Process responses viz. surface roughness (Ra) and kerf width of the cut surface were measured for each experimental runs. Lower kerf width means industry can cut more metal in same period of time as a result of less material wastages which ultimately results in more profit and less surface roughness making finished product more suitable for assembly and easy handling. For minimum surface roughness and minimum kerf width, process parameters were optimized using the RSM and Analysis of Variance (ANOVA) was performed to get the contribution of each process parameters on responses and it was found that cutting current and gas pressure had the most significance on the surface roughness and kerf width respectively. This paper concludes that superior surface finish, cost effective cutting and longer life of consumables can be achieved if cutting is performed at optimum parameter.

Keywords: Cutting speed, cutting current, gas pressure, RSM, low carbon steel, surface roughness, kerf width, Anova.

1.0   INTRODUCTION

Plasma could also be referred to as the fourth state of matter, it is an electrically charged gas as a result of the increase in temperature of the gas and the plasma arc operates at temperatures as high as 30,000º C (Nemchinsky and Severance 2006). At the increase in temperature of a solid a change of state occurs thereby transforming this solid into liquid and if the process continues the liquid is converted to gas. When the gas is heated further, it gets converted into a plasma state (Patel et al. 2018). Plasma cutting is a thermal cutting process which makes use of plasma to cut metals of thickness ranging up to 80 mm which are electrically conductible, the PAC process can be employed in various fields of engineering and manufacturing industries (Pawar and Inamdar, 2016). The use of plasma arc cutting offers several advantages over other thermal cutting techniques with respect to cutting speed and cost when compared to oxy-fuel cutting and water jet cutting, also, plasma arc cutting has the capability to cut through the greater metal thickness when compared to the laser beam cutting technique (Krajcarz, 2014). The PAC process can be employed in the cutting of mild steel, stainless steel, high hardness and high melting point metals and other metals which are difficult to machine (Xu et al. 2002). Due to a pressurised gas flow from the arc, a groove is created and the pressure of the gas blows away the molten metal in the groove. Before cutting takes place an electric arc is created between the electrode and the workpiece,

water or air is used to cool the electrode placed in a nozzle of the torch. A transmission of the plasma gas through the nozzle enabling the plasma gas to forcefully pass through the orifice of the nozzle thereby increasing the velocity and of the gas, the temperature of the gas is increased and the atoms become electrically charged thereby creating plasma. The gas returns back to its normal state as a result of heat transfer when it comes in contact with the surface of the workpiece. To begin the PAC process, and electrically charge the gas, a small initial arc is created, it is responsible for increasing the temperature of the gas. The main arc is then created and since it has more resistance to electricity than the initial arc, it ignites and extinguishes the smaller arc. (Ferreira et al. 2009).

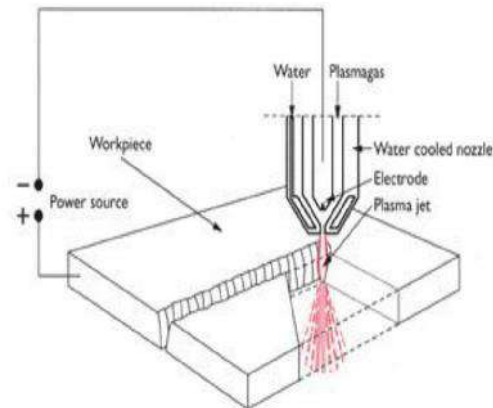## 1.1   Mode of Operation of Plasma Arc Cutting

Figure 1: Principle of Plasma Arc Cutting(Patel et al. 2018).

The fundamental principle of the PAC boils down to the copper nozzle with a hafnium electrode which creates an arc between the electrode and the surface of the workpiece. Also, the plasma gas flow is increased during cutting so that a deeper penetration can be achieved to enable the high velocity plasma to cut through the material and remove all the molten material present in the groove created (Radovanovic, 2011).

Most plasma cutting operation is guided by the mindset of the operator which is typically as a result of the recommendations of the manufacturers of the machines and the consumables. These recommendations don't always yield the best result in terms of quality of cut as they are proffered to boost the business of the manufacturer. As a result of this, the machine operator try's to improve the cutting operation by trial and error method every time a cutting operation needs to be performed, the trial and error method is time consuming, permits the wastage of material and cannot be repeated. (Bidajwala and Trivedi, 2014). Although, this process could prove to be effective when used by an operator who has the relevant experience, but it is not a dependable optimization process. Therefore, it does not allow for repetition or further usage of the knowledge that was acquired in this manner. The disadvantages of this process can be avoided through the use of design of experiments (DoE), as a means of attaining empirical models that can be used to predict the optimal process parameters in cutting operations that have not yet been performed. Bidajwala and Trivedi, (2014) carried out a review on the optimization of the plasma cutting process parameter of stainless steel 304L. It was noted that proper care has to be taken while trying to optimize the plasma cutting process, the parameters has to be adjusted properly putting in focus the most recent standard in other to achieve the best results, therefore, failure investigation can focus on the further issue of plasma arc cutting technology i.e. selecting the machining parameter which causes decrease in the surface roughness and increase the metal removal rate. Ferreira et al. (2009) carried out an optimization of the plasma cutting process using response surface methodology. From the results of the investigation, it was discovered that to

obtain the optimum cutting parameter all the process variable had to be considered, also, it was discovered that the current and gas pressure plays a vital role in determining the quality as they cause an increase in energy and flow of the plasma gas respectively. In the work of Adalarasan et al. (2014) carried out the multi variable optimization of the plasma cutting process on stainless steel 304L material using the grey taguchi based response surface methodology (GT-RSM), The results of the experiment showed that with a speed of 2335 mm/min, a better quality output was achieved because the increase in cutting speed causes the arc to loose stability thereby creating a deviation from the torch and in turn increasing the size of the kerf width. Maity and Bagal (2015) employed the hybrid approach to determine the effect of process parameter on the quality of the plasma arc cutting of stainless steel. It was discovered that all the machine parameters affected the quality of the cut directly with some minor interactions. The objective of this research is to investigate the effect of plasma arc cutting parameters on the quality of low carbon steel material of 5mm thickness using design of experiment via the response surface methodology to determine the experimental pattern. Analysis of variance is also performed to check the significance of the process parameters on the responses.

2.0   Materials and Methods

2.1   Materials

Low carbon steel of 5 mm thickness was selected as the workpiece material for this study. It is the most widely used type of steel as a result of its cost effectiveness, it contains 0.05-0.25 % carbon which makes it malleable and ductile with suitable application in general purpose engineering and construction (Groover 2010).

2.2 Experimental Design

In this study the experimental design used is the response surface methodology of the design of experiment. The cutting speed, cutting current and gas pressure was selected as the input parameters. The Box-Behnken approach of the response surface methodology was selected for this research over the central composite design because Box-Behnken requires three different levels for three factors and a total of fifteen experimental runs which is significantly easier for DOE as less time will be required, and the runs do not include factors outside the minimum/maximum values of the study area. The number of experiments required for 3 factors is 15 as prescribed by the DOE.

The cutting operation was performed in Prototype Engineering Development Institute, Ilesha, Osun state, Nigeria, using the Hyperthem Powermax 1650 plasma cutting machine. The independent variable selected are the cutting speed, cutting current and gas pressure as shown in the Table 1.

A total of 15 runs as shown in Table 2 was carried out without blocks or repetition. The experimental design consists of 3 process parameters and the DOE prescribes three levels which are low represented as -1, medium as 0 and high as 1. The design of the numbers of experimental runs are shown in Table 1.

Table 1: Factor levels for process parameters.

Variables	Unit	Coded Level		
		L_1	L_2	L_3

Cutting Speed CS	mm/m	1000	1500	2000
Cutting Current CC	A	60	80	100
Gas Pressure GP	bar	5.5	6.0	6.5

Table 2: Experimental design matrix

Runs	CS (mm/min)	CC (A)	GP (bar)	CS	CC	GP
1	-1	-1	0	1000	60	5.5
2	1	-1	0	2000	60	5.5
3	-1	1	0	1000	100	5.5
4	1	1	0	2000	100	5.5
5	-1	0	-1	1000	80	5.0
6	1	0	-1	2000	80	5.0
7	-1	0	1	1000	80	6.0
8	1	0	1	2000	80	6.0
9	0	-1	-1	1500	60	5.0
10	0	1	-1	1500	100	5.0
11	0	-1	1	1500	60	6.0
12	0	1	1	1500	100	6.0
13	0	0	0	1500	80	5.5
14	0	0	0	1500	80	5.5
15	0	0	0	1500	80	5.5

2.4 Experimental setup

The cutting of low carbon steel was conducted as specified by the experimental design. All experimental runs were carried out using the Hyperthem Powermax 1650 CNC Plasma cutting machine. The cuts were carried out on the 5mm thick low carbon steel sheets.

Figure 1: The Specimen.

The specimens were made up of a 150 mm by 100 mm rectangle, this is in order to measure the surface roughness and the kerf. The measurement of the kerf width was performed first as the cutting operation was going on, three measurements were taken on each side and the average was recorded as the value for that cut. The measurement was done with a digimatic Vernier caliper. The surface roughness was measured after the material had cooled and it was done on each surface at the middle of the surface of the cut after which the average was recorded as the overall response. The surface roughness was measured using the SRT-6200 surface roughness tester.

Figure 2: Plasma cutting machine and workpiece

3.0 Result and discussion

3.1 Signal to Noise (S/N) ratio

The lower the better attribute was used to calculate the signal to noise ratio for the surface roughness and kerf width. The smaller the better was utilized in this study because a lesser surface roughness and kerf width is required. The signal to noise ratio was used to generate the main effect plot for each individual response in order to generate the optimized value for each individual response. Equation (1) represent the Smaller the Better attribute for signal to noise ratio.

$$S/N = -10 \text{ x log} \left(\frac{1}{N} \sum_{j=1}^{N} \frac{1}{y_{ij}^2} \right) \qquad (1)$$

where i is the total number of experimental runs, y is the observed data, n is the number of observations and j is the trial number. Equation (1) represents S/N ratio for smaller the better responses.

3.2   Analysis of variance

The analysis of variance (ANOVA) was carried out using Minitab 17 software for each of the quality parameter to obtain the effect of each process parameter on the quality. Table 4 shows the ANOVA for the surface roughness while Table 5 shows that of the kerf width. The ANOVA analysis was done with the 90% confidence interval as prescribed by Meyers et. al (MYERS et al. 2009).

Table 3: Experimental Results and Signal to Noise Ratio

Runs	Input					S/N Ratio	
	CS (mm/min)	CC (A)	GP (bar)	SR (μm)	KW (mm)	SR	KW
1	1000	60	5.5	2.49	2.02	-7.93	-6.11
2	2000	60	5.5	2.56	2.19	-8.17	-6.81
3	1000	100	5.5	2.59	2.78	-8.27	-8.88
4	2000	100	5.5	2.00	2.49	-6.02	-7.92
5	1000	80	5.0	2.21	2.52	-6.89	-8.01
6	2000	80	5.0	2.48	2.29	-7.89	-7.20
7	1000	80	6.0	1.30	2.58	-2.28	-8.23
8	2000	80	6.0	2.64	2.34	-8.43	-7.38
9	1500	60	5.0	2.10	2.38	-6.44	-7.53
10	1500	100	5.0	2.30	3.14	-7.24	-9.94
11	1500	60	6.0	2.19	2.30	-6.81	-7.24
12	1500	100	6.0	1.56	2.40	-3.86	-7.60
13	1500	80	5.5	1.80	2.47	-5.11	-7.85
14	1500	80	5.5	1.86	2.53	-5.39	-8.06
15	1500	80	5.5	1.78	2.44	-5.01	-7.75

Table 3 shows the result of measured data obtained for the surface roughness and kerf width and their calculated signal to noise ratio respectively. The smaller the better quality characteristics shown in equation 1 was used to calculate the signal to noise for both the surface roughness and kerf width respectively. From the experimental result presented in Table 3, it can be observed that vary the parameters affect surface roughness and kerf width of workpiece while using the CNC plasma cutting machine, also observed is that at higher cutting speed, the surface roughness and hardness increases and this is because an increase in cutting speed causes the flame to spread more across the cut surface. The more time the flame stays on the surface of cut material, the more irregularities are observed on the surface, also, an increase in the cutting current increases the surface roughness which is as a result of the extra energy needed to perform the cutting operation. The surface of the cut was also exposed to more heat due to the extra energy causing the microstructure of the cut region to change. A low current indicates a low cutting energy (Nemchinsky and Severance 2006).

Table 4: Anova for Surface Roughness

Factor	DOF	SS	MS	F	P
CS	2	1.0344	0.5172	17.39416	27.97813
CC	2	1.2358	0.6179	20.78084	33.42554
GP	2	1.1891	0.59455	19.99554	32.16241
Error	8	0.237873	0.029734125		6.433916
Total	14	3.697173	0.264083786		100
S = 0.453657		R-sq = 72.17 %		R-sq (adj) = 52.07 %	

Table 5: Anova for Kerf Width

Factor	DOF	SS	MS	F	P
CS	2	0.23291	0.116455	11.47858	22.6176
CC	2	0.2833	0.14165	13.96197	27.51091
GP	2	0.4324	0.2162	21.31012	41.98982
Error	8	0.08116333	0.010145416		7.881669
Total	14	1.02977333	0.073555238		100
S = 0.263323		R-sq = 66.33%		R-sq (adj)= 54.73%	

It can be observed in Table 4 that the cutting current has the most effect of 33.43% on the surface roughness, while the gas pressure and the cutting speed have the following effect, 32.16% and 27.98% respectively. Due to the increase in the cutting speed beyond a certain limit, the speed of the torch makes it impossible for the plasma arc to maintain its stability, therefore the plasma arc cannot remain vertical during the cutting process, thereby causing the creation scratch lines on the surface of the cut. The gas pressure was observed to have the most effect on the kerf width as observed from Table 5 having a P value of 41.99% followed by the current with a P value of 27.51% and the least significant parameter is the cutting speed with P value of 22.62%. With increase in pressure, kerf width increases, this is as a result of too much pressure on the cutting zone which reduces the temperature of the surface, this is a result of the cooling effect of the gas, this causes a difficulty in blowing away the molten metal from the workpiece. It can be observed from Figure 3 that the optimum values for the surface roughness is obtained at CS of 2000 mm/min, CC of 100 A and GP of 5.0 bar. This implies that the height of the

nozzle when the current was at 100 A is sufficient for the gas pressure of 5.0 bar to blow out the melted portion without heating the material (Ferreira et al. 2009). The optimum process parameter for the kerf width as observed from Figure 5, is a cutting combination of CS of 1000 mm/min, CC of 100 A and a GP of 5.0 bar will be required. This implies that sufficient gas pressure of 5.0 bar was supplied at 100 A and 1000 mm/m to enable cutting and blowing away of the molten material without wastages there by reducing the amount of heat that may affect the workpiece.
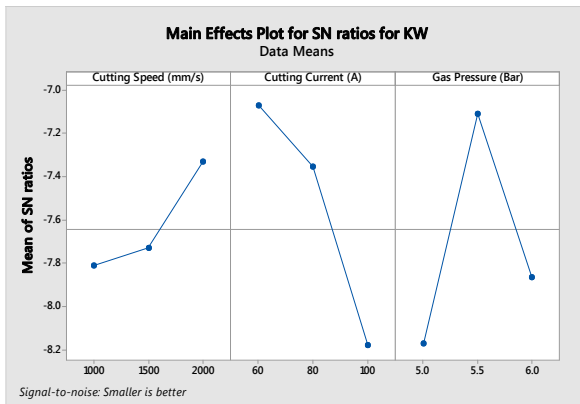
Figure 3: Main effect plot for surface roughness.
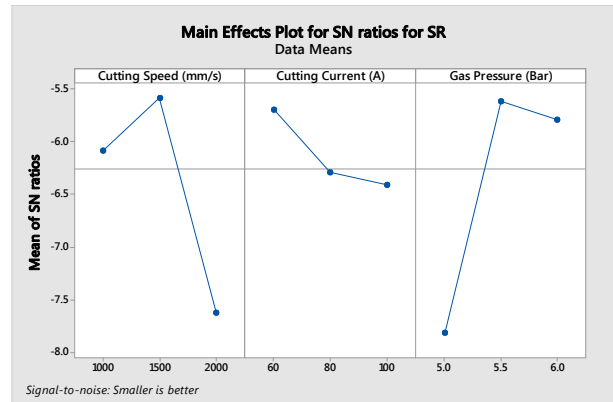
Figure 4: Main effect plot for kerf width roughness
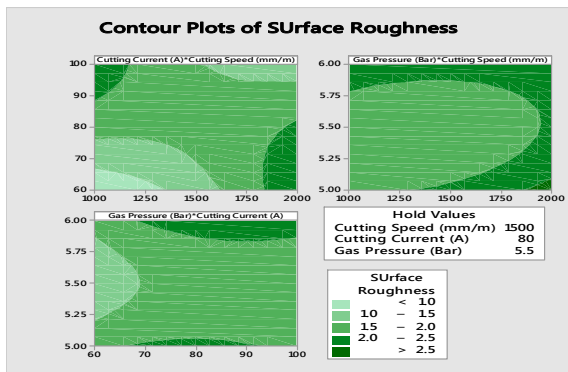
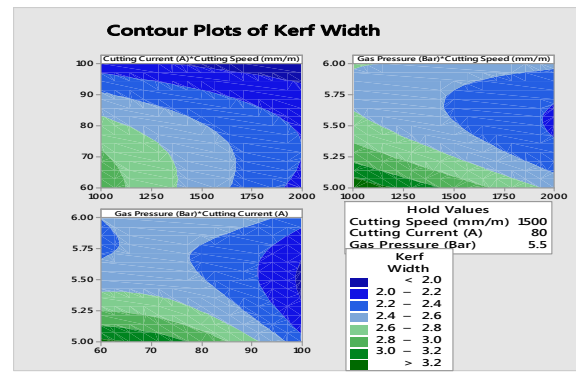

Figure 5: Contour plot for surface roughness

Figure 6: Contour plot for kerf width

Shown in Figure 4 is the effect of CS and CC, CS and GP, CC and GP on the SR. The SR reduces by reducing the value of the CS and increasing the value of the CC while holding the GP at 5.5 bar, also, the SR is reduced by reducing the CS and reducing the GP while holding the CC at 80 A, the last combination will result to a decrease of the SR when the CC is reduced and the GP is reduced while holding the CS at 1500 mm/min.

Figure 6 shows contour based interactions analysis between the various input parameters on the kerf width. It can be observed that there was a significant interaction between the CC and CS in the first graph and GP and CS in the second graph due to the elliptical nature of the contour plots.

3.3   Development of empirical model

For the optimization of the surface roughness and kerf width, the empirical model equation below which was developed from Minitab 17 software was used;

Surface Roughness (µm) = 0.38 + 0.0000496 CS + 0.0188 CC- 0.096 GP   (2)
Kerf Width (mm) = 3.41 - 0.000238 CS - 0.00659 CC - 0.197 GP   (3)

Substituting the optimum values from Figure 3 and Figure 5 resulted in an optimal value of 1.05µm for surface roughness and 1.46mm for kerf width.

4.   Conclusion

In this study, the experimental analysis was carried out to determine the effect of PAC process parameters on the surface roughness and kerf width of low carbon steel. Further analysis was carried out to identify the values of the cutting parameter which will yield the best quality output. The RSM experimental design method was found to be a very viable method of performing the trend analysis of optimization of cutting parameters in plasma arc cutting with respect to various combinations of design variables. Also, the design of experiment was found to be a suitable replacement for the conventional one factor at a time approach

Acknowledgement

References

Adalarasan, R., Santhanakumar, M. & Rajmohan, M., 2015. Application of Grey Taguchi-based response surface methodology (GT-RSM) for optimizing the plasma arc cutting parameters of 304L stainless steel. Internation journal of advanced manufacturing technology.

Bidajwala, R.C. & Trivedi, M.M.A., 2014. Parametric Optimization On SS 304L Using Plasma Arc Cutting- A Review. international Journal for Innovative Research in Science & Technology, 1(7), pp.147–149.

Ferreira, P. et al., 2009. Plasma Cutting Optimization By Using The Response Surface Methodology. Faculty of Science and Technology , The New University of Lisbon UNIDEMI., pp.213–218.

Groover, M.P., 2010. Fundamentals of modern manufacturing: materials, processes and systems 4th Ed., United State of America: JOHN WILEY & SONS, INC.

Krajcarz, D., 2014. Comparison Metal Water Jet Cutting with Laser and Plasma Cutting. Procedia Engineering, 69, pp.838–843. Available at: http://dx.doi.org/10.1016/j.proeng.2014.03.061.

Maity, K.P. & Bagal, D.K., 2015. Effect of process parameters on cut quality of stainless steel of plasma arc cutting using hybrid approach. Internation journal of advanced manufacturing technology, 78(April), pp.161–175.

MYERS, R.H., MONTGOMERY, D.C. & ANDERSON-COOK, C.M., 2009. RESPONSE SURFACE METHODOLOGY Process and Product Optimization Using Designed Experiments Third Edit. D. J. Balding et al., eds., New Jersey: John Wiley & Sons, Inc. Available at: http://www.wiley.com/go/permission.

Nemchinsky, V.A. & Severance, W.S., 2006. What we know and what we do not know about plasma

arc cutting. JOURNAL OF PHYSICS D: APPLIED PHYSICS, 39, pp.423–439. Available at: stacks.iop.org/JPhysD/39/R423.

Patel, P. et al., 2018. Study the effect of process parameters in plasma arc cutting on Quard-400 material using analysis of variance. Materials Today: Proceedings, 5(2), pp.6023–6029. Available at: https://doi.org/10.1016/j.matpr.2017.12.206.

Pawar, S.S. & Inamdar, K.H., 2016. FACTORS AFFECTING QUALITY OF PLASMA ARC CUTTING PROCESS : A REVIEW. Internation journal if advanced engineering and technology science, 4(12), pp.868–874. Available at: www.ijates.com.

Radonanovic, M. & Madic, M., 2011. Modeling The Plasma Arc Cutting Process Using Artificial Neural Network. Nonconventional Technologies Review, (4), pp.43–48.

Xu, W.J., Fang, J.C. & Lu, Y.S., 2002. Study on ceramic cutting by plasma arc. Journal of Material Processing Technology, 129, pp.152–156.

SYNTHESIS OF CARBON NANOTUBES VIA CATALYTIC DECOMPOSITION OF ACETYLENE ON BI-METALLIC SUPPORT INTERACTION OF CO-MO/MGO

Shehu A. Buhari[1], A. S. Abdulkareem[2] and I. B. Akintunde[1]

[1]Department of Mechanical Engineering, Federal University of Technology Minna, Nigeria

Department of Chemical Engineering, Federal University of Technology Minna, Nigeria

Abstract

The research work investigate the viable utilization of acetylene as the precursor for the synthesis of carbon nanotubes (CNTs) with the aid of bimetallic Co-Mo/MgO support catalyst via catalytic chemical vapour deposition (CCVD). The experimental results show the presence of nano sized and hollow core of the tubular carbon structure. An increase in the heat treatment temperature enabled Co-Mo/MgO catalysts in growing CNTs at higher yield, the results show an increase in the diameter when the treatment temperature is raised from 700ºC-800ºC.

Keywords: Synthesis, Bi-metallic alloy, Catalytic Chemical Vapour Deposition, Electron microscopy

1. INTRODUCTION

There have been rapid developments in the production of carbon nanotubes (CNTs) materials that lie within the nanometer scale from precursor materials since it was first discovered by Sumio Iijima in 1991(1). Carbon nanotubes are tubular in shape, made of graphite. The mind breaking interest in the carbon allotrope is attributed to their unique structural, mechanical, thermal, optical,chemical and electronic properties (2). These have drawn the attention and prompt most researchers in the field of science and technology to conduct research in this area of study, significant scientific studies have reveal the potential of CNT applications which include: super capacitors, reinforcements in high performance composites, hydrogen storage (3), catalyst support (4), selective adsorption agents (5) and field emission devices (6).

Till date, various methods have been developed to synthesis carbon nanotubes this includes arc-discharge (7), laser ablation(8) and chemical vapor deposition (9). Although arc-discharge is one of the earliest methods used in the production of CNTs, catalytic chemical vapour deposition (CCVD) has become the most promising and versatile method due to its large production capacity at an extremely low cost with high purity (10). Furthermore, CCVD also offers the opportunity to control and adjust multiple physico-chemical properties of the nanotubes. Properties such as morphology, diameter, length, surface structure and alignment of the CNTs have been synthesized (11).

Cobalt (Co), among transition metals from group VIII, was considered as a result of its ability to grow hollow and higher graphitized CNTs (12-13). Also the choice of Molybdenum (Mo) as the catalyst promoter to enhance the performance of the catalyst is due to its suitability to be paired with Co to form a bimetallic catalyst which is efficacious for high yield synthesis of CNTs of high quality (14-16).

Alkaline earth metal oxide (MgO), considering it's easily dissolution in mild acid, was chosen as the catalyst support in the research study. MgO has been reported to be a good support for bimetallic Co-Mo catalyst for the synthesis of high quality and yield CNTs (14, 17, 18). Numerous researches have been conducted in the production of viable CNTs from precursor. Yeoh et al. in 2013 (18) reported

effective synthesis of carbon nanotubes via catalytic decomposition of methane on support interaction of Co-Mo/MgO catalyst, Lee et al. in 2010 (19) conducted research on the optimization of carbon nanotubes synthesis via methane decomposition over alumina-based catalyst. Chai et al. in 2006 (20) reported the preparation of carbon nanotubes over cobalt-containing catalysts via catalytic decomposition of methane. The previous researches conducted make use of alkane in (methane) as the precursor; this research is conducted to investigate the effect of alkene in (acetylene) as the precursor on the synthesis of carbon nanotubes via catalytic decomposition on bi-metallic support interaction of Co-Mo/MgO catalyst.

2. Materials and method

2.1. Materials

The material used for the investigation are Co $(NO_3)_2$*$6H_2O$ and Mo $(NO_3)_3$*$6H_2O$ as received from Kem light lab. Mumbai India, distilled water from Dana Pharmaceuticals Co. Ltd Minna, MgO from Kermel china and H_2SO_4 from Guangdong Guanglua Sci-Tech Co. Ltd (JHD), all with (99%) chemically pure were procured.

2.2. Method

2.2.1. Preparation of Co-Mo/MgO Catalyst

The bimetallic Co-Mo/MgO Catalyst was prepared by conventional impregnation method, with weight ratio set at 54.5**:**3.4**:**42.1. The right amounts of Co $(NO_3)_2$ $6H_2O$ and Mo $(NO_3)_3$ $6H_2O$ were dissolved in distilled water and then the solution was impregnated onto MgO. The impregnated samples were stirred using magnetic stirrer for 20 minutes at the speed of 1500 rpm for 12 hours at the temp of 115ºC in an oven. The dried samples were ground and calcined in air at 700ºC for 5hours. The prepared catalysts were then used without a prior hydrogen reduction (19).

2.2.   Synthesis of CNTs

CNTs were synthesized by the decomposition of acetylene in a chemical vapour deposition (CVD) reactor. The synthesis was carried out in a horizontal quartz reactor (with length and diameter 1050 mm and 65 mm, respectively) at an atmospheric pressure. The catalyst (bi-metallic Co-Mo catalyst on MgO support) was placed on a quartz boat (100×50×50 mm length, width and depth respectively), located at the middle of the reactor. Acetylene and nitrogen play the role of carbon precursor and inert gas respectively (19). Acetylene gas was used as a carbon precursor due to its stability at high temperatures, which can avoid self-pyrolysis that causes the formation of amorphous and other graphitic carbon (21). After the reaction, the reactor was cooled down to ambient temperature in nitrogen atmosphere. The ceramic boat was then removed and weighed to determine the quantity of CNTs produced (19).

2.3. Characterization

The as produced carbon nanotubes deposit were characterized by XRD (Panalytical X'Pert Pro, Cu K radiation, = 0.1789 nm) at 40 KV and 30 mA. The XRD patterns were measure in 2 ranging from 10º to 9º with a step of 0.02º and measuring time of 2 sec per point. SEM images in SE mode were taken with a Zeiss Supra 35 field emission SEM equipped with energy dispersive X-ray (EDX) analyzer. Samples for transmission electron microscopy were prepared by dispersing powder in ethanol, placing in an ultrasonic bath, and then putting droplets onto 3 mm copper grids coated with amorphous carbon film and drying in air at room temperature. High-resolution TEM (HRTEM) images were obtained using a 200 kV JEOL JEM-2100F transmission electron microscope, equipped with a field emission gun and EDX analyzer (22).

3. Result and discussion

3.1. TEM analysis

The TEM representative image of the carbon nanotubes deposits is presented in Fig. 1 and 2. From the TEM images, it is observed that clusters of rope like carbon nanotubes structures were grown on the catalyst. The carbon nanotubes structures possessed appreciable hollow cores which indicate that the structures are carbon nanotubes and not fibres. This confirms that CNTs can be synthesized using acetylene as the precursor material and metal support interaction of Co-Mo/MgO Catalyst. The synthesis calcined at 700ºC produced a CNT with narrow diameter distribution and further increases in heat treatment temperature to 800ºC lead to an increase in the diameter of the CNTs distribution.

Fig. 3 and 4 shows the EDX spectrum of the CNT synthesized, this reveals the presence of Mg, O_2, C, S and Co as the constituents of the CNT produced. The peaks of Co and Mg elements are from the catalysts while the peak of O element is probably from the dissolution of H_2O, H_2SO_4 and the catalyst MgO. The Sulfur peak could be attributed to the presence of H_2SO_4.
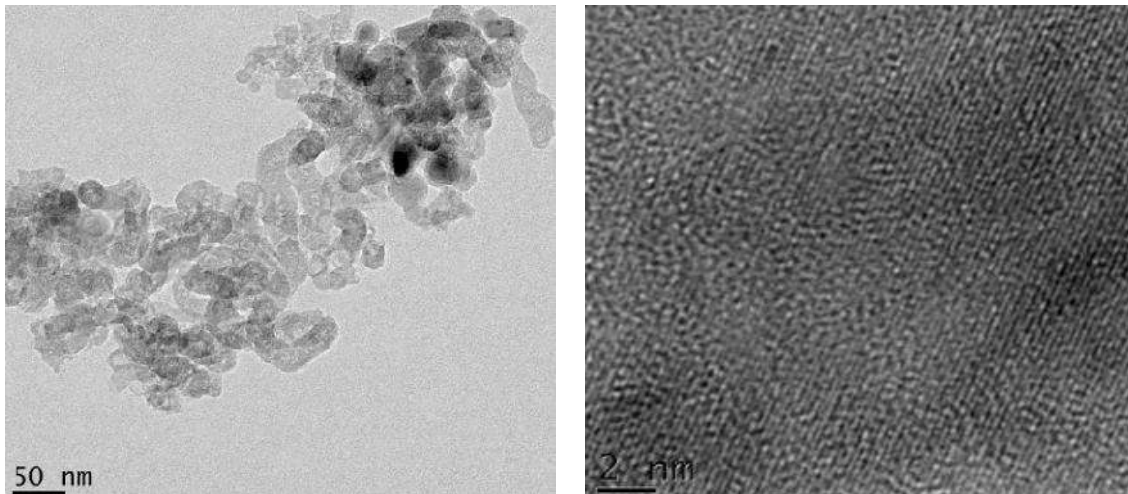

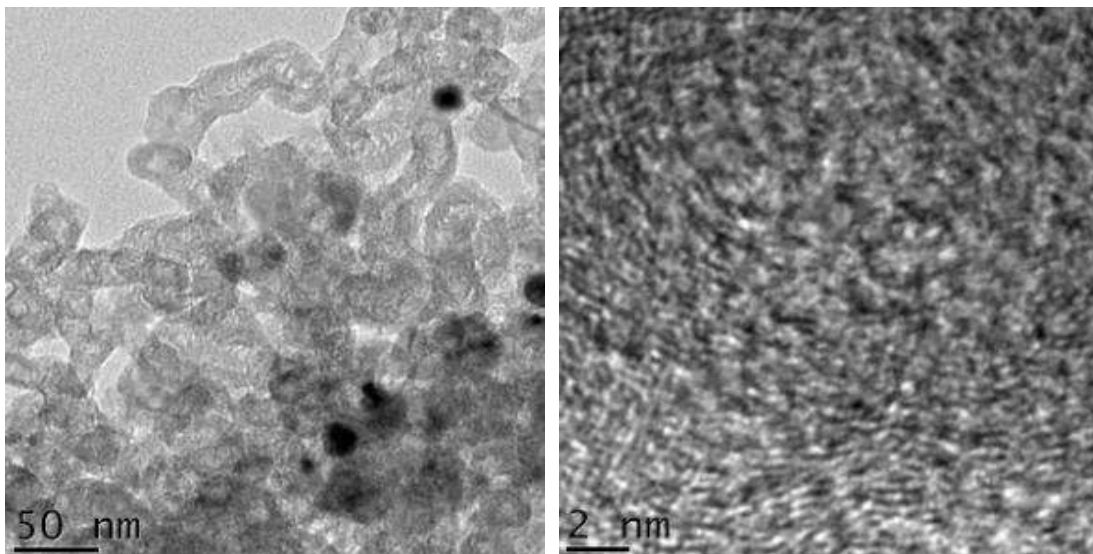Figure 1 TEM images of the as-synthesized CNTs at 700ºC

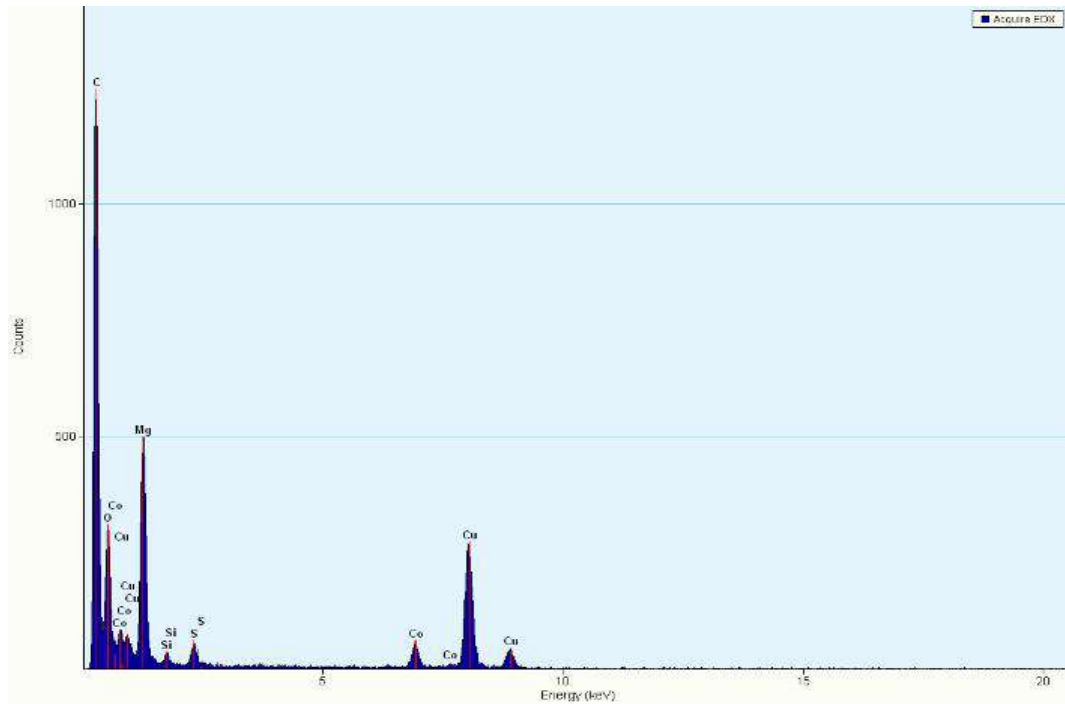Figure 2 TEM images of the as-synthesized CNTs at 800ºC
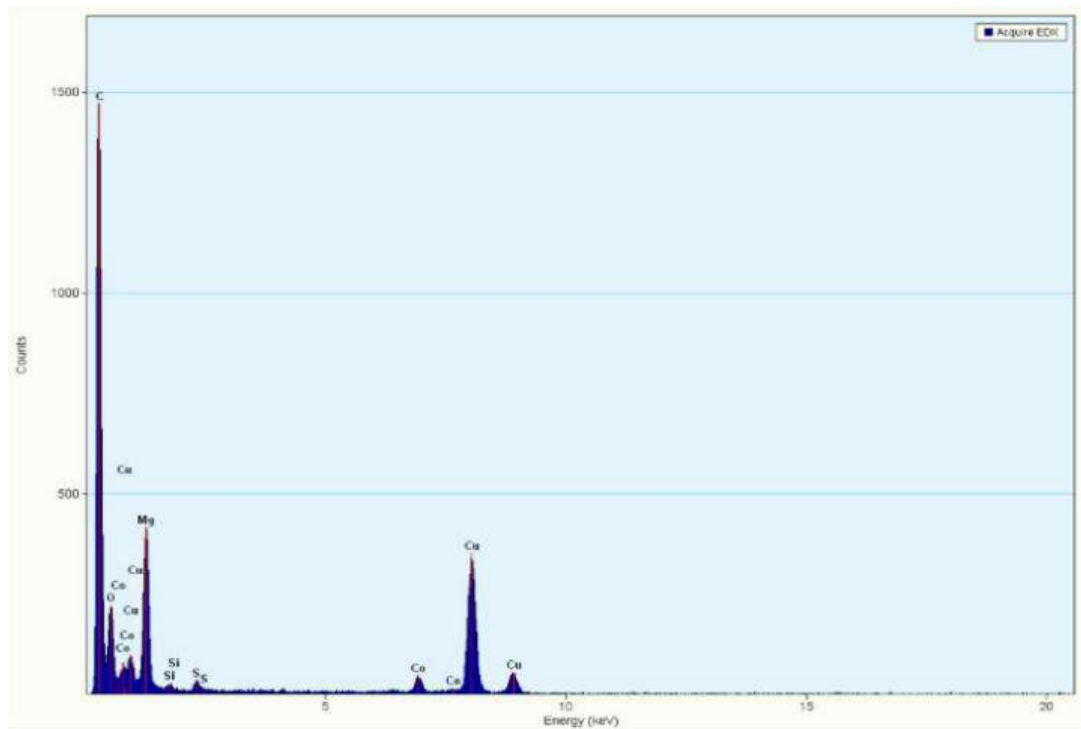
Figure 3 EDS of CNTs at 700ºC

Figure 4 EDS of CNTs at 800ºC

3.2. SEM Analysis

Figure 5, 6 and 7 shows a SEM image of the as-synthesized CNTs in the catalytic chemical decomposition reaction of Co-Mo/MgO. The obtained carbon nanotubes are formed as a network of

rope like structure with different densities. CNTs diameters can be estimated as between 10 and 120 nm and length up to 10 µm. The figure shows a SEM image of the CNT surfaces, fairly homogeneously distributed.
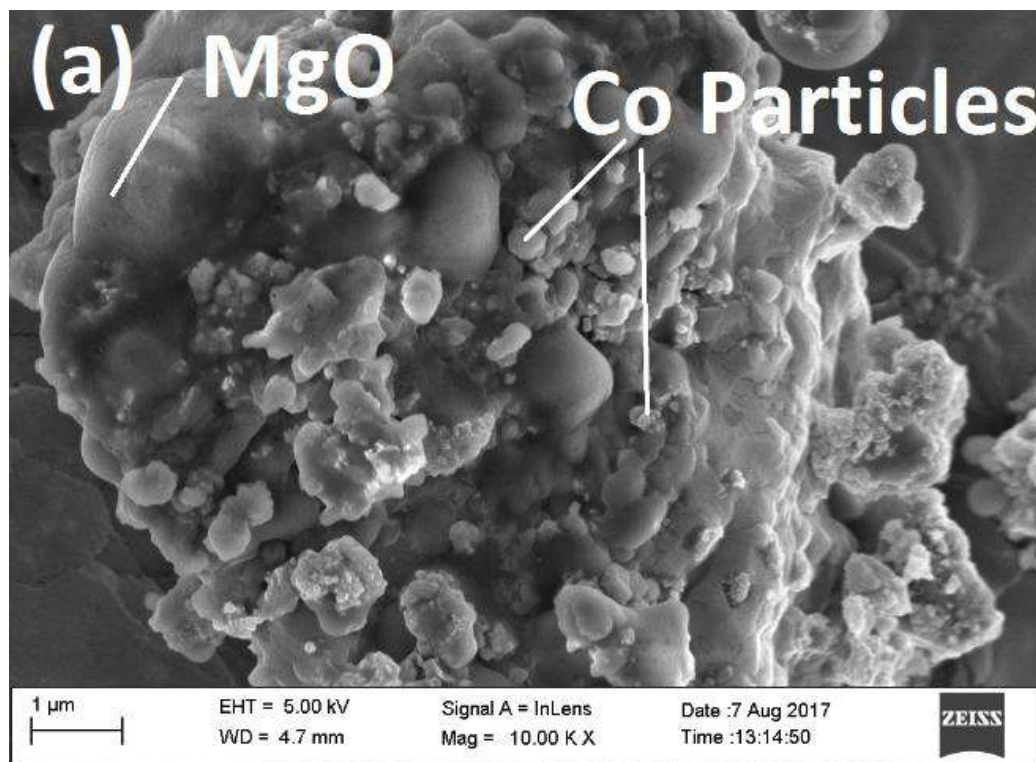

Figure 5 SEM images of the as-synthesized CNTs showing Co and MgO catalytic support
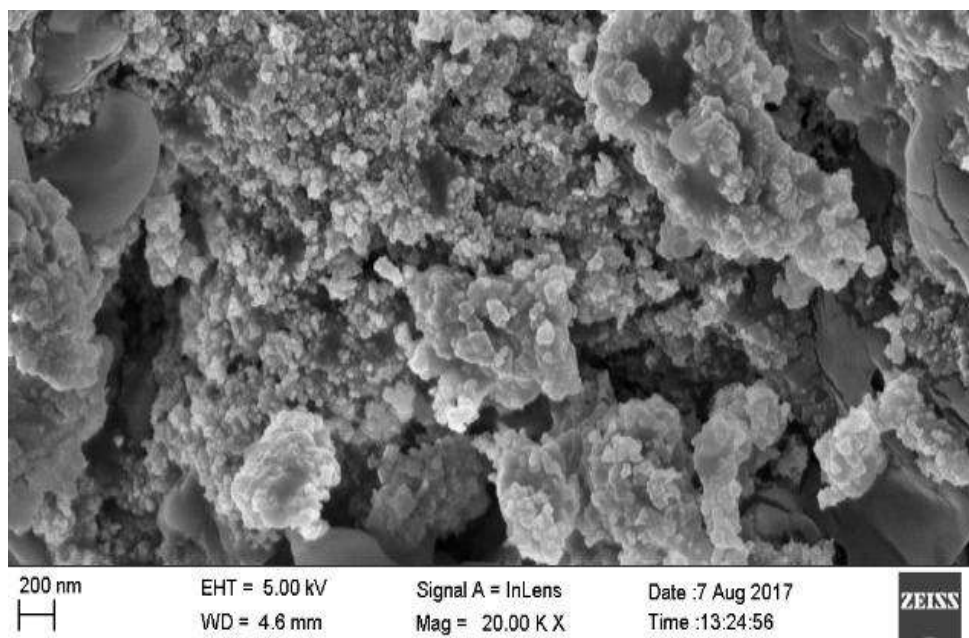

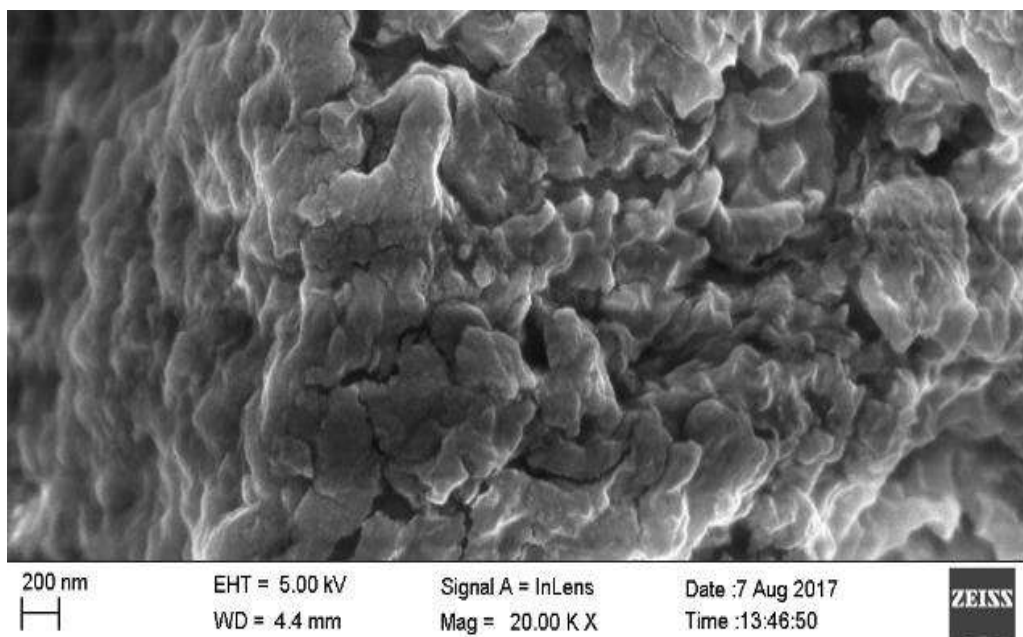Figure 6 SEM images of the as-synthesized CNTs at 700ºC

Figure 7: SEM images of the as-synthesized CNTs at 800ºC

3.3. XRD analysis

From the XRD spectra as shown in Fig. 8, the emergence of diffraction peaks of CoMgO, CoO and MgO compound in the diffraction pattern of the CNTs produced. Heat treatment conducted at high temperatures healed the defect of crystals, giving the catalyst compounds of better crystallinity. $MgMoO_4$ and $CoMoO_4$ are thermally stable compounds up to 1000ºC, and have the same role as MoO_3 for the prevention of extensive agglomeration of CoO species on the catalyst support (23).

Relatively to that was the decrease in MgO and CoO species content in the catalyst due to the incorporation of both MgO and CoO species into $MgMoO_4$ and $CoMoO_4$, respectively.
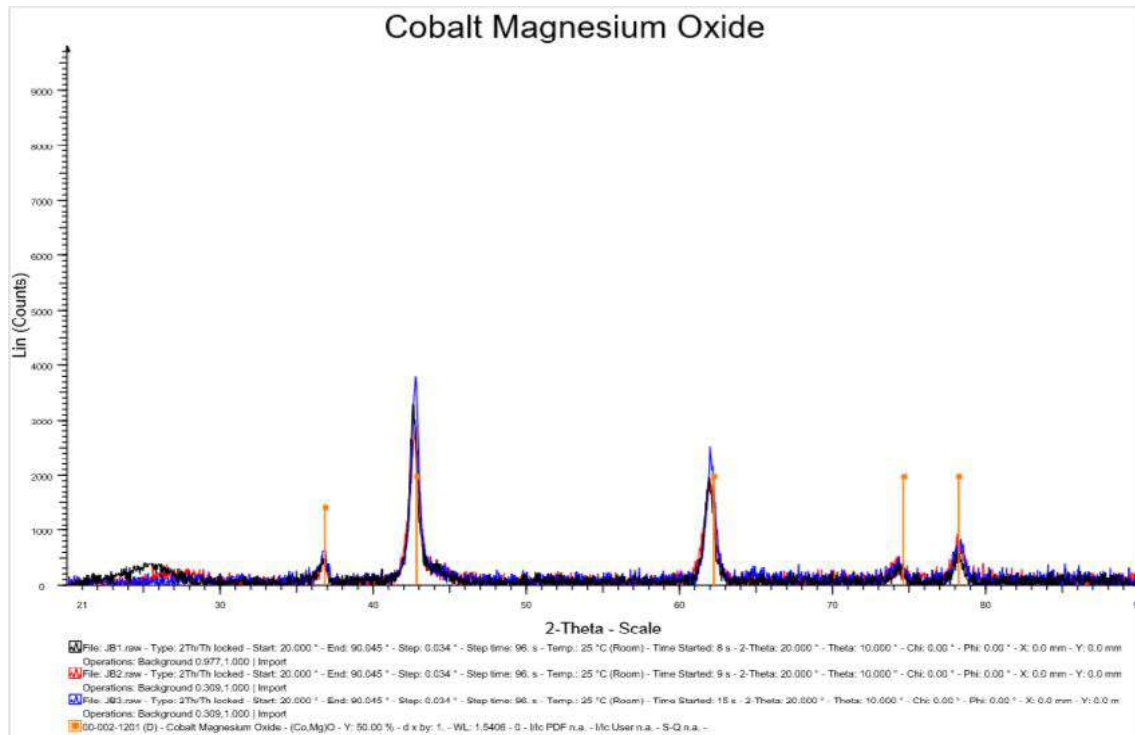
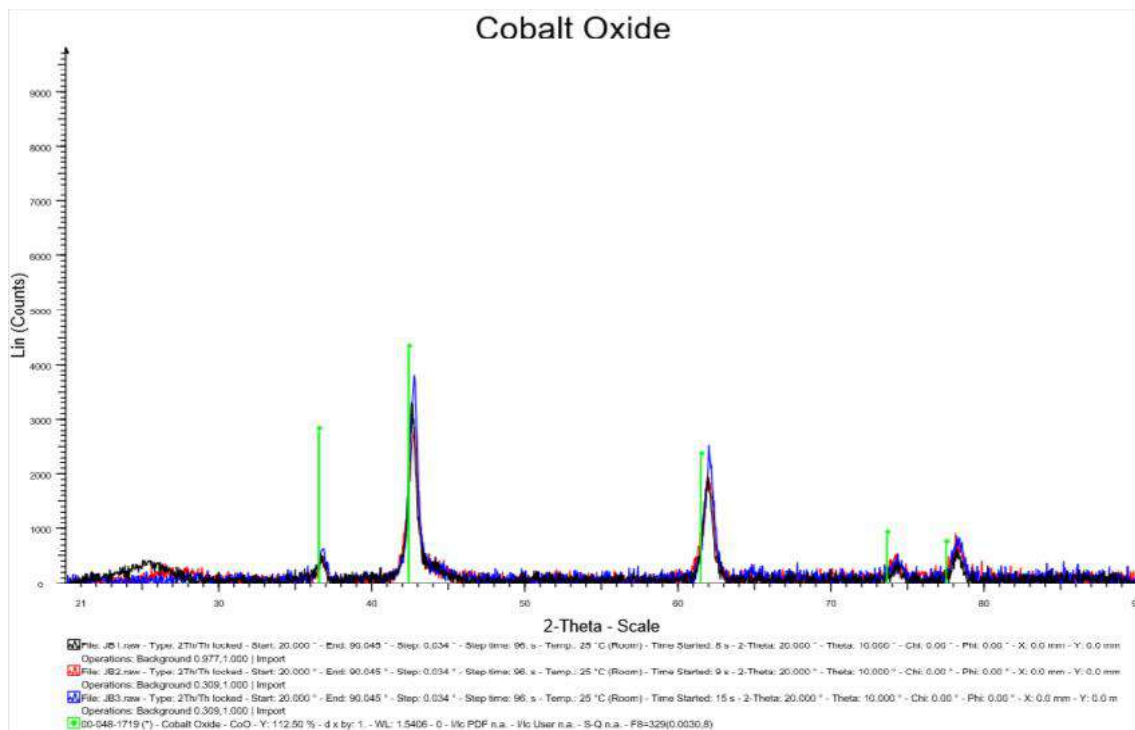Fig. 8a. XRD spectra of as-synthesized CNTs revealing CoMgO

Fig. 8b. XRD spectra of as-synthesized CNTs revealing CoO
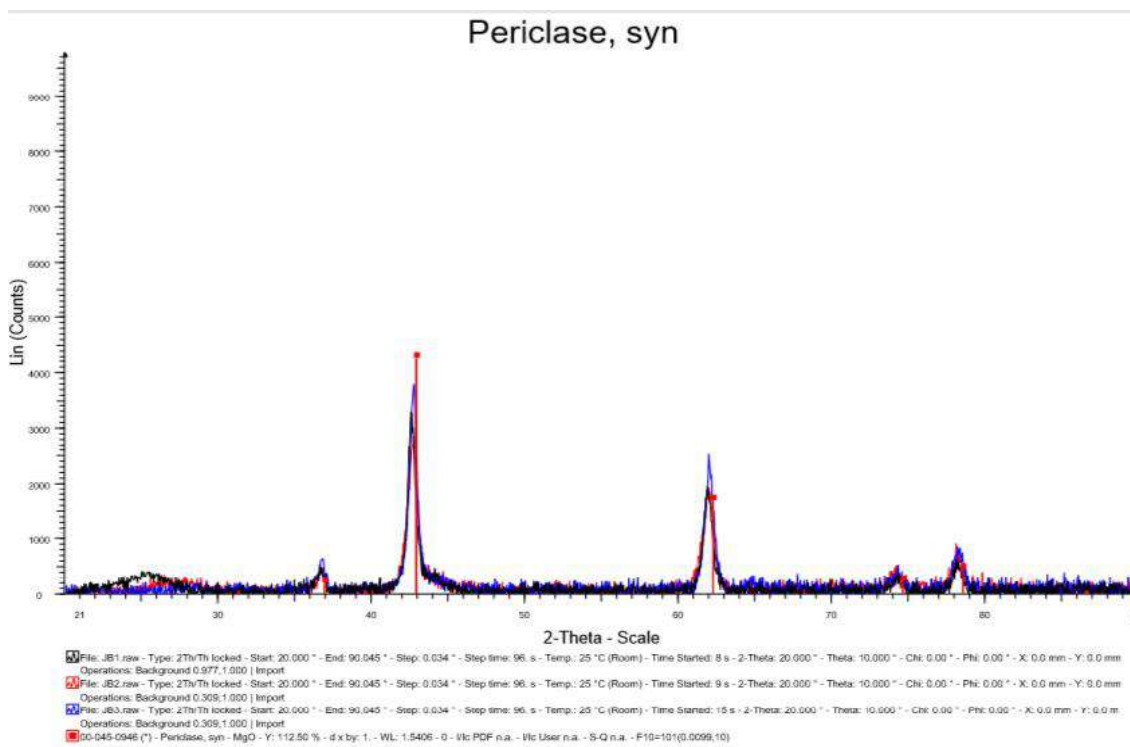
Fig. 8c. XRD spectra of as-synthesized CNTs revealing MgO

The catalytic performance is dependent on the strength of interaction between active metal and the support. The mobility of active metal on its support is governs by the metal-support interaction (MSI) of catalyst and this directly affects the agglomeration tendency of the active metal at elevated process temperature (24). In accordance to this, bimetallic Co-Mo/MgO catalyst with strong MSI will enhance the dispersion of CoO species on MgO for preventing its extensive agglomeration at 800ºC during the CCVD process.

4. Conclusions

The research shows that acetylene can be utilized as precursor in the production of CNT via chemical vapour deposition as demonstrated in this work. This involves the production of the catalyst follow by the synthesis of the CNT using acetylene as the material in the CVD.

Need for further research

There will be need for further research in this area to know the amount and diameter of the CNT produced at various calcination temperatures.

Also there will be need to conduct the research at various calcination temperature and examine the phases of the CNT formed.

Acknowledgments

References

1. Iijima, S. (1991): Helical microtubules of graphitic carbon. Nature, Pp. 354- 356.

2. De Lucas A., Garrido A., Sáchez, P.Romero A. Vavverde J.L. (2005): Growth of nanofibers from Ni/Y zeolite based catalysts: effect of Ni introduction method, reaction temperature and reaction gas composition, Ind. Eng. Chem. Res. 44. Pp. 8225-8236

3. Liu, C. Fan, Y.Y., Liu, M., Cong, H.T., Cheng, H.M., Dresselhaus, M.S., (1999): Hydrogen storage in single-walled carbon nanotubes at room temperature, Science 286 Pp. 1127-1129.

4. Toebes, M.L., Zhang, Y., Hájek, J., Nijhuis, T.A., Bitter, J.H., vanDillen, A.J., Murzin, D.Y., koningsberger, D.C., deJong, K.P., (2004): Support effects in the hydrogenation of cinnamaldehyde over carbon nanofibers-supported platinum catalyst: characterization and catalysis, J. Catal. 226 Pp. 215–225.

5. Fujiwara, A., Ishii, K., Suematsu, H., Kataura, H., Maniwa, Y., Suzuki, S., Achiba, Y. (2001): Gas adsorption in the inside and outside of single-walled carbon nanotubes, Chem. Phys. Lett. 336 Pp. 205-211.

6. Zhang, M., Yudasaka, M., Iijima, S., (2001): Single-wall carbon nanotubes: a high yield of tubes through laser ablation of crude-tube target, Chem. Phys. Lett.336 196-200.

7. Paradise, M. & Goswami, T. (2007) Carbon nanotubes - production and industrial applications. Mater. Des., 28 Pp. 1477.

8. Guo, T., Nikolaev, P., Thess, A., Colbert, D. T., and Smalley, R. E. (1995): Catalytic growth of single-walled nanotubes by laser vaporization. Chem. Phys. Lett., 243 Pp. 49.

9. Amelinckx, S., Zhang, X. B., Bernaerts, D., Zhang, X. F., Ivanov, V., and Nagy, J. B. (1994): A formation mechanism for catalytically grown helix-shaped graphite nanotubes. Science, 265 Pp. 635.

10. Wei-Ming Yeoh, Kim-Yang Lee, Siang-PiaoChai, Keat-TeongLee, Abdul Rahman Mohamed (2013): Effective synthesis of carbon nanotubes via catalytic decomposition of methane: Influence of calcination temperature on metal-support interaction of Co-Mo/MgO catalyst Journal of Physics and Chemistry of Solids 74 Pp. 1553–1559

11. Ago, H., Imamura, S., Okazaki, T., Saito, T., Yumura, M., Tsuji, M., (2005): CVD growth of single-walled carbon nanotubes with narrow diameter distribution over Fe/ MgO catalyst and their fluorescence spectroscopy, J. Phys. Chem. B 109 Pp. 10035-10041.

12. Hsieh, C.T., Lin, Y.T., Lin, J.Y. Wei, J.L. (2009): Synthesis of carbon nanotubes over Ni- and Co-supported $CaCO_3$ catalysts using catalytic chemical vapor deposition, Mater. Chem Phys. 114 Pp. 702-708.

13. Tsoufis, T., Jankovic, L., Gournis, D., Trikalitis, P.N., Bakas, T. (2008): Evaluation of first-row transition metal oxides supported on clay minerals for catalytic growth of carbon nanostructures, Mater. Sci. Eng. B 152 Pp. 44–49.

14. Tang, S., Zhong, Z., Xiong, Z., Sun, L., Kiu, L., Lin, J., Shen, Z.X., Tan, K.L. (2001): Controlled growth of single-walled carbon nanotubes by catalytic decomposition of CH4 over Mo/Co/MgO catalysts, Chem. Phys. Lett. 350 Pp. 19-26.

15. Ni, L., Kuroda, K., Zhou, L.-P., Kizuka, T., Ohta, K., Matsuishi, K.and Nakamura, J. (2006): Kinetic study of carbon nanotube synthesis over Mo/Co/MgO catalysts, Carbon 44 Pp. 2265–2272.

16. Niu, Z., and Fang, Y. (2007): Effect of composition of catalyst on the preparation of single-walled carbon nanotubes synthesized over W–Co–MgO catalysts, Super lattice Microstruct. 41 Pp. 62-70.

17. Colomer, J.F., Stephan, C., Lefrant, S., VanTedeloo, G., Willems, I., Konya, Z., Fonseca, A., Laurent, C., Nagy, J.B. (2000): Large-scale synthesis of single-wall carbon nanotubes by catalytic chemical vapor deposition (CCVD) method, Chem. Phys. Lett. 317 Pp. 83–89.

18. Yeoh, W.-M., Lee, K.-Y., Chai, S.-P., Lee, K.-T., Mohamed, A.R. (2010): The role of molybdenum in Co–Mo/MgO for large-scale production of high quality carbon nanotubes, J. Alloys Compd. 493 Pp. 539-543.

19. Kim-Yang Lee , Wei-Ming Yeoh , Siang-Piao Chai , Satoshi Ichikawa & Abdul Rahman Mohamed (2010): Optimization of Carbon Nanotubes Synthesis via Methane Decomposition over Alumina-Based Catalyst, Fullerenes, Nanotubes and Carbon Nanostructures, 18 (3), Pp. 273-284

20. Chai, S.P., Zein, S.H.S., Mohamed, A.R. (2006): Preparation of carbon nanotubes over cobalt containing catalyst via catalytic decomposition of methane, Chem.Phys. Lett. 426 Pp. 345-350.

21. Dai, H. (2002) Carbon nanotubes: Opportunities and challenges. Surface Science, 500 Pp. 218.

22. Dobrzanskia, L.A., Pawlytaa, M., Krztonb, A., Liszkab, B., Taic C.W. and Kwasnya, W. (2010): Synthesis and Characterization of Carbon Nanotubes Decorated with Gold Nanoparticles Journal, Acta Physica Polonica A Vol. 118 (3) Pp. 483-486

23. Hu, M., Murakami, Y., Ogura, M., Maruyama, S., Okubo, T. (2004): Morphology and chemical state of Co-Mo catalysts for growth of single-walled carbon nanotubes vertically aligned on quartz substrates, J. Catal. 225 Pp. 230-239.

24. Tran, K.Y., Heinrichs, B., Colomer, J.F., Pirard, J.P. and Lambert, S. (2007): Carbon nanotubes synthesis by the ethylene chemical catalytic vapour deposition (CCVD) process on Fe, Co and Fe-Co/Al_2O_3 sol-gel catalysts, Appl. Catal. A: Gen. 318 Pp. 63-69.

EFFECT OF CHILLS OF DIFFERENT MATERIALS ON MECHANICAL PROPERTIES OF Al11.9%Si ALUMINIUM ALLOY

T. Adebayo & M. S. Abolarin

Department of Mechanical Engineering, Federal University of Technology, Minna, Nigeria.
Email: tayoade2@gmail.com

ABSTRACT

This research work investigated the effect of chills on mechanical properties of aluminium alloy. Green sand gating system was designed with incorporation of external chills. Brass, mild steel and cast iron were selected as chill materials for investigation. Plate castings of Al11.9%Si alloy were produced and cooled using the chills, each of which were made into nine (9) blocks of same shapes but varying thicknesses of 10mm, 15mm and 20mm. A control sample was cast without a chill for the purpose of making comparison. For every casting chilled with a chill material, test samples were taken at three regular distances from the point of contact between castings and chills to the free ends. The samples were tested for Ultimate Tensile Strength (UTS) and Brinell Hardness Number (BHN). The results revealed that UTS and BHN decreased with increase in distances from the edges of contact between the chills and castings and increased with increase in chills thicknesses. The highest volume (20mm thick) chills gave the maximum values (173MPa & 113BHN, 164MPa & 99BHN, and 158MPa & 83BHN for Brass, Cast iron and Mild steel respectively) across all chill materials used, both for tensile strength and hardness. Compared to the results of UTS and BHN obtain from unchilled casting, brass chill was the most effective, having increased the UTS and BHN by 15% and 34% respectively. Second to brass was cast iron which improved UTS by 10% and hardness by 28%. Mild steel was the least effective, having raised the properties by 7% for UTS and 13% for hardness.

Keywords: Al11.9%Si, unchilled, external chills, plate castings, control sample, ultimate, hardness.

1.0   INTRODUCTION

Generally speaking, the grain refinement of cast and wrought alloy is beneficial in improving room temperature mechanical properties such as strength, hardness, ductility and so on. The dendrite grain size often influenced by rate of solidification is an important determinant of mechanical properties of aluminium alloy casting [8]. Incorporation of metallic chills into a mould for faster heat extraction is one of several methods available.

[1] investigated the effect of chills and riser placement on mechanical properties of premium sand casting and found the relationship between soundness, solidification rate and fatigue properties in alloy A206. [6] worked on the hardness and micro structural characteristics of rapidly solidified Al-8-16%Si alloy. Rapid solidification by melt-spinning technique was used to examine the influence of the cooling rate/conditions on microstructure and mechanical properties. Evaluation of microstructure and micro hardness of chill cast Al-B4C composites was done by [5]. The chill material was observed to have a significant influence on the microstructure and hardness of the cast specimens. Finer structure and better hardness were observed with the specimens cast using copper chills, whereas, cast iron and stainless steel chills gave rise to coarse grain structure with reduced hardness.

Effect of chills on soundness of Al4.5%Cu alloy casting was conducted to study the influence of end chill of varying volumetric heat capacity (VHC) on bar type castings of the alloy by [7]. It was established that the rate of heat extraction of the chills depends on the VHC of the chill materials and their presence greatly improves the mechanical properties.

Meanwhile, using green sand casting technique, this research investigated three chill materials, namely: brass, cast iron and mild steel; each was machined into blocks of equal volume. Aluminium-Silicon alloy was chosen for this study. The alloy was cast into plate castings of equal dimensions. The mechanical properties investigated on the casting were ultimate tensile strength (UTS) and Brinell hardness.

2.0 Materials and Methods

The material used includes:
  i. Aluminium scrap: Toyota car engines' pistons
  ii. Chills: cast iron, mild steel, and brass:
  iii. Sand Mould: silica sand, bentonite, and water
  iv. Fluxes: aluminium fluoride, sodium chloride and potassium chloride

The equipment used were:

  i. 20kg capacity coal fired lift-out crucible furnace
  ii. Brinnel hardness testing machine: universal hardness tester, Location: Kaduna Polytechnic, Kaduna, Kaduna State.
  iii. A tensile testing machine: Monsanto Tensometer type 'W', serial number 10975, UK., Capacity: 50KN, Location: Kaduna Polytechnic, Kaduna, Kaduna State.
  iv. A metallurgical microscope: 40X-1000X, model: ME300TZ-2L, made in Germany. Location: Latex Labs, shop 4, Gidan Matasa, Bosso, Niger State.

2.1 Moulding Process

The moulding sand was prepared with compositions as per American Foundry Society's Grain Finess Number (AFS-GFN) of 80, which is generally considered normal for aluminium alloy casting [4]. Typical sand mix composition for non-ferrous metals (Griffiths, 1999) was used: 90% silica sand, 6% bentonite and 4% water.

  i. The drag was moulded using wood patterns. Measured according to chill thicknesses.
  ii. Gating system was then cut, which include the runners, ingates and sprue well.
  iii. The cope was then moulded incorporating sprue, pouring cup and feeder.
  iv. Pattern was removed and metallic chills carefully inserted into the mould, as show in figure 2
  v. Both flasks were assembled and ready for pouring as shown in figure 3.
  vi. Steps 1 to 5 above was repeated for other eight (8) other castings and finally for unchilled casting. The chills were placed into the mould as shown in figure 2, having direct contact with the molten metal in order to enhance easy heat transfer from same to the chills.

The dimension of each of the chill of cast iron, steel and brass was 120mm x 20mm x (10mm, 15mm and 20mm), Figure 1. Figure 4 shows flow diagram of entire process.

Figure 1: Chills of Different Materials

Figure 2: Brass Chill and Gating in position
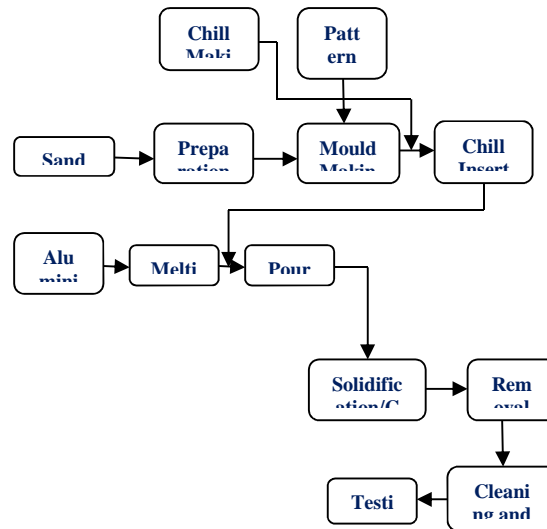

Figure 3: Assembled Flasks

Figure 4: flow diagram of casting process.

3.0   Results and Discussion

3.1   Chemical Composition of Aluminium Alloy Used

The results of chemical composition analysis carried out on the scraps of Toyota car pistons melted confirmed that the alloy was Al.11.9%Si. Silicon was found to be 11.9%, an amount which is pretty close to eutectic point. Silicon if present in aluminium alloy up to 17% can increase strength drastically [3]. The alloy under investigation contained 0.10% copper. This amount improved the ultimate tensile strength (UTS) and hardness of the alloy to a little extent.

The maximum benefit in terms of copper composition is achieved at about 6.5%. Hence the not-so-high values of UTS and Brinell hardness obtained. Table 1 shows the chemical composition of the alloy.

3.2   Effect of the chills on Microstructure

In the microstructure shown by micrographs presented in Plate V, essentially two phases were observed. Firstly grey (white) spots representing ∝ phase of aluminium grain and dark spots are β phase of eutectic silicon grain. '(a)' is the structure obtained from the control sample. Through close observation, silicon grains appear larger when compared with other samples which of course were obtained from chilled castings of the various chill materials. '(b)' was a microstructure of sample cooled with cast iron chill. β Particles appear to have dissolved little as it looks finer than control sample structure. '(c)' and '(d)' were result obtained from samples chilled with mild steel and brass respectively. Brass chill turned out to have produced sample with the finest grain structure. That of mild steel is only slightly different from control sample (unchilled casting)
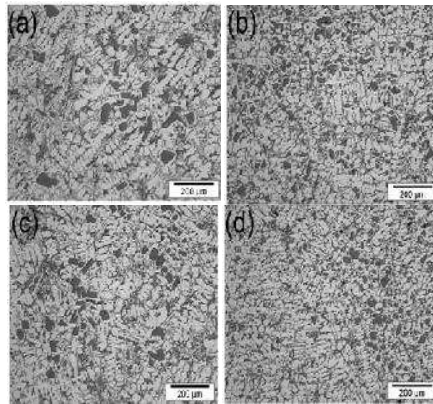
Plate V: (a) Micrograph of control sample (b) Micrograph of sample chilled with cast iron (c) Micrograph of sample chilled with mild steel (d) Microstructure of sample chilled with brass.

3.3 Effect of the chills on Ultimate Tensile Strength (UTS)

The charts shown below (Figures 5 a,b,c) give a clearer view of performance of each chill on UTS of the alloy (Al11.9%Si). Control sample has the lowest value of 151MPa. Starting with 10mm chill thickness, followed by 15mm and later 20mm, the value of UTS increased proportionately with increase in chill thickness. That means that the higher the mass of chill, the higher the cooling effects on the casting provided the mass of casting remains constant. In other words, the higher the rate of heat transfer, which in turn results in higher solidification rate of the casting. These disagree with [6]. Tables 2 and 3 present the results obtained from Ultimate Tensile Strength (UTS) and Brinell hardness tests respectively.
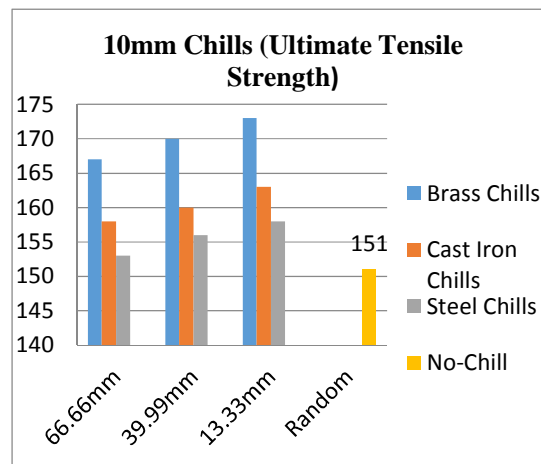
Figure 5 (a) UTS at various distances for 10mm chills
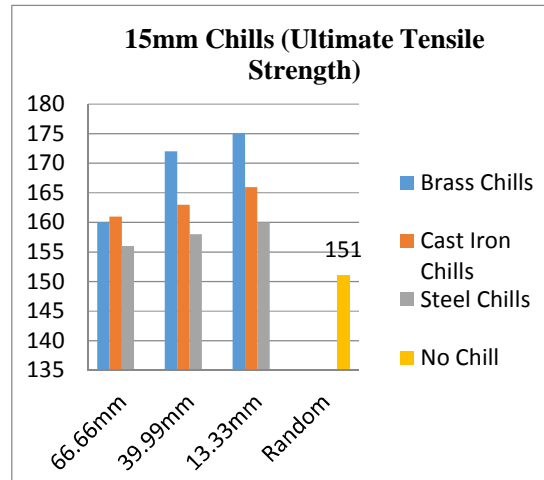
Figure 5 (b) UTS at various distances for   15mm chills.
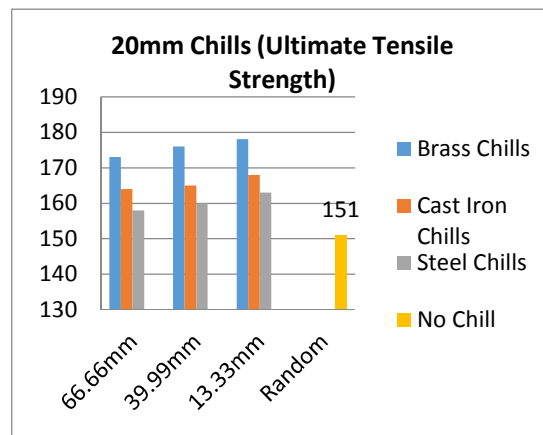
Figure 5 (c) UTS at various distances for 20mm chills

Table 1: Chemical Composition of the Aluminium Alloy.

Chemical Composition of alloy casting , wt.%									
Si	Cu	Mg	MN	Fe	Ti	Ni	Zn	Pb	Al
11.9	0.10	0.10	0.39	0.46	0.12	0.08	0.12	0.10	86.63

Table 2: UTS and Distance from Chill Edge

Distance From chill contact edge (mm)	ULTIMATE TENSILE STRENGTH OF SAMPLES (MPa)									
	Al	B_{10mm}	B_{15mm}	B_{20mm}	C_{10mm}	C_{15mm}	C_{20mm}	S_{10mm}	S_{15mm}	S_{20mm}
66.66	151	167	160	173	158	161	164	153	156	158
39.99	-	170	172	176	160	163	165	156	158	160
13.33	-	173	175	178	163	166	168	158	160	163

3.4   Effect of the chills on Brinell hardness

Similarly it was observed that results obtained from Brinell hardness lest followed the same pattern compared with UTS. Figures 6 (a), (b) and (c) represent Brinell hardness charts for chill thickness 10mm, 15mm, and 20mm respectively. Sample taken from unchilled casting was tested to have Brinell Hardness Number of 77 HB. Progressive introduction of different chill thicknesses of different material resulted in improved hardness, with the highest produced by samples chilled with brass, a similar result to that of [4] because higher thermal conductivity compare to other materials

According to the data contained in table 4, through observation, the following deduction can be made:
  i.   Chilling capacity of the tested metallic chills is independent of Volumetric Heat Capacity (VHC) from the results analysis so far, the order of decreasing positive effect on UTS and hardness is from brass to cast iron to steel. Data on   Table 4 proofs the contrary. Cast iron has the highest chilling effect, followed by brass and lastly steel.
  ii. Also from the same table, chilling capacity seems to increase with increase in thermal conductivity of chill material. Meaning that brass with thermal conductivity of 111W/m°k is expected to extract heat from the solidifying metal faster than cast iron (68 W/m°k) and cast iron than steel (36 W/m°k), all at temperature of 20°C. Suffice to say that chilling capacity is directly proportional to thermal conductivity of the chill material.
  iii. Results showed that cast iron that is slightly less dense than mild steel was more effective. It can therefore be stated that chilling effect of a metallic material is independent of density.

Table 3: Brinell Hardness and Distance from Chill Edge

Distance From chill contact edge (mm)	BRINELL HARDNESS OF SAMPLES (BHN)									
	Al	B_{10mm}	B_{15mm}	B_{20mm}	C_{10mm}	C_{15mm}	C_{20mm}	S_{10mm}	S_{15mm}	S_{20mm}
66.66	77	103	107	113	90	93	99	80	81	83
39.99	-	108	109	114	93	97	104	84	83	85
13.33	-	111	113	118	98	103	108	84	86	89

Table 4: Thermo-physical properties of the chill materials

Material	Density (g/m^3)	Specific Heat (Jk/kg^{o}K)	Thermal Conductivity (W/m^{o}K)	Volumetric Heat Capacity (VHC) (J/^{O}K) for 120mm by 80mm by 10, 15,20mm respectively.		
				96000mm^3	144000mm^3	192mm^3
Brass	8.550	0.390	111	320	480	640
Cast Iron	7.300	0.460	68	322	484	645
Steel	7.850	0.421	36	317	476	635

The results obtained at the edge of contact (about 13.33mm) between the chills and castings were slightly higher and decreased slightly, moving further away from the edge (about 66.66mm). This is in line with a work done by [2]. That was the case for all chill materials and thicknesses (10mm, 15mm, and 20mm). Evident by pattern of charts displays in figure 5 (a), (b) and (c), brass chill produced castings with highest value of UTS, followed by cast iron; and steel chill with the lowest value.
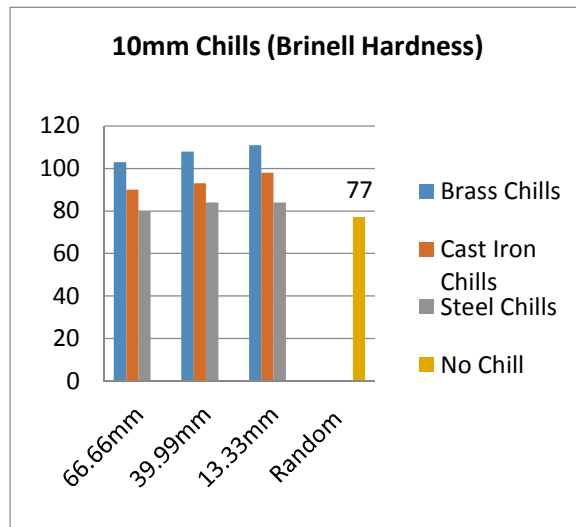
10mm Chills (Brinell Hardness)

Figure 6 (a) Brinell hardness At Various   Distances for 10mm Chills

15mm Chills (Brinell Hardness)
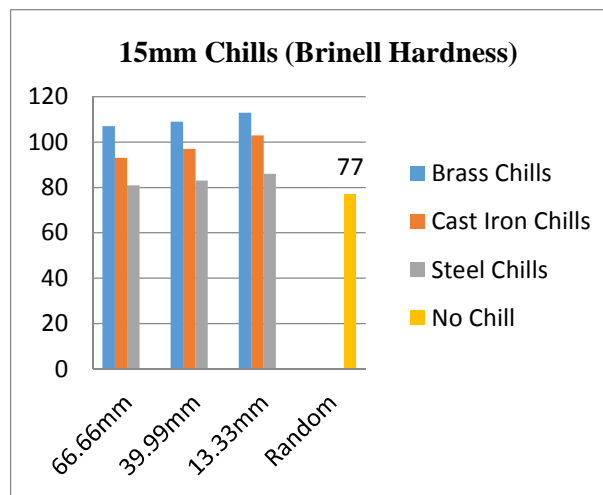
Figure 6 (b) Brinell Hardness At Various Distances For 15mm Chills

20mm Chills (Brinell Hardness)
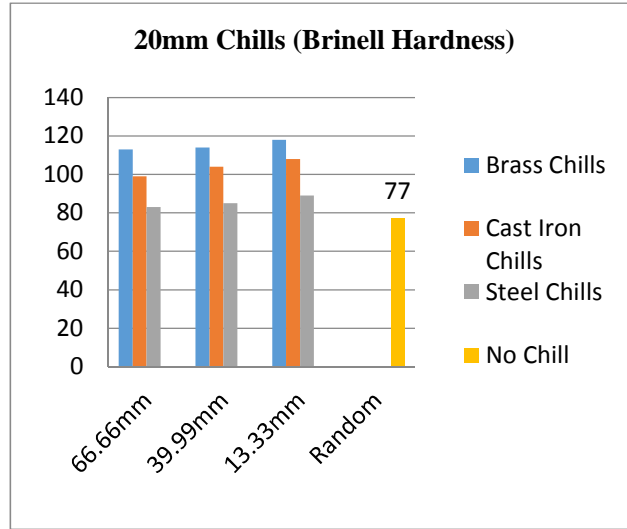
Figure 6 (c) Brinell Hardness At Various Distances For 20mm Chills.

4.0   CONCLUSIONS

The investigation carried out on the effect of chills of different materials on mechanical properties of Al11.9%Si alloy has established that the following:

I.   The gating system was designed with external chills incorporated.

II.   Castings of the aluminium alloy used were cast using brass, cast iron and mild steel as external chills.

III.   The sample taken from the alloy casting produced without a chill was tested to have UTS of 151MPa and hardness of 77BHN. Base on the results of tested samples of chilled castings, the following conclusions can be made:

 a)   For all the chill materials, the mechanical properties under investigation increased with increase in chill thickness and decrease with increase in distance from the edge of contact between the chill and castings. That is to say that the UTS and Brinell hardness were maximum at 20mm chill thicknesses and 13.33mm distance.

 b)   Brass chill produced maximum values of UTS and hardness of 178MPa and 118BHN respectively. In other words brass chill improved UTS and hardness by 15% and hardness by 34% compared to the unchilled casting.

 c)   Cast iron chill produced second best results. It gave UTS OF 168MPa and hardness of 108BHN. Therefore, cast iron chill has been able to improve UTS and hardness by 10% and 28% respectively.

 d)   Mild steel chill was the least in terms of effect on the properties. It gave UTS of 163MPa and hardness of 89BHN, which implied that it has been able to raise the values of UTS by 7% and hardness by 13%.

References

1.   Chakrabarti A. K (2005). Casting Technology and Cast Alloys, PHI Learning Pvt. Ltd. 67(16).

2. Griffiths W. (1999). The Heat-Transfer Coefficient During The Unidirectional Solidification of An Al-Si Alloy Casting, Metallurgical and Materials Transactions B. 30, 473-482.

3. Hutchings I. M & Alphas A. T (2000), Comprhensive Composite Materials, Hand Book of material Science, Green Hills Ltd 41

4. Leela, B. N. and Sreenivas, K. V. (2012). Microstructure and Micro Hardness of Chill Cast Alb4c Composites. International Journal of Mechanical Engineering and Robotics Research, 1(3), 450-456.

5. Ozun C. N, Chang-Seog K. & Jae-Ik C. (2004), Sand Casting Mould Design of Thin Walled Aluminium Case. Journal of Material Science Technology, 24 (3) 383-388.

6. Prakash, B. P. and Rajesh, V. P. (2014) Investigation On The Heat Transfer Coefficient (HTC) During Sand Casting Of A356 Alloy
   International Journal of Innovative Research and Development, 3(3), 158-161.

7. Randdy, G. P. and Pal, P. K. (1974). Influence of Chills on Aluminium 4.5 Per Cent Copper Alloy Casting Soundness, Journal of Mechanical Engineering Department, Indian Institute of Technology, Bombay, 325-327.

8. Zhang, L. Y., Jiang, Y. H., Ma Z., Shan, S. F. Jia, Y. Z., Fan, C. Z. & Wang, W. K. (2008). Effect of Cooling Rate on Solidified Microstructure and Mechanical Properties of Aluminium-A356 Alloy. Journal of Materials Processing Technology, 207, 107-111.

TUNGSTEN INERT GAS (TIG) WELDING OF AUSTENITIC STAINLESS STEEL (ASS) : EXPERIMENTAL OF CHROMIUM CARBIDE FORMATION DURING TIG OF ASS 304L

B.T Balogun[1], B. Alkali[2] M. Abdulwahab [3] and Anunuso Justice Chikeze[2]

[1] Department of Materials and Metallurgical Engineering,
Federal University of Technology, Minna, Nigeria.

[2]Department of Mechatronics Engineering,
Federal University of Technology, Minna, Nigeria.

[3]Department of Metallurgical and Materials Engineering, Faculty of Engineering,
Ahmadu Bello University Zaria, Nigeria.
Emails: balogun.tope@futminna.edu.ng, +2347068364092.

Abstract

In this paper, a 230 x 150 x 5mm dimension of austenitic stainless steel (ASS) plates of type 304Lwas investigated to observe the formation of chromium carbide when wielding current and temperature were applied at a given period of time. The plates were joined using Tungsten Inert Gas (TIG) welding process. Various lower welding current were biased to obtain a range of desirable welding temperature without the formation of Chromium Carbide at a very lower welding current and temperature. The biased current ranges from 50A to 90A and the corresponding welding temperature were recorded using thermocouple device. The result of the macro-structure gives an interesting revelation of smallest dimension of width of 1.0mm and 1.2mm within the heat affected zone (HAZ) at lower temperature between 100.6^{o}C and 200.2^{o}C. These values indicate welded materials with better mechanical properties (hardness and strength). as compared to metals welded at higher temperature of 300.8^{o}C to 500.6^{o}C which gives a higher dimension of width between the ranges of 2.2mm to 3.2mm in HAZ. The metal with higher temperature between 300.8^{o}C and 500.6^{o}C shows lower mechanical properties (hardness and strength). The result of the micro-structures also reveals that, the material welded with the lowest temperature within the range of 100.6^{o}C and 200.2^{o}C exhibit no chromium carbide formation as compared to metals welded at higher temperature of 300.8^{o}C to 500.6^{o}C which establish the formation of chromium carbide in a weld of austenitic stainless steel. This result has proven that, at control weld current and temperature, the life span of the ASS 304L can be protected and chromium carbide formation that leads to weld decay can be avoided.

Keywords: Austenitic stainless steel; Macro-structure; Chromium Carbide; Gas inert Tungsten; Heat affected zone; Microstructure.

1.0 INTRODUCTION

Austenitic Stainless Steel (ASS) is widely used in high temperature corrosive environments. They exhibit superior corrosion resistance in a wide range of environments such as petrochemical and

nuclear industry where there is existence of hot gases and high boiling liquid. However, there have been great challenges of corrosion of different kinds confronting petrochemical and nuclear industries all over the world in the exploitation of ASS (Mishra et al., 2014). This is due to a specific corrosion mechanism called "weld decay" which influences the presence of Chromium Carbide formation during welding process. These challenges pose a great danger on the life span of welded materials of high quality such as ASS in petrochemicals and nuclear industries. When these welded materials are subjected to a specific corrosion mechanism such as "weld decay", it resulted to failure which limits the lifespan of such material (Mishra et al., 2014). Most especially when such material is practically used in the industry. This research work attempt to investigate at what particular welding current and welding temperature ASS 304L can be welded to avoid carbide formation that leads to "weld decay" in order to avoid the material prone to corrosion of all kinds.

A lot of researches have been done on the welding of ASS. The work of Roy et al. (2014) specifies the use of different electrode in a shield metal arc welding by exploring the mechanical and metallurgical properties of commercially pure Copper and ASS AISI 304. Among the electrodes used, it was observed that Inconel (NiCrMo3) electrode produces a better weld joint and strength. The suitability of (NiCrMo3) was recommended for industrial practice. The discovery made by Oyetunji et al. (2013), on the effects of welding speeds and power inputs on the hardness property of ASS 304L using GIT Arc welding, reveals formation of chromium carbide at post weld as well as high level of hardness at a faster welding speed of 9.5m/min and corresponding power input of 9.2KN. Tabish et al. (2014), investigated the effects of heat input on micro-structure and mechanical property using TIG in an ASS AISI 304. The research achieved high strength and hardness of material through a low heat input parameter when heat inputs were varied at low, medium and high conditions.

The research of Moslemi et al. (2015), on the effect of welding current on micro-structure and mechanical properties of ASS 316 in a welded joint using TIG, re-affirmed chromium carbide formation at weld joint due to increase in heat input. This established that increase in welding current causes a raise in heat input. It was also concluded that current of 100A is the most suitable current that gives optimal strength and hardness in welding of ASS AISI 304 using TIG welding process. Mishra et al. (2014), studied mechanical characterization of monel 400 and 316 of ASS weldments using Gas Tungsten arc welding (GTAW) and ERNiCrMo-3 filler metal. These researchers limits their areas of study to the welding technique of GTAW, a particular material monel 400 and a filler wire of ERNiCrMo-3 without considering the outcome of the evaluation of welding parameters such as current, heat input, temperature or voltage in the experiment. In their opinion, GTAW welding was recommended for weld monel 400 and AISI 316 of ASS using ERNiCrMo-3 filler wire. But the research work recorded tensile failure in all dissimilar weldments.

The mechanical properties of AISI 4140 and AISI 316 dissimilar weldments using GTAW with and without filler metal in an ASS were assessed by Raddy et al. (2014). The report indicated the present of martensite and also recorded tensile failure in both weldments. In a recent development, Song et al. (2017) investigated the effect of high – pressure H_2 on the fracture behaviour of pipeline steel X70, ASS304L and ASS 316 type. It was discovered that 304L type of ASS is more susceptible to hydrogen brittleness than the ASS 316. A prediction model developed by Gao and Zhang (2014) on how the morphology of a molten welding pool width can be monitored and control in a laser welding process was achieved. This model predicts a high power disk laser

57

welding of ASS 304 using computer artificial intelligent device. Yang et al. (2010) studied effects of heat input on tensile properties and fracture behaviour of friction stir welded Mg-3Al-1Zn alloy, by stir welded 6.3mm thickness of the material. They established that the highest value of ultimate tensile strength of the weld was achieved with increase in heat input at shoulder diameter of 24mm. They were also affirmed that increase in the width of heat affected zone (HAZ) does not bring about increase in hardness value of the weld.

The research of Jao et al. (2016) on the effect of welding residual stress and out of plane displacement during the heat sink welding process of a thin stainless steel using computer artificial intelligent device (CAID) was tremendous. The simulation discovered that, a trailing heat sink welding has a little effects on the deformation. This is due to imposition of stress on material when there is a decrease in heat input in a conventional welding of stainless steel. The study of Mendes et al. (2013) on the influence of exposure characteristics on weld interfaces of stainless steel AISI 304L to low alloy steel (51CrV4) in a cylindrical configuration was achieved using ammonium nitrate-based emulsion and ammonium nitrate fuel (ANFO) explosives with the aid of CAID. The study affirmed that, the morphology of the welding pool was influenced by the velocity impact of the explosives used. It also ascertains that welding with ANFO explosives has a better configuration performance with both filler and base metal.

The success in optimization of deep penetration laser welding process of stainless steel using 10KW fibre laser was studied by Zhang et al; (2014). The study established that welding speed and focal position affects the quality of the weld in a laser welding process. The study also proves that, the magnitude of 10KW power in a fibre laser welding process improves the tensile strength of the material in ASS of 304 type. However, none of these researchers has considered at what applied current and particular temperature, does chromium carbide formation occurs in welding process of ASS. This paper investigates the welding current and a particular range of vibrant temperature at which ASS304L type can be welded without significant chromium carbide formations in the weld.

2.0   Methodology

The methodology comprises of three stages namely; the preparatory stage; the welding process and the metallurgical test as illustrated on Figure 1.

```
┌─────────────────────────────────┐
│   ┌─────────────────────────┐   │
│   │    Preparatory Stage    │   │
│   └─────────────────────────┘   │
│                │                │
│   ┌─────────────────────────┐   │
│   │     Welding Process     │   │
│   └─────────────────────────┘   │
│                │                │
│   ┌─────────────────────────┐   │
│   │      Metallurgical      │   │
│   │    Test/ Inspection     │   │
│   └─────────────────────────┘   │
│                │                │
│   ┌─────────────────────────┐   │
│   │       Evaluations       │   │
│   └─────────────────────────┘   │
└─────────────────────────────────┘
```
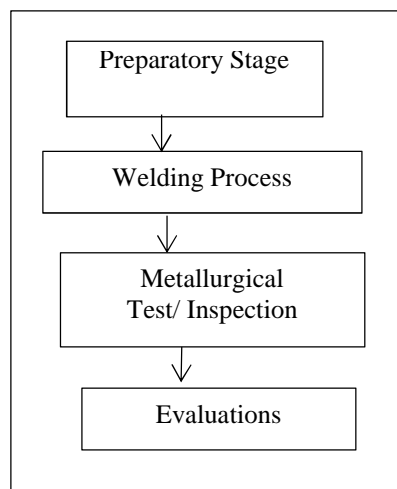
Figure 1: System Block Diagram

2.1   The Preparatory Stage

A dimension of 230mm x 150mm x 5mm thick sample of ASS 304L type of an appreciable length L was obtained. The sample was set up and cut into five (5) equal pieces of 60mm x 30mm x 5mm using power hack saw. The setup follows V-grooved butt configurations with a roof face of 1mm inclined at $30^{o}C$ and the land face of 2mm. The edge of each cut pieces was thoroughly cleaned with emery cloth and methylated spirit. Chemical composition of as-received 304L austenitic stainless steel plate was studied by infrared ray emission photo spectrometry using Raman Infrared Spectrophotometer (RIS) material analyser as illustrated in Table 1 before the welding process was carried out.

Table 1: Chemical composition base metal 304L stainless steel.

Elements	C	Mn	P	S	Si	Cr	Ni	Mo	Fe
%wt	0.03	2.00	0.045	0.039	1.00	18.04	8.09	0.36	70.38
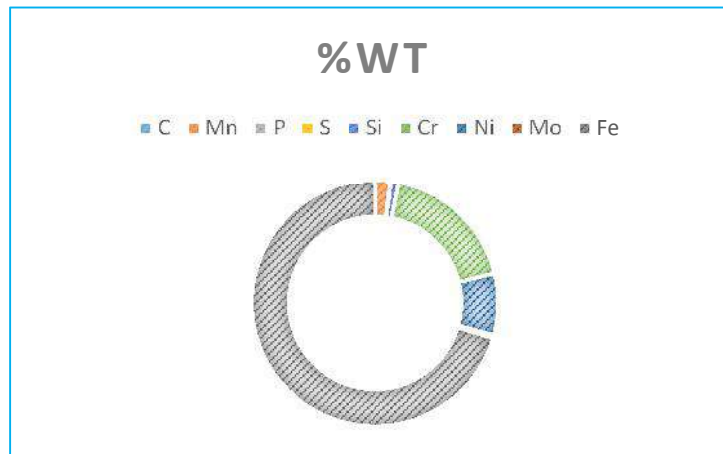
Figure 2: Chemical composition base Metal 304L stainless steel

2.2 Welding Process of ASS using TIG welding machine

The previous dimension sample sliced in to five (5) equal pieces of 60mm x 30mm x 5mm, were labelled A, B, C, D and E and further sliced in to the dimension of 30mm x 15mm x 5mm and labelled; A_1&A_2,B_1&B_2, C_1&C_2, D_1&D_2 and E_1&E_2 respectively. The samples ABCDE (1&2) were welded together at a designated welding current of 50A, 60A, 70A, 80A and 90A respectively. The corresponding welding temperature was also recorded using the K-type thermocouple digital thermometer model: HHM29. The weldments were allowed to cool gradually

59

under natural air conditional at room temperature. Table 2 and Table 3 Presents the TIG welding parameters used in this study. The welding conditions adopted were;

1. The weldments was cooled naturally in air so as to prevent the imposition of stress on the weld to avoid crack or avoid unnecessary vacancies (or area of defect or failure) in the weld.
2. It was ensured a narrow beads was deposited during welding
   No pre-heating of the base metal should be done to prevent martensite formation in the weld.

TABLE 2: TIG welding parameters employed for ASS 304L

Electrode	Filler metal	Current (A)	Electrode diam (mm)	Filler diam (mm)
EW-Th-2	Filler 308	50,60,70,80,90	3.15	3.15

Table 3: Parameters of TIG welding machine used

Machine type	Model	Power (hp)	Voltage (V)	Current (A)	Frequency (Hz)	Dimension (mm)
GYS TIG 250	AC/DC–HF	3	400	5 - 250	50/60	350x640x670

2.3   Metallurgical Test

2.3.1   Macro-structure and Micro-structure Examination

Macro-structure examination was first carried out on the parental metal of ASS 304L type as well as the weldments. Grinding of each specimen was carried out using paper grit of SiC of different grades ranges from 220-800 grit. The polishing of each samples by the use of emery clothe with alumina and water were carried out in a rotating polishing machine disc. The polished samples were etched at the weld joints using stainless steel etchant in the ratio of 10ml HNO3, 30ml HCL and 10ml glycerol. The time for etching was 2min. The width of HAZ of each samples were measured with the meter rule and each of the values were recorded.

3.0 Results and Discussion

A metal plate of austenitic stainless steel (ASS) of dimension 230mm x 150mm x 5mm was used in this research work. The dimension was sliced into five (5) equal samples of 60mm x 30mm x 5mmdimensions respectively. The sliced dimensions were further sliced into 30mm x 15mm x 5mm as specified and labelled in the methodology. The weldment of the samples was carried out

60

to investigate at what particular welding temperature ASS will be fastened together without chromium carbide formation. The results obtained from the various welding current were tabulated in Table 4 along with the welding temperature of each of the sample A, B, C, D & E. The relationship between the welding current and welding temperature is illustrated in Figure 3.

Table 4: Result of the welding current with corresponding temperature and power

Welding process	A	B	C	D	E
Welding current	50	60	70	80	90
Welding temp(c)	100.6	200.2	300.8	400.2	500.6

From Figure 3: below, it was observed that the welding temperature rises as the values of the welding current increases. This variation in the values of welding current determines the corresponding increase in welding temperature at which the formation of chromium carbide formation is likely to form. The choice of the welding machine in Table 3 was due to the aim of achieving a particular welding temperature at which "weld decay" (i.e. a significant chromium carbide formation) can be avoided when welding ASS 304L at lower temperature and also due to the available low range of current values of the Machine. The result of width dimension of HAZ of each weldments is presented in Table 5 below.

Table 5: Width dimension of HAZ od each weldments

Width of HAZ (mm)	A	B	C	D	E
	1.0	1.2	2.2	2.7	3.2

The width of HAZ illustrates the relationship between the welding current, temperature and width dimensions as the welding current and temperature increases. Figure 4 below depicts the relationship between the three (3) parameters. It was observed that the width of HAZ of each weldment measured varied at each value of welding current and corresponding temperature from 1.0mm to 3.2mm. The weldment with lowest width dimension of HAZ (i.e. sample A) with the lowest current of 50A, has the best mechanical property of ultimate tensile strength (UTS) of a material as compared with sample E with width dimension of HAZ of 3.2mm as earlier reported by (Guo et al., 2014) in their current research that the ultimate tensile strength (UTS) of a weldment material increases when the heat input is at the lowest. The relationship between welding current, temperature and width of HAZ is presented below in figure 3.
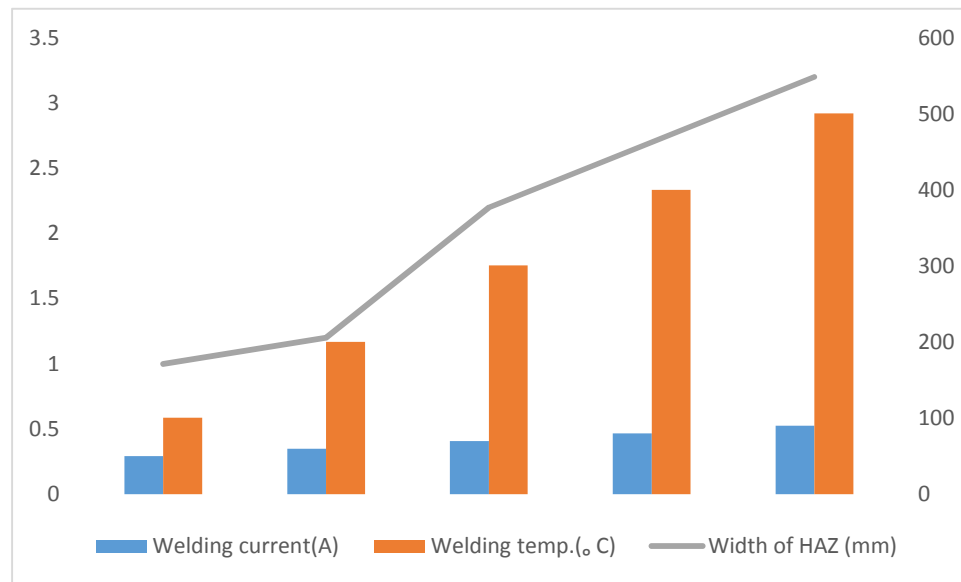
Figure 3: The relationship between welding current, temperature and width of HAZ

From Figure 3, as earlier reported by Guo et al., (2014), the ultimate tensile strength (UTS) of a weldment material increases when the heat input is at the lowest. It shows that when the heat input increases from C to E, at 2.2mm and 3.2mm with the corresponding temperature of 300.8°C to 500.6°C and current of 70A to 90A, then there is decrease in ultimate tensile strength (UTS).

The following Plates from plate 1 to Plate 6 depicts the microstructure of the parental metal used, the weldments A, B, C, D & E samples of ASS 304L type, the ASS 304L etched in a solution of 10ml HNO_3 +30ml HCL and 10ml glycerol.

3.1 Microstructure of the parental metal and the weldments

The following plates from plate 1 to plate 6 depicts the microstructure of the parental metal used, the weldments A, B, C, D & E samples of ASS 304L type, the ASS 304L etched in a solution of 10ml HNO_3 +30ml HCL and 10ml glycerol.

Plate 1: Microstructure of (as-received) of ASS 304L (Etched) using a solution of 10ml HNO3 + 30ml HCL and 10ml glycerol for 2mins.

62

Plate 2: Micro-structure of Weldment sample A of ASS 304L (Etched) using TIG with 308 filler metal at temperature of 100.6^{o}C cooled in air.

Plate 3: Micro-structure of Weldment sample B of ASS 304L (Etched) using TIG with 308 filler metal at temperature of 200.2^{o}Ccooled in air.

Plate 4: Micro-structure of Weldment sample C of ASS 304L (Etched) using TIG with 308 filler metal at temperature of 300.8^{o}C cooled in air
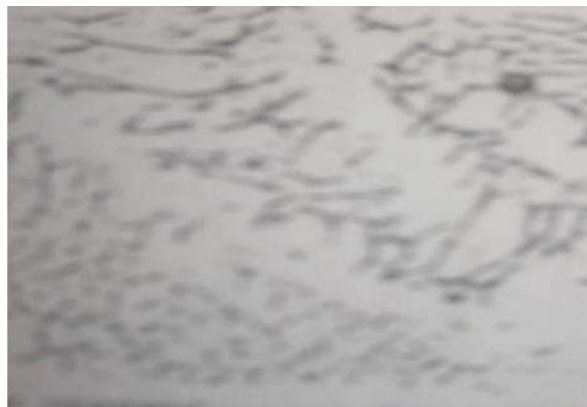
Plate 5: Micro-structure of Weldment sample D of ASS 304L (Etched) using TIG with 308 filler metal at temperature of 400.2°Ccooled in air

Plate 6: Micro-structure of Weldment sample E of ASS 304L (Etched) using TIG with 308 filler metal at temperature of 500.6°C cooled in air.

3.2   Micro-structural analysis of parental metal plate and the weldments

From Plate 1, the micro-structure of Parental metal Plate of ASS contains ferrite (dark) streaks in the matrix of austenite which is invulnerable by the etchant. Weldment sample A from Plate 2, just as similar to Plate 1, contains ferrite (dark) in a matrix of austenitic (white). The weldment B in Plate 3 has a structure that contains the same ferrite (dark) in a matrix of austenite, but the ferrite (dark) is more massive than in weldment A. Weldment C as shown in Plate 4, shows dendrite structure with excess delta ferrite (white). The structure also reveals chromium carbide formation of fine grained ferrite (dark) structure. In weldment D in plate 5 the structure consist of high chromium carbide formation of austenite grains precipitated at the grain boundaries. The structure also contains precipitated chromium carbide (small dark particles) in austenitic matrix as illustrated in Plate 5. The last weldment E, in Plate 6 reveals a micro-structure as same as that of sample D in Plate 5 that contains high chromium carbide formation of austenite grains precipitated at both inside and outside the grain boundaries. The structure also contains precipitated chromium carbide (small dark particles) in austenitic matrix as illustrated in Plate 5. The micro-structures reveals that: there is no chromium carbide formation in the weldment of sample A Plate 2 and

64

sample B Plate 3, but very obvious and significant formation of chromium carbide in weldment C Plate 4, D Plate 5 and E Plate 6.

4.0 Conclusions

The welding of ASS 304L has been carried out, using TIG welding technique. The formation of chromium carbide with increase in welding current along with the corresponding
Increase in temperature was investigated. Based on the result of macro examinations and microstructures. The following conclusions were drawn. Based on the result of micro-structures, the material of ASS of type 304L welded at lower current of 50A, 60A at a corresponding welding temperature of 100.6^{o}C and 200.2^{o}Cdo not contains chromium carbide formation in the weld. This will eventually solve the problem of corrosion due to a corrosion mechanism called weld decay in petrochemical, oil and gas, automobile, marine, robotic, aerospace and nuclear industries if a control temperature is applied.

Finally, ASS 304L type with the lowest width of HAZ (i.e. 1.0mm and 1.2mm) at a given weld current of 50, 60A with a corresponding temperature of 100.6^{o}C and 200.2^{o}C gives a better mechanical properties of strength and hardness. The experimental welding temperature commensurate with the computer simulated welding temperature, which justify the validity of weldments of austenitic stainless steel ASS 304L at lower range of temperature of 100.6^{o}C and 200.2^{o}C.

Acknowledgments

References

Gao, X. D., and Zhang, Y. X. (2014). Prediction model of weld width during high-power disk laser welding of 304 austenitic stainless steel. International journal of precision engineering and manufacturing, 15(3), 399-405.

Guo, J. F., Chen, H. C., Sun, C. N., Bi, G., Sun, Z., & Wei, J. (2014). Friction stir welding of dissimilar   materials between AA6061 and AA7075 Al alloys effects of process parameters. Materials &   Design (1980-2015), 56, 185-192.

Joo, S. M., Bang, H. S., Bang, H. S., and Park, K. S. (2016). Numerical investigation on welding residual stress and out-of-plane displacement during the heat sink welding process of thin stainless   Steel   Sheets. International   Journal   of   Precision   Engineering   and Manufacturing, 17(1), 65-72.

Mendes, R., Ribeiro, J. B., and Loureiro, A. (2013). Effect of explosive characteristics on the explosive   welding   of   stainless   steel   to   carbon   steel   in   cylindrical configuration. Materials & Design, 51,   182-192.

Mishra, D., Vignesh, M. K., Raj, B. G., Srungavarapu, P., Ramkumar, K. D., Arivazhagan, N., and Narayanan, S. (2014). Mechanical characterization of Monel 400 and 316 stainless steel weldments. Procedia Engineering, 75, 24-28.

Moslemi, N., Redzuan, N., Ahmad, N., and Hor, T. N. (2015). Effect of current on characteristic for 316 stainless steel welded joint including microstructure and mechanical properties. Procedia CIRP, 26, 560-564.

Oyetunji, A., Kutelu, B. J., and Akinola, A. O. (2013). Effects of Welding Speeds and Power Inputs on the Hardness Property of Type 304L Austenitic Stainless Steel Heat-Affected Zone (HAZ). Journal of Metallurgical Engineering, 2(4), 124-129.

Reddy, M. P., William, A. A. S., Prashanth, M. M., Kumar, S. S., Ramkumar, K. D., Arivazhagan, N., and Narayanan, S. (2014). Assessment of Mechanical Properties of AISI 4140 and AISI 316 Dissimilar Weldments. Procedia Engineering, 75, 29-33.

Roy, C., Pavanan, V. V., Vishnu, G., Hari, P. R., Arivarasu, M., Manikandan, M., and Arivazhagan, N. (2014). Characterization of metallurgical and mechanical properties of commercially pure copper and AISI 304 dissimilar weldments. Procedia Materials Science, 5, 2503-2512.

Song, E. J., Baek, S. W., Nahm, S. H., and Baek, U. B. (2017). Notched-tensile properties under high- pressure gaseous hydrogen: Comparison of pipeline steel X70 and austenitic stainless type 304L, 316L steels. International Journal of Hydrogen Energy, 42(12), 8075-8082.

Yang, J., Xiao, B. L., Wang, D., & Ma, Z. Y. (2010). Effects of heat input on tensile properties and fracture behavior of friction stir welded Mg–3Al–1Zn alloy. Materials Science and Engineering: A, 527(3), 708-714.

Zhang, M., Chen, G., Zhou, Y., and Liao, S. (2014). Optimization of deep penetration laser welding of thick stainless steel with a 10 kW fiber laser. Materials & Design, 53, 568-576.

THE USE OF GYPSUM AS AN ADDITIVE IN WATERBORNE BASE COATS FOR AUTOMOTIVE COATING.

D. J. Udoh[*] and A. A. Abdullahi

Department of Mechanical Engineering, Federal University of Technology, Minna.
[*]Email: Danielsons4flip@gmail.com

ABSTRACT

The Automobile industry focuses interest in waterborne base coat lately due to low production output, long flash off time and adhesion before curing. Efforts are been made in researching for base coat formulation to ensure reduction of flash off time while maintaining and improving their properties. The paper investigates the effect of gypsum in waterborne base coats for automotive coating, formulation, preparation and drying of the waterborne base coat samples at various temperatures. The samples of deposited coat were weighed and analysed in Minitab software using Taguchi design. The waterborne base coat was observed when sprayed, having no splashing and droplet on the sample surface. The gypsum facilitated the evaporation of moisture from the film in a shorter time at low temperature of 50°C which is called the flash off time before curing with clear coat. The flash off time of was 7-8minutes was determined at 50°C for the formulation. Adhesion test was carried out on the films and good adhesion between the primer, base coat and clear coat were achieved. Drying at 50°C helps in the reduction of energy consumption in the automobile industry.

Keywords: Automobile, Base coat, Gypsum, Flash off time, Adhesion

1.0   INTRODUCTION

The incredible changes in the automotive coating industries occurs largely due to changes in process development and chemical nature of the film former for mechanical and adhesion properties. Research continues to formulate to improve the topcoats performance and the reduction in flash off time in automotive coating industries to maximise production output. The topcoat which is the final coat in an automotive, consist of two layers which are the base coats and clear coats. The base coats gives colour to the automotive (Streitberger, 2008). They are applied over the primer surfacer and covered by the clear coats layer to protect it from the environment. The main requirements for base coat formulation are high opacity and good intercoat adhesion to primer and to clear coats (Poth, 1995). The thickness of prime surfacer, base coat and clear coat differs from each other and the base coat thickness which is approximately 15µm is shown in Figure 1 (Nelson et al, 2016).

The base coats which are of two type's solventborne base coats and waterborne base coats. The waterborne base coats are preferred over solventborne base coats due to heavy emission of solvent and in compliance with the legislative law (Poth, 1995). Waterborne base coats have become the main base coat technology for all new automotive coating industries built after the year 2000 and have captured most of the market in the world. This success is driven partly by the environmental benefits, and partly by their superior performance and robust application properties (D¨ossel,

67

2008). The waterborne base coat consists of water and the dry coating layer is form by a solid fraction of resin, pigments and additives. The drying process of these materials has to be optimised to achieve a desired quality of the final coating and to reduce flash off time. The time when an automobile is placed in the oven and begins to dry is called the flash off time (Stephan, 2005). The research described is part of the development of an innovative technology for waterborne base coats with a superior mix of material and application properties of drying and curing of films.
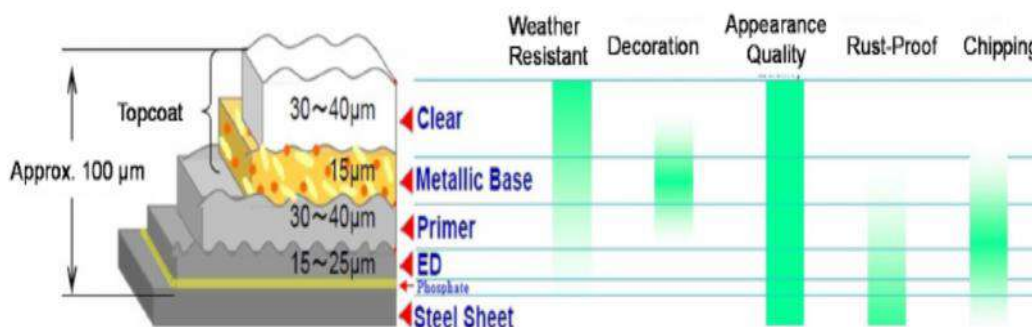

Figure 1: Automotive Coating Layers, thicknesses and purposes for An exterior Surface (Nelson et al, 2016).

2.0   Materials and Methods

2.1   Materials

The materials for formulation of automotive coating were resin (Polyvinyl formal), pigments (Titanium oxide), additive (Gypsum), distilled Water, automotive paint (clear coat), and primer surfacer. The sample surface used for the research experiment was Mild steel plates of size 160mm x 160mm × 0.8mm.

2.2   Methods

The process of coating was carried out following the automobile coating industry procedure (Prendi, 2005). The samples surfaces were cleaned and prepared for deposition of prime surfacer and was dried. The base coat was deposited after drying of the prime surfacer. The samples were inspected for application of a clear coat to determine adhesion between both coats.

2.2.1   Formulation and preparation of waterborne base coat

The mixture was in proportion by volume percentage between pigment, resin, water, and additives (gypsum). The coat was prepared following a standard ratio 25:30:40:5 (Center for Industry Education Collaboration, 2013). The mixture which consists of 25% Titanium oxide, 30% Polyvinyl formal, 40% water and 5% Gypsum was prepared for coating shown in Figure 2.
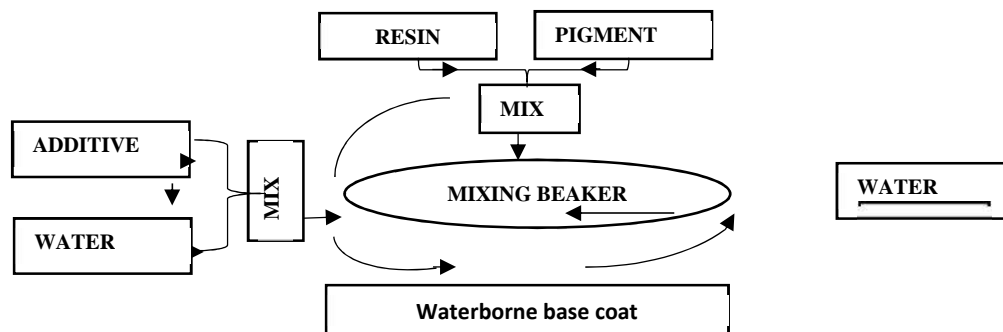
Figure 2: Preparation of waterborne base coat.

2.2.2 Drying of Samples

The waterborne base coat was applied with the gun spray vertically and horizontally. After deposition the steel plates were weighed before transferred into the oven for drying. The oven temperature was adjusted to achieve the desired flash off time for each steel plate. The temperature consider are 30°C 35°C 40°C 45°C 50°C and the flash off time are 1-5 minutes these values correspond to conditions used in the automotive industry for forced flash-off of base coats before the application of clear coat(Domnick et al, 2011). The moisture content left was determine using the drying percentage expressed mathematically in equation (1)

$$D = \frac{w_2 - w_3}{w_2 - w_1} \times 100 \tag{1}$$

Where, D is drying percentage, w_1 is weight before spraying ( ), w_2 is weight after spraying ( ), and w_3 is weight after drying ( ).

2.2.3 Factors and Drying Parameters Specification

The waterborne base coat was used with desired flash-off time and temperatures on the experimental samples using Taguchi Design. The experimental samples were analysed in three aspects by the design of experiments (DOE) which are factors, levels and responses. After editing the data with five levels and two factors each, there are 25 experimental runs taken into account in total and were two experiments were carried out manually to determine the outcome of drying.

Table 1: Factors and Level of drying parameters

Factors	Levels				
	1	2	3	4	5
Drying temperature (°C)	30	35	40	45	50
Flash off time (min)	1	2	3	4	5

2.2.4   Drying rate experiment

The best parameter of drying analyzed in the taguchi design was used to determine the rate of drying for the steel plate, placed in the oven and under constant drying conditions, the loss in weight of moisture during the drying process is determined at constant time intervals of 1minute. The rate of drying "R" can be mathematically expressed in equation (2) (Muller and Poth 2011).

$$R = \frac{S}{A}\frac{dX}{dt} \tag{2}$$

where, R is drying rate (H_2O/sm^2), S is weight of dry solid ( ), A is exposed surface area for drying (m^2), X is solid moisture content ($H_2O/$ dry solid) and t is time (s).

$$X = \frac{m_1}{m_2} \tag{3}$$

Where, X is moisture content, m_1 is mass of water ( ) and m_2 mass of dry solid ( )

2.2.5   Testing of composition

The tests were carried on the composition of mixture. The tests carried out for liquid base coat are viscosity, pH, volume solid (VS) and pigment volume concentration (PVC) expressed in equation (4) and equation (5).

$$VS = \frac{(V_p + V_R)}{V_T} x\ 100 \tag{4}$$

Where, VS is volume solid, V_p is volume of pigment, V_R is volume of resin and V_T is total volume of paint;
$$PVC = \frac{V_p}{V_p + V_R} x\ 100 \tag{5}$$

The volumes (V) are calculated as the quotient of mass (m) and density ( ): $V = \frac{m}{\rho}$ (Muller and Poth 2011).

3.0   Results and Discussion

3.1   Formulation test results of waterborne base coat

The resulting viscosity of the formulation measured at DIN4/23˚C is 15seconds and the test result for pH, volume solid and pigment volume concentration carried out are shown in Table 2. The pH 0f 9.45 is considered an alkaline having a colouration of a baking soda. The pigment volume concentration of 35.04% resulted into increases in drying of coat film, adhesion, cleanability and scrubbability.

Table 2: Results of test of formulation

Viscosity (seconds)	PH	Volume solid (%)	Pigment volume concentration (%)
15	9.45	52	35.04

3.2 Drying

The resulting amount of spray coat for each samples ranging from 1.4 – 3.3 due to the spraying machine output and recoating for samples not properly coated shown in Table 4. At 50°C the moisture content was less with a drying percentage of 52% which was the best outcome to carry out the drying rate.

At 50°C gypsum as a drying additive enables the coat release moisture at a flash off time of approximately from 7 minutes 5 seconds to 7 minutes 15 seconds and averagely 7minutes 10 seconds without interruption giving a good quality shown in Table 3. These results validated with the data obtain by (D¨ossel, 2008).

Table 3: Result of average total drying time

Temperature(°C)	30	35	40	45	50
Total average of drying time (seconds)	920	860	691	580	430

Table 4: The experiments were carried out manually and the measured values were added in the design

	Input Parameter		Output				
S/N	Temperature(°C)	Flash off time(min)	Amount of spray coat( )	Amount after drying( )	Drying (%)	SNRA1	MEAN1
1	30	1	2.2	1.5	31.820	-27.0437	15.92
2	30	2	1.9	1.2	36.840	-28.3161	18.4275
3	30	3	2.1	1.5	26.571	-25.4779	13.29125
4	30	4	1.9	1.2	36.840	-28.3161	18.4275
5	30	5	2.0	1.2	40.000	-29.0309	20.0125
6	35	1	2.7	1.8	33.333	-27.4472	16.674
7	35	2	2.7	1.8	33.333	-27.4472	16.6765
8	35	3	2.7	1.8	33.333	-27.4472	16.6765
9	35	4	2.8	1.7	39.290	-28.8753	19.6525
10	35	5	2.5	1.5	40.000	-29.0309	20.0125

11	40	1	1.5	1.0	33.333	-27.4472	16.669
12	40	2	1.4	0.8	42.850	-29.6287	21.43
13	40	3	1.4	1.0	28.570	-26.1079	14.29
14	40	4	1.6	0.8	50.000	-30.9691	25.0075
15	40	5	1.6	0.8	50.000	-30.9691	25.0075
16	45	1	1.6	0.9	43.750	-29.8093	21.8825
17	45	2	1.7	0.9	47.060	-30.4427	23.5375
18	45	3	1.7	0.9	47.060	-30.4427	23.54
19	45	4	1.7	0.9	47.060	-30.4427	23.5375
20	45	5	1.4	0.7	50.000	-30.9691	25.005
21	50	1	2.7	1.5	44.400	-29.9374	22.21
22	50	2	2.5	1.2	52.000	-31.3098	26.0075
23	50	3	3.1	1.5	51.600	-31.2427	25.8075
24	50	4	3.3	1.6	51.500	-31.2258	25.76
25	50	5	2.5	1.2	52.000	-31.3098	26.01

3.2.1 Main Effects Plots for S/N ratios for drying percentage

The result of the main effects plot for the signal-to-noise ratio was is shown in Figure 3. The best outcome based on Figure 3 using smaller is better for the analysis was 50˚C and flash off time of 5minute. This also shows the ranking lists of the two factors from the most important to the least important. Temperature is the most important factor that causes variation on drying of waterborne base coat followed by the flash off time shown in Figure 3. The temperature at 30˚C has the least effect on drying of the coat and 50˚C has more effect on drying of the coat. At 50˚C gypsum as a drying additive enables the coat release moisture at a flash off time of approximately from 7 minutes 5 seconds to 7 minutes 15 seconds and averagely 7minutes 10 seconds without interruption giving a good quality. These results validated with the data obtain by (D¨ossel, 2008).
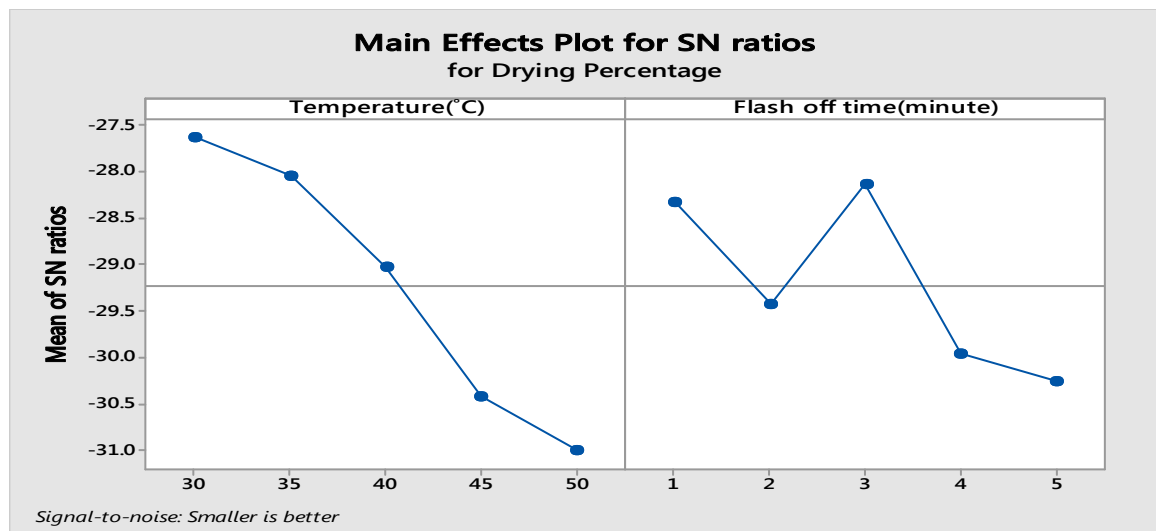

Figure 3: Main Effects Plots for Signal to Noise ratios for drying percentage.

3.2.2   Analyse of variance method (ANOVA)

In this experiment, ANOVA was used to analyse the effects of temperature and flash off time on drying percentage. The ANOVA result for the drying percentage is shown in Table 5 This analysis was carried out a 5% significance level and a 95% confidence level. The significance of control factors in ANOVA is determined by comparing the F values of each control factor. The last column of the table shows the percentage value of each parameter contribution which indicates the degree of influence on the process performance. According to Table 5, the percentage contribution of the Temperature and flash off time factors on the drying percentage is found to be 58.13% and 21.59%. Thus, the most important factor affecting the drying percentage was Temperature at 58.13%. The percentage of error was considerably low at 20.28%.

Table 5: Results of ANOVA for drying percentage.

Variance source	Degree of freedom (DOF)	Sum of squares (SS)	Mean square (MS)	F ratio	Contribution rate (%)
Temperature(°C)	4	948.4	237.10	15.24	58.13
Flash off time(minute)	4	352.3	88.09	5.66	21.59
Error	16	248.9	15.56	-	20.28
Total	24	1549.7	-	-	100

3.2.3   Drying Rate

The best outcome gotten from the Taguchi design it was implemented in experimental determination of rate of drying, 50°C ±5°C and 7 minutes was used at an interval of 1minute to determine the rate of drying. The drying rate results are presented in Table 6

Table 6: Results of drying rate

Drying Time(minute)	0	1	2	3	4	5	6	7	8
Weight after dried( )	272.0	270.7	270.1	269.4	268.7	268.2	267.5	267.1	267.1

The solid moisture content(X), slope of plotted moisture content with time and drying rate(R) were determine using equation (2) and Equation (3) shown in Table 7. The moisture content was plotted against time shown in Figure 4, the rate of drying curve was obtained by measuring the slopes of

73

the tangents drawn in Figure 6, and the values of dX/dt was obtained at values of time. The rate of drying(R) was calculated for each point using equation (2). The rate of drying curve was obtained by plotting R against solid moisture content (X) as in Figure 5.

The rate of drying curve is majorly on two points, constant and falling rate period. At time zero the initial moisture content of the solid is shown at point A depending on the solid temperature. In Figure 5 the rate of drying curve for constant drying conditions is shown. At point A the solid is at normal room temperature and when inserted in the oven of its ultimate temperature the rate of evaporation was increased and the weight of the solid decreased to Point B. At point B the temperature of solid rises which started from point A. This state of adjustment temperature and time during weighing the solid are usually quite short and is often ignored in the analysis of times of drying.

From point C to D Figure 4 there was a little decrease in temperature which leads a decrease of evaporation. From point CDEF to G the line is straight and hence the slope and rate are constant during this period. This constant rate of drying period is shown as line CG in Figure 5 at both figures the rate of drying start to decrease in the falling rate period at point C to reach point G. The falling rate period is usually shown linear and is represented in Figure 5 form point CDEF to G.

At point B, the evaporation rate was high which lead to insufficient of water on the surface at Point C in Figure 5 to maintain a continuous film of water. The solid was no longer wet and there was continuous decreases in weight at each point in the falling rate period from CDEF to G were the solid was completely dried.

The final falling rate period which began from point G were the solid was dried and there was no detectable change until the equilibrium moisture content of the solid is reached, at point H. The time required to remove an amount of moisture in the falling rate period at each point was small. This can be seen in Figure 5. The period AB for constant rate drying last for about 1minute and reduce X from 0.028 to 0. $H_2O/$ dry solid a reduction of 0.0057 $H_2O/$ dry solid. The falling rate period from B to H lasted for 6minutes and gave a reduction of X only from 0.0232 to 0.0095$H_2O/$ dry solid. The gypsum affected the drying with it capability to release water from the surface at 50˚C in a short period of time. At point A to B there was a drastic reduction of weight due to elevated temperature which occurs from room temperature to the oven temperature. The plotted rate of drying curve was validated with (Stephan, 2005) at 50˚C give gypsum an advantage to affect the drying rate curve.

Table 7: Results of Calculated solid moisture content and rate of drying

S/N	Drying Time(minute)	X ($H_2O/$ dry solid)	dX/dt	R(/s m²)
1	0	0.0280	0.0050	51.68
2	1	0.0231	0.0050	51.68
3	2	0.0208	0.0045	46.51
4	3	0.0181	0.0040	41.34
5	4	0.0155	0.0035	36.18
6	5	0.0136	0.0030	31.01

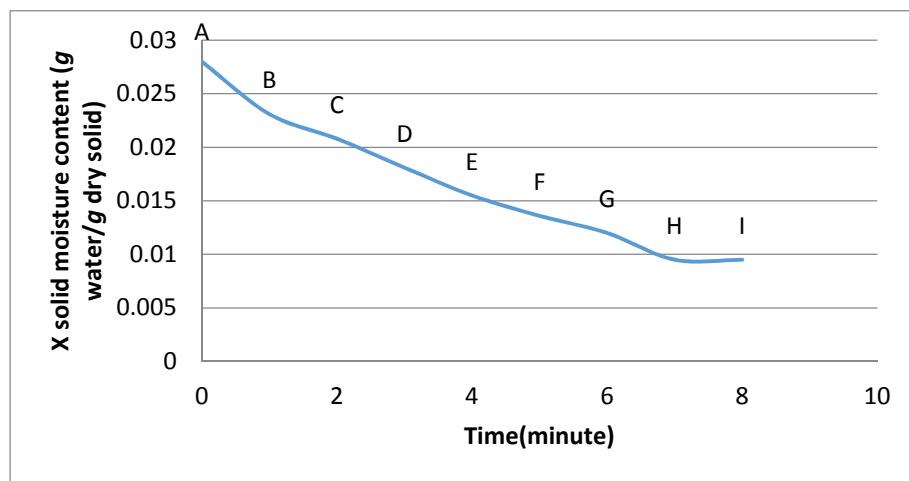|				
7	6	0.0120	0.0025	25.84
8	7	0.0095	0.0010	10.34
9	8	0.0095	0.0000	00.00

Figure 4: X solid moisture content versus time for constant drying conditions
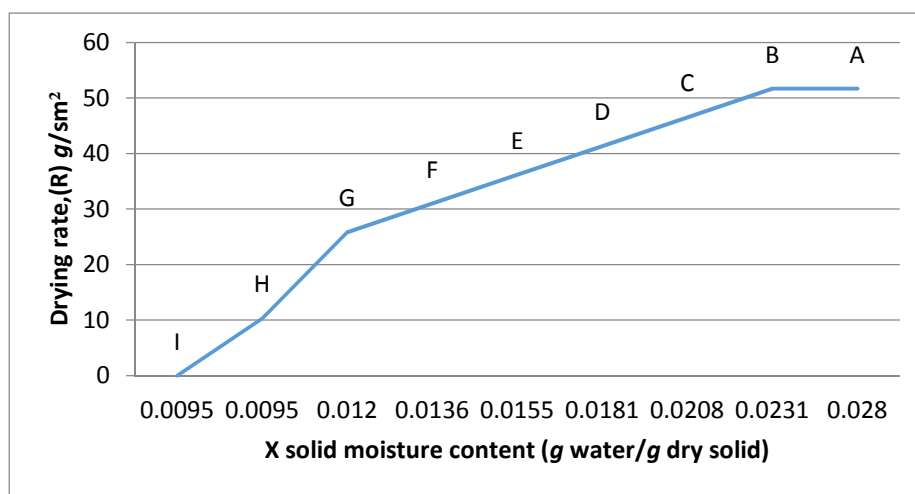

Figure 5: Rate of drying (R) versus X solid moisture content for constant drying conditions

4.0   Conclusions

The use of gypsum in waterborne base coats for automotive coating applications has been experimental investigated in formation and drying of the films. In this research, waterborne base coat formulation process was successfully developed using 5% of Gypsum as an additive indicated it use. Gypsum can be used as a drying additive in coating, additives that increase coat viscosity immediately after a surface is sprayed and thereby prevent pigment movement and disorientation. Gypsum also gives good sealing properties and protects the sample from environmental damages

and increases adhesion with the prime surface. The coat's cleanability and scrubbability increases lead to durability of the coat on the substrate.

Temperature has the strongest influence on gypsum on the total drying rate in the reduction of flash off time. The low temperature helps in the reduction of consumption of energy and reduces cost in the automobile industry.

References

Centre For Industry Education Collaboration. (2013, March 18). The Essential Chemical Industry. Retrieved July 13, 2018, From The Essential Chemical Industry Web Site: Http://Www.Essentialchemicalindustry.Org/Materials-And-Applications/Paints.Html

Domnick J., D. G. (2011). Investigations of the drying process of a water based paint film for automotive application. Chemical Engineering and Processing: Process Intensification, 595-602.

D¨Ossel, K.-F. (2008). Top Coat. In H.-J. S.-F. D¨Ossel (Ed.), Automotive Paints And Coatings (2nd Ed., Pp. 175-209). Germany: Wiley-Vch Verlag Gmbh & Co.

Muller B., Poth. U. (2011). Paint Formulation. In P. U. Müller B., Coatings Formulation (Pp. 60-70). Hanover: Vincentz Network Gmbh & Co. KG,.

Nelson K. Akafuah, Sadegh Poozesh, Ahmad Salaimeh, Gabriela Patrick, Kevin Lawler, Kozo Saito. (2016). Evolution Of The Automotive Body Coating.

Poth, U. (1995). Topcoats For The Automotive Industry. In G. Fettis (Ed.), Automotive Paints And Coatings (First Ed.). Vch Verlagsgesellschaft, Weinheim.

Streitberger, H.-J. (2008). Historical Development. In H.-J. S.-F. D¨Ossel (Ed.), Automotive Paints And Coatings (Second Ed., Pp. 1-5). Wiley-Vch Verlag Gmbh & Co.

EFFECT OF CARBON NANOTUBE CONTENT ON THE MECHANICAL PROPERTIES OF CNT-REINFORCED ALUMINIUM ALLOY METAL MATRIX COMPOSITES

Yerima, M. L[1]., Abdulkareem A. S[2]., Abubakre, O. K., [3] Ndaliman, M. B.,[4] and Khan, R. H.[5]

Mechanical Engineering Department, Federal University of Technology Minna, Nigeria[1,3,4,5]
Chemical Engineering Department, Federal University of Technology Minna, Nigeria[2]

ABSTRACT

The paper presents the results of experimental investigations of CNT-Al 2024 alloy composites having 0.5 wt%, 1 wt%, 1.5 wt%, 2 wt% and 2.5 wt% of CNT prepared through liquid metallurgy (stir cast) route. The composite specimens were machined as per test standards. Some of the mechanical properties have been evaluated and compared with Al2024 alloy. Significant improvement in tensile properties, compressive strength and hardness are noticeable as the weight percentage of the CNT increases. The microstructures of the composites were studied to know the dispersion of the CNT in matrix. It has been observed that addition of CNT significantly improves tensile strength along with compressive strength and hardness properties by 56, 61, and 9% respectively, as compared with that of unreinforced matrix.

Keywords: CNT, Al 2024 alloy-matrix composite, Stir cast, mechanical properties.

1.0   INTRODUCTION

The reinforcement of aluminium alloys with carbon nanotubes has led to the generation of new engineering materials with improved mechanical properties. Aluminium alloys attracts intense studies, owing to its low density which results to several advantages in diverse areas of applications. (Esawi 2010). These alloys have started to replace cast iron and bronze, in the manufacture high quality parts. CNT has been a good candidate for reinforcement in composites due to its outstanding mechanical properties, such as young modulus of 1TPa. Literatures have shown enhancement of mechanical properties of metal matrices as a result of addition of CNTs. Different methods has been used to disperse CNT into metal matrix. Powder metallurgy which is the most preferred method of MMCs preparation due to its low processing temperature employed in mixing the powder is quite costly and not applicable to complex shapes. Other manufacturing techniques such as squeeze, melt impregnation and spray casting methods are also constrained by certain disadvantages which include high cost as well as restricted size and limited shapes of the final product.

The present study takes advantage of stir casting technique which is proven to be more viable owing to its simplicity, flexibility and ability to produce large sized and complex shaped component. It is also attractive because it allows a conventional processing route to be used and hence minimizes the final cost of the product.

Regarding aluminium matrix composites Kuzumaki et al. (1998) were the first researchers to show a 100% increase of the tensile strength adding 10 vol.% CNT, while a maximum of 129% increase

77

in the tensile strength has been reported with the addition of 5 vol. % CNT addition (Deng, 2007). On the contrary, Salas et al. (2007) have reported deterioration in hardness in a shock-wave-consolidated aluminium composite reinforced by 5 vol.% CNT composite. Agglomeration of CNTs in the matrix and weak interface bonding led to deterioration in the properties. Noguchi et al. reported a 350% increase in the compressive yield strength in the case of 1.6 vol.% CNT addition, using the nanoscale dispersion method, which can provide a very satisfying dispersion and distribution of the reinforcements. by 5.45% and BHN value (Thomas et al., 2014). In this light an attempt has been made to develop CNT-Al 2024 alloy composites. An effort has been made in this paper to study the mechanical properties of CNT-Al 2024 alloy composite by varying the wt% of the CNT.

2.0   Materials and Methods

The matrix material used in this study is Al 2024 obtained from Scientific Equipment Development Institute, Minna, Nigeria. The CNT as presented in Plate 1 (16-50 nm diameter and approximately 33 µm length) was obtained from Centeor for Genetic Engineering and Biotechnology, Federal University of Technology Minna, Nigeria. Table 1 presents the chemical composition of un-reinforced Al2024 alloy.

Table 1: Chemical Composition of Raw Al- Cu Alloy

Elements	Al	Cu	Si	Fe	Ti	Cr	Ca	Ba	Pb	S
Percentage Composition (%)	95.432	4.112	0.204	0.149	0.021	0.02	0.02	0.002	0.002	0.038

Table 2: Mechanical Properties of Raw Al- Cu Alloy

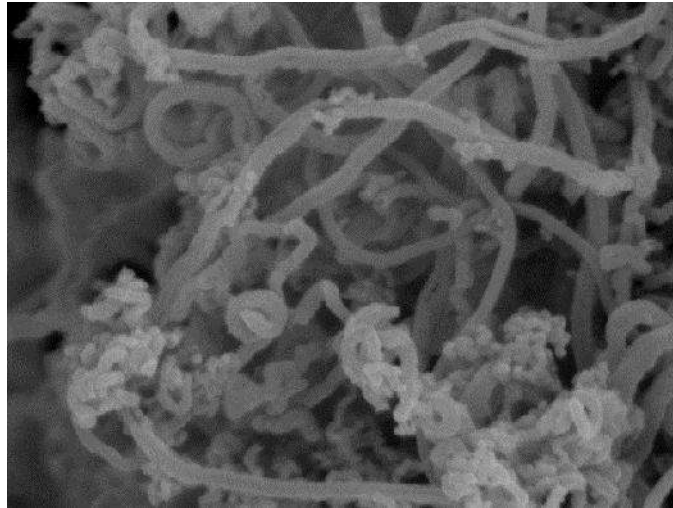| Tensile Strength, N/mm2	Compressive Strength, N/mm2	Hardness, (BHN)
100	205	69

Plate 1: Scanning Electron Microscope Image Carbon nanotubes.

The composite was prepared using stir cast experimental rig presented in Plate 2. The experiment commenced by melting 200g of Al 2024 alloy ingot in the cylindrical stainless steel crucible in the electric resistance furnace. Once the processing temperature of 690 °C of the first run was attained, the mechanical stirrer was switched to a speed of 500 rpm and lowered into the molten metal. A safe clearance of about 50mm was ensured between the impeller and the bottom of the crucible. MWNT (1.5wt%) was preheated at 200 °C for 30 min was gradually introduced into the molten metal using injection funnel while stirring continued for 150 secs. . The stirrer was raised at the end of the mixing and the mixture was poured into the prepared sand mould immediately. Digital thermocouple was used after the stirring to ensure that precise processing temperature was attained.
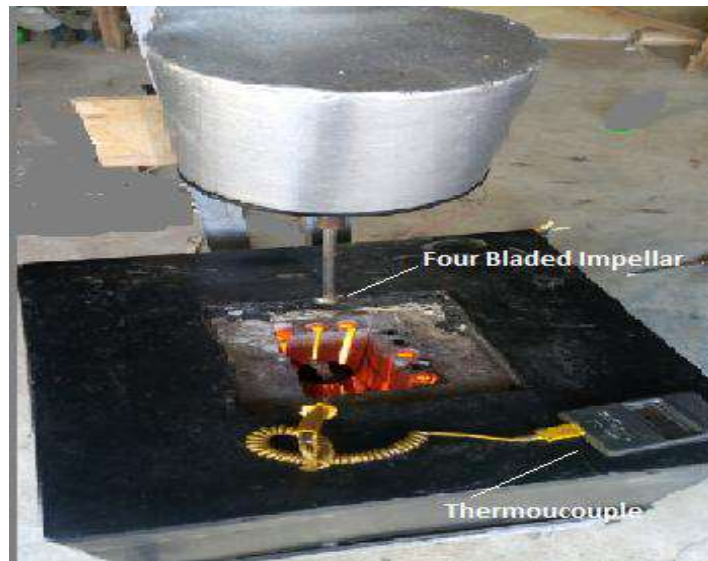

Plate 2: Stir-cast Experiment Rig

2.1 Tensile Test

Tensile testing was conducted using Dog-bone tensile test samples which were machined according to ASTM E8 standard. The testing was performed using 10kN Monsato Tensometer at a strain rate of 5 X 10^4 s^{-1}. The tensometer is equipped with data acquisition system which supplies the stress - strain curve during tensile test at room temperature. The test involves taking a sample of fixed cross-section area, and then pulling it by gradually increasing the force at a speed of 5 µm/s until the sample changes shape or breaks. The tensile test was carried out for all specimens respectively.

2.2 Compression Test

The compression test was also conducted using 10kN Monsato Tensometer, according to ASTM-E9 standard, the specimens of compression tests were prepared with diameter of 5 mm and guage length of 45 mm. in this case, the test involves gradual application of uniaxial force at a speed of 5 µm/s until the sample buckles.

2.3 Hardness Test

Brinnel hardness (BHN) test was conducted for all composite specimens. The specimens were machined to ASTM B724 standard which specified length and diameter of 10mm each. The hardness of the specimen determined by Brinell hardness testing machine with 20 kg load and 2 mm diameter steel ball indenter. The detention time for the hardness measurement was 20 seconds.

2.4 SEM of Produced Composite

SEM observation of the produced Aluminum grains in composite was performed. In preparation for SEM imaging, the composite was cut into a half-moon shape and etched using nitric acid. SEM samples were prepared by finishing the polished surface of the cross section of composites using a cross-section polisher.

3.0 Result and Discussion

3.1 Effect of CNT Weight Fraction Tensile Strength

The result obtained from the tensile test conducted to investigate the effect of CNT content on the tensile strength of the produce composite is presented in Figure 1. It is clear that the addition of CNTs results in an increase in strength at all CNT contents. It is observed that the addition of 2 wt% CNT provides the most significant strengthening of up to 50%. Further addition of CNTs (2.5 wt%) did not, however, contribute to a further enhancement.
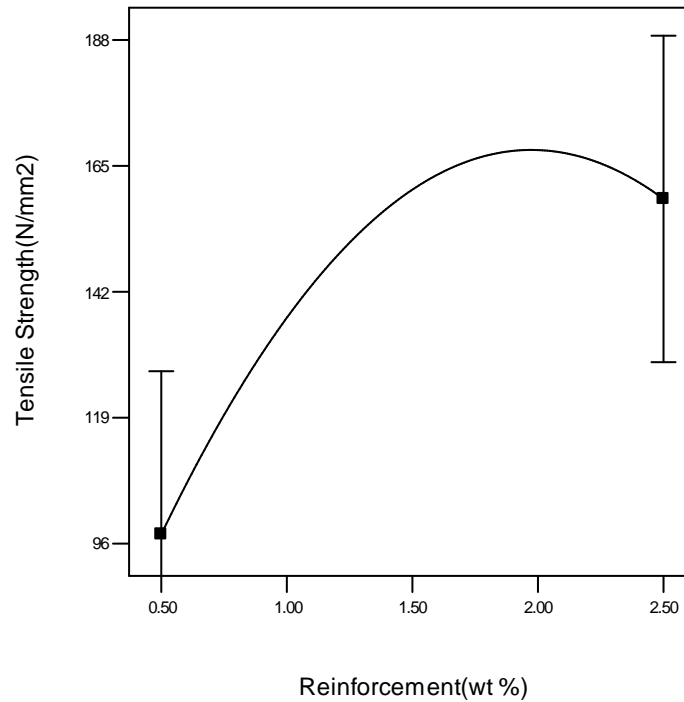
Figure 1: Effect of CNT Weight Fraction on Tensile Strength of Composite

The improvement in strength observed is also attributable to the behavior of nano size MWNT which serve as dislocation barriers. The increase in CNT weight fraction increases the number of dislocation barriers which further enhances strength. (Srinivasa, & Arvind, 2011). The decrease in strength at 2.5 wt% can be attributed to possible clustering of the CNTs at large volume fractions especially that the CNTs used in the present study have small diameters which make them difficult to disperse. In addition to poor dispersion, another factor expected to limit the strengthening and stiffening observed is the poor interfacial bond between the CNTs and the aluminium matrix which are observed to fail by CNT pull-out.

The conclusions made by various researchers on the tensile behaviour of Al – CNT composite varies greatly especially when different methods are used. Choi et al. (2009) reported the highest value of tensile strength of 629 MPa which was obtained through ball milling and hot- rolling process. Esawi et al. (2009) fabricated an Al–CNT composite coupling planetary milling and rolling process. In that case the maximum obtained tensile strength of the pure aluminium in presence of 0.5, 1 and 2 wt% CNT composite was increased by 10% compared to that of pure bulk aluminium. Esawi et al. (2009) also reported an approximately 50% increase in the tensile strength of the aluminium reinforced by 2 wt% CNTs prepared using the extrusion method.

3.2   Effect of CNT Weight Fraction on Compressive Strength

The effect of CNT weight fraction on compressive strength is presented in Figure 2. It can be deduced that the effect of CNT content on compressive strength of the composite also follow the

81

same pattern as the tensile strength. The general trend shows that increase in CNT weight fraction result in increased compressive strength. This finding can be attributed to the possibility of load transfer to the homogenously dispersed CNT in the Al matrix. However, addition of CNT beyond 2wt% weight fraction lead to decrease in the compressive strength. This could be as a result of CNT clustering and formation of weak Al_4C_3 phase at higher CNT weight fraction which eventually lead to composite (Esawi et al., 2010).
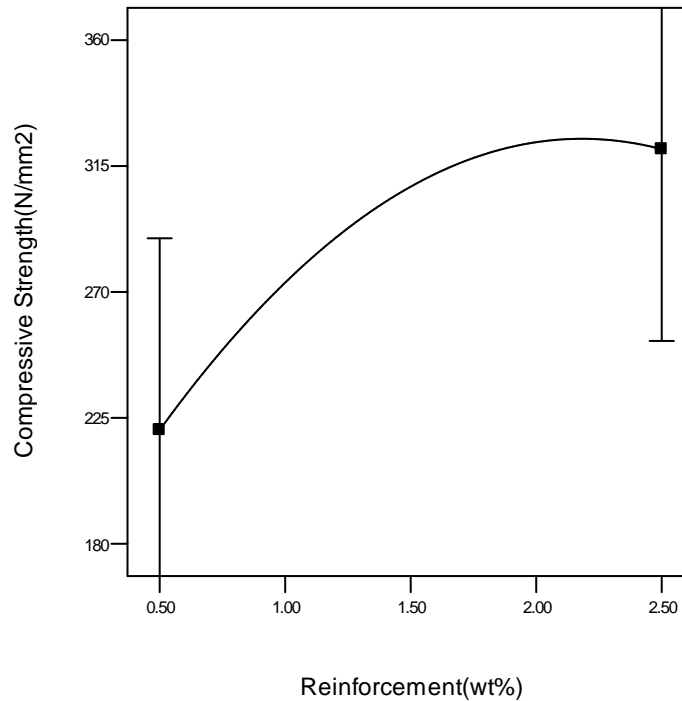
Figure 2: Effect of CNT Weight Fraction on Compressive Strength of Composite

Pure aluminium matrix composite reinforced by 2.5 wt% CNT was fabricated using unique equipment for spark plasma extrusion (SPE), and it is reported that the composite had a similar compressed strength value to that of the pure Al sample (Morsi, et al., 2010).

3.3   Effect Of CNT Weight Fraction On Hardness

The composite reinforced with 2wt% CNT revealed the highest value of hardness. Figure 3 indicated that the hardness values continued to increase steadily from run 1 at CNT weight fraction 0.5wt% until 2wt%.
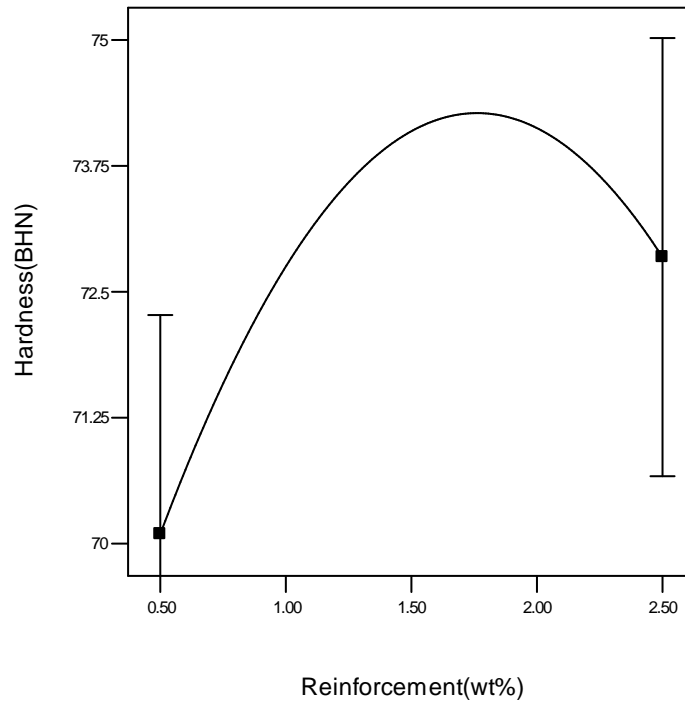
Figure 3: Effect of CNT Weight Fraction on Hardness of Composite

Further increase in CNT fraction only resulted in a weaker composite. This result is in agreement with the conclusion of Hamid et al. (2014) that CNT poses obstacles to dislocation movement which result in strengthening of composite by a mechanism known as Orowon looping. The low hardness value obtained at 2.5wt% is attributable to agglomeration of CNT due to high content of Al_4C_3. Similar observation was reported by Esawi et al. (2010).

3.5   SEM of Produced Composite

Scanning Electron Microscope Image/ EDS of CNT Reinforced Aluminium Alloy. The SEM micrograph of the produced composite is presented in Figure 3. Although it is difficult to view the CNT in the composite under the SEM image, however the accompanied EDS confirms its presence. The nanosized MWNT addition from 2 wt% lead to the refining of grains, making a coaxial finer grain structure than the matrix alloy.
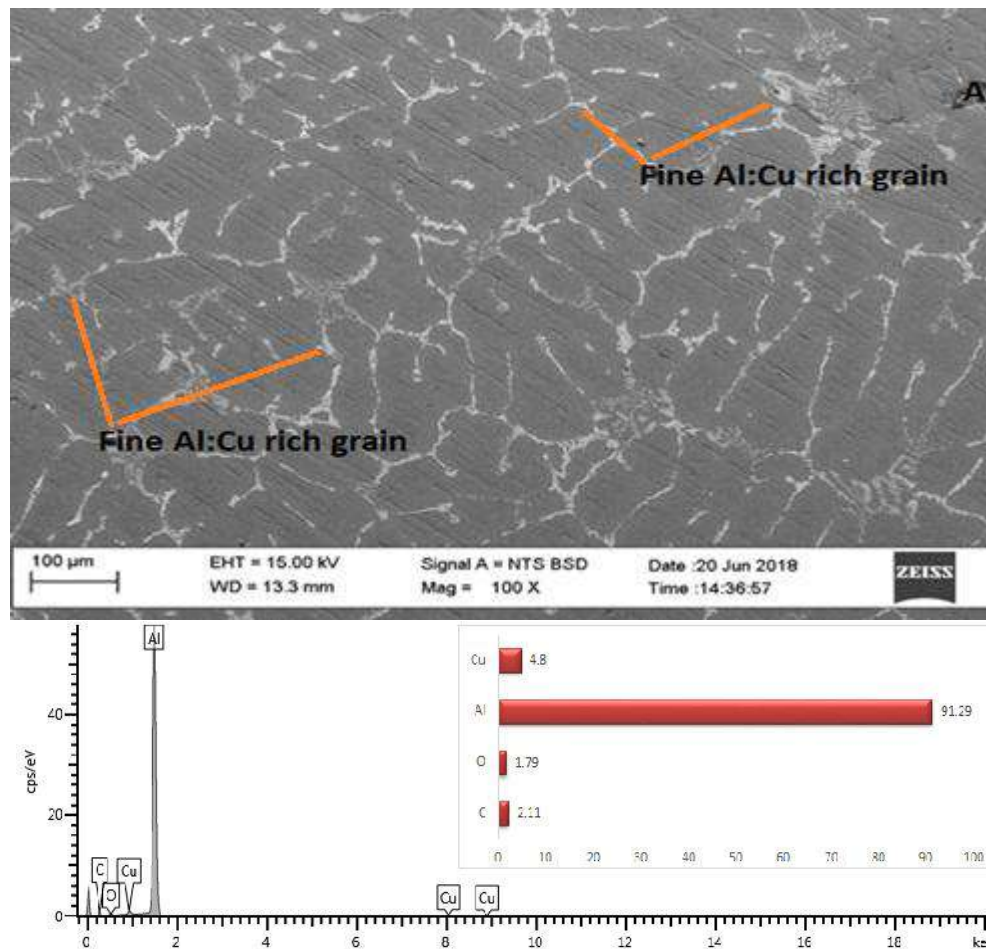
Plate 4: Scanning Electron Microscpe Image/ EDS of CNT Reinforced Aluminium Alloy

For nanocomposite materials, the grain size of the matrix depends on the particle size or the volume fraction of the particles. As the particle size decreases or volume fraction of nanoparticles increases, the grain size of the matrix decreases (Ezatpour et al., 2014). This behavior is attributed to a higher incidence of grain boundary pinning which prevents grain growth. It has been observed that grain refinement occurs when a large amount of MWNT reinforcement is added to the matrix (Ceschini et al. 2013). Choi et al., (2012) also reported the formation of ultrafine grained Al based MWNT composite. The well dispersed MWNT was observed to form strong interface with the matrix by mechanical interlocking.

Aside grain refinement, other possible strengthening mechanisms resulting from MWNT addition that could lead to the enhancement of the mechanical properties are load transfer, the thermal mismatch and orowon looping effects. (Esawi et al., 2010)

4.0   Conclusions

Based on the experimental observations made in the present research, the following conclusions have been drawn. Al2024 alloy- matrix composites have been successfully developed with fairly

84

uniform dispersion of CNTs. Addition of CNT significantly improves tensile strength of Al2024 by 56% when compared with that of unreinforced matrix. Also, the addition of CNT to Al2024 alloy matrix clearly improves the compressive strength. Above 2 wt % of CNT, the compressive strength and hardness of CNT-Al2024 composite is increased by 61% and 9%.

However, the mechanical properties decreased beyond 2wt% because at large weight fractions, the CNTs used in the present study were found to have a tendency to agglomerate and thus were difficult to disperse. The agglomeration has in turn affected the attained mechanical properties, which although were improved compared to un-reinforced aluminium alloy.

References

Ceschini, L., Boromei, I., Morri, A., Seifeddine, S., & Svensson, I. L. (2009). Microstructure, tensile and fatigue properties of the Al–10% Si–2% Cu alloy with different Fe and Mn content cast under controlled conditions. Journal of Materials Processing Technology, 209(15-16), 5669-5679.

Choi H, Shin J, Min B, Park J, Bae D. (2009). Reinforcing effects of carbon nanotubes in structural aluminum matrix nanocomposites. Journal of Material Resources;24:2610–6.

Deng, C. F., Wang, D. Z., Zhang, X. X., & Li, a. B. (2007). Processing and properties of carbon nanotubes reinforced aluminum composites. Materials Science and Engineering: A, 444(1-2), 138–145. doi:10.1016/j.msea.2006.08.057

Esawi, A. M. K., Morsi, K., Sayed, A., Taher, M., & Lanka, S. (2010). Effect of carbon nanotube (CNT) content on the mechanical properties of CNT-reinforced aluminium composites. Composites Science and Technology, 70(16), 2237–2241. doi:10.1016/j.compscitech.2010.05.004

Esawi, A.M.K., Morsi, K., Sayed, A., Gawad, a. A., & Borah, P. (2009). Fabrication and properties of dispersed carbon nanotube–aluminum composites. Materials Science and Engineering: A, 508(1-2), 167–173. doi:10.1016/j.msea.2009.01.002

Esawi, A. M. K., Morsi, K., Sayed, A., Taher, M., & Lanka, S. (2010). Effect of carbon nanotube (CNT) content on the mechanical properties of CNT-reinforced aluminium composites. Composites Science and Technology, 70(16), 2237–2241. doi:10.1016/j.compscitech.2010.05.004

Ezatpour, H. R., Sajjadi, S. A., Sabzevar, M. H., & Huang, Y. (2014). Investigation of microstructure and mechanical properties of Al6061-nanocomposite fabricated by stir casting. Materials & Design, 55, 921-928.

Kuzumaki, T., Miyazawa, K., Ichinose, H., & Ito, K. (1998). Processing of carbon nanotube reinforced aluminum composite. Journal of Materials Research, 13(9), 2445–2449

Morsi, K., Esawi, A. M. K., Borah, P., Lanka, S., Sayed, A., & Taher, M. (2010). Properties of single and dual matrix aluminum–carbon nanotube composites processed via spark plasma extrusion (SPE). Materials Science and Engineering: A, 527(21-22), 5686-5690

Noguchi, T., Magario, A., Fukazawa, S., Shimizu, S., Beppu, J., & Seki, M. (2004). Carbon Nanotube/Aluminium Composites with Uniform Dispersion. Materials Transactions, 45(2), 602– 604. doi:10.2320/matertrans.45.602

Salas, W., Alba-Baena, N. G., & Murr, L. E. (2007). Explosive Shock-Wave Consolidation of Aluminum Powder/Carbon Nanotube Aggregate Mixtures: Optical and Electron Metallography. Metallurgical and Materials Transactions A, 38(12), 2928–2935. doi:10.1007/s11661-007-9336- x

Srinivasa, R. B., & Arvind, A. (2011). An analysis of the factors affecting strengthening in carbon nanotube reinforced aluminum composites C A R B O N 4 9 5 3 3 –5 4 4

Thomas, A. T., Parameshwaran, R., Muthukrishnan, A., & Kumaran, M. A. (2014). Development of Feeding & Stirring Mechanisms for Stir Casting of Aluminium Matrix Composites. Procedia Materials Science, 5, 1182-1191.

DEVELOPMENT OF DUAL OPERATED SINGLESCREW- DRIVEN YAM POUNDING MACHINE

[1]LIFI Ibrahim Abdullahi, [1]E.A P. Egbe, [2]Alkali Babawuya, [1]M.M. Mohammed

Department of Mechanical Engineering, Federal university of Technology, Minna, Nigeria.
Department of Mechatronics Engineering, Federal university of Technology, Minna, Nigeria.

ABSTRACT

The development of dual operated single screw driven yam pounding machine was carried out by this work. The machine was developed to carried out both manual and motorized opertions and improved on the existing yam pounding machines which were observed to have being producing seedling in the pounded yam. Beaters are developed by this work to prevent formation of lumps in the pounded yam. The problem of epileptic power supply causes the pounded yam to be trapped in the machine. Therefore, manual hand winder was developed by this work to argument the motorized operation when there is power outrage. The machine is suitable for domestic use in both Rural areas and Urban cities. The stainless steel and mild steel materials were used in the design of the machine based on the availability, strength, appearance, cost and corrosion resistance. The machine consist of manual hand winder, electric motor, pulley, v-belt, barrel, screw shaft and supporting frame. The maximum volume of yam the machine can pound is $0.0000479 m^3$/min while the 1kg of yam for this work was pounded at a time of 8.07 minutes using the motorize operation and 13.18m minute using the manual operation. The coefficient of friction μ between pounded yam and the stainless steel was found to be 1:1 from experience. The crushing stress of the boiled yam was $17.59 N/cm^2$, while the density of yam before and after boiling was $1.25 \times 10^{-3} kg/cm^3$ and $1.95 \times 10^{-3} kg/cm^3$ respectively. The white yam was found to produced better homogeneous bond formation or desired texture of the pounded yam from the study.

Keywords; Pounding, Dual operated single screw-driven, Belt pulley, Friction, Pressure, Compression, Crushing or Shearing, Beaters.

1.0   INTRODUCTION

Yam is a seasonal crop that have moisture content from 56.3 to 78.6 % (FAO, 2004), **it** is a very important crop which is cultivated and consume by nearly all Nigerians on regular basis. The development of dual operated single screw driven yam pounding machine was to perform the task of converting boiled yam into pounded yam. This boiled yam is pounded in the pounding chamber by either the manual process or motorized operation, which transmit energy to the rotating pounding screw shaft that is incorporated with beaters for pounding the yam. The yam pounding machine was designed to augment or take over from the stressful nature of pounding which involved physical pounding using mortar and pestle by one or more people and the problem of motorized pounding machine which produces uncompleted bond formation of the pounded yamand also from the problem of the epileptic power supply which causes wastage of the trapped pounded yam in the machine or   from the intermittent stoppage of the machine for cooling when the electric motor becomes hot and hooked.

The word "yam" was derived from the Wolof word "nyam" which is a Portuguese name meaning "to test". Also in other African language, it can mean "to eat" (Migdnouna et al., 2003). Yam also has a Botanical name i.e. scientific name which confirms the international code known as Dioscorea. This perennial herbaceous crop is of different species such as the white yam (Dioscorea, rotundata), yellow yam (Dioscoreacayendensis). Water yam (Dioscoreaalata) and trifoliate yam (Dioscoreadumetorum) (Amuset et al., 2003). The fruit of yam consist of a membranous, three-wing capsule. The yam family is mostly of the weak-stemmed vines with large, underground food storage organs-tuber-rhizomes.

Yam has found its use in the preparation of sterohormones by the syntaz synthesis of cortisone from yam extract. Also its lower glycemic index than potatoes produce (Kay, 1987) accounts for its more sustainable energy and better protection against obesity and diabetes (Walsh, 2003). According to the food information Network in 2003 it was estimated that the world production of yam in 1993 was 28.1 million tons in which 96% of this estimate was from West Africa tropical regions and 71% from Nigeria. The figure was later reviewed in 1998 accounting for about 72.4% of the world total production of 29.6 million tons. Also, according to Federal Office of Statistics, Nigeria is the world largest producer of yams having the water yam (Dioscoreaalata) and yellow yam (Diooscoreacayenensis) as its cultivated species of yam. Norwadays, yam pounding machine incidentally is one of the most recent kitchen aid produce by Man. In this project, a more efficient, reliable, and affordable yam pounding machine is developed to ease the process of pounding.

1.1   Aim and Objectives of the Study

The aim of this study is to develop a dual operated Single Screw-Driven Yam Pounding Machine for domestic use. The objectives of the study are:

(i)   To carryout design analysis of a dual operated Single Screw-Driven Yam Pounding Machine
(ii)   To fabricate a dual operated Single Screw-Driven Yam Pounding Machine
(iii)   To carry out performance evaluation of the developed machine.

1.2   Working Principle of the Pounding Machine

The machine assemble parts was designed for both manual and motorized operation and consist of a hooper, barrel, screw shaft, supporting frame and drive mechanism. The boiled yam was measured on a weighing machine as shown in figure 1. The machine has weighting capacity of 50kilogram. The boiled yam was loaded in the hopper which then goes into the pounding chamber which is section into three regions;

a. Feeding region: This region perform the function of conveying and reducing the sizes of the boiled yam.
b. Transition region: This is the region where the boiled yam was masticated (compressed and crushed) and transformed into smooth solid pasty bonded formation.
c. Extrusion Region: This region applies the principles of extrusion and where the pounded yam is extruded out and collected in a clean plates or bowl.

Figure 1: Weighing Machine.

2.0   Materials and Method

2.1   Materials

The materials used in the development of dual operated yam pounder are listed as follows, including the specification.

1. Stainless steel - for the screw shaft, Hopper and barrel
2. Mild steel - for the supporting frame.
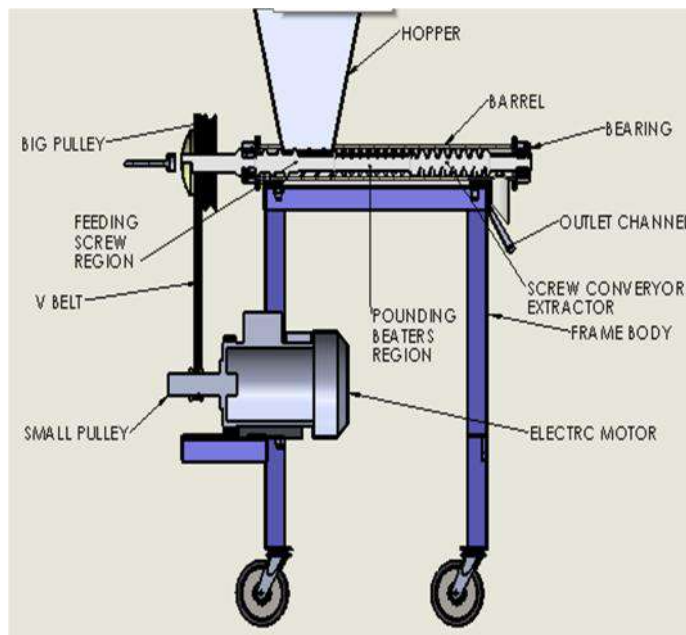3. Electric motor – AC supply.

Figure 2: Schematic of Pounding Machine

2.2 Design Analysis of Yam Pounding Machine

The machine was designed to perform the task of pounding boiled yam into pounded yam by the use of both manual and motorized operations. The design analysis was carried out to determine the torque to pound.

The crushing stress was given as, P= 17.59N/cm^2 (John, 2014)

$$P = \frac{F}{A} \tag{1}$$

Where, P is Crushing stress, F is Force acting, A is Asrea of the beaters.
So, For effective pounding, beater dimension of 8.5mm x 3.2mm is adopted in using with Otedola, (2012).

A = 0.85x0.32   = 0.272m^2
∴ Area occupied by the beaters A
A = A$_B$ x number of beaters   = 0.272 x 20   = 5.44m^3

From equation 1, the pounding force was calculated

$$P = \frac{F}{A}$$
F = P x A   = 17.59 x 5.44   = 95.69N

Therefore, the required pounding force by the machine is ≈ 9.6 N. Then, the required torque is caculated from equation 2

Torque T = F x r   (2)

Where, T is Torque to pound the yam, F is Force acting, R is Radius of the big pulley.

= 95.69 x 0.1025   = 9.81Nm

Torque in the bigger and smaller pulley are related by equation 3. So,

$$\frac{D_1}{D_2} = \frac{T_1}{T_2} \tag{3}$$
$$T_2 = \frac{D_2}{D_1} T_1 \tag{4}$$
$$= 9.81 \times \frac{0.1025}{0.035} = 28.73 \text{N.m}$$

Therefore, the torque in the motor pulley is ≈ 29 N. Also, to determine speed, equation 5 relates the diameter ratio to the speed

$$\frac{N_1}{N_2} = \frac{D_2}{D_1}. \tag{5}$$
where, hp is Motor horse power , N$_1$ is Motor Speed in revolution per minutes 1450rpm. N$_2$ is Speed of the big pulley, D$_1$is Diameter of the big pulley, D$_2$ is Diameter of the small pulley.

90

So,
$$\frac{1450}{N_2} = \frac{205}{35}$$
$$N_2 = \frac{1450 \times 35}{205} = 247.561 \text{m/s} \approx 250 \text{ m/s}$$

2.2   The Manual Hand Winder

Is the manual operational arrangement for the yam pounding machine.The torque require by this method is given by equation .6
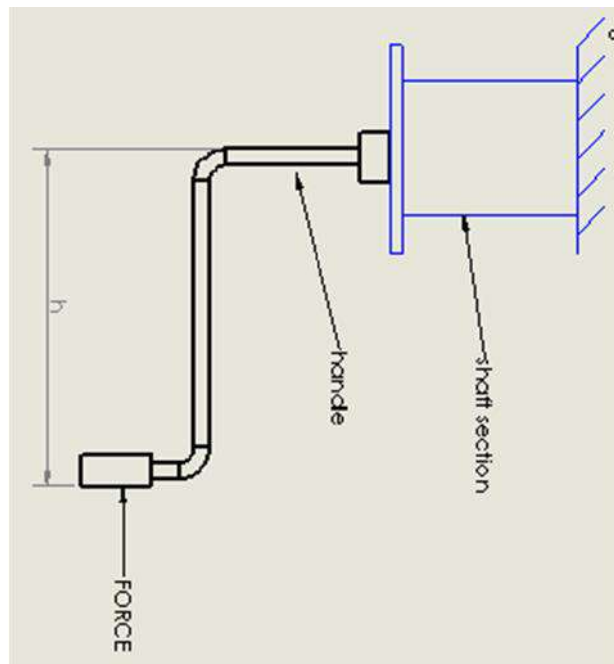
Figure 3: Manual Hand Winder.

$$T_{hand} = F_m \text{ x h} \tag{6}$$
Where,
T_h = Torque exerted by the hand
F_m = Force applied
h = Hand winder

$$h = \frac{T}{f} = \frac{28.73}{300} = 0.09576\text{mm} = 9.576\text{m}$$

The torque required by the hand to crush the yam using this machine is 98.1N, while according to (Ashish Karguppikar, 2018) that average Human hand can applied up to 300N.

2.3   Machine Pounding Capacity

Theoretical volumetric capacity (Qt)m^3/min) can be expressed, (Pratima, Lokhande, Savita, & Sangita, 2016);

$$Qt = \frac{\pi}{4}(d_{sf}^2 - d_{ss}^2)l_p n \qquad \text{(Ramesh, Karunaker, & Ramesh, 2014)} \qquad 7$$

Data:

Screw flight diameter, dsf, = 0.047m
Screw shaft diameter dss = 0.04m
Pitch length, l_p = 0.05m
Screw rotational speed, N = 0.25 rpm, (obtained from motor specification)

Therefore :

$$Qt = \frac{\pi}{4}(d_{sf}^2 - d_{ss}^2)l_p n$$
$$Qt = 0.7855\ (0.047 - 0.04) \times 0.0125$$
$$Qt = 5.6210^{-5}\ m^3/mi$$

Pounding capacity P_c = $\underline{\text{Discharge/out put}}$ 8
                                         Time

Where, P is pounding capacity ,D is discharge or output, T is time taken for complete pounding.

$$= \frac{0.8}{8.07} = 0.0991 kg/s$$

2.4   Analysis of Drive Mechanism

The electric motor provides the required torque transmitted to the screw conveyor via a V-belt and pulley system shown in figure 3.3. The drive mechanism is comprise of a smaller and bigger pulley connected by a v-belt (size). The diameter and the speed of two pulleys are related by equation 5.
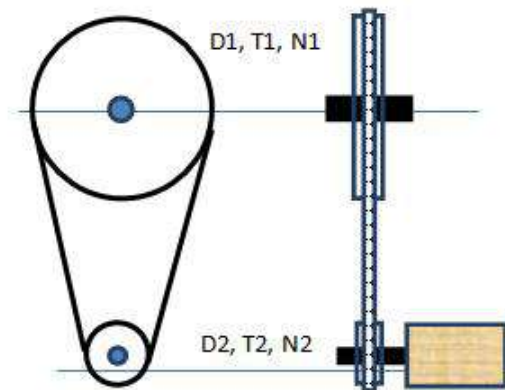
Figure 4: Drive Mechanism

And for open belt drive; the length of belt were calculated from equation 9;

$$L = \pi(r_1 + r_2) + \frac{(r_1 - r_2)^2}{x} + 2x \qquad\qquad 9$$

$$L = \pi(17.5 + 102.5) + \left(\frac{102.5 - 17.5}{400}\right)^2 + 2 + 200 = 1195.1mm = 1.195m$$

The tension in the slack side and tight side of the pulley are related by equation 10,

$$\frac{F_1}{F_2} = e^{\mu\theta} \qquad\qquad 10$$

Where, θ is the angle of lap or belt contact on a big pulley and given by equation 11,

$$\theta = 180 - 2\alpha \qquad\qquad 11$$
$$= 180 - 2 \times 3.58 = 180 - 5.14 = 176.6^0$$

Conversion from degree to radian,

$$176.6 \frac{\times\pi}{180} = 3.083 = 3.08 \text{ Rad}$$

$$\sin\alpha = \frac{r_1 + r_2}{x} \qquad\qquad 12$$

$$= \frac{102.5 + 17.5}{400} = \frac{120}{400} = 0.3$$
$$\alpha = \sin^{-}(0.3) = 3.38^0$$

$$T = F_1 \times r_1 \qquad\qquad 13$$

$$= 180.36 \times 0.1025 = 18.5N.m$$

And $\mu = 0.4$,

$$\frac{180.36}{T_2} = e^{0.4 \times 3.05} = e^{1.2209}$$

$$T_2 = \frac{180.36}{e^{1.2209}} = \frac{180.36}{3} = 52.6N$$

V_b = Volume of barrel;

$$V_b = \frac{1}{3}r^2h \qquad\qquad 14$$
$$r = 50/100;$$
$$h = 0.8$$
$$\frac{1}{3} \times 0.035^2 \times 0.5 = 0.000167m^3.$$
$$W_b = 1950 \times 0.00167 \times 9.81 = 180.36N.$$

Volume of shaft

$$V_s = \frac{1}{3}r^2h \qquad\qquad 15$$
$$= \frac{1}{3} \times 0.02^2 \times 0.57 = 7.6 \times 10^{-5}$$

The weight of the yam require to be pounded through turning by the electric pound motor.
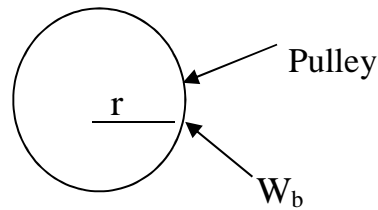
Figure 3: The Pulley Forces acting on it.

The required torque to turn the yam

$T = W_b$ x r = 180.36 x 0.1025 = 185N.m

The power

$P = Tu\ \omega$

$\omega = \dfrac{2\pi N}{60}$ rad/s $\qquad\qquad\qquad\qquad$ 16

N – motor speed rew/in

$\omega = \dfrac{2\pi \times 1500}{60} = 52.4\ \text{rad/s}$

The motor power required is P = T. w = 18.5 x 152.4 = 968.7w

$\qquad$ = 1.29hp $\approx$ 1.5hp

The motor hp calculation 1.29hp, while 1.5hp was used.

3.0   Results

The results recorded from the design analysis of the Yam pound machine are itemized as follows:

1. Volume of the hopper $\qquad\qquad$ 0.042m^3
2. Thickness of the Hopper $\qquad$ 1.3 mm
3. Screw Shaft diameter $\qquad$ 50mm
4. Length of the shaft $\qquad\qquad$ 1.075m
5. Moment of inertia, I $\quad$ 341,726.8 mm^4
6. Angle of wrap of the belt $\qquad$ 175.9^o
7. Volumetric capacity $\quad$ 4.78 x 10^{-5} m^3/min
8. Mass of the boiled yam in the hopper 0.2 Kg

The designed and fabricated machine was tested and it took about 8.7 min for the machine to pound the boiled. During testing the volumetric flow rate of the pounded Yam was measured using the weighing machine in figure 1 and equation 3 $\rho = \dfrac{m}{v}$ at an interval of 60s. Volumetric Efficiency = 81.9%.

T (min)	V (m³/min)
0	0
1	1.20E-05
2	1.62E-05
3	2.24E-05
4	3.20E-05
5	4.01E-05
6	4.78E-05
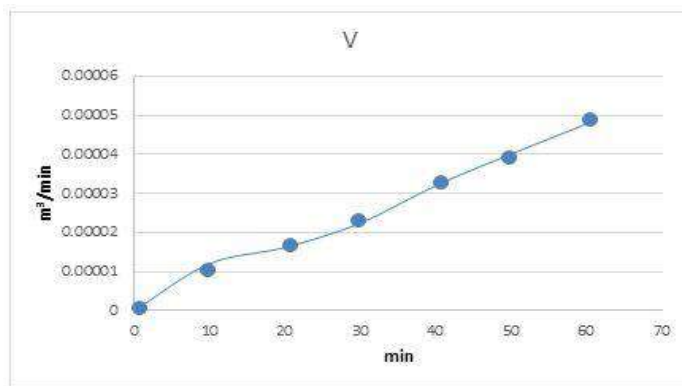
Figure 4: Results of the performance test.

According to Hamad,(2010) the efficiency of the Yam pounder is given;

$$\eta = \frac{Qa}{Qt} \times 100 = \frac{0.000478}{0.0000562} \times 100 = 85\% \quad \text{(Odesola, A., \&EHumadu, 2016)}$$

Where;
Qa = actual volumetric flow rate.
Qt = theoretical flow rate.

4.0   Conclusion

The design, fabrication and testing of dual operated Yam pounding machine using beaters and a screw conveyor extruder was undertaken. The machine was design for strength, rigidity and also, bearing mind the safety/cost of food for consumption. Therefore, stainless steel was chosen for components that have direct contact with the pounded Yam. A 1.5Hp AC supply electric motor was selected to operate the Yam pounding machine.

A comparative test conducted between the machine and the traditional method shows that the machine take about 13.18 minutes to complete the pounding of 1Kg of boiled Yam using manual handle and 8.07 minutes while using the electric motor, while the traditional method took almost 23.25 minutes to pound the same kilogram of the boiled Yam. The performance evaluation shows that the design machine has a volumetric efficiency of 85%.

References

Carvill, J. (2003). Mechanical Engineer's Data Handbook. London.: Elsevier Science Ltd, Sormerset.

CEMC. (2012). Screw conveyor componentS & design Version 2.20. Conveyor Engineeing and Manufacturing Co. Retrieved February 6, 2017, from www.conveyoreng.com

Gbasouzor, A. I., Ekwuozor, S. C., & Owuama, K. C. (2013). Design and Characterization of a Model Polythene Recycling Machine for Economic Development and Pollution Control in Nigeria. Proceedings of the World Congress on Engineering (pp. 3-5). London: WCE 2013.

Khurmi, R. S., & Gupta, J. K. (2008). A Textbook of Machine Design (Multicolor Edition ed.). New Delhi: Eurasia Publishing House.

Mayur, M. W., & Vijay, K. K. (2015). Design and Analysis of Screw Conveyor at Inlet of Ash/Dust Conditioner. International Journal of Emerging Technology and Advanced Engineering, 5(5), 291-296. Retrieved from www.ijetae.com

Odesola, I. F., A., K. R., & EHumadu, N. C. (2016, August). Design and Construction of Fish Extruder. INternational JOurnal of Sceintific and ENgineering Research, 6(8), 1378-1386.

Odior, A. O., Oyawale, & F.A. (2008). Design and Construction of yam pounding machine. .International Journal of Natural and Applied Science, 4(3), 319 – 323.

Ogiemudia, O. G., I. A., & Ejiroghene, K. O. (216). Comparative Analysis of Yam Pounding Machine and the Traditional Pounding Method . International Academic Journal of Innovative Research, 1-12.

Pratima, G. M., Lokhande, A. D., Savita, T. M., & Sangita, A. S. (2016). Peanut Sheller using Screw Conveyor. International Journal of Current Engineering and Technology, Special(4).

Ramesh, A., Karunaker, P., & Ramesh, L. (2014). Design and Analysis of Discharging of Dust in Pneumatic Conveying System by a Screw Conveyor Shafts , Advanc. e Research and Innovations in Mechanical, Material Science, Industrial Engineering and Management - ICARMMIE, (pp. 84-91). Bonfring.

Khurmi R. S & Gupta J. K (2008). A textbook of machine design, 1st Multicolor Edition, Eurasia Publishing House (PVT) LTD, New Delhi - 110055.

NUMERICAL SIMULATIONS OF FLOW IN UNCONVENTIONAL BEND TO DETERMINE MINOR HEAD LOSSES AND LOSS COEFFICIENT USING SOLIDWORKS.

Oriaifo MacLawrence Angel and Musa Nicholas Akhaze
Department of Mechanical Engineering, Federal University of Technology Minna Niger state, Nigeria

Abstract

The aim of this paper is to determine the losses that occur in unconventional bends, which find applications in pipeline network. 20^0, 30^0 and 60^0 bends were selected for study. The bends were designed in SolidWorks environment and boundary conditions were applied, to obtain pressure drops or losses, which were used to calculate the minor head loss that occurs in the respective bends and their respective loss coefficient (K). The material used was poly vinyl chloride (PVC) pipe with internal diameter of 0.0154m and the working fluid was water. The boundary conditions taken for flow rate was 0.5liters per second (0.0005m^3/s), which gave a velocity of 2.688 m/s. From continuity equation and Reynolds number evaluation, it was observed that the flow regimes were turbulent. The minor head loss obtained for 20^0, 30^0 and 60^0 bends were found to be 0.06440m, 0.06466m and 0.06746m respectively and the 20^0, 30^0 and 60^0 bends respective loss coefficient obtained were found to be 0.175, 0.176and 0.183.

Keywords: Bends, SolidWorks, simulations, pressure loss, minor head loss, loss coefficient

1.0   INTRODUCTION

Total headloss in a pipelines comprises of major headloss and minor headloss. The former is broadly an energy loss in the pipeline as a result of effect of resistance to flow of fluid, which largely depends on the fluid viscosity, wall roughness and internal diameter of the pipe, lateral length, and flow velocity . The latter is the additional energy loss due to secondary flows that are caused by fittings such as bends, elbow, reducers, valves etc. in the pipeline(Neto et al,2014) Each fitting causes pressure loss or minor head loss which is always expressed as a fraction of the kinetic head, (Yildirim2010). The evaluation of minor head loss in pipeline network should not be under minded , because in short pipeline fitted with many bends and other fittings, minor losses are more than major losses(Head Loss – Pressure Loss,2018). So they could be more important to be considered than major head loss in the design of pipe line and pumping requirement,(Balsigeret al, 2014). However Kamand(1988) reiterated that the evaluation of total head loss in pipelines is an important factor that affects the overall cost as well as the hydraulic balance of the network.

Bends are used to control and divert flows, when large radius of curvature of diversion of flow is required in flow line , But when small radius of curvature of the diversion is required, elbows are used. Convectional bends, that is, bends that are commonly available for use just like elbows, are 22.5^0, 45^0,90^0 and 180^0 bends. If the required angle of diversion of flow is between or above the angle of convectional bends, the use of convectional bends is no longer feasible.

Bends of 20^0, 30^0 and 60^0 are unconventional bends and they could be respectively employed to divert flow in flow line, that requires any angle of diversion of 20^0, 30^0 and 60^0.. But there is little or no knowledge about the head loss and loss coefficient(k factor) associated with these unconventional bends in literature. So it is the gap this research work is trying to fill by using a viable method to evaluate the head losses and loss coefficients of the unconventional bends of 20^0, 30^0 and 60^0. According to Jonuskaite,(2017), fluid flow may be very hard to predict and differential equations that are used in fluid mechanics are difficult to solve but solid works add-ins, enable one to simulate flow of fluid and efficiently analyse the effects of the fluid flow. So in this research work, simulation of pressure loss in the various bends would be carried out using SolidWork , for the determination of the head loss and the respective loss coefficient of the aforementioned unconventional bends.

2.0 Materials and Methods
2.1 Materials
The material used in this study includes
1. 20^0, 30^0 and 60^0 poly vinyl chloride (PVC) bends with each bend having 0.0154mm diameter.
2. Water , which serves as the working fluid and it was assumed to be pumped using 0.5 horse power centrifugal pump to attain a flow rate of 0.5 litre per seconds (0.0005 m^3/s), in the pipeline network for the simulation of flow(pressure loss) in the bends.
3. SolidWorks 2017 software and it was used for the simulation of pressure loss in the selected bends of 20^0, 30^0 and 60^0...

2.2 Method
The flow chart for the process of determination of pressure loss or drop, head loss and loss coefficient of the selected bends is shown in figure 1.

Make a Model

Perform Simulation using Solid Works 2017

Generate Simulation Results For

Pressure loss or pressure drop

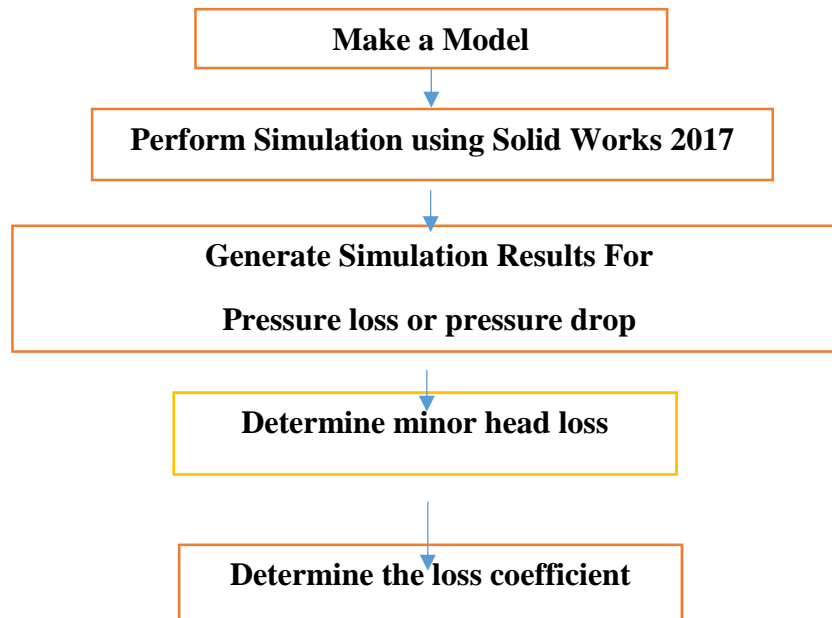**Determine minor head loss**

Determine the loss coefficient

Figure 1. Flow chart for the process of determination of pressure loss or drop, head loss and loss coefficient of the selected bends.

Estimation of fluid flow velocity and Reynold's number for the boundary conditions of the simulation with SolidWorks.

The flow rate or discharge of fluid is given as

$$Q = A\,V \tag{1}$$

Where Q = flow rate = 0.0005 m³/s and

A= area of pipe used = 0.000186 m²

V= fluid flow velocity

From equation 1,

$$V = \frac{Q}{A}$$

V = 2.688 m/s

The Reynold's Number(Re) is given as

$$Re = \frac{\rho V D}{\mu} \tag{2}$$

= Density of fluid (water) = 998.1934 kg/m³

V = velocity of flow = 2.688 m/s

D = Diameter of pipe used = 0.0154 m

μ = Dynamic viscosity of water from Thermodynamics Table (at 20°C) = 0.0010016 P.a.s

$$Re = \frac{988.19 \times 2.688 \times 0.00154}{0.001006} = 41,254$$

Since Re is greater than 2000, the flow is entirely turbulent.

2.3 Numerical Simulations

This is a process of using mathematical formulae to model a product and then testing it on a computer via a computer software, which is often referred to as virtual prototyping or virtual testing due to its importance and great advantages in engineering discipline. For it gives an insight of what the real is going to look like and its cost effectiveness. For the calculation of flows in bends, solid works was used to solve for the continuity equation, momentum equation together with the K- turbulence model. (Cui 2009).

2.4 Governing Equation and Mathematical Modelling

According to Nimadge and Chopade (2017), most fluid can be mathematically described by the use of continuity equation and momentum equation. Continuity equation is where the amount of fluid entering in certain volume and leaves at that volume or remains the same and momentum equation is about balancing of the momentum are sometimes referred to as Navier-Stokes equation, derived by considering the three direction of flows. The Navier stokes equation expresses the conservation of mass and momentum (Homicz 2004), The K-elipson turbulence model was used to satisfy the boundary layer solution and to generate pressure contours which were analyzed in this research work, in line with Sharma et al (2015).

Three-dimensional governing equations for steady state, incompressible water flow in Cartesian coordinate are expressed by:

Continuity equation
$$\left(\frac{\partial u}{\partial x} + \frac{\partial v}{\partial y} + \frac{\partial w}{\partial z}\right) = 0 \tag{3}$$

Momentum equation

$$\left(u\frac{\partial u}{\partial x}+ v\frac{\partial u}{\partial y} + w\frac{\partial u}{\partial z}\right) = -\frac{\partial p}{\partial x} + \mu \, ^2u \tag{4}$$

$$\left(u\frac{\partial v}{\partial x}+ v\frac{\partial v}{\partial y} + w\frac{\partial v}{\partial z}\right) = -\frac{\partial p}{\partial y} + \mu \, ^2v \tag{5}$$

$$\left(u\frac{\partial w}{\partial x}+ v\frac{\partial w}{\partial y} + w\frac{\partial w}{\partial z}\right) = -\frac{\partial p}{\partial z} + \mu \, ^2w \tag{6}$$

2.5   Evaluation of Minor Head loss and Loss coefficient of the Bends

The minor headlosses and loss coefficients due to 20^0, 30^0 and 60^0 bend, were evaluated using the relations given by Kumar (2014), Rajput(2013) and Jonuskaite (2017) as:

$$H_{Bend} = K \frac{V^2}{2g} = \frac{\Delta P}{\rho g} \tag{7}$$

Where H_{Bend} is the minor headloss, K is the loss coefficients, v is the average velocity of fluid in the bend , ΔP is the pressure loss or drop, obtained from the simulation result, g is the acceleration due to gravity and   is fluid density.

3.0   Results and Discussion

The flow trajectories obtained from simulation, showing fluid pressure contours or distribution in the 20^0 bend is shown in figure 2.

Figure 2. Flow Trajectories with fluid pressure contour or distribution in the 20^0 bend.

The different colours in figure 2, depict different magnitude of the fluid pressure and it can be seen from the figure 2, that the fluid pressure varied continuously along the 20^0 bend. The pressure decreased sharply in the inner part of the bend and increased steadily but increased sharply in the

100

outer part of the bend and dropped steadily. The simulation result for pressure loss in 20^0 bend is shown in Table 1.

Table 1.Simulation result for pressure loss in 20^0 bend

Total pressure loss	Total pressure loss	Total pressure at point 1	Total pressure at point 2	Density	Velocity
	0.0631457088	3.89139166e+009 Pa	3.66367906e+009 Pa	998.1934 kg/m^3	2688 m/s

Goal Name	Unit	Value	Averaged Value	Minimum Value	Maximum Value	Progress [%]	Use In Convergence	Delta	Criteria
SG Av Total Pressure 1	[Pa]	3891391661	3884193104	3868794057	3891391661	100	Yes	22597604.07	93526876.91
SG Av Total Pressure 2	[Pa]	3663679057	3661383665	3656167796	3663679057	100	Yes	7511260.36	7527113.027

It is evident in Table 1 that the inlet pressure is greater than the outlet pressure of the fluid in the 20^0 bend. The simulated pressure loss or simulated total pressure loss obtained for the 20^0 bend was 0.0632KPa. The flow trajectories obtained from simulation, showing fluid pressure contour or distribution in the 30^0 bend is shown in figure 3.
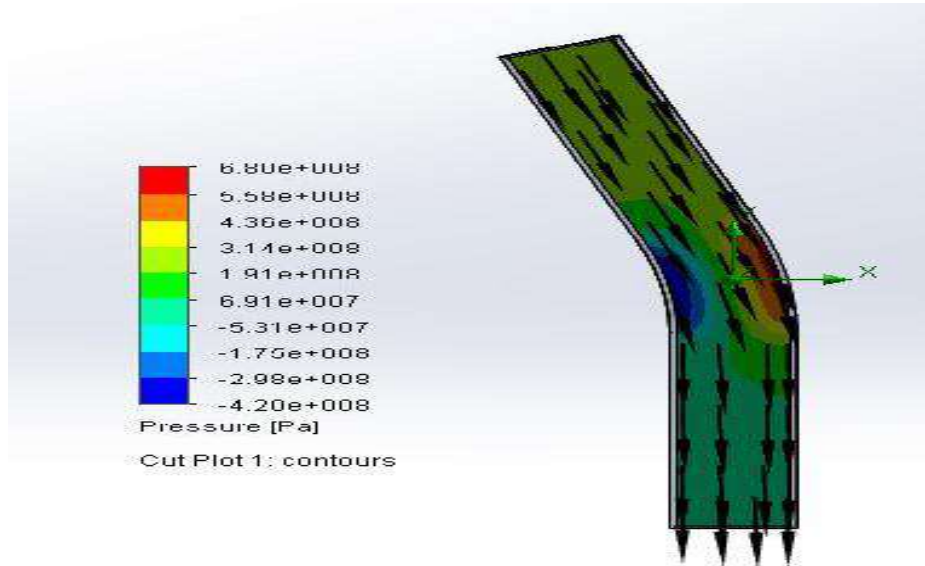

Figure 3. Flow trajectories with fluid pressure contour or distribution in the 30^0 bend

The colour variations in figure 3, reflect different magnitude of pressure and it can be seen from the figure 3. that in the lower part of the 30^0 bend, the fluid pressure dropped continuously and increased again, but in the upper part of the bend, the pressure increased steadily and dropped. The simulation result for pressure loss in 30^0 bend is shown in Table 2.

Table .2. Simulation Result for pressure loss in 30^0 Bend

	A	B	C	D	E
	Total pressure loss	Total pressure at point 1	Total pressure at point 2	Density	Velocity
Total pressure loss	0.0633151766	3.90847623e+009 Pa	3.6801525e+009 Pa	998.1934 kg/m^3	2688 m/s

Goal Name	Unit	Value	Averaged Value	Minimum Value	Maximum Value	Progress [%]	Use In Convergence	Delta	Criteria
SG Av Total Pressure 1	[Pa]	3894927856	3890584348	3875396148	3894946217	100	Yes	19550069.26	149146833
SG Av Total Pressure 2	[Pa]	3656722515	3654402280	3648254922	3656722515	100	Yes	8467593.505	9018893.384

It is clearly seen in Table2 that the inlet pressure is greater than the outlet pressure of the fluid in the 30^0 bend. The simulated pressure loss or simulated total pressure loss obtained for the 30^0 bend was 0.0633KPa.

The flow trajectories obtained from simulation, showing fluid pressure contour or distribution in the 60^0 bend is shown in figure 4.
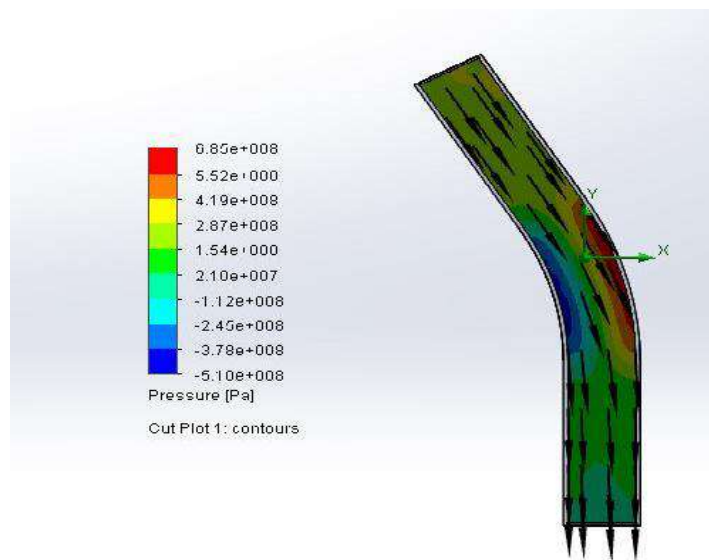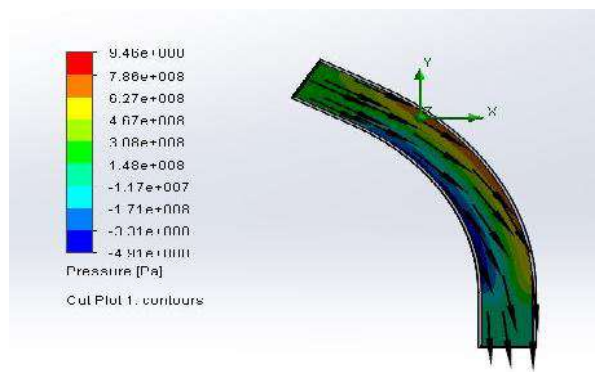

Figure 4. Flow trajectories with fluid pressure contour or distribution in the 60^0 bend.

The contrasting colours in figure 4, show the different magnitude of pressure and it can be seen from the figure 4, that in the lower part of the 60^0 bend, the fluid pressure dropped continuously and increased again, but in the upper part of the 60^0 bend, the pressure increased and decreased a little bit and finally dropped. The simulation result for pressure loss in 60^0 bend is shown in Table 3.

Table 3. Simulation Result for pressure loss in 60^0 Bend.

Total pressure loss				Total pressure loss		Total pressure at point 1	Total pressure at point 2	Density		Velocity
				0.0660553897		3.89492786e+009 Pa	3.65672252e+009 Pa	998.1934 kg/m^3		2688 m/s
Goal Name	Unit	Value	Averaged Value	Minimum Value	Maximum Value	Progress [%]	Use In Convergence	Delta	Criteria
SG Av Total Pressure 1	[Pa]	3908476234	3900792144	3885074950	3908476234	100	Yes	23401283.67	198181017.6
SG Av Total Pressure 2	[Pa]	3680152504	3676917702	3670675487	3680152504	100	Yes	9477017.62	10342485.79

It can be seen from Table 3 that the inlet pressure is greater than the outlet pressure of the fluid in the 60^0 bend. The simulated pressure loss or simulated total pressure loss obtained for the 60^0 bend was 0.0661KPa.

The result of estimation of minor headloss and loss coefficient of 20^0, 30^0 and 60^0 bends based on the obtained pressure loss from simulation of flow through the various bends is shown in Table 4.

Table 4. The evaluated minor headloss and loss coefficient of 20^0, 30^0 and 60^0 bends

Types of bend	Minor headloss(H_B) (m)	Loss coefficient(K)
20^0 bend	0.06440	0.175
30^0 bend	0.06466	0.176
60^0 bend	0.06746	0.183

It can be seen from Table 4 that 60^0 degree elbow has the highest head loss and loss coefficient of 0.06746 and 0.183 respectively, followed by 30^0 degree bend having head loss and loss coefficient

of 0.06466 and 0.176 respectively. 20^0 bend has the lowest head loss and loss coefficient in comparison with 30^0 and 60^0 bends.

4.0   Conclusion

Simulation of pressure losses in $20^0, 30^0$ and 60^0 bends fitted to a pipeline network has been carried out and head loss as well as loss coefficient of the bends have been evaluated in this study. It can be concluded, based on the result of the study, that a higher angle bend experiences greater pressure loss and minor head loss and possesses higher loss coefficient than a lower angle bend. In a nut shell, the pressure loss, head loss and loss coefficient show increasing trend with bend angle in pipeline network..

Reference

Balsiger, A., Bastos, L., Behm, J.(2014). Minor losses in pipes CIVE Hydraulics Eng. Colorado   State   University   .Retrieved from https://www.scribd.com/document/370616513/2-Minor-Losses-in-Pipes-Balsiger- Bastos-Behm on the 21st of September, 2018.

Cui, J.(2009). Numerical modelling of pressure losses caused by bends in pneumatic conveying   pipeline. Proceedings from the ASME 2009 International Mechanical Engineering   Congress and Exposition. November 13th – 19th Lake Buena Vista, Florida `USA.

Head Loss – Pressure Loss (2018).Retrived from https://www.nuclear-   power.net/nuclear-engineering/fluid-dynamics/bernoullis-equation-bernoullis- principle/head-loss/ on the 2nd of   September, 2018

Homicz, G.F. (2004).Computational fluid dynamics simulations of pipe elbow flows. Retrieved   from   https://prod.sandia.gov/techlib-noauth/access-control.cgi/2004/043467.pdfon the 20th of April, 2018.

Jonuskaite, A (2017) .Flow simulation with SolidWorks. B.Tech. Thesis, Arcada University   of Applied Sciences.

Kamand F. Z (1988) Hydraulic friction factors for pipe flow. J Irrig Drain Eng.   114(2):311-323

Kumar, D.S. (2014) A Text book of fluid mechanics and fluid power engineering. S.K.   Kataria and   sons, publications, India.

Neto, O.R., Botrel, T.A., Frizzone, J.A., Camargo, A.P(2014).Method for determining   friction headloss   along   elastic   pipes.   Retrieved   from: https://www.researchgate.net/publication/264121417_Method_for_determining_fricti on_head_loss_along_elastic_pipes on the 2nd of September, 2018

Nimadge. G.B. and Chopade, S.V. (2017) CFD analysis of flows through T-junction of   Pipe, International research Journal of Engineering and Technology. 4(2): 906-911

Rajput R.K. (2013) A Text book of fluid mechanics and hydraulic machine in SI Unit S.   Chand and   company limited New Delhi

Sharma, A.S., Sudhakar, S., Akumar, S., Kumar, B.S. (2015) Investigations of pressure contours   and velocity vectors of NACA 0015 using Gurney Flap.   International Journal of   Mechanical and Production Engineering 3(9): 12-16.

Yildirim G (2010) Total energy loss assessment for trickle lateral lines equipped with integrated in-line and on-line emitters. Irrig Sci. 28(4):341–352.

DEVELOPMENT OF A THERMOPLASTIC EXTRUSION METER

[1]TERAN Georgina Mbanengen, [1]E.A.P. Egbe, [2]Alkali Babawuya

[1]Department of Mechanical Engineering, Federal University of Technology, Minna, Nigeria.
[2]Department of Mechatronics Engineering, Federal University of Technology, Minna, Nigeria.

ABSTRACT

Thermoplastic recycling is recognized as an important method of waste reduction and it reduces environmental pollution problem posed by non-biodegradable nature of polymers. Quality plastic products can only be made from recycled thermoplastics when the melt characteristics of the material is known. Non-availability of thermoplastic extrusion meter in local plastic industries makes it difficult to ascertain the actual melt mass flow rate of recycled thermoplastics which makes it difficult to verify whether the plastic grade is within the required fluidity range and addition of plasticizers is by trial and error instead of the ISO standard. It's important to develop a thermoplastic flow meter, to determine the melt mass flow rate of thermoplastic materials for quality control in plastic industry in Nigeria. The thermoplastic extrusion meter was designed to ASTM D1238 standard, and the fabrication was made from ANSI 1018 cold rolled mild steel. The equipment was calibrated to ensure actual melt temperature and the performance of the equipment was evaluated. Procedure A was employed to determine the MFR of virgin and recycled HDPE. The HDPE for virgin was found to be 9.96g/10mins while that of first recycled HDPE was 10.88g/10mins under the same load and temperature conditions of 2.16Kg and 190°C respectively.

Keywords; Development, extrusion, thermoplastics, temperature, meter, melt flow rate.

1. 0 INTRODUCTION

Thermoplastics are high performance materials, and they are increasingly replacing the conventional materials such as metal, glass and wood in numerous applications where the combination of mechanical, thermal, electrical and chemical properties is desired [1]. However, plastic materials are non – biodegradable and as such they constitute an environmental hazard since they cannot be disposed-off like other materials. They are inflammable and if burnt they create air pollution [2]. Thermoplastic recycling is recognized as an important method of waste reduction and it reduces environmental pollution problem posed by non-biodegradable nature of polymers. Thermoplastics are widely used for different kinds of household and commercial products ranging from motorcycle helmet visors, aircraft windows, viewing ports of submersibles, and lenses of exterior lights of automobiles.

The quality of a thermoplastic product is a function of the quality of the input materials and the processing conditions. [3] Indicated that the mechanical properties of the products depend on the melt temperature, injection pressure, clamping pressure and cooling rate. The selection of these process parameters depends to a large extent on the melt flow characteristics of the particular thermoplastic.

A melt flow meter is particularly important in Nigeria because whole products (black jerry cans of varying capacities) are being made from 100% recycled thermoplastic materials of unknown characteristics. In cases where mixtures of recycled and virgin materials are being used, the plastic flow meter is not available in plastic factories to make it possible to seek a mixture with a flow behaviour that yields acceptable mechanical properties. Quality plastic products can only be made when the melt characteristics of recycled thermoplastics is known. Hence the need to develop a standard melt mass flow meter that can be used for all thermoplastics that are frequently used in Nigeria to ascertain the actual MFR of recycled thermoplastics and verify if the plastic is within the required fluidity range, and to also determine the amount of plasticizers to be added to the recycled thermoplastics.

2.0 MATERIALS AND METHOD
2.1 Materials
The major material used in the development of the thermoplastic extrusion meter is ANSI 1018 cold rolled mild steel with the following properties; density is 7850Kg/m³, Young's modulus 210GPa, ultimate tensile strength 439.6MPa and yield strength 369.99MPa. The thermoplastic material used in this study is HDPE in its virgin and recycled states because of its wide usage both for different kinds of household and commercial products in Nigeria. Heater band and the temperature unit were purchased from electrical store.

2.2 Description of Thermoplastic Extrusion meter
The thermoplastic extrusion meter (Figure 1) consists of a heating barrel with a cavity where the resin is charged. The barrel houses the die (an orifice) and piston with set of standard weights placed on the piston head. The barrel is surrounded by two heater bands, followed by fiber glass and all enclosed in a steel cylinder. The heating barrel is mounted on a vertical column via welded bracket as shown in Figure 1. The column is essentially free at the top and fixed at the base.
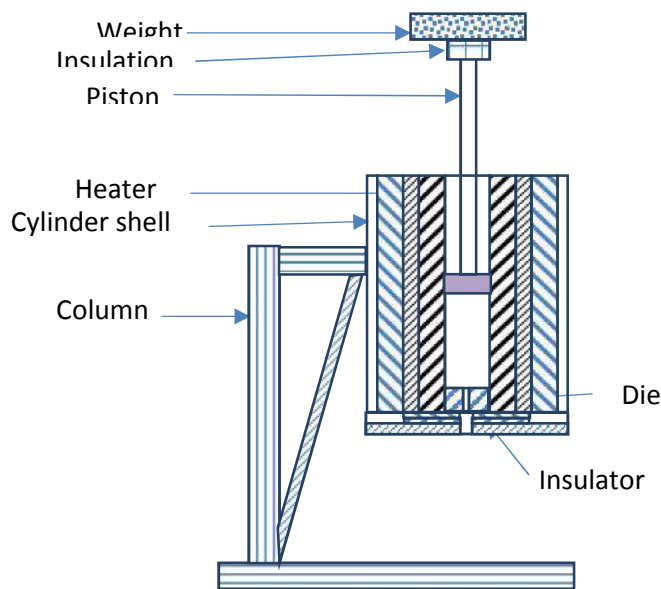

Figure 1 Schematic diagram of thermoplastic extrusion meter.

2.3 Design Analysis and Calculation
The ASTM D 1238 standard specified that internal diameter of the barrel should be 9.5504mm ±0.0076mm, outside diameter of barrel: 50mm, barrel height: 115mm to 180mm, die outer diameter: 9.55mm ± 0.005mm, inner diameter: 2.095mm and die height: 8mm ± 0.025mm.

2.3.1 Design of the Heating Barrel
The wall of heating barrel is required to transmit heat to the test material and withstand the pressure required to extrude the thermoplastic at its melting temperature. Though the difference between specified external (50 mm) and internal (9.5 mm) diameters of the barrel is high enough to have made the barrel a thick walled cylinder, the temperature monitoring hole must be relatively close to the plastic melt in order to have an adequate reflection of the melt temperature. in line with [4] the condition of thin walled pressure vessel has been adopted in this work. The tangential stress in thin cylinder wall is given by Equation 1 while the axial stress is given by Equation 2. The tangential stress is the critical stress and is used to determine the critical thickness of the barrel at the point where temperature monitoring hole is inserted.

$$t = \frac{P.D}{2t} \qquad (1)$$

$$t = \frac{P.D}{4t} \qquad (2)$$

where P is pressure, D is inside diameter of barrel and t is thickness.

The extrusion pressure depends on the specified mass for test thermoplastic. The maximum specified mass is 21.6 kg which is for polyethylene (PEa) [5].The pressure load on the barrel is given by,

$$P = \frac{F}{A} \qquad (3)$$

Where F is applied force, A is barrel area.

$$P = \frac{21.6 \times 9.81 \times 4}{\pi \times d^2}$$
$$= \frac{21.6 \times 9.81 \times 4}{\pi \times 0.0095^2}$$
$$P = 2.989 Mpa$$

And because of the thermal effect on the heating barrel; the additional thermal stress is

$$\sigma_2 = E \alpha \Delta T \qquad (4)$$

Where E is Young modulus of elasticity of steel, α is coefficient of expansion and ΔT is difference in temperature. For steel,
$E = 210 \times 10^9$,
$\alpha = 10 \times 10^{-6}$. Therefore thermal stress is,
$$\sigma_2 = 210 \times 10^9 \times 10 \times 10^{-6} \times (190 - 25)$$
$$= 346.5 MN/m^2.$$

However the heater band is fastened to the barrel with mild steel bolt which could expand at about the same rate as the heating barrel. Thus the actual induced thermal stress is only a negligible fraction of the value calculated.
Substituting the yield strength for ANSI 1018 cold rolled mild steel into Equation 3 and using a factor of safety as 3 yields,
$$\frac{369.99 \times 10^6}{3} = \frac{2.989 \times 0.0095}{2t}$$
This gives t = 0.1151mm.

Thus the temperature monitoring hole must ensure a thickness of 0.115 mm from inside wall of the barrel.

2.3.2 Frame Design

The frame shown in Figure 2 was designed as a short column with a slenderness ratio l/k less than 80 and fixed-free end conditions. The Johnson's straight line formula for short column (Equation 5) was adopted for the design [6].

$$W_{cr} = A(\sigma_y – C_1(l/k)) \tag{5}$$

where W_{cr} is critical load (which is 365 N for this work), A is cross sectional area of column, C_1 is a constant, l is length, and k is the least radius of gyration of section. The constant C_1 is defined by Equation 6,

$$C_1 = \frac{2\sigma_y}{3f}\sqrt{\frac{\sigma_y}{3CE}} \tag{6}$$

where σ_y is the yield strength, C_1 is end fixing coefficient and E is modulus of elasticity.

The end fixing coefficient C in case of one end fixed and the other end free is 0.25 [6]. In case of mild steel Equation 6 becomes,

$$C_1 \simeq \frac{2\times369.99\times10^6}{3\times3.142}\sqrt{\frac{369.99\times10^6}{3\times0.25\times210\times10^9}}$$

$C_1 = 3.76 \times 10^6$

A rectangular plate was selected for the design shown in Figure 2. For a rectangular cross section plate the width (b) is typically much more than thickness (t). Let thickness be 0.2 times the width. Therefore cross sectional area (A) in Equation 5 becomes $0.2b^2$. Substituting all known values into Equation (5), and using a factor of safety of 3 yields,

$3 \times 365 = 0.2b^2 [369.99\times10^6 - 3.76\times10^6b (\frac{0.30}{0.2b})]$

$73.99\times10^6b^2 – 1.128\times10^6b – 1095 = 0$

From $x = \frac{-b\pm\sqrt{b^2-4ac}}{2a}$ $\tag{7}$

$b = \frac{0.015\pm\sqrt{0.015^2-4\times1.45\times10^{-5}}}{2}$

$= 0.0152$m

$= 15.28$mm. Thus thickness t = 0.2 x 15.28 =3 mm. The next available plate of cross sectional width 25 mm and thickness 5 mm was used for the short column.
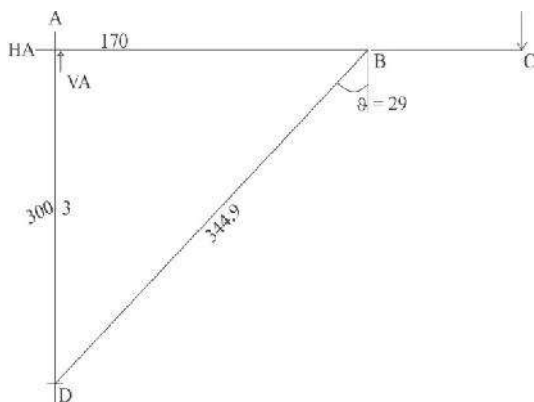
Figure 2:Free body diagram of the frame

To determine forces in members of the frame, moments of forces are taken about point A

H_D x 300 = 365x245

$H_D = \frac{365 \times 245}{300} = 298.08N$

Equilibrium of horizontal forces in frame

$H_A + H_D = 0$

Which implies that HA = -HD. Thus,

$H_A = 298.08$ N.

To obtain vertical components of reactions the equilibrium of forces and moments on link AC was considered. Taking moments about point B,

V_A x 170 = 365 x 75.

$V_A = 161.03$ N.

Going back to the equilibrium of the entire frame, equilibrium of Vertical forces in frame implies that,

$Fy = 0$

$V_D + V_A = 365$

VD + 161.03 = 365. Thus vertical reaction at D is 203.97 N.

Modelling welded joint at D as simple joint and considering equilibrium of forces at the joint
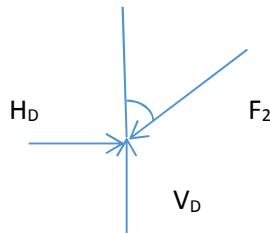
Figure 3: Free body diagram of Forces at joint D

The resultant reaction at joint D must be equal to the force in member BD (F_2). Thus,

$F_2 = \sqrt{298^2 + 203.97^2} = 361.2$ N

A similar consideration of forces in joint B gave force in member AC as 298.08 N.

Therefore the Stresses in member 1 and 2 are

$1 = \frac{F1}{A1}$ $\qquad\qquad\qquad$ (8)

Applying the same dimensional relationship between width and thickness as in column (A = 0.2b^2), and using mild steel material and safety factor of 3, Equation (8) yields,

$\frac{\dagger_1}{3} = \frac{240 x 10^6}{3} = \frac{298.08}{0.2b^2}$

Solving yields

b = 4.3 mm and thickness of 0.9 mm.

Similarly,

$\frac{\dagger_2}{3} = \frac{240 x 10^6}{3} = \frac{361.2}{0.2b^2}$

S0lving yields, b =4.8 mm and thickness of 0.95 mm.

2.3.3   Fabrication And Assembly

The developed extrusion plastometer was fabricatated. The major operations were cutting, turning, facing, drilling, welding and bolting. The frame was produced with mild steel flat bar and welded to a flat plate as the base.

Centre lathe was used to machine the heating barrel from a mild steel rod of 60mm diameter to 50mm diameter, 140mm length and a 9.55mm diameter hole was drilled through centrally.

The lagging case (the outer cylinder) was also fabricated using mild steel pipe of 150mm diameter, 140mm length and 5mm thickness.

The piston and the die were also machined from mild steel rods. The steel rod of 25mm diameter and 200mm length was on one end step turned to the head of 9.55mm diameter and 6.5mm length, that is the end to be inserted into the heating barrel, while the load carrying end to 20mm diameter, 6mm length and the remaining 187.5mm was reduced to 8mm diameter.

The fabricated extrusion meter parts were assembled thus: The die plate screwed to the heating barrel, the die and piston inserted into the barrel capillary, the heater band mounted on the barrel and the unit mounted on insulation in the outer cylinder, and then the remaining space between them was filled with insulation (fiber glass). The unit was then mounted on the frame and connected to the control unit.

2.3.4   Sample Collection and Preparation

The samples of the virgin HDPE material in granulated form were purchased from a local polymer material shop in Kaduna, Kaduna State while the recycle HDPE material was obtained by cutting the extruded virgin material. That is, cutting the extrudates (extruded material) after each extrusion into smaller pieces almost the same size as the sizes of the virgin material.

2.3.5   Experimental procedure for MFR measurement

 ASTM [7] Standard was employed for the MFR measurement. The equipment and the temperature control unit were switched on; the actual melt temperature of 190°C was correlated to the barrel via thermocouples inserted in a hole drilled in the barrel. The equipment was maintained at this temperature and a pre-heat time of four (4) minutes was allowed prior to charging. After which a minute of charging and load application was allowed. Five grams (5g) of virgin HDPE was charged into the barrel. 2.16kg weight was applied to the piston to force the molten HDPE through a 2mm orifice of the die. The stop watch was used to measure the extrusion time. The extrudates were cut into small sizes almost the same size as the virgin HDPE, collected, and weighed using an electronic weighing balance to determine the mass of the extrudate. MFR values were calculated in g/10mins. The extrusion time, temperature and mass of extrudates were recorded.

3.0 Result And Discussion

Table 1 presents the results for the melt mass flow rate MFR of virgin and recycled HDPE. The MFR for virgin was calculated to be 9.96g/10 minutes which falls within the range of 2.2 to

22g/10mins provided by the manufacturer. The effectiveness of using the developed plastic melt flow meter for characterizing the input materials for thermoplastic production has been established.

Table 1: presentation of MFR for virgin and recycled HDPE

S/NO	Material	Extrusion time (Secs)	Extrusion Temperature (^{O}C)	Force (N)	MFR (g/10mins)
1	Virgin	283	190	21.6	9.96
2	1st recycle	270	190	21.6	10.88

4.0   Conclusion

The development of a thermoplastic extrusion meter for the determination of melt mass flow rate of different thermoplastic materials was successfully carried out in this work. The equipment was used to determine the MFR of both virgin and recycled HDPE. It shows that plastic industries using recycled materials need the melt flow meter for monitoring the behaviour of production input materials

References

1. Shenoy, A. V., Saini, D. R., & Nadkarni, V. M. (2003). Rheograms for engineering thermoplastics from melt flow index. The Journal Rheological Acta Rheol. Acta , 22, 209-222.

2. Fabrizo, G. ((2016). Global Market Trends and Investment in Polyethylene and Polypropylene. Indepedent Chemical Information Service (pp. 41-49 and 103-131). Europe: Chemical Publishing Company.

3. Egbe, E. A., & Onyekpe, E. O. (1992). The effects of mould temperature and clamping pressure on medhanical properties of injection moulded thermoplastic products. The Nigerian Engineer, Journal of Nigerian Society of Engineers , Volume 27(4), 64 - 67.

4. Egbe et al, E., Lawal, S. A., Alkali, B., & Tsado, J. (2016). Design Analysis of An Extrusion Plastometer. Nigerian Institution of Mechanical Engineers. (pp. 134-143). Minna: Nimechi Minna Branch

5. ISO. BS EN 1133 (2005). Plastics – Determination of the melt mass=flow rate (MFR) and melt volume-flow rate (MVR) of thermoplastics. www.18-17.net/upload/file/20151202/

6. R.S Khurmi and J.K Gupta. Machine Design (pp. 606 – 608). New Delhi: S. Chand & company publishing company.

7. ASTM D1238 (2013). Standard Test Method for Melt Flow Rates of Thermoplastics by Extrusion Plastomer. www,astm.org/standards/D1238

MECHANICAL CHARACTERIZATION OF WELDED AISI 304L STAINLESS STEEL USING TUNGSTEN INERT GAS (TIG) AND MANUAL METAL ARC (MMA) WELDING PROCESSES

F. Sanusi[*1], O. Adedipe[*2], S. A. Lawal[*3], O. A. Olugboji[*4]
Department of Mechanical Engineering, Federal University of Technology Minna, Nigeria

Abstract

AISI 304L austenitic stainless steel is considered weldable at various fusion welding process. Manual metal arc (MMA) welding of austenitic stainless steel is often associated with probems such as residual stresses, cold cracking and inclusion in the weld metal causing premature failure. These identified welding defects can be minimised by the use of tungsten inert gas (TIG) welding process. The effects of tungsten inert gas welding and manual arc welding on the mechanical properties of AISI 304L austenitic stainless steel were investigated. A 300 x 300 x10mm plate of austenitic steel was cut into 8 pieces and each plate faces were chamfered at an angle of 30^0 and 2.5mm root gap. TIG and MMA welding processes were used to join the plates in a single V butt joint. The strength of the weld joint was evaluated for impact, bending, hardness and tensile tests. TIG weld joint was found to exhibit higher yield and ultimate tensile strength of 416MPa and 530MPa respectively while the base metal and MMA showed the least yield and tensile strength of 354MPa and 423MPa. Impact energy of 222J was absorbed by the base metal; while TIG weld joint was 207J and MMA absorbed the least energy of 201J. Microhardness values were higher at the weld metal for both welding processes and TIG joint found to give higher bending strength. Microstructural investigation also indicated that MMA weld metal had more delta ferrite than the TIG weld.

Keywords: AISI 304L stainless steel; Manual metal arc; Tungsten inert gas; Mechanical properties

1.0   INTRODUCTION

Austenitic AISI 304L stainless steels are commonly used in pressure vessels and boilers because of their high heat and corrosion resistance properties [13]. The alloy also exhibit good mechanical properties such as high strength and ductility than mild steel, and as such found useful in other applications under both high and low loading rate conditions [3]. One of the methods of achieving monolithic structure in industries is by welding. Welding produce better joint than soldering and brazing and is the most suitable for joining steels due to flexibility,cost saving and the joint reliability in service [1]. There are basically two types of welding processes and these are fussion welding and pressure welding. Fusion welding is the application of direct heat between the weld surfaces of the workpieces while on the other hand pressure welding is the application of external pressure to produce weld when the work pieces are heated to a plastic state. Gas tungsten arc welding (GTAW),shielded metal arc welding (SMAW),gas metal arc welding(GMAW) and submerged arc welding (SAW) are the common fusion welding techniques for welding stainless steel [2]. However the thermal effect associated with welding process can cause steel structure to fail at the weld joint. Residual stresses and welding defects such as porosity and hot cracking reduce the mechanical strength of the weld joint due to

113

differents in metallurgical phase caused by grain re-arrangement [8]. The use of suitable welding process together with proper filler metals are the most important factors to minimise these problems. Quite a number of work have been carried out to investigate the effect of different grades of stainless steel filler metals (austenitic, duplex and martensitic), heat inputs and welding parameters on the tensile, impact and percentage elongation of TIG welded AISI304L stainless steel. [2,4,9,10]. However, limited attempt has been made available on the effect of welding process on the microhardness variation across the weldment, bending strength and microstructure of TIG and MMA welded AISI 304L stainless steel joint. Hence this work compares the yield strength, tensile strength, impact toughness, bending strength and hardness properties of TIG and MMA of AISI 304L stainless steel.

2.0   Material and experimental procedure

The material used in this work is rolled plate of AISI 304L austenitic stainless steel of 300x 300 x10mm size obtained from Owode Onirin Lagos State. The chemical composition of the steel was investigated at Nigeria Machine Tools Osogbo and the result presented in Table 1. The plate was cut into 8 pieces and each plates was further divided into two and bevelled at an angle of 30^0. Back plate was applied to prevent distortion before tackling.

2.1   Welding process

Tungsten inert gas welding process which consist of welding machine (TIG 400), non-consumable tungsten electrode and inert gas (argon) contained in a long cylinder attached to the machine to prevent weld area from atmospheric air contamination of Hydrogen, Nitrogen and oxygen. A 1.4mm diameter 347L austenitic stainless steel filler was employed for joint strengthening and welding was achieved in a single V butt joint at 120A welding current and 28V voltage. Similarly, arc welding process consists of arc welding machine and electrode holder. Austenitic E316L stainless steel electrode of 1.4mm diameter was used. Root gap of 2.5mm was maintained and welding was achieved in a single V butt joint at100A welding current and 20V voltage. Both 347L filler and E316L electrode were selected because of their similarities with the base metal. After each laying of weld beads, chipping hammer was used to break the slag while wire brush was applied to clean the weld area. After welding mechanical test specimens were machined and filed to ASTM requirement using grinding machine and mechanical tests were carried out on the joint. Figure 1 shows the tensile test specimen design.

2.2   Mechanical tests

The tensile tests were carried out in the Mechanical Engineering Laboratory of Kaduna Polytechnic using Monsato tensile testing machine (Monsato; Serial no-9875). The specimen was clamped between the movable and the fixed grip of the machine and loaded until fracture occurred. The two fracture specimens were then brought together with final length, width and gauge length measured with Vernier Caliper to determine the elongation. Graph of applied load in kN against the extension in mm were drawn for the specimens and tensile strength was calculated by dividing the maximum load at break by the area of the sheared specimen.
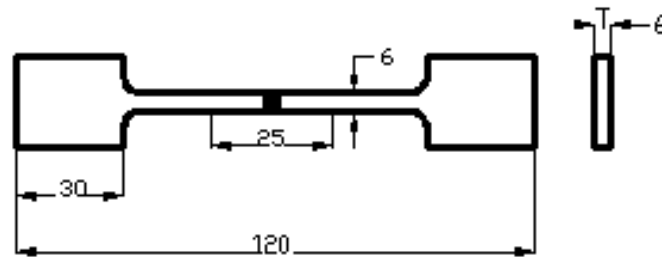
Figure 1: Dimension of tensile test specimen.
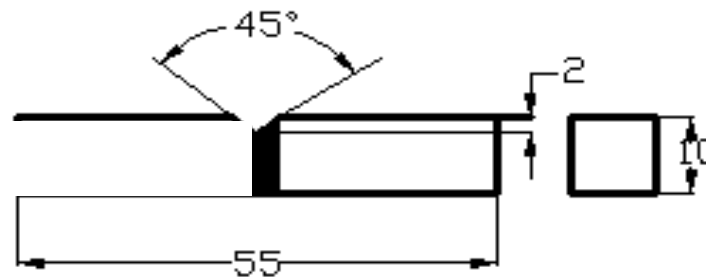
Figure 2: Dimension of impact test specimen

Figure 2 shows the impact test specimen design. Impact test was also carried out in the Mechanical Engineering Laboratory of Kaduna Polytechnic using universal impact testing machine of potential energy of 298.28J at 32.5^{0}C room temperature. A "V" notch depth of 2mm at the weld centre was achieved by machining using shaping machine and notch angle was achieved using a 45^0 tool angle. The impact test specimen was centred at the base of the machine and the pendulum stricker was released to impact the specimen at the opposite end of the notch to produce fractured sample and the energy required was recorded.
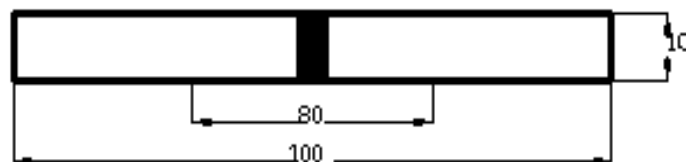
Figure 3: Dimension of bending test specimen

Bending test was carried out in the Mechanical Engineering Laboratory of Ahmadu Bello University, Zaria using Enerpac flexural machine of 100kN. The bending test specimen design is shown in Figure 3. Bending specimens were prepared and placed between the two supports and a point load was applied at the mid point until the material failed. Visual welding inspection was

115

then conducted on the bent sample to expose defects such as cracks. Hardness test was carried out using Brinell hardness tester(Brinell-ISO 6506) of 2mm diameter ball pin indenter under a load of 120kgf. Pressure was exerted on the sample by the indentor for about a minute after which the hardness value displayed on the screen.

2.3   Microstructural investigation

The specimen size 100 x 10 x 10 mm used for microstructural investigation and microhardness(using brinell hardness tester machine) were cut from each of the welded joint. These were cleaned, ground with different grits of emery paper of 180,240,320,400,600 and 1200 untill the scratches have been reduced to fine sizes. Polishing operation was done before etching with a mixture of 34% water,33% nitric acid and 33% hydrochloric acid.

3.0   Results And Discussions

Table 1: Chemical composition of parent metal and the electrodes

Element	C	Si	S	P	Mn	Cr	Mo	Ni	V	Cu	Nb
Base metal AISI 304L	0.03	0.877	0.002	0.005	1.13	18.4	0.503	8.6	0.106	-	-
AISI 347L Filler metal	0.05	0.62	0.01	0.003	1.22	19.0	0.53	9.0	-	0.12	0.4
Electrode E316L	0.012	0.02	0.14	0.025	1.62	16	-	10	-	0.12	-

3.1   Tensile and Impact Test Results

Three specimens were tested for each welding process and the average results are presented in Table 2.

Table 2: Impact and tensile result for the base metal and welded joints

Process	YS(MPa)	UTS(MPa)	Impact Energy(J)	% Elongation(mm)
TIG	416	530	207	20.00
MMA	354	423	201	14.17
BM	383	522	222	29.95

TIG: Tungsten inert gas, MMA: manual metal arc, BM: base material, YS: yield strength, UTS: ultimate tensile strength

From Table 2, it is observed that the base metal average yield and ultimate tensile results were 383MPa and 522MPa respectively which is in conformity with ASTM standard of AISI 304L stainless steel. TIG welded joint exhibited the highest yield and tensile strength of 416MPa and 530MPa which are higher than the strength reported by [12]. This could be as a result of presence of Niobium in 347L stainless steel filler metal which might have impacted strength into the weld. Scanning electron microscope SEM micrograph revealed that the width of the TIG heat affected zone was 140µm while the average of MMA heat affected zone was 346µm under the same magnification. This implies that the influence of residual stresses may be more in MMA weld joint. Increase in width of heat affected zone as a result of heat input was also reported in the work of [10]. MMA joint exhibited the least yield stress and ultimate tensile strength of 354MPa and 423.3MPa which is also in agreement with the results that are reported in [12] and [7] for similar materials. However, the strength and impact energy of the stainless steel reduced compared with TIG joint. In the base metal, more energy (222J) was absorbed compared with the welded specimens. This result is close with the one specified in AISI 304L ASTM standard, which was reported to be 216J. TIG joint absorbed an energy of 207J, which is 7.2% lower than that of the parent metal while MMA joint exhibited the least energy of 201J which is also 9.5% lower than that of the parent metal. This could be explained by the presence of more delta ferrite which reduces ductility [14]. Grain structures in both weld metal and the heat affected zone of TIG weldment were also found to be finer than in MMA which might also account for higher energy displayed by TIG. Similar observation was also reported by [11].

3.2   Hardness test result and discussion

Table 3 shows the brinell hardness experimental results for both TIG and MMA weldments, while the hardness profiles are plotted in Figures 4 and 5.

Table 3: Microhardness values across TIG and MMA weldment

Distance from weld center	TIG weld	MMA weld
-2.5	175	197
-2	197	197
-1.5	149	175
-1	130	175
-0.5	217	217
0	261	285
0.5	197	259

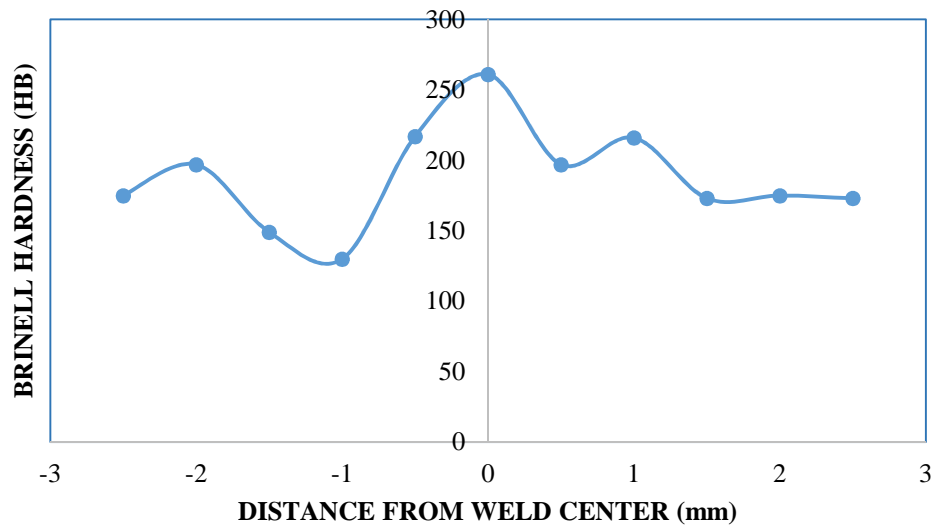|		
1	216	236
1.5	173	175
2	175	197
2.5	173	197
Average	188	210

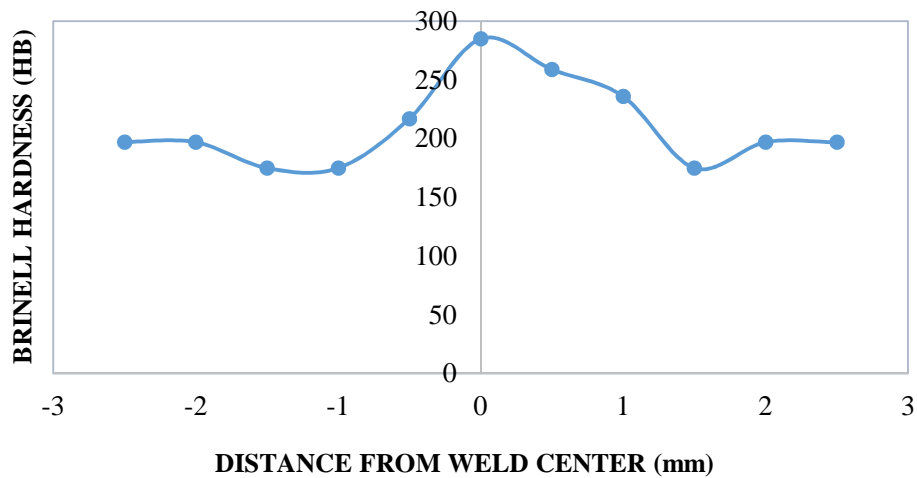Figure 4: Micro-hardness from the weld center for TIG weld.

Figure 5: Micro-hardness from the weld center for MMA weld

Hardness profile in Figure 5 shows that MMA joint exhibited higher hardness of 285HB at the weld metal than TIG hardness value of 261HB (figure 4), which is an indication of brittleness in MMA weld metal. The average microhardness value of 188HB was obtained across the weldment for TIG joint and 210HB for MMA weldment. This implies that TIG weldment has better ductility. The higher hardness value in the MMA weld metal could be due to the delta ferrites which are more in the weld metal and their ability to increase hardness and reduce ductility [14]. Other variation in hardness may also be attributed to heat retention and residual stresses caused by the heat input. The hardness test result is in agreement with the work of [5] and [6].

3.3 Bending strength result and discussion

Bending test carried out on both the weld face and the root face is presented in the Table 4(a and b).

Table 4 (a): Bending test result for MMA welding

Specimen	Bending load kN		Bending strength (MPa)		Average bending strength(MPa)
	Weld face	Root face	Weld face	Root face	
1	18.59	15.12	84.50	68.73	76.62
2	18.45	16.75	83.86	76.14	80.00
Average					78.31

Table 4(b): Bending test result for TIG welding

Specimen	Bending load (kN)		Bending strength (MPa)		Average bending strength(MPa)
	Weld face	Root face	Weld face	Root face	
1	22.10	20.20	100	91.82	95.91
2	23.42	19.90	106	90.45	98.23
Average					97.07

From the Tables, it is observed that ductility of TIG weld was found higher with average bending strength of 97.07kN/mm^2 while MMA joint exhibited lower ductility with bending strength of 78.31kN/mm2. TIG process gives better ductility because of the quality of the weld with minimum welding defects. Visual inspection also shows that there is better fusion and good weld penetration

119

between the weld metal and the parent metal in TIG than MMA; this might have contributed to its ductility.

3.4 Microstructural Examination Results

The micrographs from the microstructural examination are shown in Figure 6 (a-g)

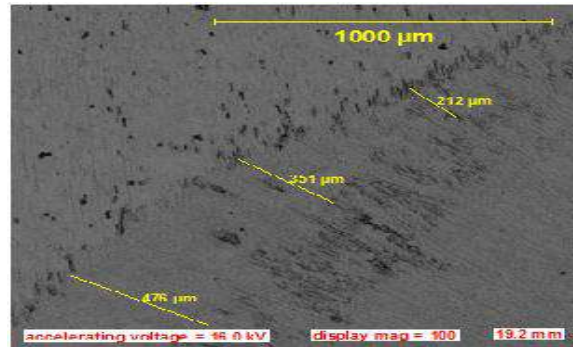Figure 6(a): Microstructure of parent AISI304L stainless steel   (200X)

Figure 6(b): Microstructure of HAZ,Fusion boundary and MMA weld metal
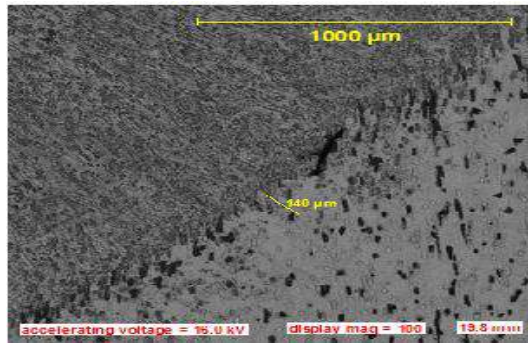

Figure 6(c): Microstructure of HAZ ,fusion boundary and TIG weld metal.

Figure 6(d): Microstructure of heat affected Zone of MMA joint (200X)

Figure 6(e): Microstructure of heat (200X) affected zone of TIG joint (200X)

Figure 6(f): Microstructure MMA weld metal

120

Figure 6(g): Microstructure of weld metal of TIG joint (200X)

The microstructure of the parent metal 304L stainless steel is shown in figure 6(a). The alloy possesses a uniform grain distribution consisting of two micro-consistuent namely ferrite (dark) and austenite (light) at 200X magnification. The microstructure of heat affected zone of both welding process figure 6(d & e) show no Cr depletion but grain refinement taken place. Figure 6(f) shows the microstructure of MMA weld metal in which the dark phases are not pearlite but acicular dendrite structures called delta ferrite in which the delta ferrite may be acicular, vermiculite, lacy or lathy in morphology. Figure 6(g) shows the microstructure of TIG weld metal consisting of less delta ferrite than MMA and with finer grains.

4.0   Cconclusions

AISI304L stainless was welded using tungsten inert gas and manual metal arc welding processes and the joint mechanical strengths were investigated. The following conclusions were drawn:

1.   The microstructural result shows that AISI 304L base metal consists of uniform grain distribution of two micro consistuents of ferrite and austenite, MMA weld metal consist of delta ferrite while TIG weld metal maintained higher austenite structure.
2.   The TIG welded joint displayed better mechanical properties compared with MMA welded joint because it yields better ultimate tensile strength, toughness and ductility.
3.   Microhardness values were higher at the weld metal for both welding processes with maximum hardness of 285HB for MMA joint and 261HB for TIG due to more delta ferrite in MMA weld metal.

Reference

[1]   Amentani, E., Espositor, R., & sepe, R. (2007). "The Effect of Thermal Properties and Weld Efficiency on Residual Stresses in Welding" Journals of Achievements in Material and Manufacturing Engineering,Vol.20, page 319-322.

[2]   Amudarasan, N.V., Palanikumar, K., & Shanmugam, K. (2012). "Tensile and Impact Properties of AISI 304L Stainless Steel Welded JointsUsing Austenitic and Duplex Stainless Steel Filler Metal" International Journal of Engineering Research and Technology, Vol.1 Issue. 9, page 1-5.

[3]   Bayode, A., & Esther, T. (2016). "Characterisation of Laser Metal Deposited 316L Stainless Steel" Journals of Proceeding of the World Congress on Engineering",Vol.2. page 978-988.

[4]   Halillbrahim, A. (2013). "Study on Microstructure,Tensile Test and Hardness of 304L Stainless Steel Jointed by TIG Welding" International Journals of Science and Technology ,Vol.2, Issue. 2, page 40-45.

[5]   Hussein, M., Shwetanshu, G., Teetu, K.,& Sharma, P. (2017). "Mechanical Characterisation of SA-508Gr3 and SS-304L Steel Weldment" International Journal of Advanced Production and Industrial Engineering,Vol.2, No. 1, page 41-46.

[6]   Manish, P., Basanth, K.,& Suhash, R. (2014). "Mechanical Properties and Microstructural Characterisation of Friction Stir Welded AISI 316 Austenitic Stainless Steel"Journals of Procedia Saterials science, Vol.5, page 2376-2381.

[7]   Mohadans, T., Reddy, M.,& Naveed, M. (1999). "A Comparative Evaluation of Gas Tungsten and Shielded Metal Arc Weld of a Ferritic Stainless Steel" Journals of Material Process Technology, Issue. 94, page. 133-140.

[8]   Navid, M., Norizah, R., Norhayati, A.,& Tang, N. (2015). "Effect of Current on Characterisation for 316L Stainless Steel Welded Joint Including Microstructure and Mechanical Properties" Procedia CIRP, Vol.26, page 560-564.

[9]   Nnuka, E.,& Okonji, P. (2015). "Effect of Welding Current and Filler Metal Types on Percent Elongation of GTAW Austenitic Stainless Steel Weld Joint" European Journal of Material Sciences, Vol.2, No. 1,page 26-31.

[10]   Tabish, A., Abbas, T., Farhan, M., Atiq, S.,& Butt, Z. (2014). " Effect of Heat Input on Microstructure and Mechanical Properties of Tungsten Inert Gas Welded Joint of AISI 304 Stainless Steel" International Journals of Scientific and Engineering Research, Vol.5,Issue 7,page 1532-1541.

[11]   Taminu, I., Danjuma, Y.,& Shekarau, A. (2013). "Effect of Gas Metal Arc Welding Techniques on the Mechanical Properties of Duplex Stainless Steel" Journals of Minerals and Material Characterisation and Engineering, Vol.1, page 222-230.

[12]   Vinoth, V., Madhavan, R.,& Tharanitharan, G. (2015). "Investigation on Property Relationship in Various Austenitic Stainless Steel 304L weld" International Journals of Scientific and Research Publications. Vol.5, No.3, page 1-4.

[13]   Viranshu, K., Pradeep, J., Shivdayal, D., Hirendra, S., Sukhja, S.,& Shallesh, K. (2015). "Analysis of the effect of sensitization on austenitic stainless steel 304L welded by gas tungsten arc welding" International journal of technology innovation and research, Vol.14, page 1-12.

[14]   Zendron, M., & Perina, M. (2009). "Influence of Delta Ferrite on Mechanical Properties of Stainless Steel Produced by MIM" 20th International Congress of Mechanical Engineering, Gramado, Brazil.

WELDING SEQUENCE EFFECT ON THE MECHANICAL PROPERTIES OF BS460B MEDIUM STRENGTH OFFSHORE STEEL

A. Babatunde, O. Adedipe, S.A. Lawal , O.A. Olugboji

Department of Mechanical Engineering, Federal University of Technology Minna, Nigeria
Corresponding Email: aberemotunde@gmail.com

Abstract

In this paper the optimum welding sequence to enhance the mechanical performance of offshore structure fabricated with medium carbon steel was presented. This was achieved by investigating the influence of altering the sequence of welding on the mechanical properties of three welded separate thick plate of dimension 120 x 120 x 120 mm from the same material. Double "V" edged preparation, the same electrode, manual metal arc welding process (SWAM) with the same welding parameters were used for weld plate manufacture. The first plate tag welding sequence one was fully welded in the upper groove before the down groove while the second plate (welding sequence two) was welded half way in the upper groove and halfway in the down groove. Both grooves were then completely filled simultaneously. The third plate (welding sequence three) was welded half way in the upper groove followed by complete filling up of the down groove before the upper groove was then completed. Specimens for tensile, compressive, impact and hardness strength test were extracted from the weld metal zone and the heat affected zone. The result of the mechanical tests carried out on these specimens revealed that welding sequence two possess the highest tensile strength of 686(Mpa) and 421 Mpa in un-weld metal region (HAZ). The weld metal regions of the same welding sequence two possess the optimal performance in compressive and impact strength but with the least average hardness value. This experimental investigation revealed that welding sequence two is the best welding sequence for the offshore steel used.

Keywords - Welding sequence; Mechanical properties; Medium strength steel; Offshore structure.

1.0 INTRODUCTION

Steel is the mostly used engineering material. The areas of application include automobile industry, civil engineering, manufacturing, oil and gas. Steel has wide area of application due to the variation of its carbon content (6). The complexity of steel arises as result of addition alloy element to iron-carbon alloy system. Steel with carbon content varying from 0.25 and 0.65 are classified as medium carbon steel while those with carbon content up to 0.25% C are classified as low carbon steel. Between 0.65-1.5% C are termed high carbon steel. Medium carbon steel is used for fabrication of fixed platform in oil and gas industry as a result of its low cost and ease of fabrication (5). Mechanical structure in offshore consist of varying steel component in term of size and geometry which are joined together mostly by welding. Welding has been identified as the preferred method of joining steel as most steels are weldable (18). Welding process is classified as either pressure welding or fusion welding. Pressure welding process is a suitable

123

welding process of thin plate ranging from 0.5-6.0mm thick. (4). These welding processes are further classified in (17). Fusion welding process is a preferred welding method of fabricating offshore platform because of its flexibility, versatility and efficiency in welding thick plate. Prominent among the fusion welding of offshore is the shield metal arc welding (SMAW). When steel is welded, the weld portion, the heat affected zone (HAZ) and the unaffected parent material have different microstructure which depend on several factors which includes material type, heat input, welding type, and type of electrode.

Weld induced residual stress is another factor that affects the integrity of weldments depending on the residual stress (tensile or compressive) type. Residual stress distribution in welds depend plate thickness as well as local melting or fusion process (3, 5). Welding sequence has also been mentioned in (3) as one of the factors that affect residual stresses in welds. Welding sequence is defined by American welding society (AWS) as the order of carrying out weld in a weldment. It is classified by number of passes into single pass and multiple pass welding sequence. Single pass welding sequence is used to perform welding on a thin component by dividing the weld head into short section. Consideration is given to order of filling the weld. The common single pass welds are progressive, backstep, symmetry and jump. Welding sequence for multiple pass includes: Build-up edge in which the first layer is completed along the entire weld length through single pass sequence (progressive, backstep, symmetry and jump) (8). This is followed by first, second, third or the number of desired welding sequence. Build-up edge is applied in large diameter butt welded pipe joints frequently used in boiling water reactors, oil pipe line transport system and steam piping system. Another welding sequence is the Block welding type. In this sequence, a given block of the joint is welded completely and then the next block is welded. Cascade welding sequence is similar to block welding sequence; the main difference is that in the block welding type, the block overlap in cascade.

Previous literatures have revealed that in welding medium carbon steel with carbon content greater than 0.3 percent, pre-heating is required to archive a satisfactory weld. The differential cooling rate between the core and the surface of thick plate during welding has been reported to enhance the weld crack (7). Preheating and the use of low hydrogen electrode have been suggested to reduce the tendencies of weld crack (5). The appropriate temperature ranges for pre-heating before welding medium carbon steel with combine thickness greater than 40 mm according to sources have been suggested to be 250 ^{O}C (10, 11, 17). Unlike in thin plates, welding of thick plate require edge preparation which include shapes like V, U, J and square. These shapes can be single or double edge preparation depending on the thickness of the material. The V groove preparation has the advantage of welding accessibility as well as ease of machining, but it is prone to residual stresses if the right welding methods are not employed (3). In references 2 and 3, the range of groove angle for material thickness greater than 19 mm was mentioned to be 60º-75º.

In references 1 and 14, certain fundamental problems that should be addressed pertinent to weldments were outlined for designers and fabricators of engineering structure. Such structures include offshore structures which are designed for 20 to 25-year service lives (9). Offshore structures are subjected to highly dynamic fatigue loads in harsh marine environments throughout their service lives. These loads result into origination of cracks, which could lead to propagation and failure of such structures. Since fatigue cracks usually originate from the weld

HAZ and grow into the parent material, the variation of the mechanical properties of such weldments needs to be understood in order to establish the optimum welding sequence that will ensure reliability, safety and efficiency of the structures. In this paper, three different welding sequences have been employed to weld BS460 medium strength offshore steels. Mechanical tests which include, tensile, compressive and hardness were carried out on samples that were extracted from the three weld sections. These are discussed in the following section.

2.0 MATERIALS AND METHODS

2.1   Materials

The material that was used for this research was a BS460B rectangular steel block of dimension 500 mm x 120 mm x 120 mm. The material was sourced from the Ajaokuta Steel Company Kogi State, Nigeria and the material composition is shown in table 1. The electrode that was used for welding was a 4 mm thick, 350 mm gauge length low hydrogen electrode designated E7018.

Table 1: Chemical Composition of BS460B steel

Element	Composition (%)
C	0.33
SI	0.289
S	0.003
P	0.005
Mn	0.029
Cr	0.090
Mo	0.05
Ni	0.027
V	0.03
Fe	0.147

2.2 Methods

The rectangular steel block was cut into three square blocks of 120 x 120 x 120 mm using a power arc saw. Figure 1 shows one of the square blocks. During the cutting operation, it was ensured that adequate lubrication was used in order to get a satisfactory output from the cutting blade.

Figure 1: 120 x 120 x 120 mm steel block

2.2.1 Edge preparations

The edge preparations were carried out cutting each of the three blocks into two equal halves of dimension 120 mm x 120 mm x 60 mm on milling machine using the slating saw. Each of the halve block was further milled to 35 mm in order to achieve a 70^0 grove angle. The two halve milled plate were then brazed to ensure the desire angle is maintained and to allow for safe handling during pre- heating and welding. Electrode of 3 mm thickness was inserted between milled plate before brazing to serve as weld. Also 4 mm weld root face was left on the milled surface according to (ISO Standard design). The brazed plates were then pre-heated to 250 ^{0}c before welding to prevent cracking of the weld metal.

2.2.2 Welding Sequences of the plates

The model for welding thick plate developed by (8) was used to fill weld each of the double "V" groove in which each of the two grooves of each block were divided into two portions using the height of each groove as a reference point. The welding sequence that was adopted was similar to the one designed for thick butt welds in reference 8 as shown in Figure 2. Each of the portion was labeled 1 ,2 ,3 and 4. Each of these portions of the steel block were weld filled in different order with the same electrode, current, voltage setting and the same preheating temperature of 250 ^{0}c.
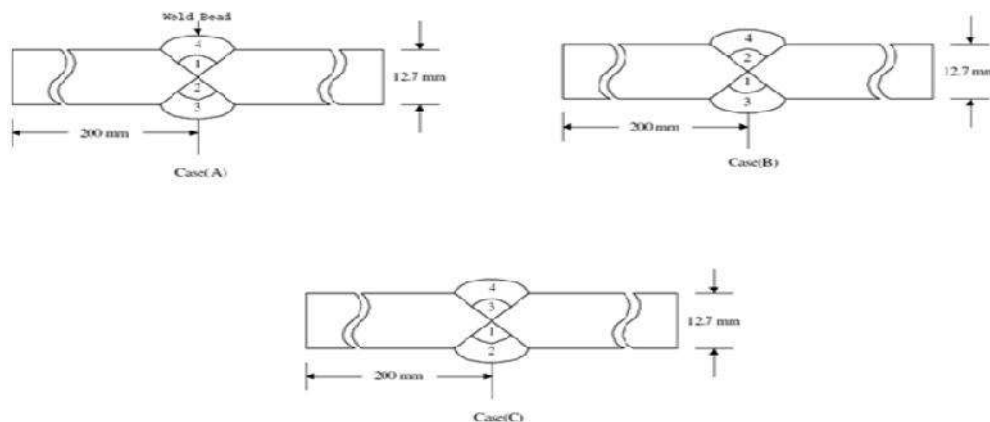
Figure 2: Different welding sequence for butt weld

(i)   In welding sequence one, portion one and two was completely welded before portion 3 and 4

(ii)   In welding sequence two the filling of upper and lower groove were done interchangeably. That is half of the lower grove followed by half of upper groove. The welding sequence was completed by filling the lower groove and lastly the upper groove.

(iii)   In welding sequence 3, half of lower groove was filled first, followed by completely filling the upper grove and finally the last portion of the lower groove. Figure 3 shows the sample of the complete welded plate

Figure 3: Sample of welded steel plate (block)

2.2.3 Slicing of the welded steel block into plates:

In order to extract specimens from different zones of the weld for mechanical tests and for etching so as to reveal the weld, the welded blocks were sliced into different thickness according to the requirement of thickness and dimensions of the test piece. The slicing was carried out on universal milling machine while the etching was done with 2% Nital.

2.2.4 Design and Extraction of Specimens from the sliced plates

Specimens to be used for tensile, compressive and impact tests were extracted within the weld metal and outside the weld metal regions of each welded block as shown in Figure 4 and Figure 5. The figures show standard tensile test specimen design. The black portion on Figure 4 and 5 is the weld metal portion while the remaining portion contain the heat affected zone and the un-affected base metal. The designs of impact and hardness test specimens are shown in Figures 6 and Figure 7.
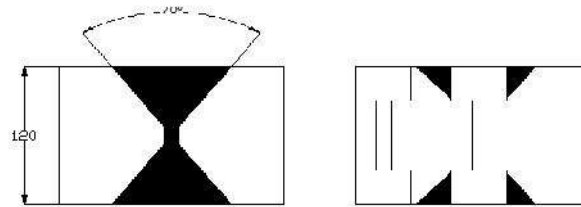
Figure 4: Positions of tensile and compressive specimens on weld block
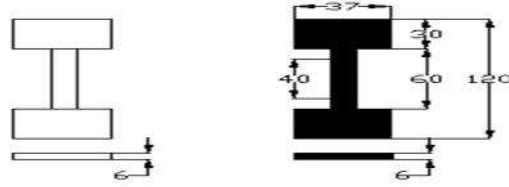
Figure 5: Tensile and compressive specimens design
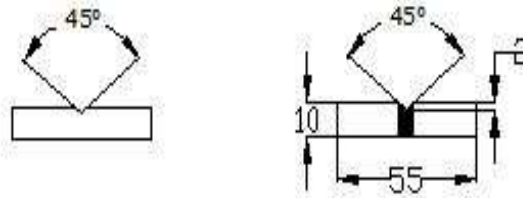
Figure 6: design of the impact test specimen
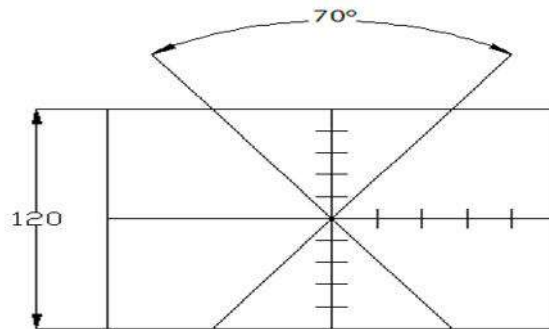
Figure 7: Design of the hardness test specimen

2.3 Mechanical Tests

For tensile tests, twelve numbers of specimens were used; four specimens were extracted from each welding sequence; two each from un-weld metal/(HAZ) and weld metal region. Monsanto tensometer was used to carry out the tensile and compressive tests. The initial gauge lengths, original widths, original thickness of specimens were measured and recorded. The tensile specimen was clamped on the Monsanto tensometer. The load was gradually applied to the specimen by turning the hand wheel gradually and steadily. The applied load readings at the hand wheel at every 0.2 mm interval of extension on the dial gauge were observed and recorded until the specimen fractured. The fractured test pieces (specimen) as well as the extensometer were carefully removed from the machine. Thereafter, the two pieces of fractured specimen were joined together, the final gauge length was measured and recorded, the final width and thickness of fractured point were also measured and recorded. The graph of the load against extension was automatically plotted by the machine. For compressive tests, the same number of specimens as those used for tensile tests was selected. The compressive specimen was firmly clamped on the tensometer vial a suitable compression gauge, after which the load gauge was reset to zero. The

128

machine is equipped with a compression device that reverses the tensile pull of the machine to compressive load on the specimen. The load was gradually applied on the specimen by turning the hand wheel of the tensometer until it buckled. The load which buckles the specimen was observed and recorded. The buckled specimen and compression gauge were gently removed from the machine.

An Avery Birmingham impact testing machine was used to carry out the impact tests. The pendulum arm of the machine was allowed to swing freely to ensure freedom of movement after which it was positioned to its rest. The room ambient temperature of 35°c was observed via the thermometer. The specimen was firmly clamped such that the notch faces the striker, after which it was engaged by clamped lever. The loose pointer was then adjusted to the fixed point's position. Thereafter, the striking medium was set in such that the flat surface was facing the release direction. The release lever was carefully disengaged which allow the pendulum arm to swing and strike the specimen and fractured it. The final energy reading on the scale as registered by the loose pointer was observed and recorded. The clamping lever was unlocked and the fractured specimen was removed from the vice. The above procedures were repeated for other specimen. Hardness test was carried out using Brinell hardness tester. The hardness was carried out on different portion (phases) of the plates. A was applied load to the surface of the material to be tested via a hardened steel ball of known diameter (Indenter). The diameter of the resulting permanent indentation in the tested metal was measured and the Brinell hardness number was calculated using the relationship in equation 1.

$$BHN = \frac{2P}{fD(D - \sqrt{D^2 - d^2})} \qquad (1)$$

Where;
BHN = Brinell Hardness Number,
P = Applied Load (kgf)
D = Diameter of indenter (mm) = 2 mm, d = Diameter of Indentation (mm)

The three etched plates, one each from each of the welding sequence ware used as specimens for the test. Each of the plates was marked at equal intervals within the weld metal portion and across the heat affected zone and the un-affected base metal. A hardened steel ball of 2 mm diameter indenter was selected and was firmly fixed on the indenter's holder. The specimen was gently positioned on the anvil and a required load of 115 kg was added to the weight hangers of 5 kg which sum up the load to 120 kg. The load lever was released to apply the load on the plate and a stop watch was simultaneously started from zero to 15 seconds. After which the load lever was used to retract the specimen from the indenter. The process was repeated for different marked positions on the plate. The hardness values of each portion were calculated using equation 1. These procedures were repeated for the other two plates.

3.0 Result of the Mechanical Test

The result of tensile and compressive properties of three welding sequence studied are tabulated in table 2. From table 2, it can be seen that the result of the tensile strength shows variation of mechanical properties of specimen extracted at different portion of the welded plate. This variation is similar to those reported in reference 3. Differential cooling rate between the surface and core

129

of the thick plate material been welded has been attributed to this variation. Welding sequence 2 has the highest ultimate tensile strength of 686.38 Mpa and 431.30 Mpa in HAZ and weld metal region respectively. Also from table 2 the same welding sequence two has the highest strength of 342 Mpa in compression along the weld metal region. However, welding sequence one has the highest compressive strength of 388.12 along HAZ region. The tensile properties obtained from welding sequence 2 agree with the study carried out on welded joint of similar medium carbon steel (12). Welding sequence one has the least yield strength of 318.50 Mpa in weld metal region and lowest % elongation of 7.00 in weld metal region. Generally, the weld metal portion exhibited higher percentage elongation, more ductile but lower yield strength compared to un-weld metal region.

The results of impact tests are displayed in table 3 where it can be seen that welding sequence one has the highest impact energy of 30 joules in un-weld metal portion (HAZ). Tensile test result shows that this region has the highest percentage elongation among the three sequence in un-weld metal region. These results agree with those reported in references 13 and 16. The weld metal of welding sequence 2 has the highest impact strength of 177 joules with highest percentage elongation of 30 %. The weld metal region of welding sequences 1 ,2 and 3 have higher impact energy than the un-weld metal region unlike the tensile test result. This may attribute to differences in composition of weld to base metal as reported by (5 and 6). From table 4 and 5 the result of hardness value across the weld metal show that the hardness values across the three w/s vary significantly as a result of different cooling rate and re-melting after solidification as suggested by (3 ,6). Welding sequence one has the highest average hardness value 171 BHN, which may be as a result of formation of coarse grain due to high cooling rate. The center of the weld has close hardness values which may be as result of rooting that was done in a similar way before sequence filling of the groove. Figure 7 shows the hardness curve along the weld metal region

Table 2: Tensile and compressive test result of welding sequence one, two and three

Tensile Properties	Yield strength (N/mm^2)	Tensile Strength (N/mm^2)	Breaking Strength (N/mm^2)	% Elongation	% Reduction in area	Compressive strength (N/mm^2)
Plate 1&2: W/S 1 weldment	318.50 302.89	380.61 302.89	369.81 292.07	7.00 7.00	19.00 18.00	327 326
Plate 1&2: W/S 1 un-weld metal	389.08 420.00	520.12 510.20	520.18 510.20	7.00 6.00	29.00 28.00	386 388
Plate 1&2: W/S 2 weldment	331.32 320.30	431.70 412.20	317.32 355.85	13.70 11.25	60.93 43.89	342 306
Plate 1&2: W/S	589.62 506.50	686.23 633.12	686.38 633.12	6.00 7.50	13.00 17.00	570 347

2 un-weld metal						
Plate 1&2:	342.48	420.16	363.20	6.40	20.89	327
	353 .98	353.98	353.98	9.50	34.23	
W/S 3						302
weldment	542.30	542.30	538.90	4.50	20.80	344
Plate1& 2: W/S 3 Un-weld metal						
	543.98	543.98	540.98	4.50	27.00	308

W/S: Welding sequence

Table 3: Impact test result of welding sequence 1, 2 and 3

W/S 1-3	PORTION OF EXTRACTION OF SPECIMEN	IMPACT ENERGY ABSORBED (J)	% ELONGATION
WELDING SEQUENCE 1	weldment of plate 1 and 2	175.3	7.9
		158	7
	un-weld metal plate 1 and 2	25.6	3.5
		30	7
WELDING SEQUENCE 2	weldment of plate 1 and 2	159	13.7
		177	11.25
	un-weld metal of plate 1 and 2	27	6
		24	7.5
WELDING SEQUENCE 3	weldment of plate 1 and 2	122	6.4
		131	9.5
	un-weld metal of plate 1 and 2	29.5	4.15
		25.6	4.75

W/S: Welding sequence

Table 4: Hardness Test Result across the Weldment of W/S 1-3

Distance from etched plate edge (mm)	W/S 1 Hardness value (BHN)	W/S 2 Hardness Value (BHN)	W/S 3 Hardness Value (BHN)
5	159	143	159
10	159	143	159
15	179	143	168
20	179	143	168
25	179	179	179
30	229	229	229
35	168	159	179

40	143	159	179
45	143	151	143
50	143	143	143

W/S: Welding sequence

Table 5 Variation of hardness of base metal close to center of the fusion zone

Distance from center of the plate to base metal (mm)	W/S One Hardness Value (BHN)	W/S Two Hardness Value (BHN)	W/S Three Hardness Value (BHN)
3	229	229	229
6	229	2277	228
9	228	225	220
12	220	227	219
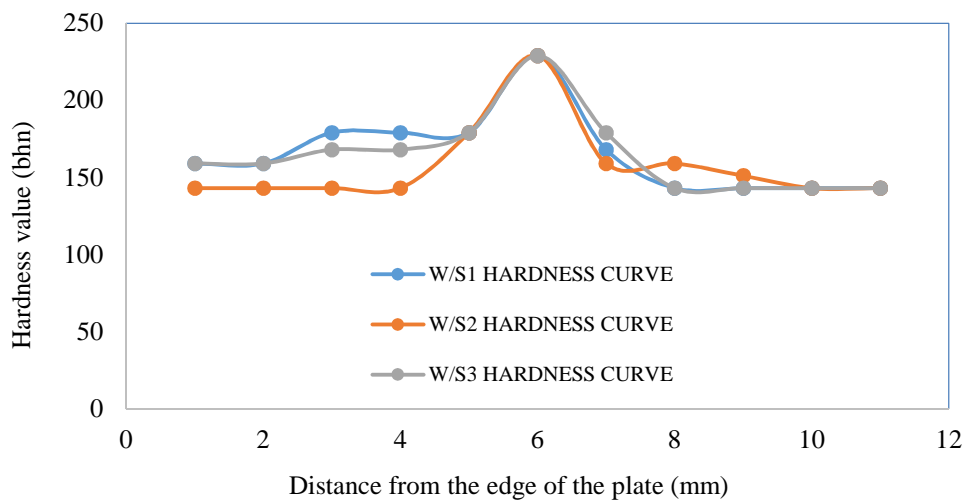
Figure 7: Variation of hardness value along the weld metal of sequence 1, 2 and 3

4.   Conclusion

The following conclusion can be drawn from the result obtained;

1. Welding sequence two has the best performance in term of tensile strength having the highest strength of 430 Mpa in the weld metal region and 686 Mpa un-weld metal region. Also welding sequence two possess the highest strength in compression especially along the weld metal where failure can emanate easily and is therefore the best welding sequence where tensile and compressive strength are desirable.
2. Welding sequence one possess the highest hardness value along the weld metal and the HAZ region and is therefore the welding sequence that has the best performance in hardness.
3. Welding sequence two also has the best value of impact energy absorbed during the impact test having the impact energy of 177 joules in weld metal region.

References

1) Ali, M., Adedipe, O., and Feargal, B. (2016) Welding Sequence effect on Residual Stress Distribution in Offshore Monopile Structure, Offshore Renewable Energy Center, Cranfield university.

2) Davies, A. C (1992). Science and practice of welding (10th ed). United Kingdom, Cambridge university press

3) Dwivedi (2003) "Heat Flow in Welding and Residual Stress". Department of mechanical engineering and industrial engineering, Indian institute of technology. Lecture module 5. Retrieved from https://www.google.com/search?q. on 27th October, 2017.

4) Dodo, M. R., Nause, T., Adamu, T., and Ibrahim, Y.M (2013). Effect of Post Weld Heat Treatment On Mechanical Properties of Arc Weld Medium Carbon Steel. Journal of Technology, vol. 35, issue. 2, page 337-343

5) Dusote, T.K., Ajiboye, A.B., and Rabiu (2012) "evaluation of mechanical properties of medium carbon steel quenches in water and oil" " journal of material science, vol. 6, issue 2.

6) Enda keehan (2004) "Effect of Microstructure on the Mechanical Properties of High Strength Steel". " PH.D. thesis, Chalmers university of technology and Göteborg university, Sweden

7) George, F., Vander, V., and Fasm (2011) "metallography of weld" Ohio, struers inc pre.

8) Isaac Harnandez Arriaga (2009) ". Welding Sequence Analysis" PH.D. Thesis, AGH University of Science and Technology. Page 3-9.

9) Kabir Sadeghi 2012 "An overview of design analysis, construction and installation of offshore petroleum platform." GAU J. SOC.& appl. Sci. 2(4), 1-16. Retrieved from www.google.com/search?q. on 10th of October, 2017.

10) Kumar Srivastava, S. P. Tewari, Jyoti Prakash (2010). "A Review on Effect of Preheating And/Or Post Weld Heat Treatmemt (Pwht) On Mechanical Behavior Of Ferrous Metals". International Journal of Engineering Science and Technology, vol. II, no. 4, pp. 625- 627

11) Lincoln electric, (2013). "What is Preheat". retrieved from .www.lincolnelectric.com

12) Mohammed R. A., Abdulwahad M., Dauda E.T. (2013). Properties Evaluation of Shielded Metal Arc Weld Medium Carbon Steel Material. International Journal of Innovation Research in Science Engineering and Technology (IJIRSET), Vol 2(8). 3351-3357. www.ijirset.com.

13) Ovat F. A., Asuquo ,L.O., and Anyandi, A.J. (2012) "Microstructural effect of electrode types on mechanical behavior of welded steel joint" Research journal in engineering and applied Science. 1(3) 171-186. www.Emergingresouce.org.

14) Oyewole Adedipe (2016) Review of Corrosion Fatigue in Offshore Structure: Present Status and Challenges in The Offshore Wind Sector. Journal of Renewable and Sustainable Energy Review. 61. 141-154.

15) Sammy-Armstrang Atta-Agyemang (20013) "Optimization of Strength and Toughness on the Wieldable HSS used in Offshore" Master Thesis, Lappeenranta university of technology. Page 26- 27

16) Tukur, S. A., Usman ,M.M., Isyaku Muhammed , Sulaiman ,N.A (2014) 'Effect of tempering temprature on mechanical properties of medium carbon steel." International

Journal of Trends and Technology (IJETT). Vol.9 (15. Retrieved from https://www.google.com/search

17) Weman Klass, (2003) Welding Process Hand Book, Woodhead Publishing Limited, Abiton Hall Cambrige Englad.page 7-18, 63-67

18) Zakaria Boumerzoug, Cheseddine Derfouf and Thierry Baudin (2010) "Effect of Welding On Microstructure and Mechanical Properties of Industrial Low Carbon Steel." Journal of engineering doi:10.4236/eng.2010.27066. (/www.SciRP.org/journal/eng)

DEVELOPMENT OF A SHEA FRUIT PULPING MACHINE

Iliya Joel Paul[1], Ademoh Nuhu.[1]

Mechanical Engineering Department Federal University of Technology Minna, Nigeria.[1]

*Corresponding author email: jpiliya8@gmail.com, +2348168077724

Abstract

This paper reviews how shea fruit (Vitellaria paradoxa) being a naturally found food/cash crop around the Sahel region of west through central and parts of east Africa can be harnessed and maximize output for both food and economical purposes. This work highlights the physical and mechanical properties of the shea, which consist of the outer mesocarp (pulp), the nut, and the kernel which is more commonly used for its oil content. The propose of this work is to explore the prospective way of utilizing post-harvest processing the shea to obtain its pulp for further preservation, processing, storage, transportation and uses by developing a machine that will effectively remove the outer mesocarp (pulp) of the shea fruit without breaking the nuts thus increasing its value and availability even when it is out of season. Developing the machine will Increase technology and practical knowhow and self-reliance of youths in Nigeria, create self-development, self-worth and also ensure conservation of useful human energy during shea butter processing, hence increase yield and income, create job openings for the skilled, semi-talented and unskilled youths of this nation.

Keywords: Shea fruits, post-harvest, Mesocarp pulping, shea nuts.

1.0 INTRODUCTION

Shea (Vitellaria paradoxa) is a part tree of the Sapotaceae family. It is the main species in variety Vitellaria, which is indigenous to Africa. The shea organic product comprises of a thin, tart and nutritious mash that encompasses a generally expansive, oil-rich seed from which shea butter is gotten. (Booth, 1988), Vitellaria paradoxa spp. nilotica found in East Africa, ranging through southern Sudan, northern Uganda, the western fringe of Ethiopia, and the northeast corner of the Democratic Republic of the Congo. While the Vitellaria paradoxa ssp. paradoxa ranges from the eastern Central African Republic westward to within a few kilometers of the Atlantic coast of Senegal (Hall et al. 1996).

Shea trees develops wildly in the semi-arid regions of the tropical belt of central Africa in a district extending from the Gambia in the west through Senegal, Togo, Benin republic, Nigeria, Niger, chad and up to Sudan in the east, as depicted in figure 1. In Nigeria, the shea trees are found around the Sahel savannah region which covers regions from Kogi, Benue, Niger, and Kaduna to the west, Gombe, Bauchi and Taraba to the east. Commonly referred to as karite in French, Kade or Kadanya in Hausa language, Eko in Nupe, Okwuma in Igbo and Ori Yoruba.

135
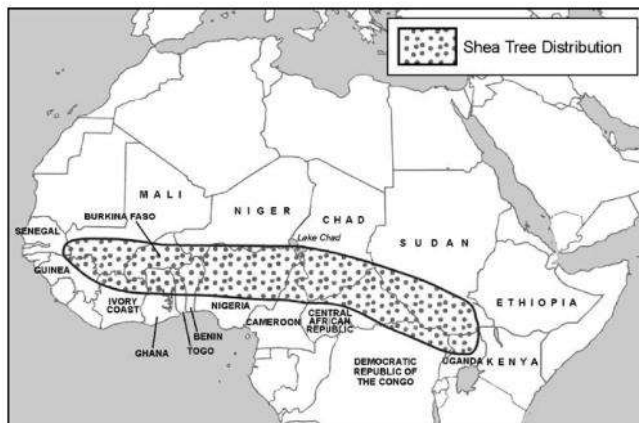
Figure 1.0 - Distribution of the shea trees (Elias & Carney, 2007).

The availability of fruits in Nigeria and many parts of Africa is only for a mean period due to lack of preservative and storage measures; as such, fruits are only obtainable for consumption seasonally. With this, it is observant that there are little or no extraction and preservation of shea pulp for use when the fruit is out of season. Hence one does not enjoy the full nutritious and flavor benefits of the shea even after its seasonal period. Shea, aside being consumed freshly, can be dried and grinded into powder form, mixed with other fruits and additives to make products such as the fruit jams, or evaporated to concentrates. These products have a good of potentials in beverage and food processing industries for local and foreign exchange earnings. Some of the products could also be used in the feeds and forage industries for its nutritional benefits adding value to the feeds/forage products. Therefore a small scale machine to pulp the mesocarp of a shea fruit is highly essential to reduce the postharvest loss and to increase the value to the commodity.

(a)   (b)
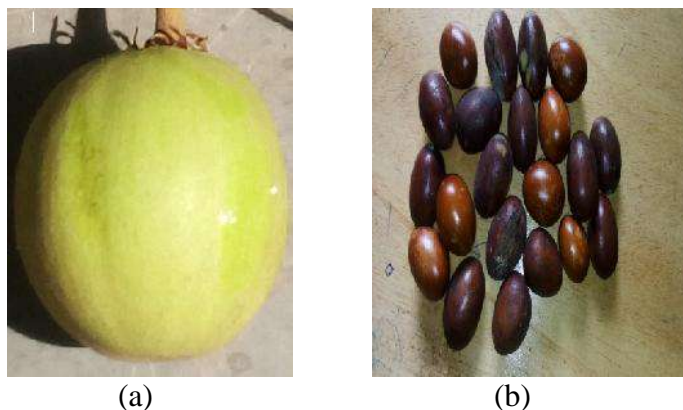
Figure 2.0 – (a) shows the shea fruit and (b) Nuts

Two main parts of a shea fruit are identified as the pulp (pericarp) and the nut, as seen on figure 2.0. The fruit pulp which is usually eaten up, allowed to ferment or dried surrounds the nut, whose shell encloses the seed (shea kennel) from which the shea butter (oil) is obtained (Hartley, 1988; Purseglove, 1995). In shea butter processing, the removal of Shea Mesocarp (pulp) is done by eating up the pulp, drying it up or traditionally by allowing it to ferment and meshed. To remove

136

the kernel from the nut, this is achieved by breaking with hammer or stone. The oldest technique in processing the shea fruit is the oldest method used before the advent of machinery and it is still being widely used by rural farmers for shea fruit processing (FAO, 2005). The food and agricultural organization went ahead to affirm that though most machinery later developed and used for shea butter extraction were principled from the observation of the traditional process, these machines have made a whole lot of contributions to the industry. However, the stages involved and unit of operations in the traditional processing of shea fruits into shea butter is quite different from the mechanical method; while the native technique separates digested shea fruits pulp mashed and discarded or dried before using the nut of the shea for further extraction of shea butter, the mechanical seeks to smoothly detach the pulp from the nuts in an efficient and faster way.

Fruits from agroforestry species have been known to supplement dietary needs. The vital nutrients and essential vitamins they contain help to improve the nutritional content of staple foods thereby curtailing malnutrition among growing children (FAO 2001). In many developing countries, edibles agroforestry species, such as wild fruits, mushrooms, honey, other known medicinal plants and insects, which are seasonal, can be developed into a basis for socio-economic sustenance. Shackleton, C.M. (2014). However, the successes and feats achieved in transforming agro-products, other related goods and services toward establishing some developmental advancement has been identified by some improvement specialists as being slow compared to other industrial sectors. Belcher B. (2007). Similar reports also revealed that the benefaction of shea to livelihood and sustainable development is not obvious, largely due to an underestimation of their value and product usability. Wunder, S.; (2014).
The main objectives of this work are;

(1) To review the popularity status of the shea fruits, its natural area of growth, its uses and medicinal value and other uses, and the demand for its product and;
(2) To explore the prospective way of utilizing post-harvest processing the shea to obtain its pulp for further preservation, processing, storage, transportation and uses. Thus increasing its value and availability even it is out of season.

The significance of this study when completed will impact the industry by opening up new research opportunities, thus adding to the knowledge-base on the ways the shea mesocarp can be effectively collected, stored, processed, preserved, packaged and transported thus making it available all year round for economical uses.

Shea fruit can be a valuable raw material in food and beverage industries as and also add more potential of modifying these collected pulps which has a lot of potential for export as against being wasted.
Developing the machine will Increase technology and practical knowhow and self-reliance of youths in Nigeria, Create self-development, self-worth and also ensure conservation of useful human energy during shea butter processing, hence increase yield and income.

Significantly do away with food contamination by the use of anti-corrosion materials, create job opportunity and means of livelihood for the skilled, semi-skilled and unskilled youths of this country.

2.0   Nutritional Value of Shea Pulp

Steven maranz et al worked on the Nutritional values and indigenous preferences for shea fruits (vitellaria paradoxa) in African agroforestry parklands. The results as depicted on table 1.0 show that Shea fruit pulp contains some amounts of water, protein, soluble solids, and major minerals. The range of values for shea indicates that there is a great deal of variability in all measured parameters.

Middle-range values compare very favorably with other important tropical fruits. The protein content (0.8-3.4 g/100 g fresh pulps) is high for a fruit. TSS (considered here to represent sugars) range from low (4.0%) to very high (33.9%). Shea pulp potassium levels could be compared to that of banana (542 vs. 357 mg/100 g mean), which is known as a rich potassium source. Many of the shea trees analyzed had a pulp potassium content of more than 1000 mg/100 g. Shea pulp is also a rich source of calcium (141 mg/100 g). Shea pulp phosphorus, zinc, and magnesium contents are quite high and cannot be ignored or lost to food losses. The only mineral was found deficient in shea pulp is copper, which did not show up as a trace in any sample.

Table 1.0 - Mean values and ranges of shea fruit pulp nutritional parameters (Maranz et al, 2004). Showing the unit percentage (%) in milligram per 100 gram of both the fresh weight (FW) and dry weight (DW).

Table 1.0

Analysis	Units[2]	Shea[1]		
		N	Range	Mean
Water	%	—	—	67
TSS	% Brix	223	4.0–33.9	13.3
Protein	g/100 g FW	126	0.8–3.4	1.8
P	mg/100 g FW	127	2.9–42.3	23
Zn	mg/100 g FW	127	0.3–5.2	1.21
Fe	mg/100 g FW	127	0.3–58.1	5.4
Mg	mg/100 g FW	127	9.4–90.6	43
Ca	mg/100 g FW	127	24–364	141
K	mg/100 g FW	127	105–1208	542
Cu	mg/100 g FW	127	0.0	0.0
Mn	mg/100 g FW	127	0–1.29	0.31
B	mg/100 g FW	127	0.3–6.5	2.4
Protein	g/100 g DW	126	2.4–10.3	5.6
P	mg/100 g DW	127	9–128	69
Zn	mg/100 g DW	127	1–16	4
Fe	mg/100 g DW	127	1–176	16
Mg	mg/100 g DW	127	28–275	129
Ca	mg/100 g DW	127	72–1103	426
K	mg/100 g DW	127	318–3660	1686
Cu	mg/100 g DW	127	0	0
Mn	mg/100 g DW	127	0–3.9	0.9
B	mg/100 g DW	127	1–20	7

138

Shea tree population means and region can affect a great deal of variation between measured parameters, as fruits from some regions may have lower TSS and water content and its rage for minerals like the phosphorus, zinc, potassium and magnesium content may vary significantly.

2.1   Economic Importance of Development Of Post-Harvest Shea Fruit Pulping Machine

The agro-processing industries in many developing countries has been largely associated with the production of export commodities, which traditional methods may not be able to compete with other modern technologies and meet demand hence Modern processing facilities have been established as a consequence of this and developing a shea pulping machine will;

1. Minimize post-harvest losses
2. Extend the shelf-life of food-produce, thus increasing food security.
3. Stabilize prices of raw materials during peak season
4. Good returns to farmers
5. Provide employment-opportunities
6. Promote economic growth of the community
7. Provides food of uniform quality, on a large scale
8. To meet the food requirements, particularly in inaccessible areas
9. To create new products of increased appeal and added value
10. To provide nutritive value
11. To promote the establishment and expansion of appropriate industries.

2.2   Work Principles of Pulping Machine

Over the years, people have worked on different machines for the post-harvest/food processing industry considering many varieties of different fruits like the baobab, palm fruits, mangos, melons etc. but little has been done with specifics to the shea fruit. Some of the pulping techniques commonly used are the digesters, graters, continues crusher with basket press etc.

The digesters are mostly of two types:
I. The beaters digesters
II. Screw digesters

The beaters types comprise shaft with beaters which are commonly used to digest boiled fruits (palm nuts) to remove the oily spongy mesocarp from the kernel through collision and squeezing. The beaters types are also group based on the positioning of the shaft. The shaft could be a vertical shaft with augers or beaters or horizontal shaft with auger or beaters. However, the locally available are vertical shaft, batch production machine with one or two through puts. Akor, (1977). Digestion involves the palm-fruits being meshed under steam-heated conditions while the raw palm oil is been pressed out. Here, twin-screw press is generally used to extract the oil from the digested product. The crude oil is further purified for consumption and/or storage. The continuous crushing system usually has a cam and follower system and metal crusher with spikes.

In order for the continuous crushing process machine to extract juice from all kinds of juicy fruits, it exerts impact, tensile and shears force. When fruits are fed into the machine, the metal crusher in the machine works by continually impacting pressure on the fruits by ramming it against a metallic plate and the juice extracted is collected through an opening specially made for that purpose. The unwanted produces are pushed out through the waste outlet. Bello et al. (2015).

The reciprocating motion of the crusher is achieved by the use of cam shaft and a follower link, which is connected to an electric motor by a means of belt and pulley. The motion of the cam and the follower is such that it converts and transmits the rotating motion of the motor to reciprocating motion of the crusher.

While the basket press consists of a horizontal perforated cylinder, a hinged cover, piston with circular plate, paddle, a hydraulic system or mechanical press and a power unit. Bello et al. (2015). The basket press needs to exerts impact shear or compressive force in order to extract juice, the incorporated paddle exerts both impact and shear force on the fruit. This is achievable when the paddle agitates the fruits in a barrel thus hitting and rotating the fruits continuously. By so doing, the pulp is then softened and separated from the nut. Compressive force can now be exerted by the hydraulic system. The piston forces the fruits against the basket and the result is the juice being compressed out of the mesocarp. Manditsera (2015).

2.3   Description of The Shea Pulping Machine

The shea pulping machine will consist of a feeding hopper, cylindrical barrel, worm shaft, pulley, electric motor, pulp outlet, nut outlet and main frame. The hopper made of a stainless steel metal, with a control valve which will serve as an adjustment for regulating the fall of materials into the barrel. A cylindrical barrel which covers a well seated worm shaft with blades of stainless steel around it arranged in a spiral pattern which serve dual purpose of piling off the mesocarp of the shea fruit and also aid conveying the nuts from the point of entry through the pulping chamber (cylindrical barrel) to the nut outlet while there is a pulp (product) outlet Undernet through where the outer mesocarp falls off.

The machine also consist of a driving system of a belt and two pulleys, a big pulley attached to the worm shaft and a small pulley attached to the electric motor at a ratio of 3:1 so as to reduce the speed of the electric motor and thus increasing the torque of the machine. The Shea pulping machine will also have a main frame made of a carbon steel angle iron and of about 500cm high with an electric motor seating conveniently attached to the stand in a way that it can be easily modified to suit a petrol engine prime mover in a situation where there is no electricity to us an electric motor.

3.0   Conclusions

The manufacturing and food processing industries could play an important role in not only preventing the post-harvest losses of farm produces, it can ensure food sustainability and availability of fruit products even when then main fruit is out of season. It can also help in providing employment opportunities and income to the rural youths, the manufacturers/developer of the shea mesocarp pulping machine, other processing industries, storages and transporters etc.

This will also trigger development process in terms of improved agricultural practices for sustainability and food surplus. The machine will also provide the opportunity for investment in rural area and in establishing the infrastructure support for the agricultural produces.

References
1. Adesoji olaniyan, akindele folarin alonge. (2007); Problems of Shea Butter Processing in Africa. Electronic proceedings of the international conference on crop harvesting and processing, 11-14 February 2007 (louisville, kentucky usa). Retrieved from https://www.researchgate.net/publication/242301859 (2018).
2. Akor, A.J. (1977). Mechanization of the Oil Palm in Nigeria. Paper presented at the Conference of Nigeria Society of Agricultural Engineers on "Agricultural Mechanization and Operation Feed the Nation". University of Ibadan, April 4-7, 1977. pp.18.
3. Alonge, A. F. and Olaniyan, A. M. (2003). Effect of processing factors on Oil yield of Shea Butter during extraction. Nigerian Journal of Technological Development published by Faculty of Engineering, University of Ilorin, Nigeria, Volume 3, No 2, page 126 - 133.
4. Babatunde, O. O. and Olaoye, J. O (1997). Improved processing procedure of shea butter oil for rural women. Nigerian Society of Agricultural Engineers Proceeding of the Annual Conference, Volume 19 pages 380-390.
5. Bello R. S., Bello M. B., Essien B. A., Saidu M. J., (2015). Economic Potentials of Oil Palm Production and Machinery Use in UDI, Enugu State, Nigeria, Science Journal of Business and Management. Special Issue: Sustainable Entrepreneurial Developments in Agribusiness. Vol. 3, No.5-1, pp. 16-20.
6. FAO. (2005) Small-scale Palm Oil Processing in Africa. Food and Agricultural Organization (FAO) Agricultural Series 148. pp. 1-55. http://www.fao.org/document/show_edr.asp?urlfile=/DOCREP/005/Y4355E/Y4355E03.html (Accessed: 2018).
7. Food Agriculture Organization, (2002) Small-scale palm oil processing, FAO Agricultural Services Bulletin 148.
8. Manditsera Dickson (2015); Wild Fruit Pulping Machine. Paper presented at the International Conference on Mechanical and Industrial Engineering (ICMIE'15) July 14-15, 2015 Harare, Zimbabwe.
9. Oje, K, Alonge, A. F and Adigun, Y. J (2001): Some engineering properties of Shea Nut relevant to mechanical processing. Ife Journal of Technology (IJT) published by Faculty of Technology, Obafemi Awolowo University, Ile-Ife, Nigeria, Volume 10, Number 2, page 17 - 20.
10. Steven maranz, walter kpikpi, zeev wiesman, armelle de saint Sauveur, and bishnu chapagain (2004). Nutritional values and indigenous preferences for Shea fruits (vitellaria paradoxa c.f. Gaertn. F.) In African agroforestry parklands
11. Dennie, MaKeish N. (2012), "Medical Benefits of the Shea Nut Tree". Biology Student Research. Paper 1. Retrieved from http://digitalscholarship.tnstate.edu/biology_students/1. (2018).

EXPERIMENTAL STUDY OF STABILITY LIMITS OF WIND TURBINE BLADES SUBJECTED TO SITE SPECIFICATION CONDITIONS

BABA Sulaiman, Oyewole Adedipe and ALKALI Babawuya

Department of Mechanical Engineering, Federal University of Technology, Minna, Nigeria
Department of Mechatronics Engineering, Federal University of Technology, Minna, Nigeria
Corresponding Email: mcbrain_133@yahoo.com

Abstract

In our planet earth, there is lot of natural energy source which makes it very comfortable for human life to live and survive. Among these energy sources is the wind energy. This free energy source comes with challenging characteristics i.e. it's very unpredictable because the strength of wind and its direction is dynamic. To produce useful amounts of power, wind turbines generally need to be large and tall, this makes the wind turbine blades longer and slender too, which is a great source of instability. Therefore, the need to experimentally determine the stability limit of wind turbine blades for different operating condition and the study location is important. In this study, three different materials (Al-alloy, wood and PVC) were used to fabricate the blades and was installed on the hub of mini HAWT at three different angles (5°, 10°, 15°) and wind speeds (2, 4, 6)m/s to analysed the stability limit of the blades. The experiment was on a static motion, where the deflection of the blades were analysed, simulated on Solidworks and recorded. In all cases tested, the data collected indicated that the PVC blade produced highest deflection of 11.41mm which is equivalent to 3.8% of the blade length. The blade is stable because this is less than 5% of the blade length. The Al-alloy and wood blade produced 1.6% each which makes them more stable. Al-alloy produce the lowest deflection of 0.0006293mm with low wind speed of 2m/s at an angle of 5°. The good agreement between the deflections computed by the Solidworks package and the experimental data has been used in the validation process where it indicates that the research can be used to estimate the stability limit of a wind turbine blade.

Keywords: Wind turbine; Blade; Stability; Deflection; Energy.

1.0 INTRODUCTION

In our planet earth, there is lot of natural energy source which makes it very comfortable for human life to live and survive. Among these energy sources is the wind energy. The wind energy is the fastest growing booming energy source in the world. In order to use the greater extent of the wind energy source, the engineers around the world are working with maximum efforts to rectify the challenges faced while trying to use the valuable renewable energy source of the world. Since early recorded history, people have harnessed the energy of the wind. Wind energy propelled boats along the Nile River as early as 5000 B.C. By 200B.C, simple windmills in china were pumping water, while vertical- axis windmill with woven reed sail were grinding grain in Persia and the Middle East (Lowa Energy Center, 2016). In recent years, wind energy has drawn more attention due to the increasing prices of fossil fuels and improving economic competitiveness of wind turbines relative to conventional generation technologies. Today, wind energy has been developed into a mature, competitive, and virtually pollution-free technology. Usually a typical large, utility scale

142

wind turbine can produce 1.5 to 4.0 million kWh annually and operates 70-85% of the time (Balat, 2009). Global wind energy production set a new record in 2011, reaching 239 GW, 3% of total electricity production (WWEA, 2012). It is predicted that by 2020 it will increase to 10% of global electricity production (Compositesworld, 2012). The wind turbine structures are designed to covert the wind energy into electricity or other forms of energy. A windmill for generating electricity is characterized by the blade which is attached to the hub, via a shaft and gearbox, the generator and the tower structure. The blades convert the wind energy into rotary mechanical movement, the wind is slow and therefore a gearbox is used to increase the rotary motion of the shaft to that of the generator. The components of windmill structure (see figure 1).
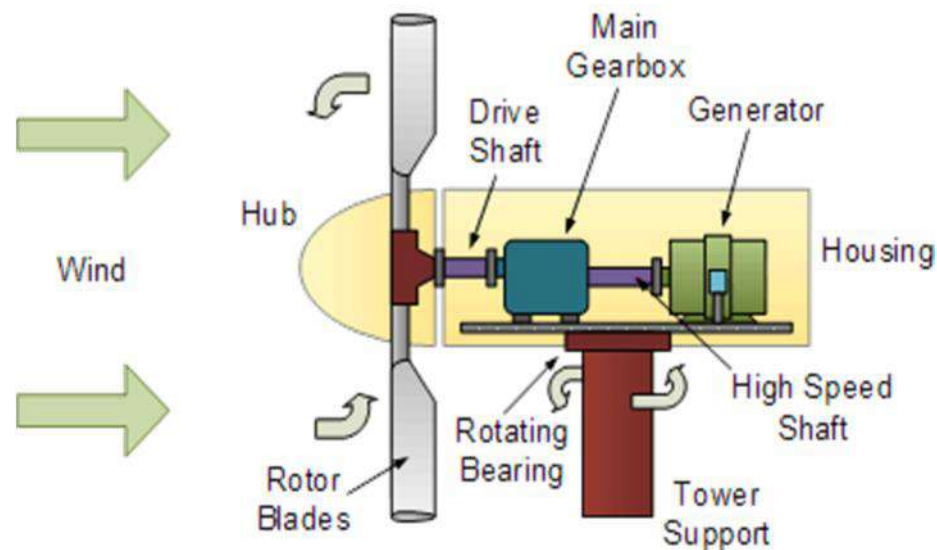
Figure 1: Components of the Windmill.

For efficient harvest of wind energy resources, the blades are required to be long and slender but also fixed at one-end. Thus functional requirement for a wind turbine blades create room for vibration of the blade structure. One of the efforts of vibration on engineering structures such as wind turbine blades is instability, which will lead to decrease in blade performance and eventual failure of the blade. (Ali & Velraj, 2013). For a wind turbine the wind impact a fatigue load on wind turbine structure such as the blade, therefore the blade must be design to sustain the continuous vibration forces and therefore work within an imputable stability limit. Three factor that affects wind turbine losses, i.e. the gear box which account for about 1% loss, the generator which account for 10% loss and the wind turbine blades which account for the rest losses. This huge loss in wind turbine performance is due to the blades performance itself, i.e. is structural geometry. The expected lifetime for a blade is usually 20 years for large wind turbines, and less than 20 years for small wind turbines (Clausen, 2000). In the wind turbine industry, many materials have been used for blades, including metals, plastics, wood and composites (Mandell, 2003).Many researchers have studies the wind turbine blade performance base on its stability and vibration, (Cacciola, 2012) and (Hernandez, 2008).

2.0 MATERIALS AND METHOD

2.1 Materials

The experimental design, experimentation and method of data analysis adopted in this research. First, a blade shape was chosen and produced from three different materials and installed on a mini HAWT for experimentation. Then, the stability analysis was performed on the experimental data obtained. Also, a 3D model of the blades of different materials at three different angles was produced and a solidworks simulation was performed on them. The equipment used for the experiment is fan, wind Anemometer and measuring device.

The materials, components and their specification used in this research are listed in table1

Table 1: Materials

S/ No	Components	Material	Specification
1	Blades`	PVC, AL-alloy, wood	(300×30)mm
2	Hub	Aluminum	(30mm)diameter/40mm
3	Turbine tower and base	PVC	250mmx4, 600mm

2.2 Study Location

The wind turbine performance is dependent on the turbine site characteristics such as high average wind speed, sufficient separation from noise-sensitive neighbor, good site access and landscape designation. The site for this experimentation is school of infrastructure, process engineering and technology,(sipet) federal university of technology, Minna. And the site characteristics are presented in table 2.

Table 2: show the site characteristic

S/No	Characteristics	Values	Remarks
1.	Average wind speed	4.3 m/s	Good
2	Noise separation	200m	Poor
3.	Good site access	20m	Very Good
4.	Landscape designation	Nill	Moderate

2.3 Blade Design

The following steps were adopted for the design:

1. The power output, $P = c_p (1/2)\rho\pi R2V3$ (Ajay, 2018)
2. Choose the suitable tip speed ratio. Normally $4<\lambda<10$ can be used for power generation
3. Determine the number of blades, B such that the structural dynamic problems should reduce. The table 3 shows the required number of blades of the rotor with appropriate tip speed ratio.

Table 3 λ and number of blade (Ajay, 2018)

B	λ
8-24	1
6-12	2
3-6	3
3-4	4
1-3	>4

2.3.1 Determination of The Swept Area

The blade swept area determine the blade radius and it is directly related with the wind turbine power generated and the density of air and the mean wind speed as shown in equation 1.

$$P = \frac{1}{2}\rho Av^3 \quad \text{(Boateng, 2014)} \tag{1}$$

But, the swept area is given as follows;

$$A = R^2, \tag{2}$$

Therefore, the power becomes;

$$P = \frac{1}{2}\rho\ R^2v^3 \tag{3}$$

Where; A = swept area
v= mean wind speed
P= power coefficient
= density of air (1.23 kg/m^3)

2.3.2 Determination of The Tip Speed Ratio

The design tip speed proportion is characterized as the connection between rotor cutting edge speed and the wind speed,

$$= \frac{\omega R}{v} \tag{4}$$

Where; = design tip speed ratio
r = radius at each stations of the blade
w = wind velocity $= \frac{v}{R}$ (rad/s)

145

3. Experimental Design

The objectives of this experimental design are to determine the stability limit of wind turbine blade material and at what blade angle does this limit is just enough. The factors under consideration are blade materials, wind speed, blade angle and the response is the amplitude of deflections of the blade. (See table 4).

Table 4: List of experimentation and their levels

Levels	Factor 1 (Materials)	Factor 2 (angle)	Factor 3 (speed)
1	Wood (M1)	5° (A1)	2m/s (S1)
2	Plastics (M2)	10°(A2)	4m/s (S2)
3	Al-alloy (M3)	15° (A3)	6m/s (S3)

Figure 2: pictorial view of the mini-HAWT

3.0 Experimental Procedure

The experimental station was set up as shown in figure 2 to provide an easily reproducible method of testing how the stability limit of wind turbine blade referring with the materials and the angle of inclination of the blades. The base of the turbine was secured to the table using tape; and the fan was positioned directly in front of the turbine, making sure that the turbine blades were fully immersed in air flow from the fan. In order to vary the wind speed, the fan was moved away from the turbine from 1m to 3m, using 1m as increment. The wind speed produced under the low, medium and high settings were measured at each position respectively, using digital wind anemometer and the amplitude of vibration (deflection) was measured with the aid of a vibration sensor and control unit. The front face of the fan and the turbine were set upward in the vertical plane. Thus air blown by the fan moved in the horizontal direction and when strong enough it caused the turbine blades to spin about the horizontal axis of the turbine. The angle of inclination of the blade was successively set to 5°, 10°, and 15°. At each angle tests were run using each of the three materials of the blades, as shown in figure 3.

a

b
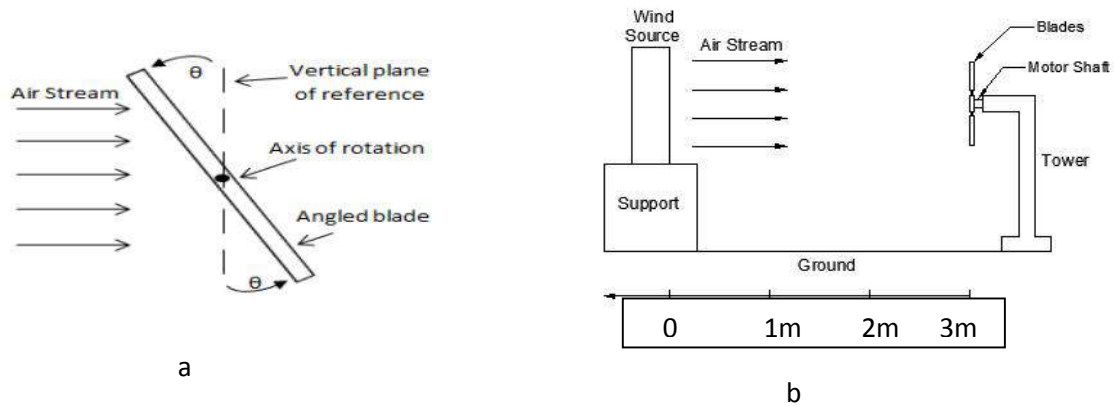
Figure 3.Experimental setup.

4.0 Results and Discussions
4.1 Experimental results

Table 5: Design results of the experiment.

S/No	DESIGN PARAMETER	VALUE
1	Power output(W)	10watt
2	Design tip speed ratio	1
3	Number of blade	3
4	Blade swept area	271 300mm
5	Blade length	300mm

In all cases tested, the data collected indicated that the maximum deflections of turbine with PVC blade produced highest deflection of 11.41mm at average wind speed of 4m/s with an angle of $10°$, its shows that a maximum deflection 11.41mm, which is equivalent to 3.8% of the blade length. The blade is stable because this is less than 5% of the blade length. The Al-alloy blade and wood blade produced 1.6% each which makes them more stable. The Al-alloy blade also produced the minimum deflection of 0.0006293mm with low wind speed of 2m/s at angle of $5°$. The wood blade and Al-alloy blade produced the same deflections 0.01879mm at high wind speed of 6m/s with the same angle of inclination $15°$. However, as the angles increased, the deflection produced by the Al-alloy blade increased. The wood is similarly to that of Al-alloy but the PVC deflections increases at $10°$, and decreases at $15°$.

4.2 Solidworks simulation result

The wind turbine blades were subjected to a static analysis with the experimental wind speed and angles. The results shows that the fixed end of the blades were subjected to different stresses, while the yield strength of the plastic used is 54MN/mm^2 wood 120MN/mm^2 and Al-alloy 324MN/mm^2. Figure 4 is displacement results of the PVC blade with a maximum deflection of 7.702e-002mm. Figure 5 and 6 are the displacement results of Al-alloy and wood blade at equal wind speed and angle(15˚), shows that the same maximum deflections of 2.506e-003mm were obtained. The Al-alloy and wood look more stable than the PVC.

The general shape of the plot of the deflection versus the angle of inclination is shown in Figure 7. A hypothetical line has been added to the plot, in order to represent the general form of the curve that would have been expected, the Al-alloy exhibits a linear relationship because is Isotropic in nature. While the wood and PVC exhibited a non-linear relationship because they are Anisotropic in nature.
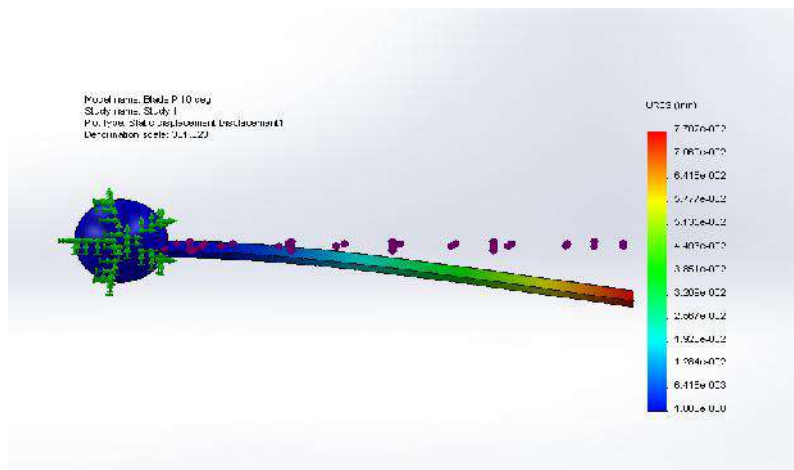
Figure 4: Static displacement of PVC blade at 10˚
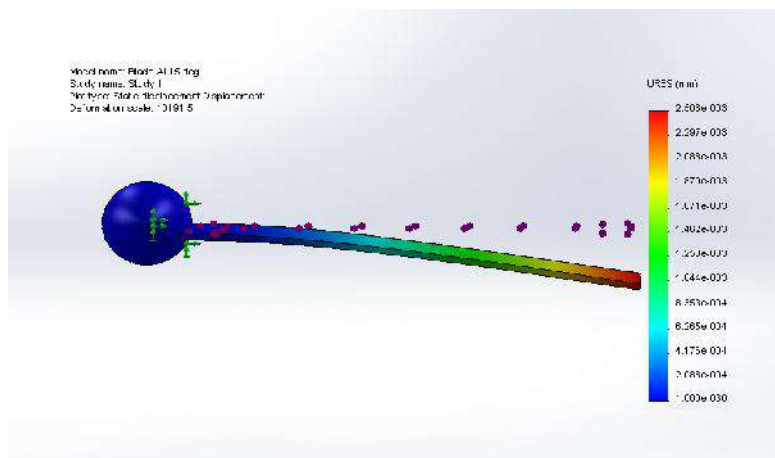
Figure 5: Static displacement of Al-alloy blade at 15˚
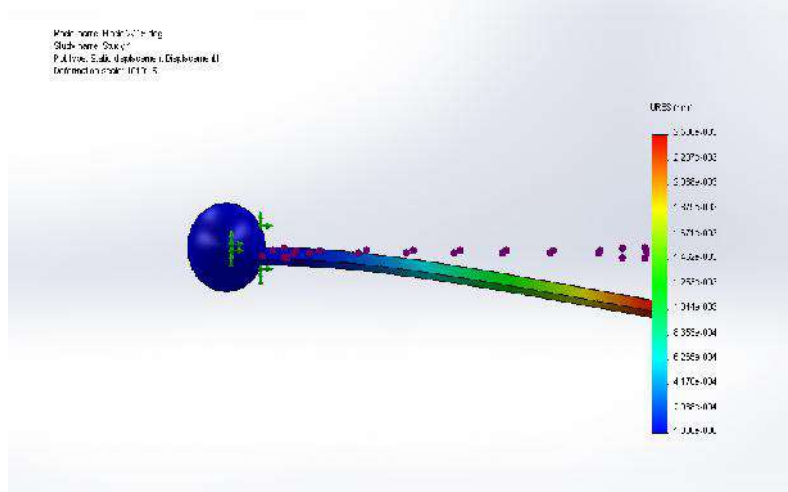
Figure 6 Static displacement of wood blade at 15°
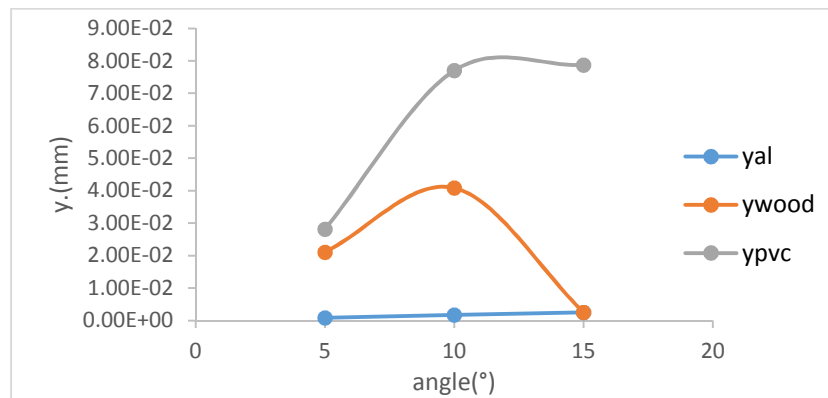
Figure 7 Graphical presentation of deflection of Al-alloy, wood and PVC blade.

5.0 Conclusion

The following conclusion can be drawn from the result obtained;

1. Fabricated blades from Al-alloy, wood and PVC were installed in a mini wind turbine hub at respective angles and were successfully tested based on experimental procedure and equipment. The testing demonstrated show that deflection produced by each blade material varied with the speed of the wind and the angle of inclination of the turbine blades. However, as the angles increased, the deflection produced by the Al-alloy blade and wood blade increased. While the PVC deflections increases at 10°, and decreases at 15°.
2. The stability limit of the turbine blades is estimated from experimental performed in deterministic conditions at discrete steps in wind speeds and angles. The stability limit is easily identified by percentages of the maximum deflections of the blades.
3. These findings support and confirm similar results that were obtained from simulation on solidworks .The Solidworks simulations computed shows the same as the deflections of

149

Al-alloy and wood increases as the wind speed and angle increases, while the PVC produced the maximum deflection at 10°. This review has also shown that Al-alloy and wood maintain the same maximum deflections of 2.506e-003mm at an angle of 15°, although in the experiment test the frequency was underestimated.

4. Detailed flow fields and frequency mode were also investigated using the Solidworks simulations. The good agreement between the deflections computed by the Solidworks package and the experimental data has been used in the validation process where it indicates that the research can be used to estimate the stability limit of a wind turbine blade.

References

1. Ali, M. A., & Velraj, R. (2013). Effect of the Tilt Angle on the Wind Turbine Performance and Wakes . 8th Asia-Pacific Conference on Wind Engineering Chennai, India: Research Publishing, Singapore. (pp. 10-14).
2. Balat, A. (2009). A Review of Mordern Wind Turbine.
3. Boateng, B. (2014). Design and Manufacturing of a one meter wind turbine blade using bamboo. Ghana: Kwame Nkrumah University of Science and Technology.
4. Cacciola, S. (2012). Wind Turbine System Identification and Stability Analysis.
5. Clausen, P. W. (2000). Recent Advances Small wind Turbine Technology. vol.24, No.3, pp. 2000 pp189-201.
6. Compositesworld. (2012). The Market Renewable Energy. Retrieved march 19, 2017, from http://www.compositesworld.com/article/the-markets-renewable-energy-2012
7. Gabriel G. M Hernandez, J. a. (2008). Stability Analysis for a Wind Turbine Blade. 12th Ercoftac NPC. Stockholm : Technical University Denmark.
8. Lowa Energy Center. (2016). History of wind energy. (K. project, Producer, & Wind Energy Foundation) Retrieved february 12, 2017, from http://www.windenergyfoundation.org/about-wind-energy/history.
9. Mandell, J. L. (2003). New Fatigue Data for Wind Turbine Blade Material. Journal of Solar Energy Engineering, vol. 125, pp 506-514.
10. Song, Q. (2012). Design Fabrication, and Test of a New Small Wind Turbine Blade. Ontario, Canada: university of Guelph.
11. Ajay, D. B. (2018). A Review on Fabrication and Performance Evaluation of Small Wind Turbine Blades. International Journal of Mechanical Engineering and Technology., pp 240- 265.
12. WWEA. (2012). World Wind Energy Association. Retrieved march 15, 2018, from htt://www.wwindea.org/home/idex.php?option=com_content&task=view&id=345&Itemid=43.

INVESTIGATION OF PHYSICOCHEMICAL PROPERTIES OF OIL BLENDS OF CITRULLUS LANATUS (MELON SEED) AND ARACHIS HYPOGEA (GROUNDNUT) FOR MACHINE OPERATIONS

[1]Sadiq Sius Lawal, [2]Mohammed Mustapha, [3]R.I. Olalekan, [4]Alkali Babawuya

[1,2,3]Department of Mechanical Engineering, Federal University of Technology Minna, Niger State

[4]Department of Mechatronics Engineering, Federal University of Technology Minna, Niger State

Corresponding E-mail: sadiq.lawal@futminna.edu.ng+2348054197676 and 07064358815

Abstract

This work focuses on the physicochemical properties of blended vegetable oil (a case study of melon seed oil and groundnut oil) and it applications as cutting fluid. The oils were blended at ratios 20:80, 40:60, 60:40, and 80:20 to obtain a suitable blending ratio. Citrullus Lanatus (melon seed) oil was blended with Arachis hypogea (groundnut) oil in different ratios stated above in order to study both the chemical and physical properties of the oil respectively. The physical properties were pour point, flash point, density, thermal stability, cloud point, specific gravity and viscosity while the chemical properties were, saponification value, acid value, iodine value and Hydrogen Peroxide value. The results obtained show that the blended vegetable oils can be used as cutting fluid in machining and other engineering operations.

Keywords: Melon seed oil, groundnut oil, Oil blends, Physiochemical, properties.

1.0 INTRODUCTION

The effectiveness of mineral oil based stock have been questioned lately due to the several negative effects they have caused in the environment and to workers' health (Norby, 2003). When inappropriately discharged, it's likely to cause damage to soil and water resources resulting to serious environmental disaster. One of the most popular vegetable crops grown in Africa is Melon botanically called Citrullus vulgaris or lanatus. It belongs to the cucumber family, from which oil can be extracted and is popularly called "Egusi" a name widely used throughout Nigeria and other West Africa. The crop grows on a sandy free draining soil and can be planted as an intercrop with maize, okra and cassava or yam because of its ability to suppress weed. It is often harvested between two and half to three months and with good management, there can be up to 350-400 kg per hectare as the seeds yielding. Analysis made on melon seed indicated that melon seed consist about 50% oil by weight, 37.4% of protein, 2.6% fibre, 3.6% ash and 6.4% moisture content of the seed, 50% is made of unsaturated fatty acids, which are Linoleic (35%) and oleic (15%) and 50% saturated fatty acids, which are stearic and palmitic acids. The presence of unsaturated fatty acid makes melon nutritionally desirable and suggests a possible hypo cholestroleric effect (lowering of blood cholesterol). Melon has an amino acid profile that compares favourably with that of soya beans as reported by Akoh and Nwosu,1920. Also melon is rich source of Sodium (Na), Iron (Fe), Manganese (Mn), Copper (cu), Zinc (Zn) and fat. The nutritional value for melon per 100g are : Carbohydrate - 7.6g, Dietary fibre - 0.4g, Fat - 0.2g, Protein - 0.6g, and Vitamin C - 8mg. The oil extracted from it can be used in manufacturing of margarine, shortening and cooking oils, while the residual cake is a useful source of protein for livestock feed. The three categories in base oils

are mineral oils, synthetic oils and vegetable oils. Traditionally, it was reported by Yunus, et al, 2006 that over 85% of base oils are refined from crude petroleum.

Groundnut oil on the other hand has sweet and flavourful edible oil. It is also called peanut oil or arachis oil and is extracted from Arachis hypogea with a mild-tasting vegetable oil derived from peanuts. The oil is available with a strong groundnut flavor and aroma, analogous to sesame oil. It is often used in Chinese, South Asian and Southeast Asian cuisine, both for general cooking, and in the case of roasted oil, for added flavor. Groundnut oil has a high smoke point relative to many other cooking oils, so is commonly used for frying foods. Its major component fatty acids are oleic acid (46.8% as olein), linoleic acid (33.4% as linolein), and palmitic acid (10.0% as palmitin). The oil also contains some stearic acid, arachidic acid, behenic acid, lignoceric acid and other fatty acids. Antioxidants such as vitamin E are sometimes added to improve the shelf life of the oil.

1.1 Uses of Groundnut Oil (Arachis hypogea oil)

Groundnut oil is the oil from the seed, also called the nut, of the peanut plant. Groundnut oil is used to make medicine. It is used to make so many of everyday house-hold products that includes; cosmetics, food, medicine, fuel, and industrial products.

2.0 MATERIALS AND METHODS

The major raw material in this work is Citrullus Lanatus oil (melon seed oil) and Arachis hypogea oil (groundnut oil) which were extracted from their seeds through the use of oil extracting machine (seed oil expeller) carried out in the Agricultural and Bio-resources Engineering laboratory of the Federal University of Technology, Minna, Niger State. These oils can also be extracted through the local or traditional method of heating the grinded seed. The oils were extracted using a seed oil expeller to prevent pre-heating of the oils which they experience while making use of the local or traditional method. The seeds were purchased in a local market in Minna, Niger State. Analytically graded reagents like Sodium hydroxide and Methanol (99 % purity, 78.1 C) was used in the study.

2.1 Determination of Acidic value

A neutral solvent was prepared by mixing petroleum ether and methanol. A quantity of about 1grams of the oil was measured and placed in a beaker on which 5ml of the neutral solvent was added. The mixture was thoroughly stirred for about 30 minutes while 0.56grams of sodium hydroxide pellet was measured and used to prepare 0.1M NaOH. Some 4 drops of Phenolphthalein indicator was added to the oil/neutral solvent in the beaker and titrated against 0.1 M NaOH until end point was reached (ASTM D 664). The acid value was calculated from the relation:

$$\text{Acid value (mgNaOH/g)} = \frac{56.11 \times V \times N}{W} \qquad\qquad 1$$

Where V is volume of standard alkali (NaOH) in ml, N is normality of standard alkali used and W is weight of oil used in grams.

2.2 Determination of Free Fatty Acid (FFA) value

According to Gregory (2005), the acid value obtained was subsequently used to determine the free fatty acid and this was defined as:

$$\text{Acid value} = \text{free fatty acid}/2 \qquad\qquad 2$$

Therefore,

$$\text{Free Fatty Acid value} \left(\frac{mgNaOH}{g}\right) \text{Acid value} \times 2 \qquad\qquad 3$$

2.3 Determination of Specific gravity

Following the ASTM D1298 method, Volume of oil is assumed to be 25ml. Weight of empty bottle is 22.712 and weight of bottle + water is 43.485. The empty calibrated bottle was filled with blended vegetable oil and reweighed; Specific gravity was calculated using the relation:

$$\text{Specific Gravity} = \frac{\text{Weight of Xml of Oil}}{\text{Weight of Xml of Water}} \qquad\qquad 4$$

2.4 Determination of Density

The density of a substance is defined as the ratio of the mass of the substance to unit volume of that substance. Density could also be described as volumetric weight of a substance and it describes the weight of the substance as given below.

$$\text{Density} = \frac{\text{Weight of substance}}{\text{Volume of substance}} \text{(g/ml)} \qquad\qquad 5$$

2.5 Determination of Viscosity at 40 ^{0}C to 120 ^{o}C

The viscosity of the blended oil sample was determined using an empty bottle on a viscometer. The samples of the blended oil as carried out by Giwa et al, 2013 were raised to a temperature of 40 C and 120 ^{0}C respectively. The viscometer was calibrated 1cm apart while the oil sample was then poured into the viscometer. At the time which the oil starts dropping into the beaker or conical flask the stop watch is started. The time, at which a specific distance of about 1cm is attained, the stop watch is stop and the time interval is taken or recorded. The procedure was repeated for about two to three times and the average value was taken (ASTM D-445).

The Kinematic viscosity was calculated from this relation:
$$V = C \times t \qquad\qquad 6$$
Where V is Kinematic viscosity (mm^2/s), t is Mean flow time (s) and C is Calibration constant of the viscosity (mm^2/s)/s.

2.6 Iodine value Determination:

The Blended oil sample was poured into beaker along with 1grams of the oil poured into a glass-stopper bottle of about 250ml capacities. A sample Carbon tetrachloride (10ml) was then added to the oil to dissolve. Subsequently, 20ml of solution was added and allowed to stay in the dark for 30 minutes. Nearly 15 ml of potassium iodide solution (KI) with 10 percentage by Weight and 100 ml of water was introduced and the mixture thoroughly mixed. The mixture was titrated with 0.1 M sodium thiosulphate solution (Na$_2$SO$_3$) using starch as indicator .A blank is carried out at the same time starting with 10 ml of carbon tetrachloride.

$$\text{Iodine value} = \frac{(Vb-Va) \times 1.269}{\text{Weight of egusi melon oil sample}} \qquad\qquad 7$$

2.7 Determination of Pour point:

The pour point is a main feature of low-temperature interactions. It is a pointer of the fluid's capability to flow at colder operational temperature. Pour point is the lowest temperature at which fluid will flow when damped below approved conditions. This temperature is known as pour point (PP) and is described as the lowest temperature at which progress of the specimen is observed. Pour point values have conventionally been determined when the sample no longer shifts on tilting the tube enclosing the sample (pour point). Pour point less than 0^0C are regarded to below (Arbain and Salimon 2009).

2.8 Determination of Flash point:

The flash point is the lowest temperature at which a liquid generates adequate concentration of vapour beyond where it will develop a flammable mixture with air. Most vegetable oils with a low flash point are greater fire hazard. The flash point is adequately great to tolerate reliable process and lower volatilization at the highest operating temperature. For the highly challenging operations, which include aviation jet engine fuel, an efficient liquid extent greater than 300°C might be essential (Gerpen and Shanks, 2004). The lesser the flash point, the comfortable it is to kindle the material. It is very important to test the flash point of the oil to be used as fuel.

2.9 Determination of saponification value

A gram of the oil was weighed into a flask. Twenty five cm^3 of 0.1M alcoholic sodium hydroxide solution was added into the flask. A reflux condenser was attached and the flask was heated on a water bath for one hour while constantly shaking it. At the end of 1 hour,the flask was removed from the water bath and 1 cm^3 of about 1% phenolphthalein indicator was added. It was then titrated with the standard 0.5M hydrochloric acid.

$$\text{Saponification value} = \frac{(Vb-Va) \times 26.05}{\text{Weight of oil}} \, (\text{mgKOH/g}) \qquad\qquad 8$$

8

Where Va is sample titre value (cm^3), and Vb is blank titre value (cm^3), AOAC, (1990).

2.10 Determination of Peroxide Value

About a gram of the oil was weighed into a clean dry boiling tube and 1g of powdered potassium iodide and $10cm^3$ of the solvent mixture were added. The mixture was allowed to boil vigorously for 30 seconds. The tube was washed twice with $25cm^3$ portions of water and the washings were added to the titration flask. With 0.002M sodium thiosulphate using starch indicator, the mixture was titrated.

The relation for peroxide value is given as;

$$Peroxide\ value = \frac{(Vb-Va)\ \times molarity\ of\ titrant}{Weight\ of\ oil}(mgKOH/g) \qquad\qquad 9$$

Where;
Va = sample titre value (cm^3),
Vb = blank titre value (cm^3)
.

2.11 Cloud Point

Cloud Point of oil is the temperature at which the oil begins to cloud and no longer gets completely soluble so as to determine its physical resistance towards lower temperature. Cloud point is very useful in identifying the minimum temperature of oil storage (Roiaini et al,2014).

2.12 Determination of thermal stability:

The thermal stability of the blended oil was determined in accordance to the American Society of Testing Materials (ASTM).The thermal stability was determined by dipping 40ml stainless steel viscometer rotor in a beaker containing the heated blend oil and the rotor was set to a revolution of 60rpm.

3.0 Results and Discussion

3.1 Presentation of Results

Table 1: The table below shows the properties obtained for the various percentage oil blends

PROPERTIES PERCENTAGE OIL BLENDS				
	20:80	**40:60**	**60:40**	**80:20**
Acid value (mgNaOH/g)	1.122	2.244	2.806	3.367
Free Fatty Acid (mgNaOH/g)	2.244	4.488	5.612	6.734
Specific gravity(g)	41.150	41.376	41.438	41.575
Density (g/mL)	1.646	1.655	1.658	1.663

Viscosity 40^{0}C	23.30	21.40	18.40	16.30
Viscosity 120^{0}C	5.30	4.50	3.90	3.60
Iodine value (mgKOH/g)	192	119	139	117
Pour point (^{0}C)	-1	-2	-3	-4
Cloud point (^{0}C)	14	13	13	9
Flash point (^{0}C)	174	168	192	204
Saponification value(mgKOH/g)	121	107	118	177
Hydrogen peroxide (mgKOH/g)	3.98	4.29	4.17	4.49

3.2 Discussion

Based on the analysis obtained, the physiochemical properties of oil 60%:40% provides a suitable results for use as a cutting fluid in machining operations with the following results: acidic value (2.806mgNaOH/g), free acid value (5.612mgNaOH/g), specific gravity (41.438g), density (1.658g/mL), viscosity at 40^{0}C (18.40pa.s), viscosity at 120^{0}C (3.90pa.s), iodine value (139 mgKOH/g), pour point (–3^0), flash point (192^{0}C), saponification value (118 mgKOH/g), Hydrogen peroxide value (4.17 mgKOH/g) and cloud point (13^{0}C). The thermal stability of this ratio is also appreciable for cutting fluid. The blends also correspond with the physicochemical properties of SAE 35. The physicochemical properties also confirmed the quality of the extracted oil for cooking and industrial potentials such as cutting fluid and lubricating fluid. Hence blending is a good choice for manufacturing oils of good quality and characteristics for the various applications. The physical, chemical, and functional properties of groundnut that relate to specific end products have to been determined and refined to facilitate screening breeding material for such properties. With these desirable physicochemical properties, blending of traditional oils with this nonconventional oil is a good choice by manufacturers. The food value of the oils and blends can also be predetermined to provide the safest food for consumers.

4.0 Conclusion

The oil samples have been investigated and physicochemical properties of this oil suggest they are within the requirements of cutting fluids as well as any other oil. It impact on the environment and health of those who handle them all along the production chain, until their final disposal makes it appreciable for machines operations. They safe safety handling while used as lubricant, non-toxic nature to human population and in the event of oil spills do not put at risk the environment like forest, water bodies and areas of agricultural activities. These reason, influenced the demand to development of novel formulation of blends with significantly increased biodegrading rate compared to those obtained from mineral source is necessary as this study have shown.

References

1.   Akoh, C.C, and Nwosu C.V (1920: Fatty acid composition of Melon seed oil Lipids and Phospholipids, J.Am. Oil Chem. Soc.,69 pp. 314-317

2.   Arbain N., and Salimon J., (2009).Synthesis and Characterization of ester trimethylolpropane based jastropha curcas oil as biolubricant base stock.Joutnal of Science and Technology,47-59

3.   Gerpen, V.J., Shanks, B. (2004) Biodiesel Production Technology, National Renewable Energy Laboratory, Colorado.

4.   Giwa S., Luqman, C.A., and Nor, M.A., (2013). Transesterification reaction optimization and evaluation of biodiesel produced from seed oil of Citrullus Colocynthis L. AIE Vol. 1, Pp. 1 – 9

5.   Gregory I., Onwuka (2005). Food Analysis and Instrumentation: Theory and Practice. Naphthali Prints, Surulere, Lagos, Nigeria, pp. 100 – 108

6.   Norby, T. Environmentally adopted lubricants-Where are Opportunities? Statoil Lubricants R & D, 2003.

7.   Roiaini M., Ardiannie T., and Norhayati H., (2014), Physiocochemical Properties of Conola Oil,Olive Oil and Palm Olein Blends, International Food Research Journal 22(3):1227-1233.

8.   Yunus A.,Cengel B., and Michael A. (2006). Thermodynamics: An Engineering approach. 5ᵗʰ Ed. McGrawl – Hill College, Boston, pp. 1 – 3

ASSESSMENT OF HYDRO-ELECTRIC-POWER POTENTIAL IN NIGERIA

A. K. E. Bako[1], J. Y. Jiya[1], A. Nasir[1] and H. T. Abdulkarim[2]

[1]Department of Mechanical Engineering, Federal University of Technology, Minna
[2]Department of Electrical/Electronic Technology, College of Education, Minna

Abstract

Nigeria is blessed with many human and natural resources; hence there is the need to harness these resources to meet human and national needs. The paper reviews the hydro power potentials in Nigeria, the current status and investment opportunities. Renewable Energy (RE) remains the cleanest, inexhaustible and most reliable type of energy and this nation is endowed with varieties of this renewable energy resources. This work therefore looks into the availability of Small hydropower (SHP) potentials, which is one of the most readily available renewable energy resources in Nigeria. Nigeria had the potentials of over 277 dispersed small hydro power sites capable of generating electric power of about 734.2 MW out of which only 30MW has been harnessed as at 2005, and the potential as at today is estimated to reach 3,500MW. This of cause is good enough to attract any serious investors considering the overwhelming population of the country as well as the high demands of electricity in all the surrounding villages of the said potential small hydro sites. Nigeria Hydropower sector experienced up to 360% growth within about 35 years (between 1971 and 2005) and yet only about 5% of the SHP potential is tapped by the few plants built between 1923 and 1964. Operating and maintenance costs are in favor of SHP development in the country, being the lowest when compared with the situation in European countries.

Keywords: Hydropower, Power generation, capacity factor, Turbines, falling water

1.0 INTRODUCTION

1.1 The Working Principles of Hydropower

Hydroelectricity is generated by water falling under the force of gravity that turns the blades of a turbine, which is connected to a generator. Electricity generated by the spinning turbine passes through a transformer and out to transmission lines supplying domestic and industrial demands. The principle and the technique for generating electricity from hydropower is the same regardless of the size of the project, and plants can be tailor-made to fit a community, country or an export market. The amount of power that can be generated is dictated by the following:

- The vertical height of water above the turbines, often referred to as the hydraulic head
- The rate of flow through the turbines

Hydropower is an efficient form of energy generation. Typically the efficiency of a modern day hydropower plant in converting potential energy to electrical energy is about 90% (USBR, 2005). The basic principle of Hydropower plants (HPP) is that they convert pressure from water into mechanical power by turbines which then can be utilised to generate electrical energy by generators. A typical schematic diagram of a hydropower scheme is illustrated in Figure 1.
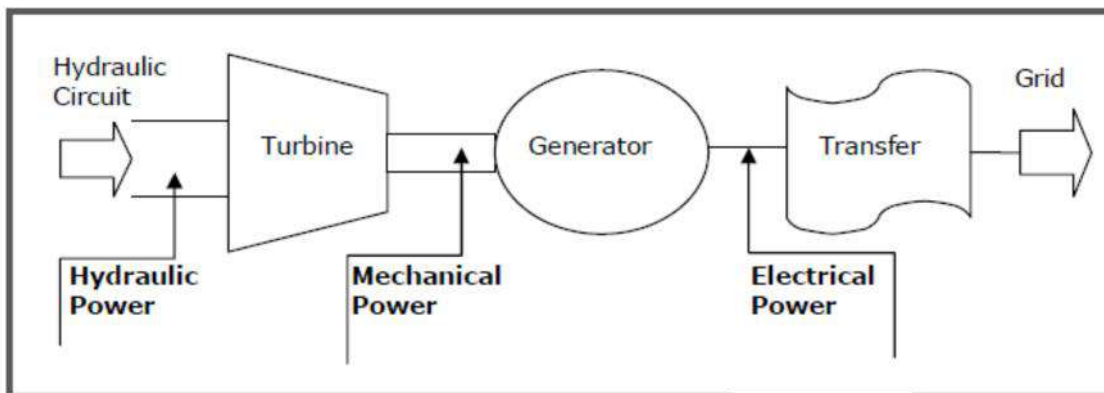
Figure 1: Electrical Power Conversion Scheme (Source: Raja, 2006)

The production of power from a HPP is directly proportional to the head available and the flow of the river. The amount of water (in m^3/s) that flows in a certain amount of time of a cross section of the river is known as the flow of the river. While the vertical difference in the level (in meters) the water falls down is known as the head.

Theoretically;

$$P = Q \times H \times c \qquad\qquad\qquad 1$$

Where: Q = volumetric flow rate in m^3/s
       H = Hydraulic Head in metres
       c = constant and is equal to the product of the density of water and the acceleration due to gravity (g) (Raja, 2006)

If P is measured in Watts, Q in m^3/s and H in meters, the gross power generated due to the flow of water can be calculated as:

$$P = g \times Q \times H \qquad\qquad\qquad 2$$

The hydro turbine converts the hydraulic power available to mechanical power. The generated power is only some fractions of the gross power available because the turbine cannot convert all energy into hydroelectricity due to loss and other mechanical factors. Equation 3 gives the net power practically produced by the HPP (Raja, 2006):

$$P = \quad \times g \times Q \times H \qquad\qquad\qquad 3$$
Where   = efficiency of HPP and
g = acceleration due to gravity

The efficiency of a HPP is always less than 100%; hence, the gross production capacity is always higher than the actual power produced.

1.2 Hydropower Assessment in Nigeria

Nigeria is endowed with abundant natural energy carrier resources including crude oil, natural gas, coal and lignite, tar sand, hydropower (large and small), solar radiation, wind, biomass (fuel wood, animal and plant wastes) and nuclear element deposits. Some of these resources are yet to be exploited while the maximum utilization of others is not in view, thus making energy a major concern and priority in the country. Hence, rapid growth in the energy demand above production. Hydropower was the type in use in Nigeria before the discovery of crude oil. However, there was a shift in attention to fossil fuels due to the vast deposits in the country leading to the decay of the hydropower sector. The result was that the existing hydro plants (Kainji, Jebba and Shiroro) were neglected to the extent that they performed below installed capacity. And yet no interest was shown in building new hydro plants, until recently when the energy situation showed clearly that conventional energy sources had failed the nation in spite of all the fossil based Independent Power Projects licensed as at February 2009 (Jiya et al, 2015)

1.2.1 Kainji Hydropower Plant

The Energy generated capacities of the Kainji HPP from 2004 – 2014 are presented on Table 1 below with the average running hours per year and their corresponding capacity factors.

Table 1: Kainji Energy Generation in MWh and Running Hours from 2004 to 2014

(Jiya et al, 2015)

Year	Actual Energy Generation (MWh)	Energy Used (MWh)	Energy Sent Out (MWh)	Average Running Hours	Capacity Factor
2004	2878774	41749.8	2837024.2	7808.248	0.52
2005	2586929.35	18478.7	2568450.65	7808.248	0.45
2006	2366716.477	6398.307	2360318.17	7304.106	0.43
2007	2816749.4	7068.86	2809680.8	7377.249	0.51
2008	2695223	6334.73	2688889.3	6632.087	0.49
2009	2505663	6818.89	2498844.11	6961.706	0.52
2010	2300991	4960	2296031	6478.8	0.48
2011	1769060	6143.74	1762916.26	5682.557	0.37
2012	1392353	6473.1	1385879.9	6420.172	0.34
2013	935868	5602.22	930265.78	7456.653	0.83
2014	735062	4238.2	730824.79	5389.286	0.25

Average	2089399.021	10387.87	2079011.36	6847.192	0.47
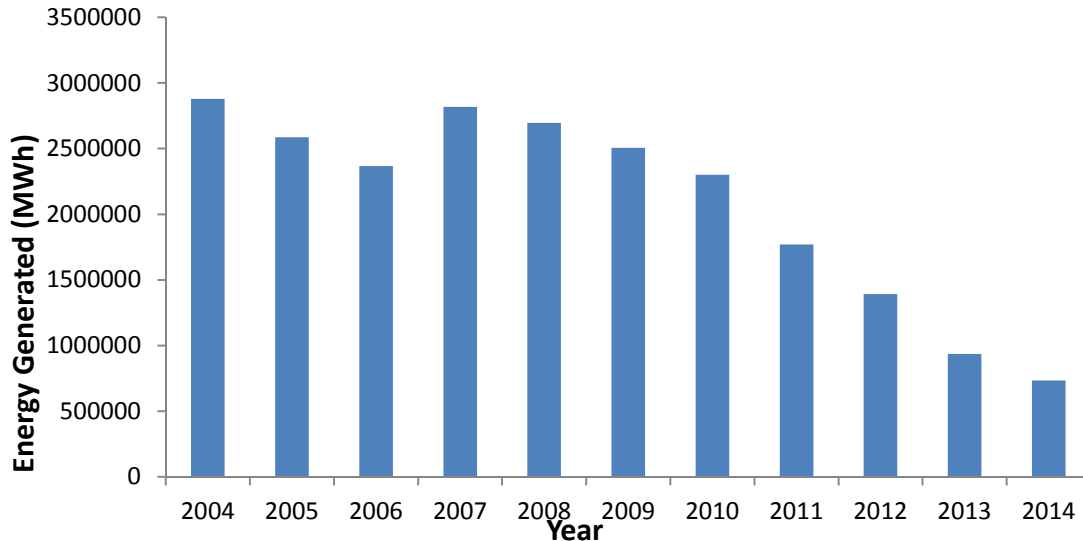
Figure 2: Energy Generated from 2004 – 2014

Figure 2 shows the total energy generation from 2004 -2014, with the highest amount of energy generated in 2004, and the lowest in 2014, this is an indication that there has been a depletion of generation over the years, and emphasizes the need for urgent retrofitting and rehabilitation of the plants. The average generation during the period being considered is 2089399 MWh with average running hours of 6847.192 hours.
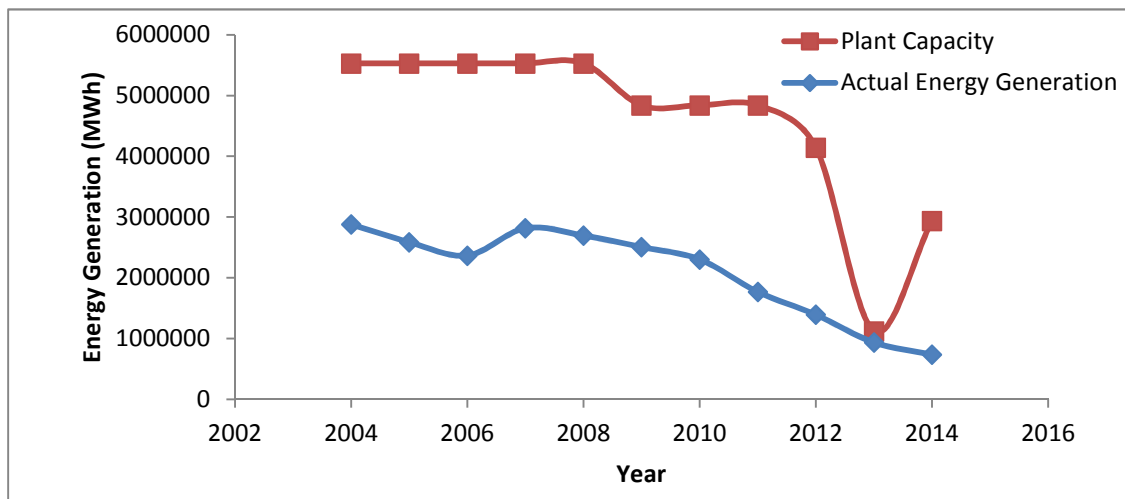
Figure 3: Variation of Actual Energy Generated with Plant Energy Capacity from

2004 – 2014.

Figure 3 reveals the variation of the actual energy generated by Kainji HPP with the installed capacity, from the presentation; it is obvious that the station's operation is below its rated capacity. In the year 2013, only two units were available, unit 1G6 of 120 MW and unit 1G11 of 100 MW capacities. The available energy capacity for that year was 1123200 MWh and there was a recorded generation of 935868 MWh.

1.2.2 Shiroro Hydropower Plant

Table 2 shows the energy generated for Shiroro HPP for the period under study with the running hours and the plant use factor. The full load installed capacity expected from the Shiroro plant is 600 MW, but the capacity generated within this research period is 279.484 MW

Table 2: Shiroro Annual Power Generation Reduction from 2006 to 2014 (Jiya et al, 2015).

| Year	Energy Plant Capacity (P_{ic}, MWh)	Energy Generated Capacity (P_{gc}, MWh)	Energy Generation Reduction (MWh)	Running Hours T_{oh}	Plant Use Factor (PUF)
2006	5256000	2438031	2817969	7024.53	46.30
2007	5256000	1473924	3782076	5844.23	28.04
2008	5256000	1941344.04	3314655.96	6029.17	36.94
2009	5256000	2282098.8	2973901.2	6724.53	43.42
2010	5256000	2905339.2	2350660.8	7844.96	55.28
2011	5256000	2373993	2882007	6087.41	45.17
2012	5256000	2664630	2591370	7539.54	50.70
2013	5256000	2481615.6	2774384.4	7757.17	47.21
2014	5256000	2078005.96	3177994.04	6687.36	39.54
Total	47304000	20638980.6	26665018.4	61538.9	Avg. = 43.63
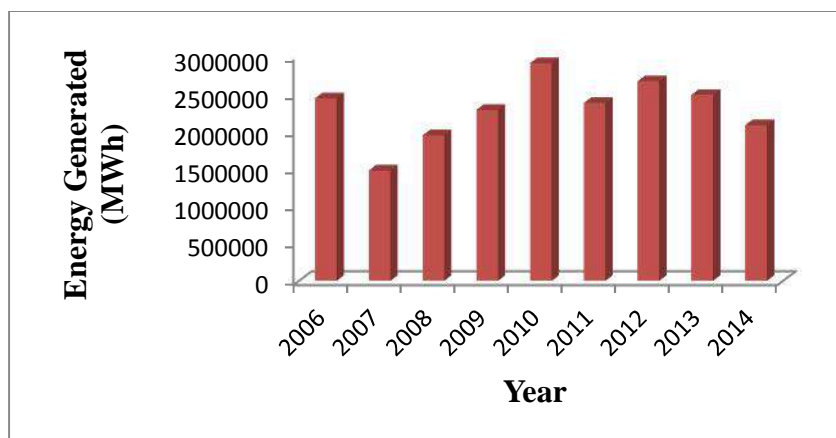
Figure 4: Actual Energy Generated from 2006 – 2014

The actual Energy production for year 2006 to 2014 is shown in Figure 4, year 2010 recorded the highest energy generation of about 2905339.2 MWh, whereas the lowest Energy generation of 1473924 MWh was recorded in 2007.
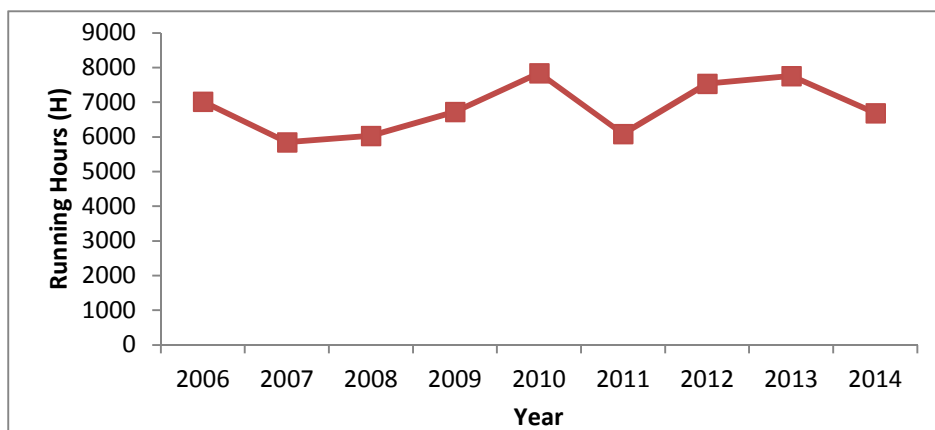
Figure 5: Average Running Hours from 2006 to 2014

The running hours for Shiroro hydropower plant is shown on Figure 5. The highest operating hours was recorded in 2010 which proportionally records the highest energy generation too, whereas 2007 records the lowest operating hours and consequently yields the least energy output.

According to Kela, Usman, & Tijjani, (2012), Energy consumption in Nigeria by type and by total vindicates hydropower as covering up to 23.9% in 2007; it was 14.2% in 2003, the sudden growth from 14.2% to 23.9% between 2003 and 2007 shows that, there is improvement close to 100% within four years. Details as shown in figure 6 below:
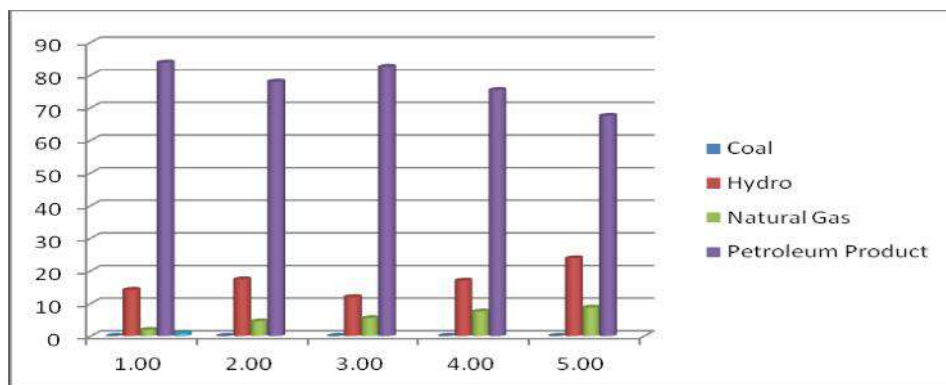
Figure 6: Energy Consumption by Type from 2003 to 2007

2.0   The Current Status of Small Hydropower (SHP) in Nigeria

Nigeria ranked ninth in hydropower potential in Africa with technical hydropower energy at 32,450 GWh/yr. It used 21.5% (6986 GWh/yr) of its potential for the year 2001; the situation in other African countries with respect to the exploitation of their respective hydropower potentials was similar (Kalitsi, 2003). In 1976, Nigeria was divided into 11 river basins through the establishment of River Basin Development Authorities for the purpose of irrigation, water supply,

navigation, hydroelectric power generations, fisheries and recreational facilities, and accomplished through the construction of small, medium and large dams to impound surface waters. Nigeria has a good topography which ranges from lowlands along the coast and in the lower Niger valley to high plateaus and mountains in the north as well as along the eastern border with elevation ranging from 600 m to a 2042 m. Most of the rivers and dams are favored with good elevation for various SHP utilizations. The large hydro power plants comprising Kainji (760 MW), Jebba (570 MW) and Shiroro (600 MW) were constructed on the Kainji and Shiroro Rivers while Mambila, a proposed project on the Benue River, has a capacity above 2600 MW. (Jiya et al, 2015). All of these rivers and dams have several adequate heads for SHP development.

According to Ohunakin et al, (2011), Hydropower has received a renewed interest in recent years although its share in total electricity production shows a decreasing trend when compared with thermal plants (Fig. 7). However, until the proposed 2600 MW Mambilla large hydropower is completed together with the adoption of small hydropower (SHP) plants and technologies, the decreasing trend is expected to continue as water inflow into the Kainji lake which feeds Kainji and Jebba power plants will soon witness a drastic reduction and especially if the dam proposed by Niger Republic on the Niger River is constructed.
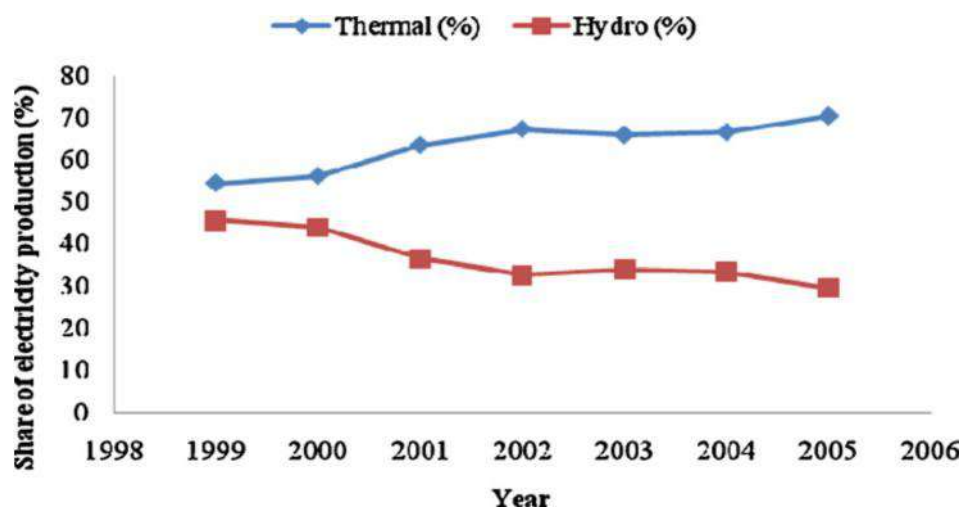
Figure 7: Thermal and hydropower contribution to total electricity production in Nigeria between 1999 and 2005. Source: National Bureau of Statistics (2006).

According to ECN (2006), Nigeria has a gross large hydro potential of 14,750 MW out of which 14% amounting to 1930 MW is harnessed, contributing approximately 30% of total installed grid connected electricity generation. SHP has been in existence in Nigeria since 1923, 45 years before the commissioning of the country's first large hydropower (Kainji). Today, SHP technology is still at its infancy with the schemes operated in only three States of the Federation (ECN, 2006). Unlike in developed countries where SHP plants find broad adoption in electricity production and other applications, little attention is given to its significance in spite of the vast potential and the high energy need in Nigeria. It was also established through a 1980 survey of some States that an SHP potentials of 734 MW is available in 277 sites (Table 3); however, a 2004 estimation indicated a

total SHP capacity of 3500 MW representing 23% of the nation's hydropower potential if the remaining States were surveyed (ECN, 2006).

Table 3: Summary of Small Hydro Potential Sites Nigeria (Source: UNIDO-RC-SHP in Africa, Abuja, 2009)

S/N	State	Potential Sites	Cumulative Power Estimates (MW)
1	Adamawa	3	28.600
2	Akwa Ibom	13	
3	Bauchi	1	0.150
4	Benue	10	1.306
5	Cross River	5	3.000
6	Delta	1	1.000
7	Ebonyi	5	1.399
8	Edo	5	3.828
9	Ekiti	6	1.247
10	Enugu	1	
11	FCT	6	
12	Gombe	2	35.099
13	Imo	71	
14	Kaduna	15	25.001
15	Kano	2	14.010
16	Katsina	11	234.340
17	Kebbi	1	
18	Kogi	2	1.050
19	kwara	4	5.200
20	Nassarawa	3	0.454
21	Niger	11	110.580
22	Ogun	13	15.610

23	Ondo	1	1.300
24	Osun	8	2.622
25	Oyo	3	1.062
26	Plateau	14	89.100
27	Sokoto	1	
28	Taraba	9	134.720
29	Yobe	5	
30	Zamfara	16	

Furthermore, according to Ohunakin et al, (2011), the projected power demand for SHP as shown in Fig. 8 revealed that the country needed 190, 490, 1280 and 3315 MW for 2000, 2010, 2020 and 2030 respectively and yet only 30MW capacity is being harnessed, representing approximately 16% of the 2000 demand indicating a wide disparity and deficiency in supply relative to demand. In view of this, SHP potential is underexploited in Nigeria even though the potential exists to meet the projected 2030 demand, if other sites are fully harnessed.
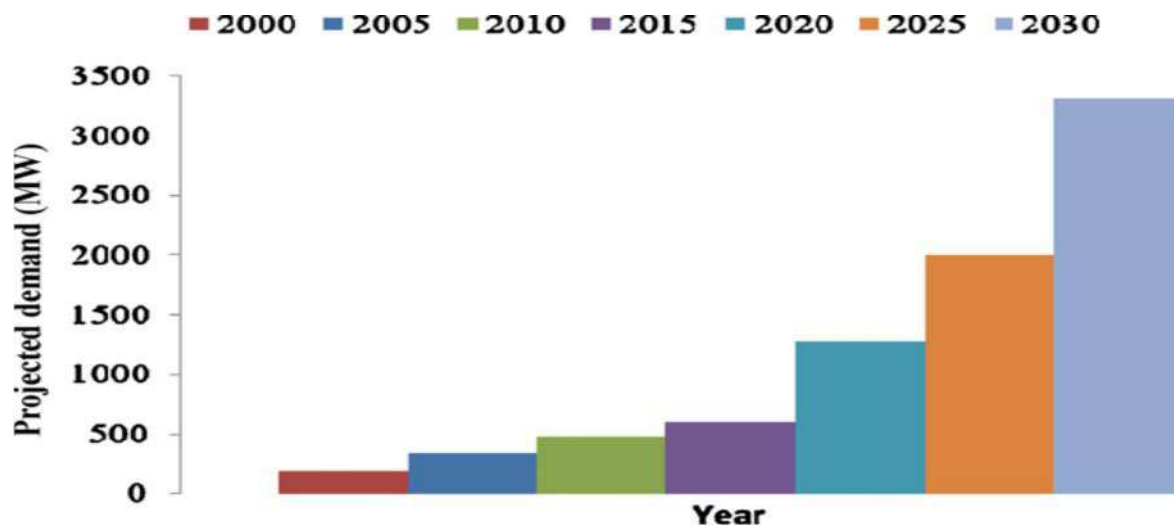
Figure 8. Projected demand of SHP in MW (ECN, 2005)

A study of SHP potential in Nigeria had also being considered for support by African Development Bank, (UNIDO, 2009). According to (Brian and Emma, 2009), UNIDO has concluded two of four designed pilot projects planned to build awareness and generate capacity for micro-hydro power development in Nigeria. The project in Enugu State (30KW capacity) and Bauchi State (150KW) were undertaken through a partnership, with UNIDO providing the equipment and proficiency, and states and local government providing erstwhile logistics and labour in-kind. Power generated from the projects will supply electricity for lighting, agricultural processing and information and communications technology (ICT) for local communities. The projects also provide technical

166

training and energy efficiency responsiveness to ensure the technology is maintained locally and sustainably. Furthermore, the National Agency for Science and Engineering Infrastructure, NASENI is developing capacity in the manufacture of SHP Equipment (NASENI, 2011). With this prospective in SHP, there will be a rising demand for local capacities in the expansion of this technology in the country. In the late 2007, UNIDO brought in NASENI to a Stakeholders summit on the Local Manufacturing of Small Hydro Power Equipment in the African constituency. NASENI has been identified as the Host Agency and the delegate of the Nigerian Government on the mission. Whereas UNIDO awaits Nigeria's complementary subsidy, cross flow turbine has been chosen for the first manufacture involving Nigerian engineers and using domestic technology. In spite of the frameworks put in place to encourage renewable energy investments as in shown in this study, private sector participation has increased only in fossil-based sources rather than in hydropower and other renewable sources. There is still little awareness of the benefits and opportunities of SHP as a power generation source if we compare the quantity exploited with the existing potentials, while at the same time a current and extensive hydrological database is not in existence for prospective investors. So far, private sector participation in renewable energy implementation in the country is in the area of importation and marketing of components (Jiya, et al, 2015).

3.0 Conclusion

The Nigerian Government has taken steps to diversify energy sources in order to promote renewable energy development by encouraging private investments in the energy sector through reforms, but this may not be adequate as there remain barriers against SHP development in the country. SHP has been in existence in Nigeria since 1923, 45 years before the commissioning of the country's first large hydropower (Kainji). Today, SHP technology is still at its infancy with the schemes operated in only three States of the Federation. With full private sector involvement in hydro generation, especially in the form of investment towards the maximum utilization of SHP potential as encouraged by this study, Nigeria's economically feasible hydropower potential is expected to exceed 29,800 GWh/yr.

References

1. Energy Commission of Nigeria (ECN) (2005). Renewable Energy Master Plan (REMP). Abuja; 2005.

2. Brian Shaad and Emma Wilson, (2009). Access to Sustainable Energy. International Institute for Environment and Development (IIED).

3. Jiya, J. Y**.**, Abdulkarim, N., Ogboo, H. U., & Salihu, A. (2015). Performance assessment of hydropower generating plants. 1st International Engineering Conference (IEC) (pp. 321-327). Minna: Federal University of Technology Minna

4. Kalitsi E. A. K. (2003). Problems and Prospects for Hydropower Development in Africa, The Workshop for African Energy Experts on Operationalizing the NGPAD Energy Initiative. 2003.

5. Kela, R., Usman, K. M., & Tijjani, A. (2012). Potentials of Small Hydro Power in Nigeria: The Current Status and Investment Opportunities. International Journal of Scientific & Engineering Research., 3(5).

6. National Agency for Science and Engineering Infrastructure (NASENI), (2011). Small Hydro Power (SHP).

7. National Bureau of Statistics (2006). The Nigerian Statistical Fact Sheets on Economic & Social Development, Federal Republic of Nigeria.

8. Ohunakin, O. S., Ojolo, S. J., & Ajayi, O. O. (2011). Small hydropower (SHP) development in Nigeria: An assessment. Renewable and Sustainable Energy Reviews, 15, 2006-2013.

9. Raja, A. K., Srivastava, A. P. & Dwivedi, M. (2006). Power Plant Engineering. New Delhi: New Age International Ltd.

10. UNIDO, (2009). The Nigerian capacity to host the Regional Centre for SHP, UNIDO Regional Center for Small hydro Power, Abuja, Nigeria.

11. United States Bureau of Reclamation (USBR), (2005). Hydroelectric power. USA.

DEVELOPMENT OF SINGLE SPECIMEN CREEP TESTING MACHINE

[1]B.O Okonkwo,[2]I.C Ugwuoke, [3]O.A Olugboji

[1,2,3] DEPARTMENT OF MECHANICAL ENGINEERING

Federal University of Technology, Minna, Niger State Nigeria
o.obenson@yahoo.com, 08061300249

ABSTRACT

The work intends to provide single specimen creep testing machine for laboratory use. This will enhance selection of appropriate materials for national building/advancement. The method employed involves selection of material, design of components of machine, production of components and assembling of the components. The machine comprises of a lever arm, supported with pivot pin and rest pin on the columns. The effort portion of the lever arm is fixed with load hanger while the load (test) portion is fixed with dial gauge, the ends of specimen were fixed in fixture devices on lever arm and base table at a distance of 90 mm. Development of the machine was based on the application of bending moment (simple supported beam) and equilibrium theory to calculate the forces acting on the specimen and components of the machine which is obtained as $F=(1.596 + 5.99m)g$ Newton. Using solder as specimen, tests were carried out with the machine at room temperature under different loads, concept of strain were obtained. Three stages of creep were achieve, creep constants of solder (m and B) were obtained experimentally as 6.25×10^{-3} and 4.0×10^{-4} respectively. The experiment indicates that at a constant stress 31.13 MPa, the creep rate was obtained as 2.1×10^{-3} /min while at 38.60 Mpa, the creep rate was obtained as 6.2×10^{-3} /min. The results indicate that the creep rate increases at higher stress, the creep working hypothesis were confirmed.

Keywords: Creep Testing, deformation, temperature, melting scale

1.0   INTRODUCTION

Single specimen creep testing machine is use to predict the strength and dimensional changes of materials which occur as a result of constant applied load and temperature over a period of time. Creep is defined as time dependent deformation of material under constant load and temperature. In design of a product, allowances for creep are made based on the reliable experimental data in estimating the service life of the material. It is equally important to be able to extrapolate creep data into regions where creep data are not available. Creep problems are prevalent and need optimum consideration in design of products. In as much as it not easy to eliminate the problem of creep entirely, it is necessary that creep data be made available for any material through scientific research, before such material can be employed in engineering services. Creep can occur at any temperature higher than approximately half the absolute melting point in Kelvin scale. Solder has a melting point of 183 ^{0}C (456 K), so room temperature at 25 ^{0}C (298 K) is more than

169

half the melting point.Therefore creep is expected to occur at room temperature in solder when subject to a sufficient stress,

The objectives of this research includes: To develop a single specimen creep testing machine using locally sourced materials; To demonstrate creep as a phenomenon in metals using solder as specimen; To obtain creep rate of solder and constants using experimental data.

Ishikawa et al, (1997) Studied creep behaviour of high purity aluminum at room temperature, it was found that steady state creep could be observed at room temperature, with the creep rate depending upon the applied stress. Ritu and Rajeev (2014), Performed creep tests on five pieces of 2 mm diameter solder of the same gauge length at different temperature, under constant load (1.5 kg). The results shows that, fastest strain rate occur at the higher temperature (65^0C) while the slowest strain rate occur at room temperature (30^0C). Bunnell, (2007) carried out creep tests at room temperature on five pieces of 3.1 mm inches diameter solder suspended with various weight at lower end of the specimens except one specimen with no added weight on it, the upper end of specimens were hang on a rigid body. The results reveal the following:
   i. Solder creeps at room temperature.
   ii. Strain at failure and time to failure is strongly influenced by applied stress.

2,0   MATERIALS AND METHODS

2.1   Materials

The materials used in this project are:

 i. Mild steel (AISI 1013) for columns, lever arm, table base, pins and fixture devices

 ii. Stainless steel (AISI 302) for load hanger and set of weight
iii. Solder (sn 30%, Pb 70%) for specimen.
iv. Other accessories used includes
   iv.   Thermometer   -   for measuring room temperature.
    v.   Dial gauge   -   for measuring extension.
   vi.   Vernier callipper -   for measuring diameter of specimen.
  vii.   Stop watch   -   for time reading.
 viii.   Pair of scissor   -   for cutting of specimen.
   ix.   Ruler   -   for measuring the length of specimen.

2.1   Systematic Drawing of the Creep Testing Mechanism

Figure 1: Systematic drawing of the creep testing mechanism
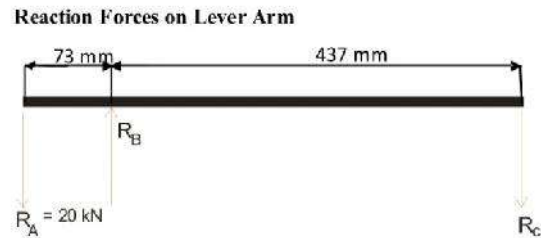
Figure 2: Free body diagram of reaction forces

2.2   Equilibrium conditions

(1) $f_y = 0$ (1)

- $R_A + (-R_C) + R_B = 0$ (2)

- $R_A - R_C + R_B = 0$ (3)

- $(R_A + R_C) = -R_B$ (4)

$20kN + R_C = R_B$ (5)

(2) $M_B = 0$ (6)

$R_C \times 437 = 20 \times 10^3 \times 73$ (7)

$R_C = \dfrac{1460000}{374}$

$R_C = 3.341kN$

$R_C = 3.341kN$:- Maximum reaction on the load hanger

The load at R_C includes the weight of load pan and rod.

Therefore to calculate the reaction at B, equation (5) was applied.

171

$20 \times 10^3 + 3.341$kN $= 23.341$kN, maximum reaction on the column B (R_B).

2.3   Calculation of Forces Acting on Lever Arm and Specimen
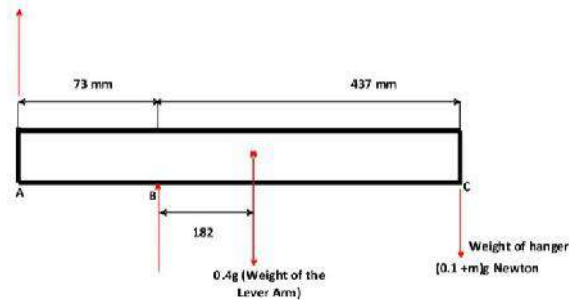
Figure 3: Forces acting on lever arm and specimen.

Applying the theory of equilibrium

$$F_R \times 0.073 = (0.1 + m)0.437g + 0.4g \times 0.182 \tag{8}$$

$$F_R = \frac{g}{0.073}\left((0.1 + m)0.437 + 0.4 \times 0.182\right) \tag{9}$$

$$F_R = \frac{g}{0.073}(0.0437 + 0.437m + 0.0728) \tag{10}$$

$$F_R = \frac{g}{0.073}(0.1165 + 0.437m) \tag{11}$$

$$F_R = (1.596 + 5.99m)g \text{ (Newton)} \tag{12}$$

   m = total mass of the hanger (kg)

   F_R=Resistant force acting on the lever arm at point A

   g = Gravitational pull = (9.8 m/s^2)

   $F = F_R$

   Where F = tensile force acting on the specimen.

2.4   The Developed Single Specimen Creep Testing Machine

Figure 1: Creep Testing Machine

2.5   Experimental Procedure

  i.   Cut four lengths of solder to 120mm each and straighten the specimen with finger strength to remove bends.
 ii.   Measure the diameter (do) of the gauge length of specimen.
iii.   Rise the lever arm up and insert the rest pin in the column.
 iv.   Install the top and bottom end of the specimen in upper and lower fixture device and tighten both ends with finger strength.
  v.   Hang a known mass on the load pin.
 vi.   Measure the gauge length (Lo) of the specimen.
vii.   Adjust the dial gauge to zero and set stop watch to zero too.
viii.   Read and record the room temperature with thermometer.
 ix.   To start the experiment, gently remove the rest pin and immediately, set the stop watch on.
  x.   Record the extension at one minute intervals.
 xi.   Calculate the strain and plot the graph of strain versus time

3.0   Experimental Results

Table 1 Value of time, change in gauge length and strain for 0.25 kg

T (min)	ΔL(mm) Change in length	Strain
0	3.556	0.0395
1	4.318	0.0479
2	6.477	0.0719
3	7.874	0.0875
4	9.915	0.1022
5	10.211	0.1135
6	11.049	0.1227
7	11.811	0.1312
8	12.446	0.1383
9	13.132	0.1459
10	13.716	0.1468
11	14.351	0.1595
12	14.935	0.1659
13	15.443	0.1716
14	15.951	0.1772
15	16.459	0.1829
16	16.967	0.1885
17	17.449	0.1939
18	17.907	0.1989
19	18.364	0.2040
20	18.872	0.2097
21	19.355	0.2151
22	21.082	0.2340
23	22.838	0.2532
24	24.562	0.2729

Load = 0.25 kg
Temperature = 33 ^{0}C
L_0 = 90mm
d_0 =1mm
Instantaneous strain ε= 0.0395
σ = 38.60 Mpa
Tensile force (F) = 30.32 N

Figure 4 Strain versus time for 0.25 kg mass attached to specimen

$$\overline{E} = \frac{d}{dt} = \frac{0.19 - 0.11}{18 - 5} = \frac{0.08}{13} = 6.2 \times 10^{-3} \text{ /min}$$

Table : 2 value of time, change in gauge length and strain for 0.20 kg

T (min)	ΔL (mm) Change in length	Strain
0	2.286	0.0254
1	3.048	0.0339
2	3.911	0.0434
3	4.521	0.0502
4	5.105	0.0567
5	5.537	0.0615
6	5.892	0.0655
8	6.752	0.0751
10	7.442	0.0826
12	8.001	0.0889
14	8.559	0.0951
16	9.017	0.1002
18	9.449	0.1050
20	9.906	0.1100
22	10.287	0.1143
24	10.668	0.1185
26	11.049	0.1228
28	11.379	0.1262
30	11.811	0.1312
32	12.192	0.1355
34	12.573	0.1397
36	12.954	0.1439
38	13.335	0.1482
40	13.919	0.1547

Load = 0.20kg

Temperature 31 ^{0}C

L_0 = 90mm

d_0 = 1mm

Instantaneous strain = 0.0254

σ = 34.86 Mpa

Tensile force (F) = 27.38 N
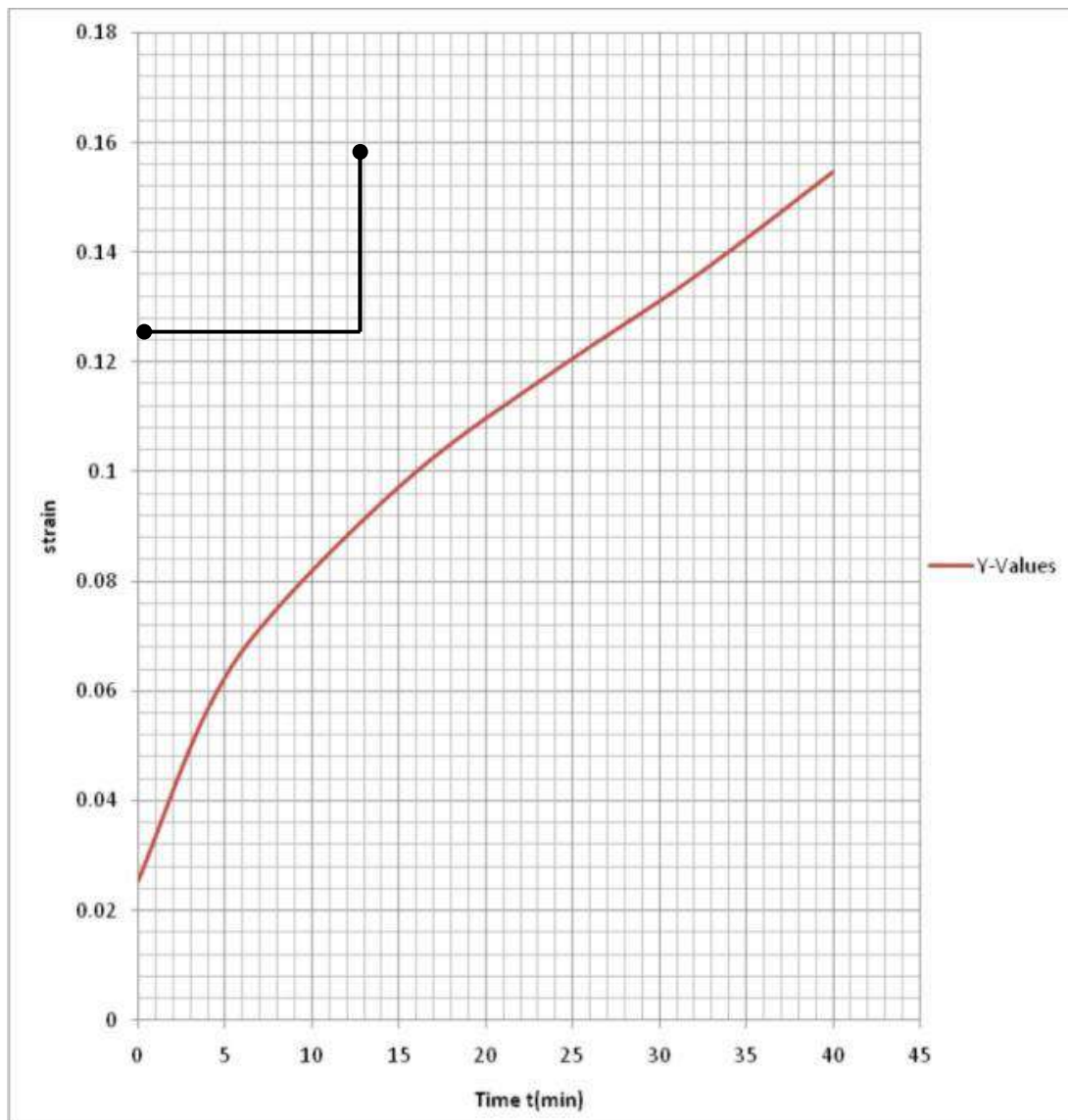
Figure .5: Strain versus time for 0.20 kg mass attached to specimen

$$\bar{E} = \frac{d}{dt} = \frac{0.137 - 0.072}{31 - 7} = \frac{0.065}{24} = 2.7 \times 10^{-3} \text{ /min}$$

Table: 3 Value of time, change in gauge length and strain for 0.15 kg

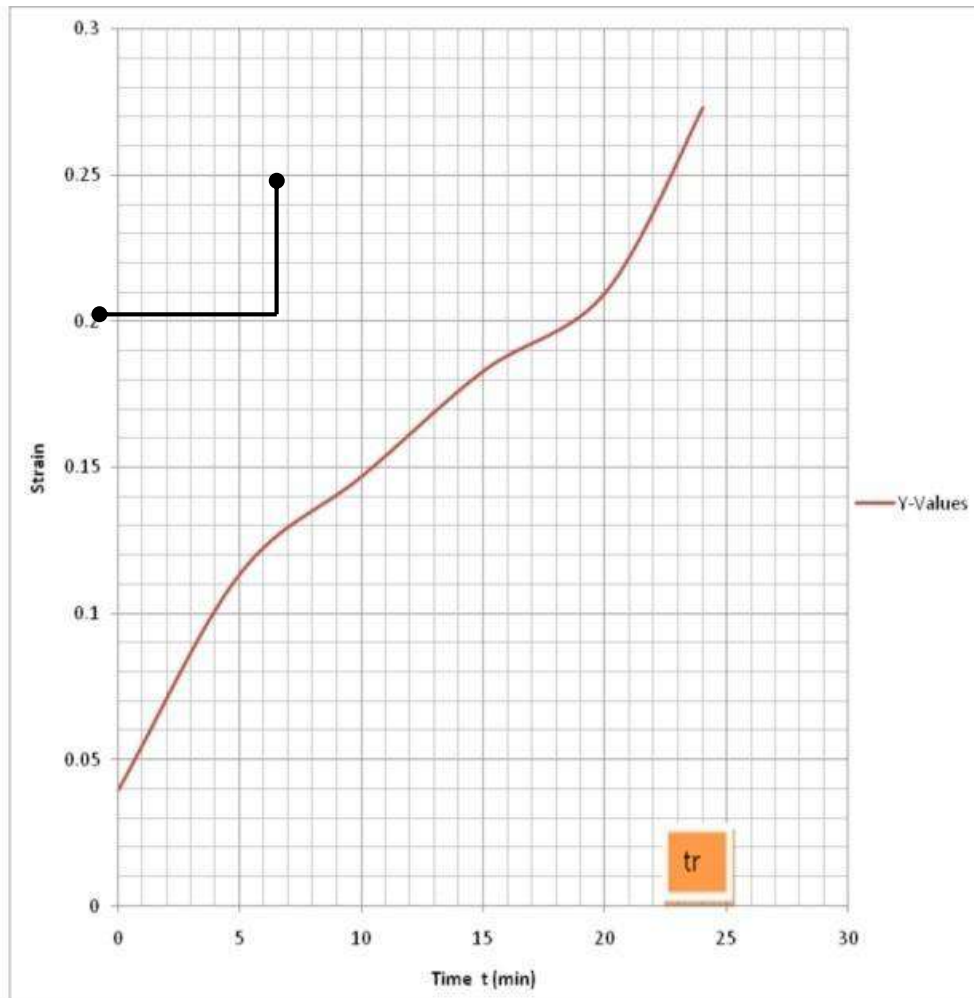| T (min)	ΔL (mm) Change in length	Strain
0	0.635	0.0071
1	0.889	0.0099
2	1.397	0.0155
3	1.905	0.0212
4	2.362	0.0262
5	2.743	0.035
6	3.022	0.0338
7	3.302	0.0367
8	3.581	0.0373
10	4.064	0.0451
12	4.495	0.0499
14	4.928	0.0548
16	5.283	0.0587
18	5.588	0.0621
20	5.893	0.0655
22	6.147	0.0683
24	6.426	0.0714
26	6.655	0.0739
28	6.934	0.0770
30	7.188	0.0799
32	7.442	0.0822
34	7.722	0.0858
36	8.010	0.0890
38	8.163	0.0907
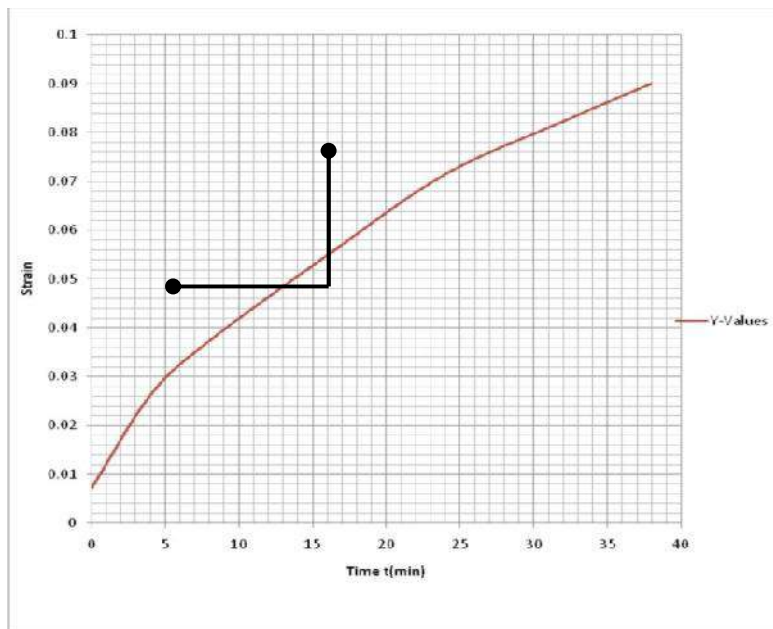
Figure 6: Strain versus time for 0.15kg mass attached to specimen

$$\overline{E} = \frac{d}{dt} = \frac{0.072 - 0.04}{24 - 9} = \frac{0.032}{15} = 2.1 \times 10^{-3} \text{ /min}$$

Table: 4 Value of time, change in gauge length and strain for 0.10 kg

T (min)	ΔL (mm) Change in length	Strain
0	0.254	0.0028
1	0.381	0.0042
2	0.508	0.0056
3	0.635	0.0071
4	0.711	0.0079
5	0.812	0.0090
6	0.889	0.0099
8	1.016	0.0113
10	1.168	0.0129
12	1.295	0.0144
14	1.448	0.0161
16	1.549	0.0172
18	1.651	0.0183
20	1.778	0.0198
22	1.879	0.0209
24	1.981	0.0220
26	2.083	0.0331
28	2.184	0.0243
30	2.286	0.0254
32	2.388	0.0265
34	2.489	0.0277
36	2.590	0.0288
38	2.692	0.0299
40	2.790	0.0310

Load = 0.10 kg
Temperature = 31^0C
L_0 = 90mm
d_0 = 1mm
Instantaneous strain ε = 0.00282
σ = 27.39 Mpa
Tensile force (F) = 21.5 N
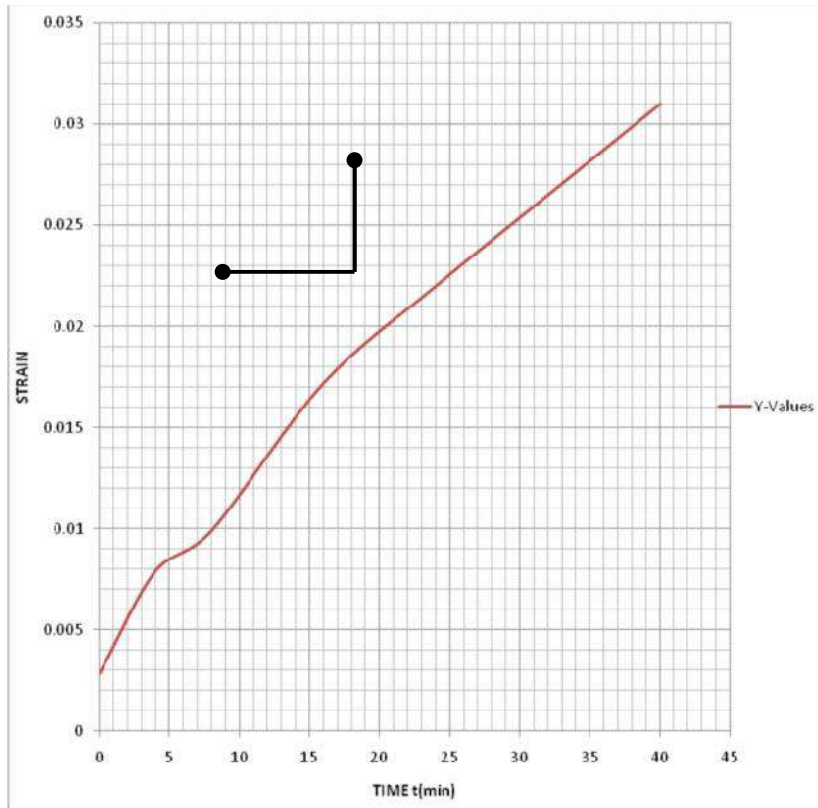
Figure 7: Strain versus time for 0.10 kg mass attached to specimen

$$\overline{E} = \frac{d}{dt} = \frac{0.025 - 0.017}{29 - 16} = \frac{0.008}{13} = 6.2 \text{ x } 10^{-4} \text{ /min}$$

Table: 5 Logarithms of creep rate and applied stress

Mass kg	Applied stress (Mpa)	Log applied stress	Creep rateE /(min)	Log E
0.10	27.39	1.44	0.00062	-3.21
0.15	31.13	1.49	0.0021	-2.68
0.20	34.86	1.54	0.0027	-2.57
0.25	38.60	1.59	0.0062	-2.21
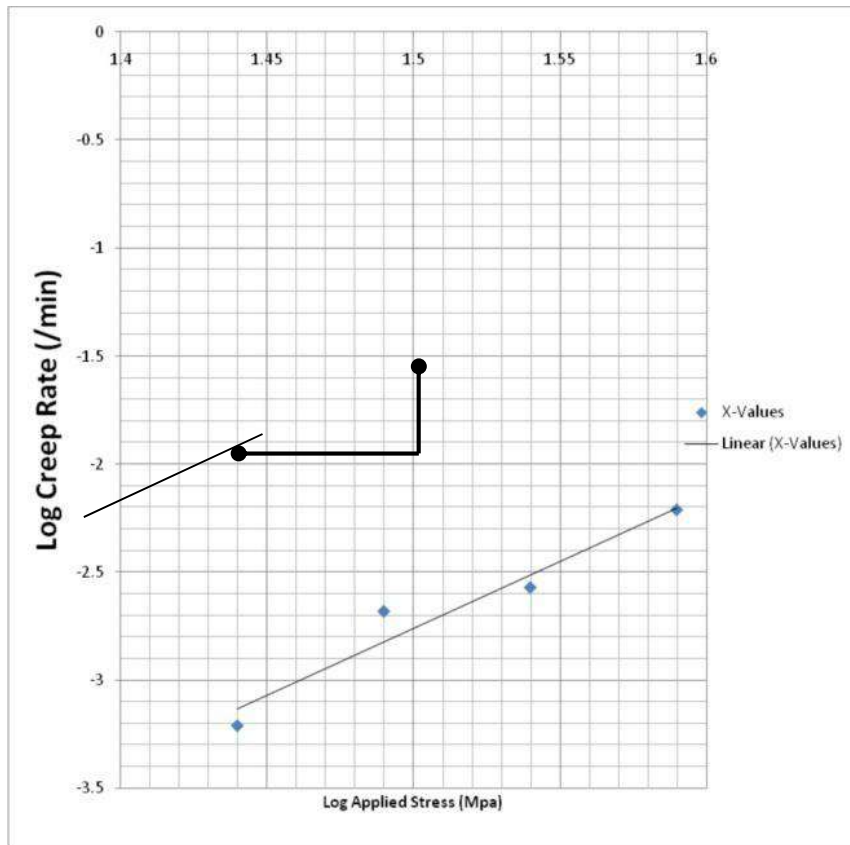
Figure 8: Log creep rate versus log applied stress

Intercept= log (B) = -3.4 ∴ B = $10^{(-3.4)}$ = 4.0 X 10^{-4}

Slope (m) = $\dfrac{-2.3 - -2.8}{1.57 - 1.49}$ = $\dfrac{0.50}{0.08}$ = 6.25

Discussions

From the results, figure 4 reflected a typical creep curve where the three stages of creep curve can be clearly identified. Primary stage takes 3 minutes, secondary stage takes 17 minutes and tertiary stage takes 4 minutes. Creep rupture occurred at 24 minutes, under a constant load of 0.25 kg and room temperature of 33^{0}C with creep rate 6.2×10^{-3}/min.

In figure 5, primary stage takes 4.5 minutes and secondary stage takes 35.5 minutes. At 40 minutes, the gauge length increased to 104.2mm, tertiary stage did not take place and creep rupture did not occur under a constant load of 0.20 kg and room temperature of 31^{0}C with creep rate of 2.7×10^{-3}/min. In figure 6, primary stage takes 6 minutes and secondary stage takes 32 minutes. At 38 minutes, the gauge length extends to 98.3mm, tertiary stage did not take place and creep rupture

did not occur under a constant load 0.15 kg and room temperature of 31^0C with creep rate of 2.1 x 10^{-3}/min.

In figure 7, the primary stage takes 8 minutes and secondary stage takes 32 minutes. At 40 minutes, the gauge length of specimen extends to 92.8 mm, tertiary stage did not take place and creep rupture did not occur under a constant load of 0.10 kg and room temperature of 31^0C with creep rate of 6.2 x 10^{-4}/min. Figure 8 is a linear graph, shows the relationship between logE and Logδ in creep power law equation $\left(log\bar{E} = logB + mlog\ \delta - \frac{E}{RT}\right)$ (13) (m) and (B) can only be determined experimentally from the slope and intercept of the graph respectively, which is agreed with Hearn (1985).

4.0 Conclusions

A single specimen creep testing machine was developed; four experiments were carried out with the machine under different loads and room temperature. The results of the creep rate obtained indicate that the higher stress applied to the specimen, the faster the creep rate, also the result agreed with Bunnell, (2007), Ritu and Rajeev, (2014).

References

Bunnell, L.R. (2007). Creep of lead-tin solder (60/40) at room temperature, southridge High school, Kennewick, retrieved on May 20, 2017, from www.materialsinstem.org, WA 99338

Hearn, E.J. (1985). Mechanics of materials 2nd Edition, volume 2 Oxford, England.Pergamon press ltd,

Ishikawa, K. Okuda, H. and Kobayashi, Y. (1997). Creep behavior of highly pure Aluminum at lower temperatures, Material science and Engineering A, 234-236 (0) 154-156

Ritu, S. and Rajeev R. (2014).Design and fabrication of a creep testing machine and analysis of creep behavior of soldering wire, international journal of IT and knowledge management. 7(2) 1-8

INVESTIGATION ON HYDRAULIC TURBINE OPERATION OF SHIRORO HYDROPOWER STATION, NIGERIA

Y. Mohammed[1], A. Nasir[1], J. Y. Jiya[1] & H. T. Abdulkarim[2]

[1]Department of Mechanical Engineering, Federal University of Technology, Minna
[2]Department of Electrical/Electronic Technology, College of Education, Minna

Abstract

This work concerns a study conducted to ascertain the actual power output and operational efficiency experienced in the running of the water turbine installations in the Shiroro Power station in Nigeria. Facts from the study show that there is no steady linear trend in the generation of electricity over the eighteen years and that the generation of electricity only fluctuated by 1.4% on the average over the eighteen years under study. This could be the reason why all plans that are based on the assumption of steady linear increase in generation of electricity do always fail to succeed because the linear trend does not exist in generation. Again, from the study, the correlation coefficient of **0.976** indicates that turbine discharge contributes most to energy generation. Similarly, the correlation coefficient of **0.752** indicates that lake level contributes next to energy generation in the plant. The correlation coefficient of **0.612** also indicates that lake level contributes significantly to turbine discharge in the plant. Hence, turbine discharge and lake level remain the key performance indicators relating to energy generation in Shiroro power station.

Keywords: Performance, hydro-turbine, generation, reliability, turbine discharge, lake level

1.0   INTRODUCTION

Energy is the prime mover of any economic growth and development. This is why major advances in civilization throughout human existence have been accompanied by increased energy consumption (Agboola, 2011). Energy consumption seems to be directly related to the standard of living of people and the degree of industrialization of the country. In 2006, World-wide, an installed capacity of 777 GWe supplied 2998 TWh of hydroelectricity. (Stachowiak and Batchelor, 2014), this was approximately 20% of the world's electricity, and accounted for about 88% of electricity from renewable source. Hydropower is an important part of global energy strategies and about the only renewable resource currently used on a large scale to generate electricity (Martinez et al, 2019). In 1998 hydropower contributed 2.7% of global primary energy and between 15-20% of the world's electricity supply (McCauley, 2014). In recent years, there has been an increase in the concern about environmental and increase in global energy demand, which give rise to researches in energy towards reducing carbon dioxide emissions. Further development and utilization of renewable energy is expected. In particular, hydraulic energy is the most powerful renewable energy source, and by 2035, it is predicted that the usage capacity of hydraulic energy will exceed 1400 GW (Yasuyiki et al., 2019).

Shiroro hydroelectric power station, one of ten power stations dotted across the country owned by the Power Holding Company of Nigeria (PHCN), is situated in Niger State, 550 metres down - stream of the confluence of Kaduna river with its tributary leading into the Dinya river, which is about 60 kilometres North - East of Minna, the state capital. President Ibrahim Badamasi Babangida officially commissioned it on 20thJune1990 but technical commissioning actually started with unit 411g4 on October3, 1989 with the commissioning of the last unit – unit 411g2- being completed on January 21, 1990. (Shiroro Magazine, 2014). Figure 1 below shows the area view of the Shiroro Power station.

The decision to build a dam across river Kaduna in the area of Shiroro -a small farmers' village near Minna in Niger state that got its name from the gorge where the project is located –has its origin in the survey carried out in the early 1950s in pursuance of the exploitation of the energy potential of the Nigerian river system. The survey led to the implementation of what today are known as the 760 MW Kainji and the 540 MW Jebba power stations on the Niger River, and 600 MW Shiroro power station on the Kaduna River, which is one of the tributaries of the Niger River (Shiroro Hydropower Magazine, 2014).The final design of the whole project was prepared for NEPA now PHCN by Chas T. Main International Inc. of Boston USA, while construction of the civil works was awarded to the Italian firm ,Torno S.P.A. towards the end of 1978 (Shiroro Hydropower Magazine, 2014). According to Ibitoye et al, (2007), other Components of the projects were awarded to different companies, which included the Austrian firm, Voest Alpine for the supply and installation of the hydraulic turbines and governors, Ingra Rade Koncar of the Federal Republic of Yugoslavia for the supply and installation of the generator and excitation system, Mitsubishi/Toshiba of Japan for the generator transformers, and GEC of UK for the protective relays and control equipment. Siemens AG of the Federal Republic of Germany supplied high voltage switchgears and other switchyard equipment, while CBI of Italy handled electrical installations and ancillary plant items. A Spanish company, Bynsa, supplied the project cranes. In a similar vein, Tam Pella of Finland supplied both the power intake and spillway gates together with the associated electro-hydraulic control equipment. The engineering division of NEPA (PHCN) managed the Shiroro hydroelectric project, significantly under the leadership of a project engineer. (Shiroro Hydropower Magazine, 2014)

Fig. 1: Spill gates & Penstock of Shiroro Power Station.

The station has a total installed capacity of 600 MW from 4 generating units rated at 150 MW each at a head of 97 metres. Each unit comprises a vertical Francis hydraulic turbine unit controlled by an electro - hydraulic governor. The turbine drives a synchronous generator of salient pole construction having a net output of 150 MW. A static self –excitation system, excites the generator. The speed of rotation for the unit is 150 rpm. These turbine generators are capable of independent operation. Power is generated at 16 -KV voltage levels. A generator transformer steps up the voltage to 330-KV voltage level for connection to the national grid via the agency of a 330-KV switchyard. The national grid constitutes a "power pool" to which all the power stations and load centres are connected. During its first nineteen years of operation from January 1997 to December 2015, the station generated 41.307 TWH of energy accounting for a plant capacity factor of 41.36%. As part of an effort to improve the reliability of power supply in the country, the machines at Shiroro power station have been equipped with the necessary control devices to enable the station quickly restore supply to a section of the NEPA grid following a total collapse of the power system (Shiroro Hydropower Magazine, 2014). This results in a shorter restoration time for the entire power grid. Each generator in Shiroro is also capable of operating as a synchronous condenser to supply reactive power to the grid to provide voltage support (Boost low voltage at other station). An important milestone in the history of Shiroro power station of recent has been the establishment at the site, of a new national control centre equipped with state –of the art SCADA (Supervisory Control and Data Acquisition) and EMS (Energy Management System) facilities to supplement the older one at Oshogbo. This is to ensure a more effective system operation and control (Obadote, 2009).

2.0   RESEARCH METHODOLOGY

2.1 Data Collection, Presentation and Statistical Analysis.

The data used in this research work were collected through a secondary source to investigate and empirically evaluate the performance of the Shiroro Power Station. Before the actual data analysis, data were classified into purposeful and logical categories in order to facilitate analysis. Hence, the process of analysis is partially concurrent with data collection and presentation. Therefore, the need to present the summary of the original data, in tabular form, prior to analysis to reflect the originality of the data collected from the Shiroro Power Station through the secondary source.

Table 1: Case Summaries

SNO.	Years	Generation (MWh)
1	1998	2,156,687
2	1999	1,997,155
3	2000	2,300,002
4	2001	2,119,957
5	2002	2,046,908
6	2003	1,944,825
7	2004	2,057,483
8	2005	2,229,044
9	2006	2,337,215

185

10	2007	2,262,482
11	2008	2,229,671
12	2009	2,675,201
13	2010	2,198,944
14	2011	2,538,834
15	2012	2,425,629
16	2013	1,236,081
17	2014	2,432,640
18	2015	2,230,761

3.0   Results And Discussions

To investigate, from the data, using time series analysis (Lindeman, et al, 2014).whether the annual generation of electricity over the seventeen years under study (from 1998 through 2015) follows a linear trend. In other words, whether the seventeen year electricity generations have any pattern of steady increase or not. The time-series linear modelling and trend analysis, at the 5% level of significance, is hereby employed for the analysis as stated by the following hypothesis and depicted in the tables.

Hypothesis:
$H_0 : s = 0$ (There is no steady linear trend in the generation of electricity over the seventeen years under study)
$H_1 : s \neq 0$ (There is steady linear trend in the generation of electricity over the seventeen years under study)

Level of Significance:
$r = 0.05$

Test statistic:
$$F* = \frac{MS(Regression)}{MSE}$$
Where, F = Facial Statistic, MS = Mean Square and MSE = Mean Square Error.

Decision Criterion:
Reject H_0 if $p < 0.05$ otherwise accept H_0

Computations:
The computations are summarized on the following Model summary, ANOVA and coefficients tables:

Table 2: Model Summary

R	R Square	Adjusted R Square	Std. Error of the Estimate
0.119	0.014	-0.048	310702.5

Table 3: ANOVA

Source of Variation	Sum of Squares	Df	Mean Square	F	Sig.
Regression	22102762203.5	1	22102762203.5	0.229	0.639
Residual	1544576889910.1	16	96536055619.4		
Total	1566679652113.6	17			

Table 4: Model Coefficients

	Unstandardized Coefficients		Standardized Coefficients		
	B	**Std. Error**	**Beta**	**T**	**Sig.**
Case Sequence	6754.2	14115.6	0.119	0.478	0.639
(Constant)	2125808.0	152791.8		13.913	0.000

3.1 Conclusion for Time-Series Trend Analysis

From Table 3, above, since $p = 0.639 > 0.05$, we cannot reject the null hypothesis and conclude that there is no steady linear trend in the generation of electricity over the seventeen years under study. This was further confirmed in Table 2, above where the coefficient of determination (R square) of 0.014 (or 1.4%) implies that the generation of electricity only fluctuates by 1.4% on the average over the seventeen years under study. This could be the reason why all plans that are based on the assumption of steady linear increase in generation of electricity do always fail to succeed because the linear trend does not exist in generation. This is graphically shown in figure 2 below.
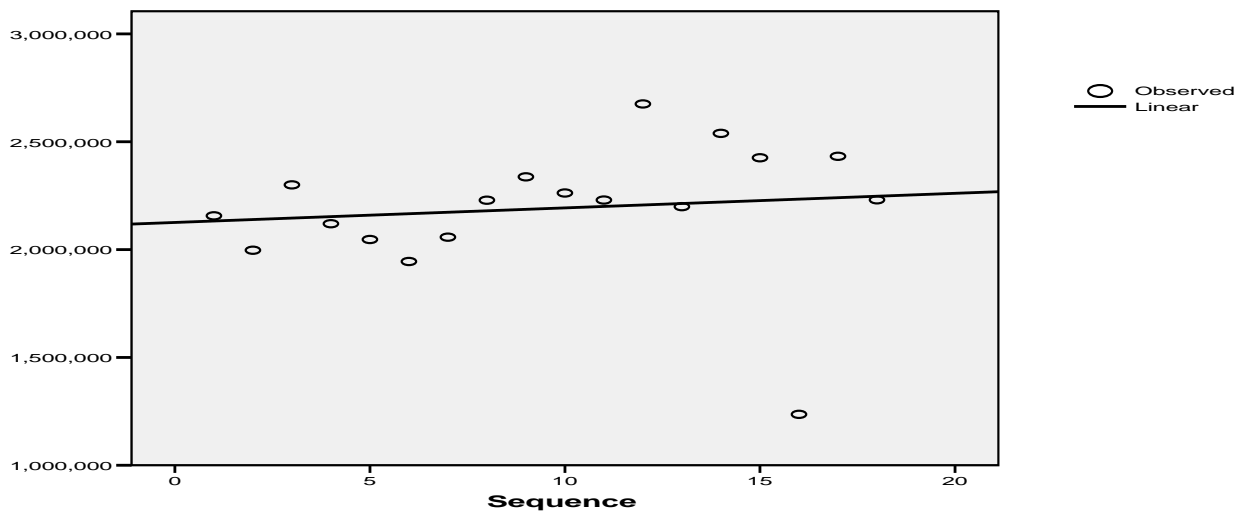

Fig. 2: Generation Linear Sequence (MWh)

To investigate, identify and establish the levels of key performance indicators relating to turbine discharge, energy generated and the lake level. The pair-wise product-moments correlations with their test of significance, (Younger, 1995), at the 5% level of significance, is hereby employed for the analysis using the data on turbine discharge, energy generated and the lake level from January through December 2016; as stated by the following hypothesis and depicted in the tables.

3.2 Pair-Wise Correlation Analysis for Turbine Discharge, Energy Generated and Lake Level

Hypothesis:

$H_0 : \cdots_{ij} = 0$ (There is no significant indicator relationship between turbine discharge, energy generated and the lake level)

$H_1 : \cdots_{ij} \neq 0$ (There is a significant indicator relationship between turbine discharge, energy generated and the lake level)

Level of Significance:
$\Gamma = 0.05$

Test statistic:

$$\cdots_{ij} = \frac{\sum_{i=1}^{n}(X - \bar{X})(Y - \bar{Y})}{\sqrt{\sum_{i=1}^{n}(X - \bar{X})^2 \sum_{i=1}^{n}(Y - \bar{Y})^2}}$$

Decision Criterion:
Reject H_0 if $p < 0.05$ otherwise accept H_0

Computations:
The computations are summarized on the following Case summaries, Descriptive and correlation tables:

Table 5: Case Summaries for Turbine discharge, Energy Generated and Lake Level

S/No.	Month	Turbine discharge (10^9 M^3)	Energy Generated (MWh)	Lake level
1	January	0.9879	255,007	372.10
2	February	0.7724	193,805	368.12
3	March	0.5753	137,458	364.50
4	April	0.3751	85,769	361.92
5	May	0.4743	103,974	359.42
6	June	0.6018	131,566	358.60

7	July	0.9700	210,884	362.23
8	August	1.0089	240,737	372.98
9	September	1.0894	285,867	379.37
10	October	0.8605	229,805	378.54
11	November	0.8331	220,849	375.85
12	December	0.5222	135,040	373.68
Total		9.0709	2,230,761	4427.31

Table 6: Descriptive Statistics for Turbine discharge, Energy Generated and Lake Level

Performance Indicators	Mean	Std. Deviation	N
Turbine discharge (10^9 M^3)	0.7559	0.2388	12
Energy Generated (MWh)	185,896.75	64,832.43	12
Lake level	368.94	7.44	12

Table 7; Correlations for Turbine discharge, Energy Generated and Lake Level

Performance Indicators		Turbine discharge (billion M cube)	Energy Generated (MWh)	Lake level (M)
Turbine discharge (10^9 M^3)	Pearson Correlation	1	0.976	0.612
	Sig. (2-tailed)		0.000	0.035
Energy Generated (MWh)	Pearson Correlation	0.976	1	0.752
	Sig. (2-tailed)	0.000		0.005
Lake level(M)	Pearson Correlation	0.612	0.752	1
	Sig. (2-tailed)	0.035	0.005	

3.3 Conclusion for Correlation Analysis and their Tests of Significance

Table 5 above shows the Case Summaries for Turbine discharge, Energy Generated and Lake Level, while Table 6 above shows their Descriptive Statistics (McConway et al, 1999). From Table 7, above, since all the p-values are less than 0.05 i.e. $p < 0.05$, we reject the null hypothesis in each case and conclude that there is a significant indicator relationship between turbine discharge, energy generated and the lake level. To investigate, identify and establish the levels of key

189

performance indicators relating to turbine discharge, energy generated and the lake level, we simply consider the pair-wise product-moments correlations. Again, from Table 7, the correlation coefficient of **0.976** indicates that turbine discharge contributes most to energy generation. Similarly, the correlation coefficient of **0.752** indicates that lake level contributes next to energy generation in the plant. The correlation coefficient of **0.612** also indicates that lake level contributes significantly to turbine discharge in the plant. Hence, turbine discharge and lake level remain the key performance indicators relating to energy generation. This can be depicted graphically in Figures 3 and 4 below.
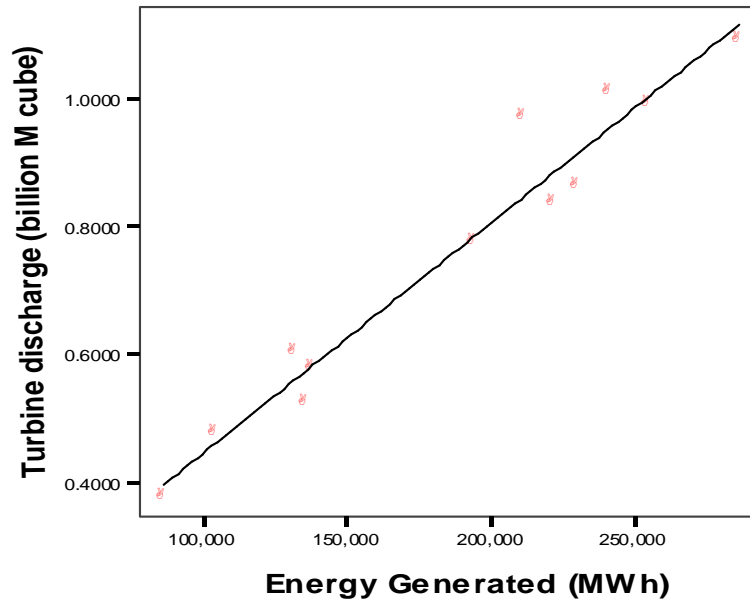

Figure 3. Scatter Diagram for Turbine discharge and Energy Generated.
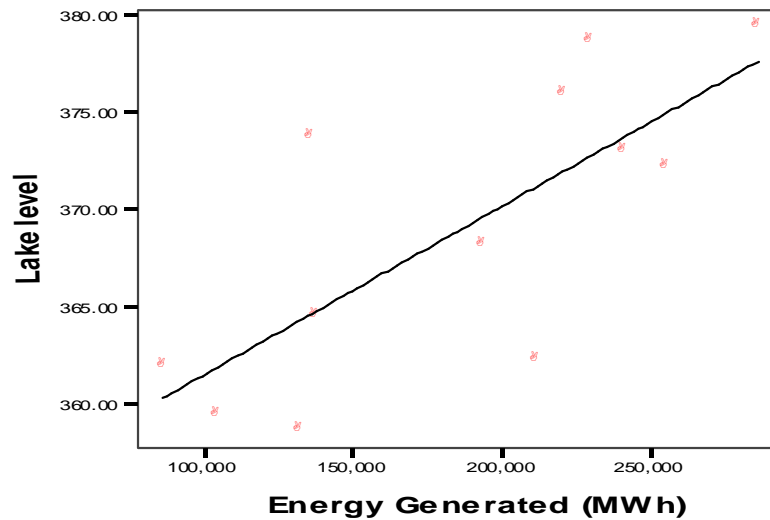

Figure 4. Scatter Diagram for Lake Level and Energy Generated

4.0   Conclusion

From the findings on the performance of the reaction hydro-turbines (Shiroro Power station), their major problem seems to be the unreliability of the hydrological data of the stations, Generator ground fault and Shear pin breakages. The problems with the machines themselves are those that pertain to the control system and to the electrical auxiliaries.

References

1. Agboola, O. P. (2011). Independent power producer (IPP) participation: Solution to Nigeria power generation problem. Proceedings of the world congress on Engineering, WCE 2011, vol. III, London, UK, July 6–8, 2011.

2. Aliyu, U. O. and Elegba, S. B., (1990) –Prospects for Small Hydropower Development for Rural Application in Nigeria, Nigeria Journal of Renewable Energy, 1(1), pp.74-86.

3. Ibitoye, F. I. & Adenikinju, A. (2007). Future demands for electricity in Nigeria. Applied Energy Journal; 84(5): 492–504.

4. Lindeman, H. R. Morenda, F. P, & Gold, R. Z. (1980). Introduction to bivariate and Multivariate analysis. London: Scott, Foresman and Company.

5. Martinez,J.J.,Deng, Z. D., Titzler, P. S., Duncan, J. P., Mueller, R. P., Tian, C., Trumbo, B. A., Ahmann, M. L., And Renholds, J. F. (2019). Hydraulic And Biological Characterization of A Large Kaplan Turbine. Renewable Energy, Volume 131, February 2019, 240-249.

6. McCauley, Patrick (2001). Silenced Rivers: The Ecology and Politics of Large Dams.Zed Books.

7. Obadote, D. J. (2009). Energy crisis in Nigeria: technical issues and solutions. Power sector conference, Abuja, Nigeria, June 25–27.

8. Stachowiak, G.W., Batchelor, A.W. (2014), Engineering tribology. Boston: Butterworth-Heinemann. P 525

9. Shiroro Hydropower Annual Magazine (2014)

10. Yasuyuki, N., Genki, S., Daishi, S., Terumi, I. Norio, K. (2019). A study of the flow field of an axial flow hydraulic turbine with a collection device in an open channel. Renewable Energy 130 (2019) 1036-1048

11. Younger, M.S. (1995). A first course in linear regression (2nd ed.). Boston: Duxbury.

AN INVESTIGATION ON THE CHEMICAL AND PHYSICAL PROPERTIES OF GADA AND MUVUR SILICA SAND FOR GLASS MAKING

[1]G.A. Duvuna , [2]Z.S Johnson , [2]Davou I. G. Chomo and [3]Sadiq Sius Lawal,

[1]Department of Mechanical Engineering, Federal Polytechnic, Mubi, Adamawa State,
[2] Department of Mechanical Engineering, Plateau State Polytechnic B/Ladi Plateau State.
[3] Department of Mechanical Engineering, Federal University of Technology, Minna.
[1]e-mail: ayubagideon2@gmail.com

Abstract

The suitability of silica sand deposits of Gada and Muvur in Mubi North Local Government Area of Adamawa State, Nigeria for commercial glass production was assessed based on the chemical and physical properties of the silica sand samples collected along the river sides.The test was carried out at National Metallurgical Development Centre (NMDC) Jos. Chemical analysis was carried out using x-ray florescence spectrometer (XRFS) and the physical properties such as the particle size, grain morphology and specific gravity examinations were carried out using mechanical shaker (sieving method), electronic microscope to reveal the shape of the samples and the specific gravity testing machine respectively. The results obtained were assessed and compared with the standard requirements for glass making. Gada had the highest percentage of silica content of 81.00% and Muvur had the lowest percentage of silica content of 79.40%, but all samples are within the acceptable limits for glass making. The iron oxide content in all the samples was found to be high, with highest value of 1.33% for Muvur and lowest value of 1.28% for Gada. However, the iron content for all the samples was above 1% thereby limiting the range of applications to coloured and amber glass manufacturing. The physical properties that is, the grain morphology which was found to be angular with specific gravity of 2.50 for both the samples were found to satisfy the standard requirements for glass making.

KEY WORDS: Silica sand, iron oxide, grain morphology, glass.

1.0   INTRODUCTION

Glass is a solid that possess a non-crystalline (i.e amorphous) structure that exhibits a glass transition when heated towards the liquid state. Silica, soda ash and lime are the main ingredient in glass making, but many other chemicals can be added to the mixture to create certain properties which makes it one of the most versatile of engineering materials.

Silica sand is the primary component of all types of standard and specialty glass. It provides the SiO_2 component of glass formulation. The requirement falls into two main groups, namely the degree of purity as indicated by it chemical property and the physical characteristics of the sand [1].

The presence of metallic oxides in silica sands usually results in coloured glass. If iron is present, the resulting glass is coloured. The iron level is consequently the most critical parameter in determining whether particular sand can be used to make clear or coloured glass [2]. According to [3], window glass sand may contain 0.1% to 0.5% iron oxide (Fe_2O_3) and dark green bottle glass

192

as much as 2% to 3% iron oxide. For colourless glass containers, generally may contain less than 0.035% Fe_2O_3, for flat glass in the range of 0.040% to 0.1% Fe_2O_3 [4].

Glasses may be devised to meet almost any imaginable requirement for many specialized applications. According to [5], glass can be made by melting together several minerals at very high temperature. Silica sand by itself can be fused to produce glass, but the temperature at which this can be achieved is about 1700^0C. The addition of sodium carbonate (Na_2CO_3) known as soda ash, to produce a mixture of 75% silica (SiO_2) and 25% sodium oxide (Na_2O), will reduce the temperature of fusion to about 800^0C. However, a glass of this composition is water-soluble and is known as water glass. In other to give the glass stability, other chemicals like calcium oxide (CaO), magnesium oxide, aluminum oxide, lead oxide and barium oxide are needed [2]. [5], reported that, most glasses have roughly similar chemical composition of 70% – 74% SiO_2, 12% - 16% Na_2O, 5% - 11% CaO, 1% - 3% MgO, 1% - 3% Al_2O_3, within these limits the composition is varied to suit particular product and production method.

Grain morphology is another physical property that determines the suitability of the sand for glass making. Grain roundness describes the relative sharpness of the grain corners and edges [6]. The visual comparator presented by [7] is one of the widely used devices of grain roundness studies. According to [3], the roundness of the grain must be angular rather than rounded.

Heavy minerals such as sallimanite, kyanite, andelusite, zircon, spinel, garnet e.t.c represent an inclusion in the finished glass. These particles can survive the glass melting process and comes out as solid inclusion or stone defects. Minerals such as these have their specific gravity greater than 2.65. Thus for any sample whose specific gravity is greater than 2.65, the sample is not desirable for glass making [6].

This paper therefore, intends to access the physical and chemical properties of the two sand samples for glass making.

2.0 Materials and Method

Two samples of silica sand were collected along different stream sides of Mubi-North Local Government of Adamawa State namely Gada and Muvur. Test on chemical and physical properties of the silica sand samples were carried out at [8] the National Metallurgical Development Centre (NMDC) Jos, Plateau State, Nigeria.

The silica sand samples were first cleared coned and quartered to obtain the representative fraction. The coning and quartering involved pouring the silica sand samples on the flat surface, such that it formed a cone which was divided into four equal parts by using a straight edge. The two alternative quarters were mixed again for further quartering. After which the representative fraction for each sample was later crushed and ground separately to pass through 120 mesh (BS) sieve. This ground silica samples were then used for the chemical analysis.

(i) Chemical Analysis

An X – Ray florescence spectrometer (XRFS) was used for the analysis. The samples for the analysis were presented to the spectrometer in a homogeneous reproducible form either milled or ground to give a flat surface.

The silica sand samples which were earlier prepared were further ground and sieved to 75µm particle size 4g of the sieved samples was intimately mixed with 1g of lithium tetraborate binder (Li_2BO_4) and passed in a mould under a pressure of 10 – 15 tonnes/in^2 to a pellet. The pressed pellets were dried at 1100^0C for 30 minutes in an oven to get rid of any absorbed moisture and were finally stored in desiccators for analysis. The spectrometer was switched on and allowed to warm up in order to stabilize the optics and the x – ray tube. It was then calibrated to determine the expected elements or compounds present in the silica sand.

(ii) Particles Size Analysis

Dry sieving method was adopted and the represented silica sand samples were obtained from the quartered silica sand samples. The samples were first dried in an oven and from each samples, 100g was weighed and arranged on a mechanical shaker with the coarsest on top. The machine was operated for 15 minutes. After sieving the samples, the samples were then emptied onto sheet of paper and weighed one after the other, then, the cumulative percentage by weight of the particles passing each sieve was calculated and recorded.

(iii) Grain Morphology Test

The shape of the silica sand determined the suitability of the silica sand sample for glass making. The silica sand samples were viewed under electronic microscope to reveal the shape of the samples and their suitability for glass making.

(iv) Specific Gravity Examination

The specific gravity was obtained directly from the specific gravity tester. The silica sand samples were introduced into the machine, which automatically carried out the test and displayed the values of the specific gravity digitally on a visual display unit.

3.0 RESULTS AND DISCUSSION

Tables I, II and III shows the chemical composition, physical properties and the calculated cumulative percentage weight of the silica sand particles passing each sieve aperture of the samples.

The main ingredient for glass making is the silicon oxide or silica and it varies based on the type of glass to be made. The results in table I shows, the chemical contents analyzed for the silica sand samples obtained from the four different rivers. The percentage of the silica sand are 81.0% for Gada and 79.40% for Muvur as shown in table I, which are high and adequate for glass making [5]. However, the percentage of iron oxide obtained is high and can only be suitable for coloured and amber glass [9]. This is because the iron content is greater than 1%.

The percentages of MgO for the two samples were obtained as 0.18 and 0.19 for Gada and Muvur respectively. The percentages of CaO obtained for the two samples were 0.20 and 0.20 for Gada and Muvur, respectively. The percentages of Al_2O_3 obtained for the four samples were 7.30 and 8.02 for Gada and Muvur respectively.

The percentages of the entire main ingredient mentioned above (MgO, CaO and Al_2O_3) obtained in the silica sand samples shown in table 1 were very low for glass making when compared with

194

the standard percentage composition requirements of 4-5% of CaO and MgO required for sodalime and lead glasses manufacturing [10, 11].

The percentages of Na_2O and K_2O for the four samples were found to be adequate compared with the standard percentage needed for various glass formulation, as such, the two samples can be used for borosilicate glasses, lead glasses, fibreglasses and to some extent alumina silicate glasses, since the requirement falls within the range of 2-9 percentage by weight [12, 2, 11].

Table I: Chemical Compositions of the Silica Sand Samples of Gada and Muvur

S/N	Composition	Gada % by Weight	Muvur % by Weight
1	Al_2O_3	7.30	8.02
2	SiO_2	81.00	79.40
3	K_2O	7.11	7.45
4	CaO	0.20	0.20
5	TiO_2	0.20	0.07
6	Cr_2O_2	0.10	0.11
7	MnO	0.04	0.02
8	Fe_2O_3	1.28	1.33
9	NiO	0.01	0.008
10	CUO	0.05	0.05
11	ZnO	ND	ND
12	Ga_2O_3	ND	0.05
13	SrO	0.03	0.02
14	RB_2O	0.05	0.05
15	BaO	0.22	0.19
16	Nb_2O_5	0.04	0.05
17	ZrO_2	0.05	0.04
18	Na_2O	2.01	4.03
19	AU	0.02	0.02
20	Na_2O	4.01	6.30

21	MgO	0.18	0.19

Key: ND =   not detected

Grain morphology or shape, specific gravity (SPG) and the grain fitness number (GFN) are the physical properties of silica sand that determine the suitability of silica sand for glass making. The grain morphology for the four samples is angular as shown in table II. According to [3], the grain shape or morphology must be angular rather than rounded. Also the specific gravity for the four samples is 2.50. According to [6], for silica sand with specific gravity greater than 2.65 is not suitable for glass making. Thus, all the two samples are suitable for glass making when compared with the standard requirements for glass making.

Table II: Physical Properties of the Four Silica Sand Samples Gada and Muvur

S/N	Composition	Gada	Muvur
1	Grain morphology	Angular	Angular
2	Specific gravity (SPG)	2.50	2.50
3	Grain fitness number (GFN)	23.14	16.10

From the results of particle size distribution shown in table III. All the two samples were found to be suitable for glass making, because over 90% of the particle size lie within 15-100 mesh (BS sieve number) [13].

Table III: Calculated cumulative percentage weight of the silica sand particles passing each sieve aperture for the four samples (Gada and Muvur)

Sieve Aperture	Mesh Number	Gada % by weight	Product	Muvur % by weight	Product
1.40	14	18.22	-	28.34	-
1.00	18	13.11	183.54	21.32	298.48
0.71	25	19.29	347.22	22.32	401.76
0.50	35	21.06	526.50	15.41	385.25
0.355	45	15.94	557.90	8.45	295.75
0.250	60	8.55	384.75	3.07	138.15
0.180	80	2.23	133.80	0.49	29.40
0.125	120	0.97	77.60	0.25	20.00

0.090	170	0.25	30.00	0.08	9.60
0.063	230	0.10	17.00	0.07	11.90
0.063	-230	0.24	55.20	0.12	27.60
		99.96	2313.51	99.92	1617.89

4.0 CONCLUSION

The percentage of silica content obtained as 81% and 79.40% for Gada and Muvur respectively which is the major glass forming oxide in the four samples were found adequate for glass making because the percentage values lies within the minimum standard requirements of 70%. All the two silica sand samples were found to have the physical properties that met the requirements for the manufacture of glass since the grain morphology were all angular rather than rounded. The percentage of iron oxide in the silica sand samples obtained as 1.28% and 1.33% for Gada and Muvur respectively were a little bit higher than 1%, for this reason, it limits its applications to coloured and amber glass production. All the silica sand samples analyzed have additional chemicals or compounds that could be added to improve the quality of the glass produced. Therefore, the silica sand samples investigated are adequate for glass manufacturing and therefore, should be utilized.

Reference

[1] RMRDC. " Raw Materials Research and Development Council, Federal Ministry of Science and Technology, Multi – Disciplinary Task Force – report of the Techno-Economy Survey on Non-Metallic Mineral Products Sector" 3rd Update Abuja, Nigeria. Pp 14 – 15 and 49, 2001.

[2] David M.I. " A Study of Silica Sand Quality and End Uses in Surrey and Kent" www.1st-glass.1st-things.com/articles/glasscolouring.html, accessed on July, 12, 2016.

[3] Waudby J.E. "A Summary of the Known Deposit of Glass in Nigeria (Unpublished)" 1994.

[4] BGS. " British Geological Survey, Silica Sand Supply Chain.UK" www.mineralszone.com/minerals/silica.html, accessed on Sept. 29, 2017.

[5] BGMC: " British Glass Manufacturers Confederation, 9 Churchill Way, Chapeltown, Sheffield, South Yorkshire, 5352PY.UK" www.britglass.org.uk/types-glass, accessed Sept. 29, 2017.

[6] Tooley F.V. Hand Book of Glass Manufacturing. 2nd Edition Ogden Press, New York, 1987.

[7] Powers M.C. A New Roundness Scale for Sedimentary Particles. John Willey and Sons Inc. New York, 1983.

[8] " National Metallurgical Development Centre Jos, Plateau State (NMDC)" Nigeria, 2015.

[9] Sintali I.S and Egbo G. " Investigation on the Chemical and Physical Properties of Dapchi, Ngala and Gwoza Silica Sand for Glass Making" Journal of Engineering and Technology (JET) Vol. 2, No. 2, Bayero University Kano, Nigeria, 2007.

[10] George, R. " Substances Used in the Making of Coloured Glass" www.britglass.org.uk/history-glass, accessed on Augt. 4, 2017.

[11]   IMA-NA. " Industrial Minerals Association-North America"
                www.britglass.org.uk/about-glass, accessed on July, 12, 2016.
[12]   Manas C. Science of Engineering Materials. Macmillan Company Publishers India, 1979.
[13]   BS2975: " British Standard Methods for Sampling and Analysis of Glass-Making Sands"
                www.Britannica.com, accessed on July, 29, 2016.

PERFORMANCE EVALUATION OF SOYABEAN OIL AS CUTTING FLUID FOR MACHINING OF EN8 CARBON STEEL

Mohammed A.O.[1], Abu, J.O.[1]
[1]Mechanical Engineering Department, Federal University of Technology, PMB 65, Minna, Niger State, Nigeria.
Corresponding author email: mohammedaliyu95@gmail.com, +2347034218757.

ABSTRACT

Due to increasing demand for environmentally acceptable products and the limits of vegetable oil application as metal working lubricants and has become an area of research, which leads to this research to focus on modified soyabean oils being developed to promote biodegradable emulsion cutting fluid across the world using two different emulsifiers. This research also throws light on the physicochemical properties of modified soyabean oils as emulsion cutting fluid and its performance when machining unalloyed medium carbon steel (EN8). With pH values of 4.6 and 6.3, it indicates that the formulated oils with potassium soap as emulsifier is more acidic than the formulated oil with ammonium bromide as emulsifier. The specific gravities of the formulated oils are less than the specific gravity of water, and the specific gravities are within the range of 0.72 to 0.92, which is the standard range of lubricants. The flash point of both oils being 289ºC and 285ºC respectively indicate that both oils can be used as cutting oil since vegetable oils have high flash points which are safe in fire vulnerable processes. The performance of soyabean oil with respect to temperature and surface roughness in the turning process of EN8 carbon steel are studied and reported. The lowest cutting temperatures of 47.00 ºC, 45.80 ºC, 44.60 ºC and the best surface finishes of 3.882 µm, 3.840 µm, 3.721µm respectively, for the three cutting fluids used were all obtained when machining at a speed of 126rpm, with depth of cut at 0.5mm and using a feed rate of 0.6mm/rev. The research reveals that soyabean oil offers an alternative, eco-friendly and sustainable cutting fluid for the future of manufacturing.

Keywords: Cutting Fluid, Emulsifiers, Soyabean Oil, Surface Roughness, Temperature, Turning Operation

1.0   INTRODUCTION

Metal by definition is extremely tough and therefore difficult to cut, a range of devices and measures have to be developed, each of which is the best option for a particular type of metal or desired shape. Often, small sections of the metal will need to be removed, in order to make holes for screws, bolts and rivets. For jobs which are too large or deal with materials which are too robust to make manual metal cutting a practical proposition, machine cutting has to be applied, and this comes in various forms, which include turning, drilling, grinding, and facing. In carrying out any of these operations, the selection of the appropriate tools, feeds and speeds is a compromise as the higher the speed of operation, the higher the efficiency but the shorter the cutting tool life [1].

The development and introduction of new modern machining techniques, improved materials, modern cutting tools capable of working at high speeds and generation of heat in the process, imply that more cutting fluid options are required. Machining processes result in the generation of enormous heat due to the friction between the cutting tool and the workpiece material, and between the tool face and the chips gliding over it [2]. This, to a great extent, affects the tool life and the surface integrity of machined products. To minimize the effect of friction and the resultant heat on tool life, and the consequent effect on the integrity of the machined surface, cutting fluid is used as a means of conducting heat from the cutting zone [3].

Vegetable oil-based emulsions are also a part of recent research to produce stable emulsions to use as metalworking fluids and in other applications [4]. With the current level of health and environmental awareness, it is of great importance that cutting fluids that are not injurious to the operator and are environmentally friendly be developed. Also, considering the economic situation in Nigeria and the world at large, along with the rate at which machining activities requiring cutting fluids are in demand, it is essential that these fluids be readily available and cost less in order to make machining operations more cost effective. A comprehensive review of the application of vegetable oil-based metalworking fluids in machining ferrous metals by Lawal et al. [5] shows that a better performance can be achieved during machining processes using vegetable oil-based metalworking fluid. Sujan et al. [6] also reviewed environmental friendly cutting fluids and cooling techniques in machining. Vegetable oil-based cutting fluids are environmentally friendly, renewable, less toxic and economical in the reduction of the waste treatment costs due to their inherently higher biodegradability [7]. Machining industry concerned with the development of preventive legislation and the increased interest in almost green products reduces the soil pollution by biodegradability which makes the manufacturing processes a clean process [8].

Vegetable oil-based cutting fluids seem to be the best alternatives to mineral oil based cutting fluids due to certain inherent chemical properties and their biodegradability ability. The better performance of vegetable oil-based cutting fluids can be traced to its high flash point, high viscosity index, high lubricity and low evaporative loss compared to mineral oils [9]. Poor oxidative and hydrolytic stability, high temperature sensitivity of tribological behaviour and poor cold flow properties are the limitations of vegetable oils for lubricants [10]. However, these shortcomings in the vegetable oils can be addressed with addition of chemical additives such as emulsifier, corrosion prevention, pH regulator, binding, anti-foaming, odour prevention, flash point improver, spreading and wetting to improve its functions as lubricant.

Jacob et al. [11] developed a vegetable-based emulsion that can be used in the metal working industry, to replace partially or completely the commonly used petroleum based emulsions. Lawal et al. [12] evaluated the effect of vegetable and mineral oil-in-water emulsion cutting fluids in turning AISI 4340 steel with coated carbide tools on the surface roughness and cutting force. The study involved the selection of cutting fluid additives for the formulation of oil-in-water emulsion, using palm kernel and cottonseed oils. Avila and Abrao's [13] work investigated the effect of emulsion without mineral oil, emulsion synthetic, emulsion with mineral oil on tool wear, tool life,

surface roughness and chip formation during turning of AISI 4340 steel with alumina tools. Onuoha et al. [14] studied, the effects of false walnut and groundnut oils based cutting fluids and commercial cutting fluid on surface roughness during turning of AISI 1330 alloy steel using high speed steel tool. Lawal et al. [15] studied the effect of emulsifier content on the properties of oil-in-water emulsion cutting fluid formulated using vegetable oil (palm kernel oil). Sanusi et al [16] evaluated the performance of cutting fluids from neem seed oil and commercial cutting fluid on surface roughness and flank wear in turning of aluminium manganese alloy with carbide tools. Belluco and De Chiffre [17] used three vegetable based cutting oils including additives and a straight cutting fluid for performance study in turning, reaming and tapping operations. Results indicated that vegetable based cutting oils were superior to mineral oil.

In the present work, soyabean oil based cutting fluids with different emulsifiers were formulated and tested for their performance in machining. Also, physicochemical properties of the fluid like thermal conductivity and dynamic viscosity were measured at room temperature to understand the behavior of the fluids. The details of experimentation and results are presented in the following sections.

2.0   MATERIALS AND METOHDS

2.1   Materials

1.   Cutting Fluids

The two cutting fluids used in this study were sourced from soyabean oil. MobilMet424 cutting fluid was also used in order to compare results of the formulated cutting fluids. Refined soyabean oil was sourced from Falke Industries Limited, Kaduna Nigeria. And the formulation of oil-in-water cutting fluids was done at a ratio of one litre of cutting oil to nine litres of water (1:9) for each of the oils.

The following additives were used in the formulation of the cutting oils.

   i.   Emulsifiers (Potassium soap and ammonium bromide).
  ii.   Zinc dialkyldithiophosphate were used as anti-aging additive, antiwear additive and corrosion inhibitor.
 iii.   Sulfonate was used as detergent and it also prevents corrosion.
 iv.   Phenolate was used as biocide and dispersant.
  v.   Silicon polymer was used as anti-foaming additive and viscosity index improver.
 vi.   Diamine was used as metal deactivator.
vii.   Organic sulphide was used as antioxidant.

The quantities of all these additives were constant with the exception of the emulsifiers and each formulated oil contained one emulsifier. Detergent, antiwear additive, friction modifier, and

corrosion inhibitors, was added in reduced quantities in the oil due to the presence of phosphate, sulphate and the content of oleic acid in the soyabean oil. There was no need for extreme pressure additives and passive extreme pressure additives, as machining is not done under pressure and the cutting oil is not a solid lubricant.

2.   Workpiece

Round EN8 carbon steel bars of diameter 38mm and length 2200mm each: purchased and cut to size of 38mm diameter and length of 150mm at Folor – Hammed Unique Technical Limited, Kaduna. The elemental analysis of the material is presented in Table 1, and the hardness of the material is 201-255 Brinell [18].

Table 1: Elemental analysis of EN8 carbon steel

	Carbon	Silicon	Manganese	Sulphur	Phosphorus
Minimum weight (%)	0.36	0.10	0.60	-	-
Maximum weight (%)	0.44	0.40	1.00	0.05	0.05

Source: Smith, 2017.

3.   Machine/Cutting Tool and Measuring Instruments

Mitchell of Keighly Lathe and three High Speed Steel Tools (HSS); available at Folor – Hammed Unique Technical Limited, Kaduna were used in this study. Surface roughness tester was used to determine the surface finish of each work piece and a digital thermometer was used to obtain the cutting temperature.

2.2   Method

2.2.1   Experimental Design

Three machining parameters were varied during machining, it was determined that 9 experiments were carried out per cutting fluid, to obtain adequate results for comparison of the formulated cutting fluids and MobilMet424 cutting fluid. The parameters to be varied are cutting speed, depth of cut and feed rate, with surface finish and temperature to be measured after each machining operation as results to be analysed. Twenty-seven (27) experiments were carried out in total (9x3).

Table 2 shows the experimental design for the machining process of EN8 carbon steel with the formulated cutting fluids and conventional cutting fluid.

Table 2: Experimental design for machining

S/No.	Cutting Speed (rpm)	Depth of Cut (mm)	Feed rate (mm/rev)
1	93	0.5	0.4
2	93	1.0	0.6
3	93	1.5	0.8
4	126	0.5	0.6
5	126	1.0	0.8
6	126	1.5	0.4
7	159	0.5	0.8
8	159	1.0	0.4
9	159	1.5	0.6

2.2.2   Machining Conditions

The machining process involved the turning of the workpieces on a Mitchell of Keighley Lathe. The turning of each sample was carried out for 3 minutes and cutting temperature was measured during the machining and the surface roughness of each workpiece was measured after machining was complete.

2.2.3   Physicochemical analysis

Physicochemical analysis has to do with measuring the various physical properties of a sample. These include, thermal properties (thermal conductivity, flash point, pour point), electrical properties (conductivity). Physical properties (viscosity and density) were also measured on the formulated oil samples. All the physicochemical analysis of the formulated oils was carried out in the Chemical Engineering Laboratory of Kaduna Polytechnics and Spectral Laboratories, Kaduna.

Figure 1: Digital Thermometer and Surface roughness tester

3.0   RESULTS AND DISCUSSION

3.1   Results of Physicochemical Analysis

The colour of soyabean oil with potassium soap as emulsifier before being mixed with water presented a golden yellow colour while, that of soyabean oil with ammonium bromide also presented a golden yellow colour and that of conventional cutting oil presented a dark tan colour. The colour of soyabean oil with potassium soap as emulsifier after being mixed with water presented a milky colour while, that of soyabean oil with ammonium bromide presented a light grey colour and that of conventional cutting oil presented a milky white colour. Fourteen physicochemical analyses were carried out. These analyses included, viscosity, kinematic viscosity, thermal conductivity, flash point, pour point, density, specific gravity, fire point, free fatty acid test, acid value, iodine value, PH value, refractive index, saponification value. The results of the influence of these additives on these physicochemical properties of soyabean oil are as presented in Figures 3, 4 and 5, and discussed.

Table 3: Physicochemical Properties of Pure Soyabean Oil

S/No	Properties	Value
1	Specific gravity	0.964
2	Flash point (°C)	298

3	Pour point (°C)	-10
4	Kinematic viscosity (40°C) (c. St.)	6.079
5	PH value	5.9
6	Free fatty acids (as % Oleic acid)	7.5
7	Refractive index	1.474
8	Viscosity (c. St.)	6.300
9	Fire Point (°C)	310
10	Thermal conductivity (W/mK)	0.18
11	Density (mg/l)	1.003
12	Iodine Value ($I_2/100_g$ of oil)	73.34
13	Saponification Value (mg KOH/g)	210.38
14	Acid value (mg KOH/g)	15.15

Physicochemical properties of soyabean oil with potassium soap as emulsifier (SBOP).

Below in table 4 is presented the physicochemical properties of soyabean oil with potassium soap as emulsifier.

Table 4: Physicochemical properties of soyabean oil with potassium soap as emulsifier.

S/No	Properties	Value
1	Specific gravity	0.910
2	Flash point (°C)	289
3	Pour point (°C)	-11
4	Kinematic viscosity (40°C) (mm^2/s)	6.125
5	PH value	4.6
6	Free fatty acid (FFA) (%)	6.8
7	Refractive index	1.885
8	Viscosity (mm^2/s)	6.590
9	Fire Point (°C)	296
10	Thermal conductivity (W/mK)	0.23
11	Density (kg/m^3)	910
12	Iodine Value (I$_2$/100$_g$ of oil)	52.06
13	Saponification Value (mg KOH/g)	212.87
14	Acid value (mg KOH/g)	16.85

Physicochemical properties of soyabean oil with ammonium bromide as emulsifier (SBOA).

Below in table 5 is presented the physicochemical properties of soyabean oil with potassium soap as emulsifier.

Table 5: Physicochemical properties of soyabean oil with ammonium bromide as emulsifier.

S/No	Properties	Value
1	Specific gravity	0.915
2	Flash point (°C)	285
3	Pour point (°C)	-14
4	Kinematic viscosity (40°C) (mm^2/s)	6.198
5	PH value	6.3
6	Free fatty acid (FFA) (%)	6.9
7	Refractive index	1.960
8	Viscosity (mm^2/s)	6.660
9	Fire Point (°C)	292
10	Thermal conductivity (W/mK)	0.20
11	Density (kg/m^3)	915
12	Iodine Value ($I_2/100_g$ of oil)	50.35

13	Saponification Value (mg KOH/g)	210.27
14	Acid value (mg KOH/g)	10.78

As seen in Table 4, 5 and 6 the selected additives had a significant effect on the physicochemical properties of the cutting oil. Presence of free fatty acid encouraged oxidation reactions which are exothermic in nature thus emitting more heat [19]. There was an increase in the density, specific gravity, pH value, viscosity, kinematic viscosity, refractive index, density, and thermal conductivity of the formulated cutting oils when compared to results of the physicochemical analysis of the pure soyabean oil. There was also decrease in the fire point, fire point, pour point, iodine value, acid value, and free fatty acid content of the formulated cutting oils when compared to results of the physicochemical analysis of the pure soyabean oil. The emulsifiers used in the formulation of the cutting oils helped to preserve the stability of the cutting oils in water, and the oils were very miscible in water after it has been mixed with water.

With pH values of 4.6 and 6.3, it indicates that the formulated oil with potassium soap as emulsifier is more acidic than the formulated oil with ammonium bromide as emulsifier. With increase in acidity, there will be an increase in the assembly of oxidation effects in the oil, as acidity of oil provides a source for monitoring oil state during use [20] and according to Hong and Broomer 2000, [21] the pH of a coolant can help to reduce corrosion of workpiece and machine tool and influences the microbial activity. The specific gravity of the formulated oils is less than the specific gravity of water, and the specific gravities are within the range of 0.72 to 0.92, which is the standard range of lubricants [22]. The flash point of both oils being 289°C and 285°C respectively indicate that both oils can be used as cutting oil since vegetable oils have high flash points which are safe in fire vulnerable processes [18]. The flash points of both oils can be compared to the flash point of other vegetable oils.

3.2   Cutting Fluid Performance on Machining

The performance of the formulated fluids was compared with that of the conventional cutting fluid using the experimental design by evaluating surface finish and temperature. The emulsified cutting oil was mixed with water in the ratio of 1 litre of modified oil to 9 litres of water. Machining with cutting fluid with potassium as emulsifier was carried out next then, the cutting fluid with ammonium bromide as emulsifier was used and machining with conventional cutting fluid was carried out finally. The results of the machining process are presented in tables 6, 7, and 8.

Table 6: **Result of machining with emulsified cutting fluid with potassium soap as emulsifier (SBOP).**

Cutting Fluid	Cutting Speed (rpm)	Depth of Cut (mm)	Feed rate (mm/rev)	Surface finish (µm)	Cutting Temperature (°C)
SBOP1	93	0.5	0.4	5.640	44.00
SBOP 2	93	1.0	0.6	8.041	56.80
SBOP 3	93	1.5	0.8	10.480	65.10
SBOP 4	126	0.5	0.6	3.882	47.00
SBOP 5	126	1.0	0.8	8.981	62.60
SBOP 6	126	1.5	0.4	7.120	63.10
SBOP 7	159	0.5	0.8	10.920	56.90
SBOP 8	159	1.0	0.4	9.980	64.60
SBOP 9	159	1.5	0.6	12.001	68.60

Table 7: Result of machining with emulsified cutting fluid with ammonium bromide as emulsifier (SBOA).

Cutting Fluid	Cutting Speed (rpm)	Depth of Cut (mm)	Feed rate (mm/rev)	Surface finish (µm)	Cutting Temperature (ºC)
SBOA1	93	0.5	0.4	6.620	41.00
SBOA 2	93	1.0	0.6	7.580	51.60
SBOA 3	93	1.5	0.8	9.161	67.70
SBOA 4	126	0.5	0.6	3.840	45.80
SBOA 5	126	1.0	0.8	8.484	61.10
SBOA 6	126	1.5	0.4	7.881	68.40
SBOA 7	159	0.5	0.8	10.720	46.40
SBOA 8	159	1.0	0.4	7.401	63.50
SBOA 9	159	1.5	0.6	14.320	68.90

Table 8: Result of machining with conventional cutting fluid (CCF).

Cutting Fluid	Cutting Speed (rpm)	Depth of Cut (mm)	Feed rate (mm/rev)	Surface Finish (µm)	Cutting Temperature (ºC)
CVO1	93	0.5	0.4	7.841	44.40
CVO2	93	1.0	0.6	8.001	54.70
CVO3	93	1.5	0.8	8.360	68.80
CVO4	126	0.5	0.6	3.721	44.60
CVO5	126	1.0	0.8	8.481	63.60
CVO6	126	1.5	0.4	7.241	69.80
CVO7	159	0.5	0.8	10.480	50.60
CVO8	159	1.0	0.4	8.321	63.20
CVO9	159	1.5	0.6	11.521	68.00

3.3 Observations and discussions about the performance of cutting fluids on machining.

After the machining process was completed the following observations were made from the results of the surface finish and temperature in relations to the objectives of this research work:

i. The emulsion cutting fluids formulated and were able to perform their basic functions as metal cutting fluids during machining, which proved that the objective of formulating emulsifiers for soyabean oil was duly achieved.

ii. With both increase and decrease in some of the physicochemical properties of the formulated cutting fluids, the cutting fluids when mixed with water, showed the same reaction conventional cutting fluid made with water when mixed. The colour of the water and the oils emulsified with the water nonviolently.

iii. From the results of the dry machining using the intermediate parameters of (126rpm, 1.0mm, 0.6mm/rev), the surface finish (8.441µm) and cutting temperature (87.90^{o}C) was improved with the use of all the three cutting fluids during machining.

iv. When machining with the soyabean oil with potassium soap as emulsifier, the oil preserved the surface of the steel (i.e. there was no corrosion), it cooled the cutting tool and workpiece, when compared with the performance of conventional cutting fluid. As presented in Table 4.3, the cutting temperature of 87.90^{o}C for dry machining was reduced considerably to when machining with cutting fluid. The reduced cutting temperature ranged between 41.00^{o}C to 69.60^{o}C, as the was changes in cutting conditions which in turn affects the cutting temperature.

v. The lowest cutting temperatures of 47.00 ^{o}C, 45.80 ^{o}C, 44.60 ^{o}C respectively, for the three cutting fluids (SBOA, SBOP, CCF) used were all obtained when machining at a speed of 126rpm, with depth of cut at 0.5mm and using a feed rate of 0.6mm/rev.

vi. The formulated cutting fluids, also had similar effects on the surface finish and cutting temperature, when compared to the effects of the use of conventional cutting oil on the surface finish and cutting temperature.

vii. The best surface finishes of 3.882 µm, 3.840 µm, 3.721µm respectively, for the three cutting fluids (SBOA, SBOP, CCF) used were also obtained when machining at a speed of 126rpm, with depth of cut at 0.5mm and using a feed rate of 0.6mm/rev.

viii. When machining with the soyabean oil with ammonium bromide as emulsifier, the oil performed the functions of a cutting fluid, but as the experimental workpiece was removed from the machine and left for a while the surface of the workpiece started to corrode mildly. This is being due to the increased pH value (6.3) of the formulated oil which in turn led to acidity of the oil being reduced.

ix. The formulated cutting fluid did not give off any offensive smell, it was not reactive on the skin of the operator and was easily absorbed when droplets of the fluids dropped on the floor of the workshop.

4.0   Conclusion

The cutting temperatures and surface finish results obtained from machining with the formulated oils ascertained that presence of these additives in the oils improved the effectiveness as cutting fluids, as the oils were miscible with water due to the addition of emulsifier and performed the basic functions of metal cutting fluids according to Abu, 2011 [1].

From the results of cutting temperatures and surface finish obtained from machining with conventional cutting fluid compared with those of soyabean oil with potassium soap as emulsifier, it is satisfactory to say that, emulsified soyabean oil with potassium soap as emulsifier is a very good metal cutting fluids. It is also concluded that, using ammonium bromide as emulsifier is not advisable, due to the corrosion of the EN8 carbon steel observed after machining.

Soyabean oil is available in abundance and can be easily sourced in some major cities in Nigeria. Although soyabean oil is an edible vegetable oil, the financial implication of using it as cutting fluid is very low due to the fact that, soyabean is abundantly available in Nigeria.

From the results of the physicochemical analysis and observations made during the application of the formulated cutting fluids, soyabean oil can be used as an alternative to conventional cutting fluid, as it is environmentally friendly, easily degradable and it is also renewable.

Reference

1. Abu, J.O. (2011) Manufacturing Engineering and Production Management, Aboki Publishers, Makurdi, 290.
2. Abu, J.O. (2011) Manufacturing Engineering and Production Management. Aboki Publishers, Makurdi, 275-287.
3. Abu, J.O. (2011) Manufacturing Engineering and Production Management. Aboki Publishers, Makurdi, 289-291.
4. Alander, J. and Warnhein, T. (1989) Model Microemulsions Containing Vegetable-Oils 1, NONIONIC Surfactanct systems. Journal of the American Oil Chemists Society, 66, 1656-1660.
5. Lawal, S.A., Choudhury I.A. and Nukman, Y. (2012) Application of Vegetable Oil-Based Cutting Fluids in Machining Ferrous Metals—A Review. International Journal of Machine Tools & Manufacturing, 52, 1-12.
6. Sujan D., Moola M. R., Qua S. Y., (2014). Environmental friendly cutting fluids and cooling techniques in machining: a review. Journal of Cleaner Production 83 33e47.
7. Cetin, M.H., Ozcelik, B., Kuram, E. and Demirbas, E. (2011) Evaluation of Vegetable Based Cutting Fluids with Extreme Pressure and Cutting Parameters in Turning of AISI 304L by Taguchi Method. Journal of Cleaner Production, 19, 2049-2056.
8. Alves, S.M. and Oliveira, J.F.G. (2006) Development of New Cutting Fluid for Grinding Process Adjusting Mechanical Performance and Environmental Impact. Journal of Materials Processing Technology, 179, 185-189.
9. Adhvaryu, A. and Erhan, S.Z. (2002) Epoxidized Soybean Oil as a Potential Source of High Temperature Lubricants. Industrial Crops Production, 15, 247-254.
10. Erhan, S.Z. and Asadauskas, S. (2000) Lubricant Base Stocks from Vegetable oils. Industrial Crops Production, 11, 277-282.
11. Jacob, J., Bhattacharya, M. and Raynor, P.C. (2004) Emulsions Containing Vegetable Oils for Cutting Fluid Application. Colloids and surface A: Physiochemical Engineering Aspects, 237, 141-150.
12. Lawal, S.A., Choudhury, I.A., and Nukman, Y. (2014) Evaluation of Vegetable and Mineral Oil-in-Water Emulsion Cutting Fluids in Turning AISI 4340 Steel with Coated Carbide Tools. Journal of Cleaner Production, **66**, 610-618.

13. Avila, R.F. and Abrao, A.M. (2001) The Effect of Cutting Fluids on the Machining of Hardened AISI 4340 Steel. Journal of Material Processing Technology, **119**, 21-26.

14. Onuoha, O.J., Abu, J.O., Lawal, S.A., Mudiare, E. and Adeyemi, M.B. (2016) Determining the Effect of Cutting Fluids on Surface Roughness in Turning AISI 1330 Alloy Steel Using Taguchi Method. Modern Mechanical Engineering, **6**, 51-59.

15. Lawal S.A, Ugheoke B.I, Woma T.Y., Ikporo J.U., Ogundare T.A, Nonye C., and Okoye I.G, "Effect of Emulsifier Content on the Properties of Vegetable Oil Based Cutting Fluid." American Journal of Materials Engineering and Technology, vol. 3, no. 3 (2015): 63-69. doi: 10.12691/materials-3-3-3.

16. Sanusi O. M., Bello Y., Akindapo J. O., (2015). Evaluating the performance of different types of cutting fluid in The machining of aluminium-manganese alloy in turning operation. International journal of innovation sciences and research Vol.4, no, 8, pp.355-360. Available online at Http://www.ijisr.com

17. Belluco, W. and De Chiffre, L. 2001. "Testing of Vegetable- Based Cutting Fluids by Hole Making Operations", Lubrication Engineering, Volume 57, pp 12-16

18. Smiths Metal Centres, (2017), EN8 Technical Datasheet, sales@smithmetal.com, www.smithmetal.com. 21/4/2018.

19. Gulizar Atmaca (2004). Antioxidant effects of sulfur-containing amino acids. Yonsei medical journal. 45(5), 776-788. Doi: 10.3349/ymj.2004.45.5.776.

20. Oseni, M. I., Agbi, B. E., and Ogamenyi. I. O. (2014). Extraction and Analysis of Chemo-Physical Properties of Yellow Oleander Oil as Lubricant, British Journal of Applied Science and Technology 4(6): 1020-1029.

21. Hong, S. Y., and Broomer, M. (2000). Economic and ecological cryogenic machining of AISI 304 austenitic stainless steel. Clean Prod. Proc. 2:157–166.

22. Godfrey, D., Herguth H. R. Back to basics; physical and chemical properties of industrial mineral oils affecting lubrication. Parts 1-5. Society of Tribologists and Lubrication Engineers, Illinois. 1995. Available: http://www.stle.org/

DESIGN OPTIMIZATION OF A SMALL SCALE WIND TURBINE FOR GENERATING ELECTRICITY CONSIDERING SITE-SPECIFIES

[1]**OSENI Jelili Olaoye,** [2]**Alkali Babawuya,** [3]**Yusuf Samiu adedeji,** [3]**Cliford Ogeneme O. and** [4]**Paul Obandoma**

[1]Department of Mechanical Engineering, Federal University of Technology, Minna, Nigeria
[2]Department of Mechatronics Engineering, Federal University of Technology, Minna.
[3]Department of Mechanical Engineering, Wairi Umaru Federal Polytechnic, Birnin Kebbi.
[4]Department of Mechanical Engineering, Niger State Polytechnic, Zungeru

Abstract

Wind turbines are complex engineering systems, subject to highly fluctuating and irregular loads. The wind energy has been utilized in Nigeria, may be because of the technology know how. A three blade horizontal wind turbine was design, fabricated and tested to supply 400W electricity. Also, a computer simulation in other to determine some deign parameters was carried. The optimal design of wind turbines, in particular the blades is a nontrivial task. The fluctuation of the out-of-plane bending moment at the blade root was minimized by maintaining the required power of the wind turbine. Through the redistribution of the section force in the radial direction between both the primary and tip regions. A wind speed of 3.8 m/s was recorded at the test site and a maximum power of 278W was produced by the turbine. The designed wind turbine has an extraction efficiency of 18%. The maximum power was recorded in the mid-night.

Key Words: Horizontal, Wind, Turbine, Blade, Tip- speed ratio.

1.0 INTRODUCTION

The availability of energy plays a major role in every aspect of our socio-economic life. Energy is, and will always be, a key component of the economic, social and political development of Nigeria. Inadequate supply of energy restricts socio-political development, limits economic growth, inclusive growth in particular, and adversely affects the quality of life of citizens, both in urban and rural areas. Improved energy supply results in improved standards of living, which manifests in increased food production and storage, increased industrial output, provision of efficient transportation, adequate shelter, improved healthcare and enhancements in other human services. Nigeria is blessed with abundant primary energy resources. These include non-renewable energy sources such as natural gas, crude oil, coal and tar sands; and renewable energy sources such as hydro, biomass, solar and wind. The Nigerian energy commission has developed a wind energy target programme and proposes 55 MW, 631 MW and 3,211 MW by the year 2015, 2020 and 2030 respectively. According to (Nigerian Energy Commission, 2015), presently Nigeria generates less 10 MW of electricity and there is 0 MW of wind turbine for electricity. Therefore, the set target has not been met. This may be due to non-availability of home grown wind technology.

There has been increasing demand for renewable energy since 1980s due to the oil crisis. In recent time, the Nigerian oil reserve have been estimated to finished in less than 50 years if the 2.4 Million barrel extraction continues, this mean that the future of sustainable energy supply is on the

215

renewable energy source such as wind. This reason explains the exponential increasing global demand and installation of wind capacity as shown in figure 1.
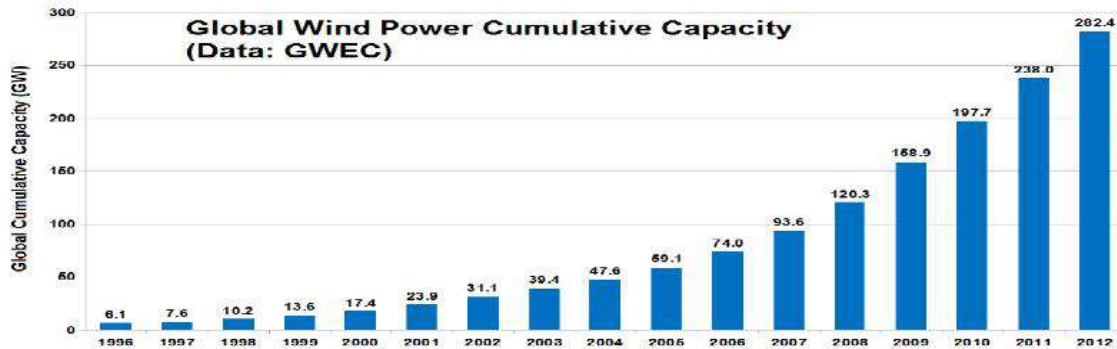

Figure 1: Global wind power cumulative capacity (Xiaomin, 2014)

According (Liu & Jia, 2015), wind turbine is a mechanical device which converts wind energy into electric energy. And it is the most important part of wind energy industries. Many types and kinds of wind turbine have been developed and installed as found in (**sources**) but according to (Xiaomin, 2014) there two types of the wind turbines i.e. Horizontal axis wind turbine (HAWT) and vertical axis wind turbine (VAWT). This research is focus on horizontal axis wind turbine, because they were to found to have high efficiency in power production. The differences between the two is that, for HAWT rotor-shaft and generator axis are horizontally aligned, while the VAWT rotor-shaft-generator are align to vertical axis, (see figure 1.1).

(a)   (b)

Figure 2: Wind Turbines Types. (a) HAWT, (b) VAWT.

2. MATERIALS AND METHOD

2.1 Materials

This section presents the details specification of the materials used and the method of the design analysis of the 400W wind turbine. In the methodology, the wind turbine structure was designed for strength and stability in the operating condition, this was followed the optimization of the critical components, this includes the blade, shaft, gearbox and the tower.

The materials used and their specifications are listed in table 1;
Table 3.1: List of Materials Used.

S/No	Material	Specification
1.	Turbine Blade	PVC Material
2.	The Tower	Mild steel
3.	Generator	400W, 12 V DC
4.	The casing	Al-alloy
5.	Shaft	PTFE (Teflon)
6.	Hub	Al-alloy

2.1.1 Description and Concept of the HAWT

The basic configuration of a HAWT is shown in figure 1, this is comprise of a generator which produces electricity by turning the coil inside a magnet at certain speed and configuration. Therefore, blade was used to rotate a shaft which also turns the coil in a generator that produces electricity. The wind low speed from the wind was stepped up with a pulley – robe drive. (figure 1). The wind turbine is required to effectively operate at a height of <=10m.

217
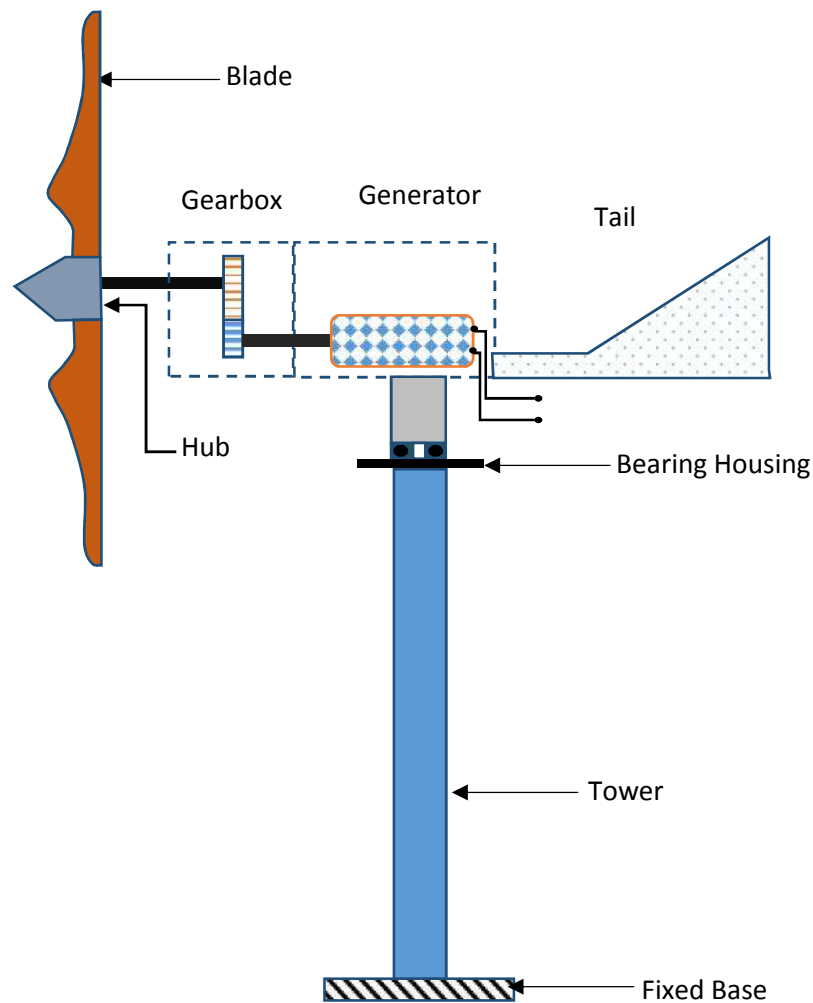
Figure 1: Schematic Drawing of Wind Turbine.

3. Design Analysis and Calculations

3.1 Design Requirement and Criteria

The following are design requirements based on the working environment and desired capacity of the wind turbine.

- Mean wind speed of the study site 4.3m/s
- Maximum Power 400W.
- Operating Height 15 m above sea level.
- The wind turbine should be able to follow the wind direction.

The criterion for design of the Wind turbine is for small wind turbine with a start velocity of 2 m/s and has 3 plastic blades.

3.2 Design Analysis and Synthesis

The approach used for the design of the wind turbine is modular design approach, i.e. each of the components was designed in turn. The site specific considerations that are important to this design is the lowest and average wind speed of 2 m/s and 4.3 m/s respectively. FUT Minna wind data were retrieved from WASCAL, FUT Minna. It shows that Minna has air average maximum wind speed of 8.3m/s, mean wind speed of 2.25m/s and average minimum of 4.3m/s.

3.2.1 Blade design

Blade utilizes wind power to generate a rotating motion. Therefore, parameters such as its area, thickness, volumetric flow rate, power are estimated as follows:
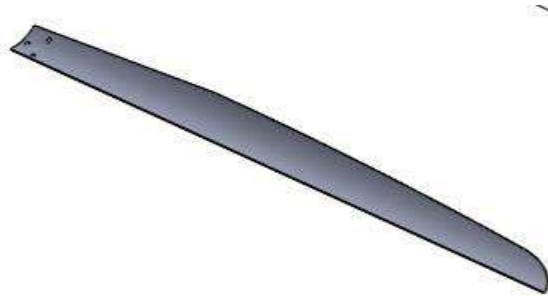
Figure 3.2: Isometric view of the blade

Mass of the blade, M_b = 0.175Kg.
Density (ρ_b) = 1300 kg/m³.
Thickness of blade - 5 mm.
Modulus of Elasticity, E = 241 N/mm^2
Yield Stress, = 145MN/mm^2.
The shape of the blade is in the form of a trapezium, and the area of a trapezium is given by;

$$A_b = \frac{1}{2} (A + B) \times l \quad \text{(Myszka, 2004)} \tag{1}$$

Where A is chord of the smallest station, B is chord of the largest station and I is length of the blade or rotor radius

$$A_b = \frac{1}{2} (0.06 + 0.12) \times 0.8 = 0.072 m^2$$

The actual delivered power P_a of the rotor must be equal to the required power.

218

Hence, equating equation (4) and (5)

$$P = \frac{1}{2} A_s v^3 C_p$$

This implies;

$$400 = \frac{1}{2} \, 1.23 \times A_s \times 4.3^3 \implies A_s = 8.18 \, m^2$$

Where A_s is swept area, v is mean wind speed, C_p is power coefficient and   is density of air (1.23 kg/m^3). For a Horizontal Axis Wind Turbine (HAWT), the swept area is circular. Thus, the area of a circle is given by;

$$A_s = \frac{\pi}{4} D^2 \text{ (Myszka, 2004)} \tag{3}$$

From the above equation, the diameter of the rotor can be calculated as;

$$D = \sqrt{\frac{4 \times 8.18}{}} = 2.2 \, m$$

Hence, the rotor radius is given by;

$$R = \frac{D}{2} = \frac{3.23}{2} = 1.14m$$

Therefore, the blade angular speed ( ) is also given by;

$$\text{angular speed,} \quad = \frac{v}{R} \tag{4}$$

$$= \frac{4.3}{1.14} = 3.77 \, rad. \, s^{-1}$$

Taking a design speed of; $v_d = 2.3$ m/s. Then, the design angular speed can be calculated as thus;

$$= \frac{v_d}{R} = \frac{2.3}{1.14} \tag{5}$$

$$_c = 2.02 \, rad. \, s^{-1}$$

Hence, the theoretical torque (T_t) is given by;

$$T_t = \frac{P_w}{\omega} \tag{6}$$

$$= \frac{156.5}{1.43} = 109.4 \, N. \, m$$

Also, for the design angular velocity ($_d = 2.3$ rad/s);

$$T = \frac{P_w}{\omega_d} = \frac{156.5}{2.3} = 68.03 \, Nm \tag{7}$$

3.2.2 Tip Speed Ratio

The tip speed ratio is defined as the relationship between rotor blade velocity and relative wind velocity. The dimensions are calculated as:

$$= \frac{\omega R}{v} \text{ (Schubel \& Crossley, 2012)} \tag{8}$$

$$= \frac{2.3 \times 1.61}{4.3} = 0.5$$

A higher tip speed demands reduced chord widths leading to narrow blade profiles. This can lead to reduced material usage and lower production costs. The design tip speed ratio is calculated using the formula below;

$$\lambda_d = \frac{\omega_d R}{v_d} \tag{9}$$

$$= \frac{1.19 \times 3.23}{2.3} = 0.861$$

The coefficient of starting torque is given as;

$$C_{T_{start}} = \frac{1}{2\lambda_d^2} \tag{10}$$

Where; $C_{T_{start}}$ = coefficient of starting torque

$\cdot$ = design tip speed ratio

$$C_{T_{start}} = \frac{1}{2 \times 0.861^2} = 0.67$$

3.2.3 Calculation of blade setting angle (ß)

The blade is divided into six (6) equal segments with a step of 0.27m. The blade setting angle can be obtained from the following relation;

$$= \frac{2}{3} \tan^{-1} \frac{1}{\lambda_r} \text{ (Douglas et al., 2006)} \tag{11}$$

Where ⌐ is blade setting angle, and $_r$ is mean of the local tip speed ratio

Hence, $_r = \frac{\lambda_d \, X \, r}{R} \tag{12}$

Where   is design tip speed ratio, r is radius at each stations of the blade and R is rotor radius.

3.2.4 Shaft Design

The Shaft transmits twisting moments from rotation of the blade and simultaneously subjected to bending due to the weight of the loads on it. Therefore, the equivalent twisting moment was obtained from equation 13,

$$T = \sqrt{(K_m \times M)^2 + (K_t \times T)^2} \quad \text{(Babawuya, 2009)} \tag{13}$$

Where K_m = combined shock and fatigue factor for bending

K_t = combined shock and fatigue factor for twisting

Were;

$$T = \frac{\pi}{16} X \cdot X \, d^3 \quad \text{(Babawuya, 2009)} \tag{14}$$

Where, τ = maximum shear strength of mild steel

d = shaft diameter (mm)

M = maximum bending moment (Nm)

T = torque developed (Nm)

The schematic of the shaft is shown in figure 3.3; from which the maximum bending moments was obtained by considering the equilibrium conditions of the beams.
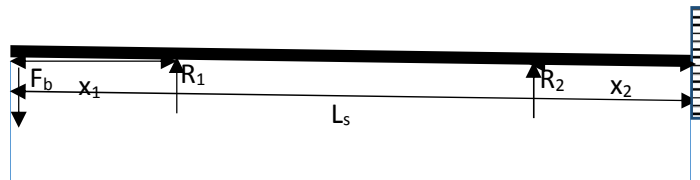

Figure 3.3: The shaft.

Considering the equilibrium of the all the loadings, determining the reaction forces and estimating the shear forces and bending moment n the shaft.

R_c = 7.43N

And R_b = 22.39N

We know that B.M at A and D = 0

The equivalent twisting moment of the shaft were estimated using the bending moment and the twisting moments on the shaft as follows:

$$T = \sqrt{(K_m \times M)^2 + (K_t \times T)^2} = \sqrt{(1.5 \times 20.1)^2 + (1.0 \times 31.53)^2} = 43.63 \text{Nm}$$

Also, the minimum shaft diameter were obtained as follows:

$$\frac{}{16} X \quad X \, d^3 = T$$

220

And therefore, d = 0.0164m = 16.4mm

3.2.5   Tower Design

The tower is the tall structures that support all other wind turbine structure and also provide the blades with the need height to be able to assess the required height. This is subjected to the loads of all other components it is carrying and the blade drags force effect. The tower is designed as column with fixed-free end conditions and its sizing was obtained using Euler Buckling formula (equation 3.25) as sited in Alkali, (2009).

From Euler Buckling formula,

$$P_{cr} = \frac{c_{ends}\pi^2 EI}{l^2}\text{(Babawuya, 2009)}$$

4.0 Results And Discussion

4.1 Design Results

The following design results were obtained from the design section of this project:

Table 4.1: Design Results

S/No	Results	Values/Units
1	Blade thickness	3.67mm
2.	Blade Swept area	$8.18m^2$
3	Blade angular speed	3.77 m/s
4.	Shaft diameter	13.67 mm
5.	Shaft torque	109.4 N.m
6.	Design angular velocity	2.3m/s
7.	Tip speed ratio	0.5
8.	Design tip speed ratio	0.861
9.	Blade wind extraction efficiency	18%
10.	Coeff. Of starting torque	0.67
11	Wind turbine coeff. Of performance	79%

The design analysis of the major components shows that the wind turbine has a wind extraction efficiency of about 18% and a tip speed ratio of 0.5. The torque transmission mechanism has a design efficiency of 79% which make the delivered torque to the wind turbine to be above 80 Nm. That is why a low speed wind turbine generator was used.

4.2 Simulation Results

The wind turbine blade was subjected to a static analysis with a wind speed of 4.3 m/s and the results in figure 4.1-4.3 were obtained. The results show that the fixed end of the blade was subjected to a stress of $3MN/mm^2$, while the yield stress of the plastic used is $69 MN/mm^2$. Also, figure 4.2 and 4.3 are displacement results of the blade, its shows that a maximum deflection 12 mm, which is equivalent to 1.5% of the blade length. The blade is stable because this is less than 5% of the blade length as recommended in the literatures.

(a)   (b)
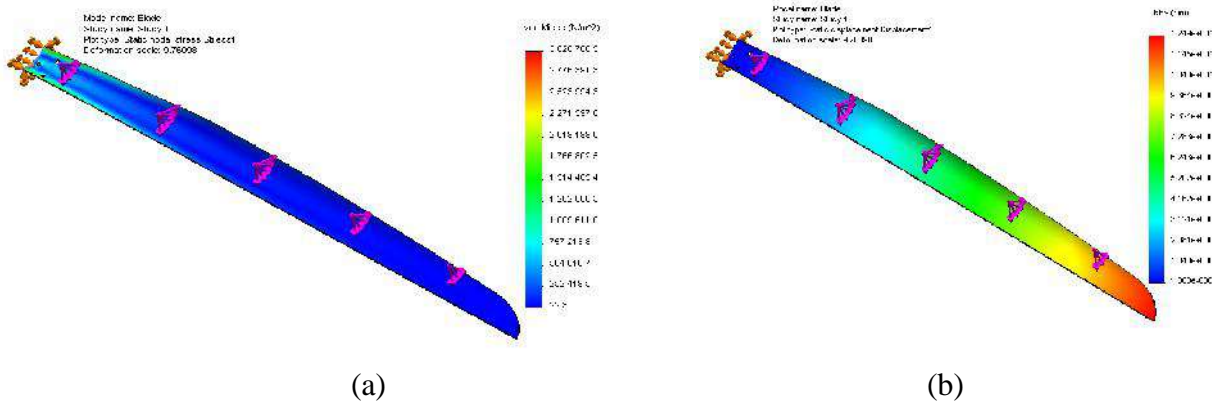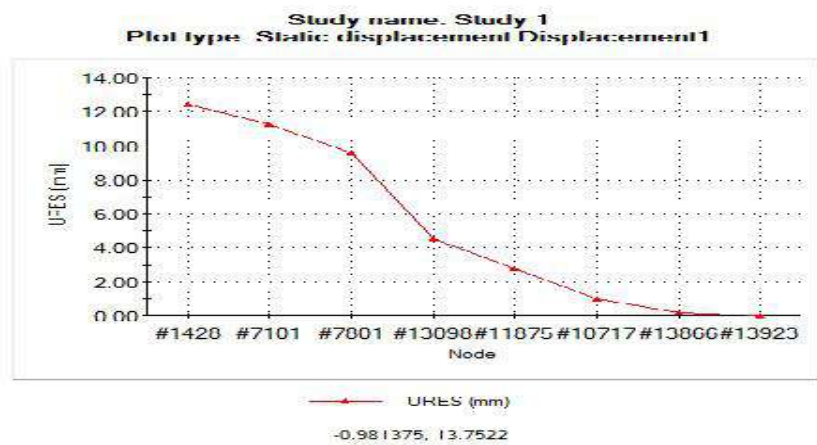
Figure 4.1: (a) stress color plot for the blade, (b) Deflection color plot for the blade.

Figure 4.3: static displacement result against the blade length.

4.3 Testing Result

The developed wind turbine was tested in the day time as while as in the night hours for four hours each. And the average power/wind speed recorded for both day and night hours are 178w/3. 01m.s and 230w/3.6m/s respectively.
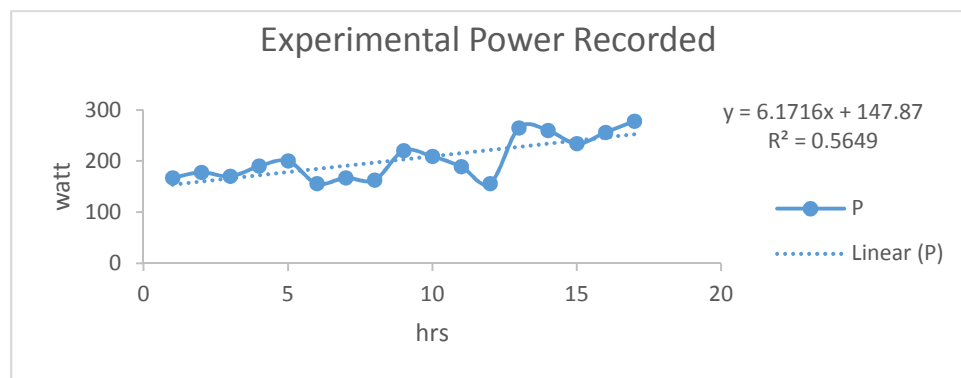

Figure 4.4: Recorded Power
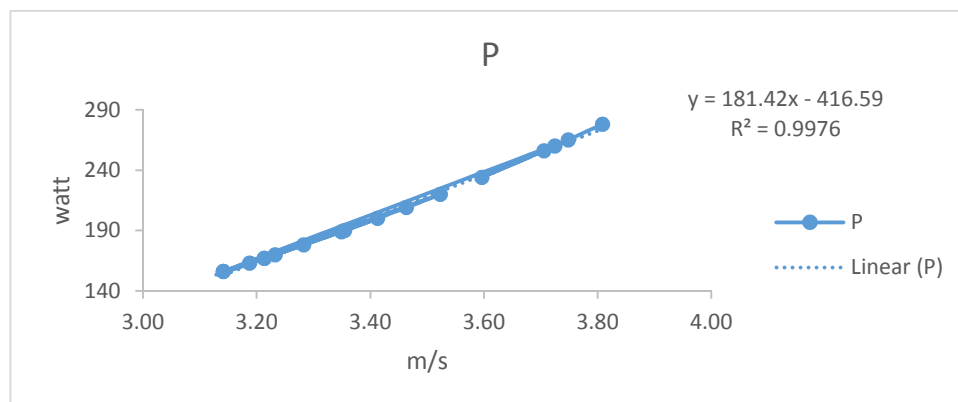
Figure 4.5: Relationship between powers generated and wind speed.

5.0   Conclusion

In this project a small wind turbine was developed using three (3) blades made from a PVC pipe. Design and optimization was performed for conditions of federal university of technology, Minna where average wind velocity is lower than International wind energy market. This different condition causes different design parameters distribution in same output power. A 18% wind extraction efficiency were calculated, while the design and produced wind turbine has an efficiency of 79%. During test the maximum power recorded is 278W from a 400W generator. Also, a wind speed of 3.8 m/s was recorded during the night hours at the test location. The torque developed was transmitted to the generator via a rope pulley arrangement.

References

Dhenge, S. D., Durge, M. P., and Wanve, A. (2015). Wind Turbine Water Pumping System. International Journal For Technological Research In Engineering.

Dodge, T. W. (2015, February 18). Illustrated history of wind power development. Retrieved from http://telosnet.com.html: http://telosnet.com/wind/early.html

Fraenkel, P. (1993). Water Pumping Devices: A Handbook for Users and Choosers. Radford Mill, Nottingham.: UK: IT Publications Ltd.

Gasiorek, J. M., Swaffield, J. A., Jack, L. B., and Douglas, J. F. (2005). Fluid Mechanics. London: Ashford Colour Press Ltd.

Gipe, P. (1993). Wind Power for Homes and Business: Renewable Energy for the 1990s and Beyond. Post Mills. VT: Chelsea Green Publishing Company.

Ijifr, V. E. (2015). Wind Turbine Water Pumping, 2(8), 2894–2897.

Lim, S., Kong, C., and Park, H. (2013). A Study on Optimal Design of Filament Winding Composite Tower for 2 MW Class Horizontal Axis Wind Turbine Systems, 3(1), 15–23.

Kothmire, P., Sharma, D., Kumbhare, B., and Choukade, S. (2015). Design and Development of Wind Turbine Operated Water Pump. Ijrerd.Com, 0869(12), 61–74.

Myszka, D. H. (2004). Machines and mechanisms. Pearson Education, Inc., publishing

N. Argaw, R. F. (2003). Renewable Energy for Water Pumping Applications in Rural Areas. Colorado: National Renewable Energy Laboratory.

Ogbonnaya, O., Edward, C., Oluseyi, P. O., and Govender. (2009). Conventional Energysources In Nigeria: A Statistical Approach.

Prasad, S. S., and Auradi, V. (2012). Optimized Design of Rotor Blade for a Wind Pump, 2(4), 4–7.

Raja, A., Srivastava, A. P., and Dwivedi, M. (2006). Power Plant Engineering. New Delhi: New Age International (P) Limited, Publishers.

Rao, S. S. (2009). Engineering Optimization. United States of America: John Wiley and Sons, Inc.

Salomonsson, S., and Thoresson, H. (2010). Wind Turbine Driven Water Pump For Small-Scale Irrigation And Domestic Use -In Lake Victoria Basin.

Schubel, P. J., and Crossley, R. J. (2012). Wind Turbine Blade Design. Energies .

Singh, R. (2006). Introduction to Basic Manufacturing Processes and Workshop Technology. Harvana: New Age International (P) Limited, Publishers.

Sun, J., and Xu, G. (2013). Deviation Analysis and Optimization of Offset Slider-crank Mechanism based on the Simulation. Information Technology Journal. , 12(12), 2390-2397.

Thomas, H. B. J. (2005). In M. Ken (Ed.), Marks' Calculations for Machine Design (p. 279). Raleigh, North Carolina: The McGraw-Hill Companies, Inc.

Vaz, C. B., and Ferreira, Â. P. (2012). Performance assessment of hydroelectric power plants Overview of Contents.

www.misouribusinees.net./article/calculating overhead and price. Retrieved on 10th February 2015

DEVELOPMENT OF SOLAR POWERED AGRICULTURAL SPRAYING MACHINE WITH THREE NOZZLES AND CHARGING STATION.

Okegbile, O.J[1], Okwum, C[1].

Department of Mechanical Engineering, Federal University of Technology, P.M.B 65 Minna, Niger State, Nigeria.
*Corresponding author email: charlesokwum@gmail.com, +243 803 8487065.

ABSTRACT

The use of pesticide and weedicide is an integral part of modern agriculture. It helps in production of quality crops be grown by farmers. For the purpose of weedicide and pesticide application. A solar operated sprayer of fifty (50) liters capacity was developed using locally available materials and its performance evaluated. The equipment is developed to eliminate the carrying of the knapsack and solar panel on the back of the farmer which is a problem in convention knapsack sprayer. The power station of 80w solar panel developed help to charge batteries continually which boast the spraying operations and increase productivity and spraying time. The developed sprayer has three nozzles which boast and increase the span of spraying especially in large hectares of farm land. The major components includes: tank, water pump, 12volts battery, delivery pipe and a sprayer handle together with lance and three nozzles. Laboratory and field test were carryout to determine flow rate, application rate, charging time, discharging with respect to time and distribution rate. Basic principle of hydraulic principles were considered for determine flow rate, while application rate was determined by effective use of walking speed on field. The result show the sprayer has a flow rate of 1207.5ml per minute, application rate of 0.1128978ml/m^2 and a spray distribution area of 0.6399m^2. The result from the laboratory test indicated that efficiency of spray decreases with decrease in voltage of battery and application rate is influenced by walking speed. However, it is recommended that a motorized trolley should be developed to aid in the movement of the tank for continues spraying and the whole system should be automated.

Keywords: Solar powered sprayer, design, application rate, charging time, nozzles, trolley.

1. INTRODUCTION

Minna city is located in the north central Nigeria. It is located 9.56$^\text{o}$latitude and 6.55$^\text{o}$ longitude and it is situated at an elevation of 243meters above sea level. The rainfall averages 1229mm. Awode (2015) reported that the average climate data in Minna has the following range ambient temperature (28.16-33.04$^\text{o}$C), solar radiation (206.24-272.55w/m^2), wind speed (1.73-4.73m/s) relative humidity (38.81-74.03%) with the data above, the city would be suitable for photovoltaic energy utilization. A sprayer is a mechanical device used in spraying the liquid like herbicides, pesticides, fungicides and fertilizers to drops in order to avoid any pest. A sprayer provides optimum utilization of pesticides or any liquid with a minimum effort.

In Nigeria farms, generally there are two types of spray pumps in use for spraying, they are

- Hand operated spray pump
- Fuel operated spray pump

Hand operated spray pumps are the most popular. The man drawback of hand operated spray pump is that the user cannot use it continuously for more than 4-5 hours since the user get tired after such a a long day. Also the fuel operated sprayer pump requires fuel which is expensive and availability of fuel at rural areas is difficult for the farmers to purchase. The knapsack spray or has been existing for more than 100 years been produce by Cooper Pegler (CP) company product. The sprayer used is reliable, precise and efficient.

Agriculture has been the backbone of Nigeria Economy which had before the advent of crude oil contributed tremendously to the infrastructural development of Nigeria and will continued to remain for a long time. In Nigeria today about 75% of population in one way or the other depends on farming as their sources of their lively hood. But most farmers are carrying sowing seed, apply fertilizers, weed and pesticides spraying and cultivating by old methods of farming.

In Nigeria today there is need for development in Agricultural sector and mostly on weedcide, pesticides and fertilizer spraying technique, the traditional ways requires more time and efforts.

I Nigeria, the concern to control weed, insects and plant diseases for quality yield of farming product is increasing. Plant spraying is employed for different purposes in traditional system of farming. In the system, spraying were done by dipping brooms, brushes or leaves into water mixed with chemical in a bucket or open container and sprinkling on the affected area. The traditional way of spraying is less effective and time consuming and of hand to push or pump to generate pressure at the interval of pray. In view of this, it becomes necessary to develop modern prayers that will overcome these problems. Several works have recently been done on different types of sprayer. Kshirsagar et al, (2016) designed and develop a solar photovoltaic sprayer which can move in field with help of manually drawn vehicle. According to Joshua et al. (2010) he developed a power sprayer with two stroke engines, it worked with fossil fuel, it could also be converted into solar sprayer worked without fuel. The stroke engine were replaced by a single motor and it can be operated by electrical energy stored in the 12V battery and could be charged by a photovoltaic panels. According to Khah, (2014) designed a knapsack sprays the level of the sprayer that pump the fluid at pressure was replaced with an electric pump that could be operated by solar panel or charged battery. Rao et al, (2013) in his work developed a multiple power supplied fertilizer sprayer. The sprayer is a modification of the existing two stroke petrol engine powered sprayer which reduces the difficult, such as the cost of fuel and pesticides, weedicides and fungicides. The full charged battery was to spray 580 liters of pesticides which covered 5 – 6 acres of land.

Sasaki et al, (2014) designed a knapsack solar photovoltaic sprayer with good spraying quality and minimize the physical effort of the farmer. He built an electric knapsack sprayer by fixing two solar panel. He evaluated the performance of his work via:

    i.   Static movement
   ii.   Potential movement

At the end of his evaluation, he discovered that while at static position he generated 2.18w, while in movement he generated 1.4W of energy.

Patil et al (2014) Reported that different types of sprayer have different effect on agriculture in term of safe gurdy. He used 37watt solar panel to capsize battery mode and direct solar panel mode. Dauda (2017) studied that backpack solar photovoltaic sprayer using 30W. Solar panel, in his work the sprayer was operated on a battery mode. Overall model design provided weight of panel as well as weight of the sprayer and battery on the shoulder of the farmer. Solar panel provided shadow on the head of the operator which gives protection from the sun intensity. The objective of the study is to develop a solar powered agricultural spraying machine with three nozzles and charging station.

2. Materials and methods
2.1 Materials

    During the course of this research work, development of solar powered agricultural spraying machine with three nozzles and charging station. The machine consists of the following components viz: Sprayer tank, Photovoltaic panel, 12v water submerge diaphragm pump, 12v Battery, Solar charge controller, Nozzles, Lance, and Switch.

2.2 Design Analysis and Calculation
2.2.1   Nozzle selection and sizing

The main function of nozzle in agricultural spraying is to break the liquid into droplet and form the spray pattern. The nozzles also determine the application volume at a given operating pressure, particles travel speed and spacing. The size of the particles is very important to both spray efficacy and spray drift on the chemical.

The nozzle types commonly used for agricultural sprayers are usually low pressure and includes, flat fan, hollow cone and full cone.

Flat fan nozzle type were selected because it has a lower pressure and have a 110^0 spray angle to 12 inch spacing overlap.(Andrew et al 2004).

2.3 Fluid Flow Analysis

The chemical pesticide in the tank was pumped into the nozzle via a tube (hose). Therefore, the pump exerts pressure on the fluid flow. The mass flow rate of the liquid is given by the equation below and this is a function of fluid density, fluid velocity and the cross sectional area of flow.

$$M = V_{av}A \tag{1}$$

Where;

A – Pipe cross sectional area

V – Average velocity

   - Fluid density

For a circular pipe, the flow velocity is zero from the pipe wall to the maximum velocity at the center of flow as illustrated in figure 1 below.
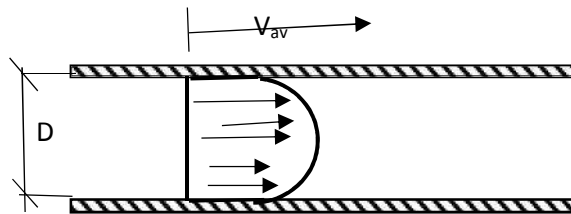

Figure 1.Velocity profile for circular pipe

The Reynolds number for the fluid flow in the pipe is expressed as given by the equation below.

$$R = \frac{V_{av}.D}{\nu} = \frac{\rho VD}{\mu} \tag{2}$$

Where;

   – Kinematic viscosity ($= \mu/\rho$), m^2/s

R_e 2300(for laminar flow).

The equation below, presents pressure drop for a laminar flow, i.e. from the pump head to the exit of the nozzle

$$P = P_1 - P_2 = \frac{32\mu LV_{avg}}{D^2} = f\frac{LeV^2}{2D} \tag{3}$$

$$f = \frac{64}{R_e} \tag{4}$$

For laminar flow, the continuity equation of the fluid flow, the equation relates the most important flow parameters expressed in the mass flow rate and Reynolds number, therefore,

$$\frac{P_1}{Pg} + \frac{V_1^2}{g} + z_1 = \frac{p_2}{pg} + \frac{V_2^2}{g} + Z_2 \tag{5}$$

2.4   Design Analysis for trolley

The forces acting on the frame of the spraying trolley in figure 2 are analyzed as follows.
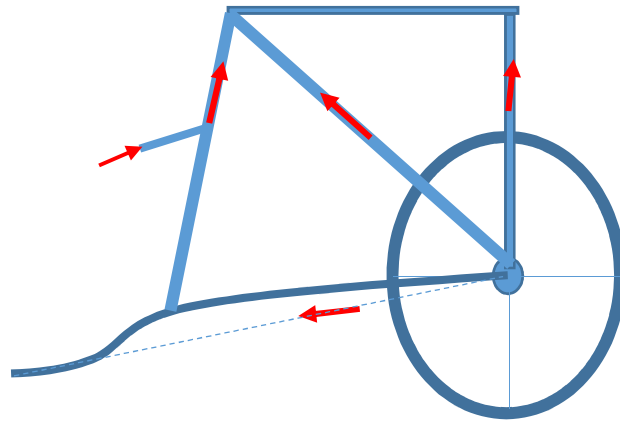

Figure 2: forces acting on the trolley.

Taking equilibrium of forces along the x and y axis and also the bending moment about the center of the wheel, gives the following equations.

$$f_x = 0 : -R_4\cos\theta_4 - R_2\cos{}_2 + R_5\cos{}_5 = 0$$

$$f_y = 0 : P_5\sin\theta_5 - P + R_1 + R_2\sin{}_2 + R_3\sin - R_4\sin = 0$$

$$m_0 = 0 : P.\frac{a}{2} - R_3.a - P_5.\sin{}_5.a = 0$$

Re-arranging equation gives;

$$R_2.\cos{}_2 + R_4\cos{}_4 = P_5.\cos{}_5$$

$$R_3.a = P.\frac{a}{2} + P_5.\cos{}_5.a$$

From the equations, the system is statically determined and therefore, will receive austere equation to solve for the four (4) unknowns in the systems of the equations. Therefore, considering the maximum deflection in beam AB

Figure 3: cross bar

The maximum bending moments

$$R_1.a - P.\frac{a}{2} = 0 \qquad R_1 + \frac{P}{2}$$

:. Therefore, the equation becomes,

$$R_2\sin{}_2 + R_3\sin\upsilon_3 + R_4\sin{}_4 = P - \frac{P}{2}$$

$$\begin{bmatrix} R_1 & R_2 & R_3 & R_4 \\ 0 & \cos\text{A}_2 & 0 & \cos\text{A}_4 \\ 0 & \sin{}_2 & 0 & \sin{}_4 \\ 0 & 0 & \frac{a}{2} & 0 \end{bmatrix} \begin{bmatrix} R_2 \\ R_3 \\ R_4 \end{bmatrix} = \begin{bmatrix} 0 \\ P \\ \frac{P}{2} \\ P.\frac{a}{2} \end{bmatrix}$$

2.4.1 Pump Selection

Various types of automobile pump that are available were considered based on the design parameters and the A V_8 cylinder washer pump was chosen for the research work base on the facts that:

1. Last longer during operation.
2. It delivers moderate pressure of the liquid similar to the designed pressure of the sprayer.
3. It is easy to be submerging in fluid.

2.4.2 Source of Power for the Pump

The capacity and durability of various types of batteries were considered, but the ac of 12volts, 7.2D was considered for the design, based on chargeability and durability.
The voltage was computed from the following equations.
V = IR from (ohm's law)
But V = Voltage
Measure in (V)
I = current measure in Ampere (A) and
R = Resistance measured in ohm's ( )
Resistance R( ) = V/I and current (A) I = V/R – 3.1

2.4.3 Pump capacity

The pump capacity was determine by using sprayer width, speed and volume applicator.

Pump capacity (L/Min)

3.0 Determinate of Flow Rate II

Q = AV

From controlling equation

Q =AV = a v

$Q = A_1V_1$

$V_1 = \quad Q = \quad 4Q$

$\qquad A_1 = \pi d^2$

3.1 From the coverage area

$V_2 = V$

$Q = A_2 V_2$

Where V_1 and V_2 indicate inletand outlet velocity

Where V = Velocity of flow measured (m/sec)

$\qquad$ Q = Discharge measure in (m^3/sec) or (Lit/sc)

$\qquad$ A= Cross section area of pipe measured in (m^2)

$\qquad$ A = Area of nozzle outlet measured in (m^2).

4.0 Result and discussion

4.1 $\qquad$ Battery Charging Of Photovoltaic Sprayer (SPV)

$\qquad$ The battery charging characteristics of the solar voltaic sprayer (SPV) operated sprayer was studied to determine the charging time and the voltage while the sprayer was in non – operating condition. The SPV panel was exposed to sunlight for battery charging. The panel voltage and time were measured.
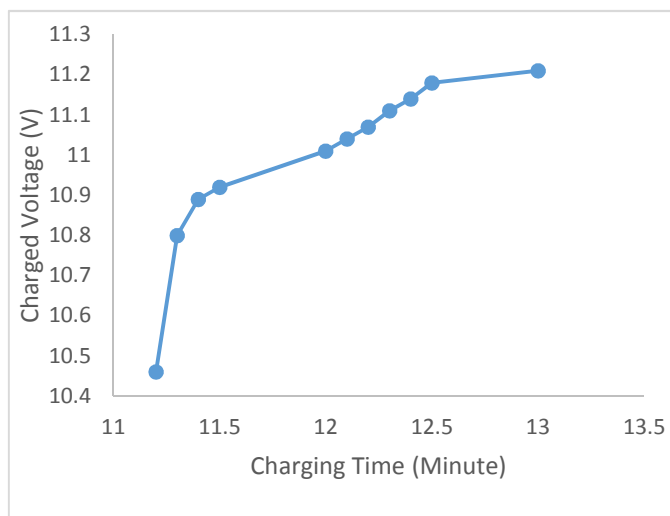

Figure 4 Battery charging time with respect to voltage

It was observed that the time interval of charging the battery to achieve a voltage of 12.22v between 11.20 am (10.46v) and 15.50 pm (12.22v) was 4hours 30 minutes.

4.2   Battery voltage and fluid discharge with respect to time

The battery discharging characteristics of the operated sprayer was studied to determine the discharging time of the battery. The various parameter recorded during the testing are summarized in table 1.

Table 1 Characteristics of battery voltage and fluid discharge with respect to time.

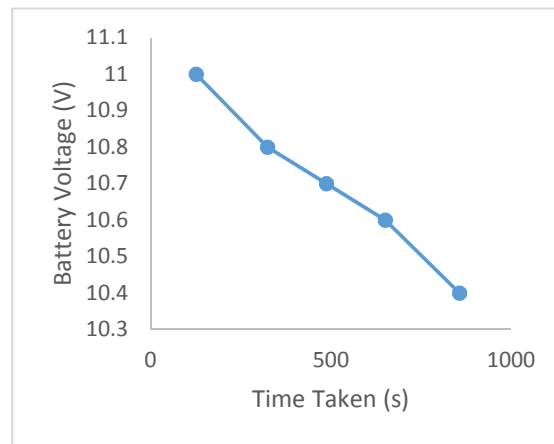| Discharge volume (Liter)	Battery voltage	Time taken (sec.)
4.00	11.00	126
6.00	10.80	320
8.00	10.70	485
10.00	10.60	650
12.00	10.40	880

Figure 5 Battery voltage and fluid with respect to time.

It was observed that the voltage of the charged battery of the sprayer decreases with increase in time as the volume of the fluid discharges.

232

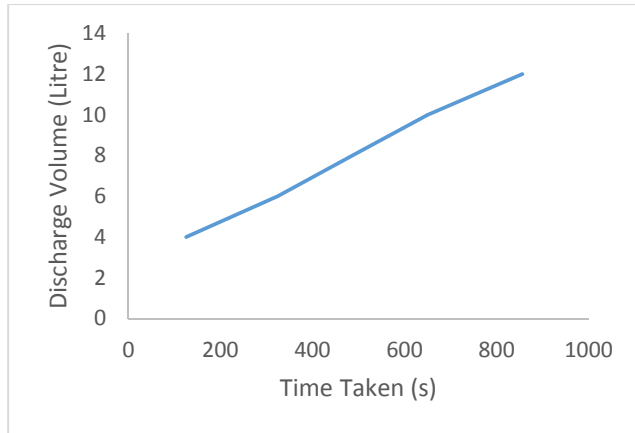### 4.3 Characteristics of discharge volume with time.

Figure 6 Characteristics of battery discharge volume with time.

It was observed that the increase in quantity of discharge volume results to an increase in time of spray.

4.4 Determination of application rate (field test)

A 50 litre capacity tank was filled up with liquid and the volume marked. The tank was mounted on the trolley. The system was switched on and the liquid was sprayed. The effective performance of the developed battery operated sprayer was determined by practical trials on a 100×100 m^{2}field. The operator walked with a speed of about 0.7m/s through the field. The discharged volumes in liters with corresponding time in seconds were recorded. The procedure was replicated five (5) times and the mean value evaluated.

Table 2 Field Test (Application Rate).

S/N	Discharge rate volume (L)	Time Taken (Sec.)	Discharge Rate (Sec.)	Area Rate Covered (m^2/s)	Application Rate (L/M^2)
1	10.00	388.2	0.02576	2.58	0.01000388
2	20.00	778.1	0.02570	1.29	0.009961
3	30.00	1168.6	0.02567	0.86	0.002999
4	40.00	1558.8	0.02566	0.64	0.039900
5	50.00	1944.8	0.02571	0.51	0.0006454
Mean	30.00	1167.7	0.02570	5.88	0.1128978

The result on Table 2 shows that the mean discharge volume is 30 liters, mean time taken to spray 1000m^{2}was 1167.7 sec. and the discharge rate per seconds was 0.02570 L/sec. This result has higher value of liquid application over the previous ULV developed by Dauda (2017), as it has a fine spray pattern and increase in number of nozzles. There is a variation in the discharge capacity recorded due to lack of constant walking speed during the field operation. This is in agreement with the finding of Olufade (1986), who reported that walking speed was responsible for altering application rate of sprayers when constant speed was not maintained.

5.0   Conclusion

A photovoltaic panel of 18v, 80 watt capacity was configured to trap and convert sun energy into useful power and was used with aid of a charged battery to perform the work of spraying. The water diaphragm pump in the sprayer tank was used to pump the fluid through the nozzles. The newly developed sprayer was evaluated in terms of laboratory and field testing. The laboratory testing of the solar operated sprayer includes charging and discharging characteristics, sprayer characteristics such as area covered and flow rate were determined. The field testing of the sprayer was done using volume rate to determine the application rate. The design analysis developed and setup solar operated system was carried out. Fabrication of various units and components were done and assembled. The research work undertaken can conclude that the spray efficiency decreases with decrease in voltage of the battery. It was also observed that the charged battery could be operated for four hours thirty minutes. The sprayer has an application rate of 0.01128978m^2 compared to 0.0006380m^2 Dauda, 2017. The developed sprayer has a higher value of liquid application over the previous ULV developed sprayers. The application rate is influenced by walking speed.

References

Andrew M., Robin B. (2001) Herbicide Application using knapsack sprayer Rice –Wheat consortium for the indo-gangeticlains

Anonymous. (2015) standardization of PV energy utilization in Minna unpublished M.Eng thesis, FUT Minna.

Anonymous (2017) Development of solar operated knapsack sprayer with two nozzles. Unpublished M.Eng thesis, FUT Minna.

Awalu A.O, J.A, Enokela, D.S Danladi, (2011). Design and evaluation of an electrically operated \ultra- low volume sprayer, the pacific joural of science and Technology.

Joshua R; vasu., V. Vincent., (2010). International Journal of Mechanical and Civil Engineering, pp 42-48

Khan Z. (2014). Unique solar operated sprayer Jet. IOSR Journal of mechanical and civil Engineering.

Olufade C. K., (1986). A two – row automatic boom sprayer Ed (S). Dodd, V. A. and P.M. race proceeding of the international congress on Agricultural Engineering Doblin, A.A. Balkena. Pp 1704 – 1706.

Patil A., Chavans. And Geete M. (2014). Performance evaluation of solar operated knapsack sprayer vol. 38 (3)

Roa V.V; Mathaptis and Amarapur B; (2013) multiple power supplied fertilizer sprayer international journal of scientific and research publications volume 3.

Sasaki R.S., M.M Texeira, D.D Filho. C.J Cesconetti A.C Silva. D.M Laite (2014). Development of solar photovoltaic knapsack sprayer, communication pp. 396-3.99

EXPERIMENTAL INVESTIGATION OF HEAT TRANSFER COEFFICIENT OF ALUMINIUM 6061 CASTING SHAPES USING GREEN-SAND MOULD

L.T.I Suleiman, K.C. Bala, & M. Godfrey

ABSTRACT

It is necessary to produce shapes such as plate and bar using casting process for developing indigenous technology of green sand mould. To have the knowledge of solidification time and temperature gradient which are governed by Heat transfer coefficient (HTC) will help to understand required temperature for achieving desired cast shape. The shapes employed for the study includes rectangular plate, square bar and cylindrical bar. Experiment was conducted and values of various temperatures were obtained using electronic temperature recorder. The solidification time of the cast shows that solidification rate is faster in plate when comparing to other shapes. The casting of shapes that involves using aluminium alloy 6061 solidified within 105 seconds after pouring of the molten metal into mould cavity and also plate was the first to solidify. The mould constant obtained for the sand mould was 3. The experimental result shows that thermal conductivity of the alloy was 102.3 WmK and the value was within range of stated value (85 - 173 W/mK) by ASTM. Heat transfer coefficient (HTC) in the cast objects was 101.1 W/m2K.

Keywords: Aluminium Alloy, Heat transfer coefficient, green sand mould.

1.0   INTRODUCTION

During solidification and casting in permanent moulds, the heat flow is controlled by the thermal resistance at the casting-mould interface. Thus Heat Transfer Coefficient (HTC) at the aluminium alloy-mould interface has a predominant effect on the rate of heat transfer (Ilkhchy, Varahraam and Davami, 2012),(Machuta, J. and Nova, I,(2015). In casting process, the effect of pressure on molten aluminium alloy will affect the rate of heat transfer at least at initial steps of solidification. The method of calculating HTC is based on the knowledge of known temperature histories at the interior points of the casting or mould together with the numerical models of heat flow during solidification (Santos, Quaresma and Garcia, 2001;(Machuta,J. and Nova, I.(2016) Maleki, Niroumandand Shafyei, 2006). These temperatures are difficult to measure due to the difficulty in locating accurate position of thermocouple at the interface. Solidification process of casting is governed by HTC which is a function of the heat flux and the temperature gradient. Since the HTC is the critical factor for achieving desired material properties of the cast metal and also cooling rate is governed by HTC, and this can be found experimentally for small geometries (Bylund, Cruz, Kalach and Tsoi, 2008).The temperature variations induced in a cast product have a direct influence on its final microstructure, and therefore play a critical role in determining its quality. According to Ayoola, Adeosun, Sanni and Oyetunji (2012), aluminium alloy could be formed into semi-finished or finished products using casting technique. Heat transfer between the solidifying casting and mould is critical for high quality casting. In addition, heat transfer between the casting and the mould is primarily controlled by conditions at the mould-metal interface.

In the present study, the casting mould is green sand. Therefore, the quality of castings in a green sand mould are influenced significantly by its properties, such as green compression strength, permeability, mould hardness and others which depend on input parameters like sand grain size and shape, binder and water (Mahesh, Pratihar, and Datta, 2008).According to Khan (2005), green sand moulding is the most commonly used casting process throughout the entire casting industry, worldwide. Green sand moulding may be defined as mixture of sand grains, clay (as a binder), water (as activator) and other materials (as additive) which can be used for moulding and casting purposes

(Khan, 2005). The sand is called 'green' because of the moisture content and to distinguish it from dry sand. The sand used for green sand moulding is critical to the soundness of casting produced. Green sand has characteristics of flowability, plastics deformation, green strength and permeability (Tiwani et. al, 2016).Hence, analysing the heat transfer characteristics of the casting shapes of aluminium alloy is of crucial importance to foundry technology. The study determined heat transfer coefficient (HTC) of aluminium 6061 casting in a green sand-mould experimentally.

3.1 Materials and Methods

The following materials are required.

    i.   Aluminium alloy 6061 ingot
    ii.   Casting equipment includes mould box, pattern, pliers and scissors, pouring cup and furnance

    iii.   Thermocouple (Electronic paperless recorder)

Table 1 indicates the composition of the Aluminium Alloy used for the study.

Table 1: Composition of Aluminium 6061

Aluminium alloy 6061 Component	Weight %
Aluminium	96.20
Magnesium	1.20
Silicon	0.75
Iron	0.70
Copper	0.40
Zinc	0.25
Titanium	0.15
Manganese	0.15
Chromium	0.20

Table 2 indicates the specification of the Aluminium Alloy used for the study.

Table 2: Specification for aluminium 6061 (ASTM)

Specification	Unit
Liquid Density (kg/m^3)	2400
Solid Density (kg/m^3)	2700
Solid Thermal conductivity (W/mK)	173
Liquid Thermal conductivity (W/mK)	85

Fusion Temperature (°C)	585	
Solid Specific Heat (J/kgK)	1050	**2.1**
Liquid Specific Heat (J/kgK)	1090	
Latent Heat of Fusion (J/kg)	381900	

3.1 Experimental methods

The mass of ten kilogram's (10 kg) of aluminium alloy 6061 ingot was used for the experiment. The ingot was heated and melted using gas furnace to obtain hot liquid metal. The melting process was done with aid of gas furnace. The molten alloy was poured into the cavities of the various prepared moulds at temperature of 700°C. The steps of the casting:

i. Pattern making: rectangular plate of 250 mm by length, 60mm by width and 10mm by thickness. Square bar of 250 mm by length, 24.5 mm for both width and thickness respectively cylindrical bar of 250 mm by length and 27.6mm by diameter
i. Moulding
ii. Core-making
iii. Melting and pouring
iv. Cleaning and inspection

Figure 1 shows the positioning of thermocouple in cast plate. The blue pigment in Figure 1 was one-quarter of the plate pattern in which thermocouple mounted onto for measuring the readings of temperature points. The measuring points of temperature in the cast include T_{if}, T_{lc}, T_{uf} and T_{uc} and these measured using thermocouple through electronic paperless recorder. The sand mould temperature (T_s) measuring point was located 50 mm from the wooden or mould box. Four points were used for positioning the thermocouple within the one quarter of the cast. The thermocouple used for measuring the temperature within the cast was positioned at 30mm ($h/2$) from the edge of both width faces (60mm) of the cast. The thermocouple helps to measure temperature at four different points within cast. The thermocouple that measured sand mould temperature was positioned at centre point between pattern and core box within the mould.
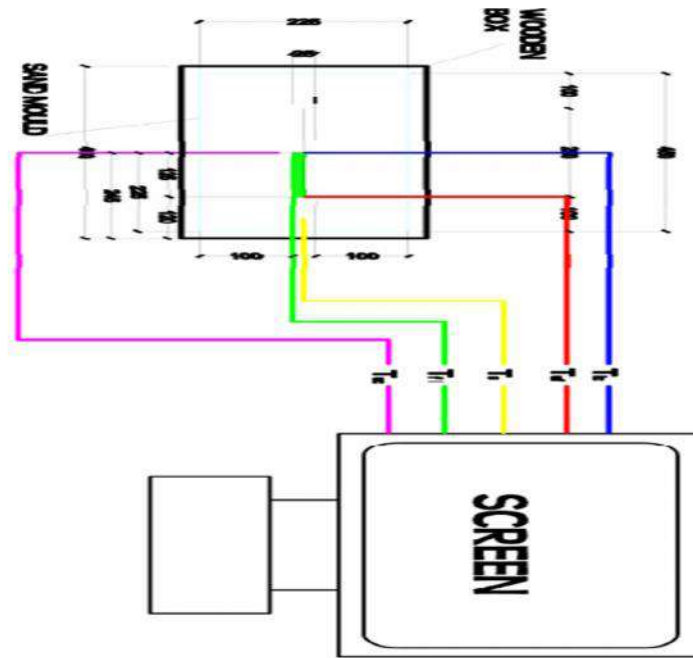
Figure 1: Positioning of thermocouple in the Casting

2.2   Determination of casting modulus

The temperature drop per unit time or cooling of the casting depends on modulus of the casting and it is defined as ratio of volume to effective cooling surface area is:

$$M = V_m/A_m \quad (3.24)$$

$$M_p = t/2 \quad (3.25)$$

$$M_s = w/2 \quad (3.26)$$

$$M_c = d/4 \quad (3.27)$$

Condition I (equation 3.24) holds if $L > 5t$

Condition II (equation 3.25) holds if $L > 5w$

Condition III (equation 3.25) holds if $L > 5d$

3.5   Determination of solidification time

The solidification time (t_s) is the time required to complete solidification process in casting and depends on heat transfer across the casting surface and mould of the casting and given by (Stefanescu, 2008; Bala and Khan, 2013; Rundman, 2013) and stated as follow:

$$t_s = B\left(\frac{V_t}{A_{r,n}}\right)^n \qquad (1)$$

$$t_s = \frac{\rho}{HTC_v(T_m-T_o)}\left(Q_f+c_m(T_p-T_m)\right)\left(\frac{V_m}{A_m}\right) \qquad (2)$$

$$B = \left[\frac{\rho_m L}{(T_m - T_0)}\right]^2 \left[\frac{\pi}{4k\rho c}\right]\left[1 + \left(\frac{c_m(T_p - T_n)}{L}\right)^2\right]$$ (3)

3.0 Results

The study boundary condition is in Table 3

Table 3: Boundary condition of aluminium 6061

Parameters meter	Quantity
Volume per workpiece	$0.00015 m^3$ (150,000 mm^3)
Length of Cast Alloy	0.25m (250mm)
Pouring Temperature	$700\,^{O}C$
Time interval	10 seconds

The cooling of the casting depends on modulus of the casting (M) and it was calculated for different cast shapes based on same length (L) 125mm.

i. Plate modulus, $M_p = \frac{t}{2} = \frac{10mm}{2} = 5mm$

$$L > 5t = 5(10) = 50mm$$

$$A_m = \frac{V_m}{M} = \frac{150,000}{5} = 30,000 \ mm^2$$

ii. Square bar modulus, $M_s = \frac{width}{4} = \frac{24.5}{4} = 6.1 \ mm$

$$L > 5w = 5(24.5) = 122.5mm$$

$$A_m = \frac{V_m}{M} = \frac{150,000}{6.1} = 24,590 \ mm^2$$

iii. Cylindrical bar, $M_c = \frac{diameter \ (d)}{4} = \frac{27.6}{4} = 6.9mm$

$$L > 5(d) = 5(27.6) = 138mm$$

$$A_m = \frac{V_m}{M} = \frac{150,000}{6.9} = 21,739 \ mm^2$$

The plate has lowest casting modulus of 5mm and this mean it has high cooling surface area of $30,000 \ mm^2$ in comparing to other shapes used for the experiment. The heat transfer coefficient (HTC) of aluminium alloy was determined using experimental records of temperature distribution in

the cast. Figure 2 shows the temperature gradient in plate cast and the pouring of molten metal was at 700ºC.
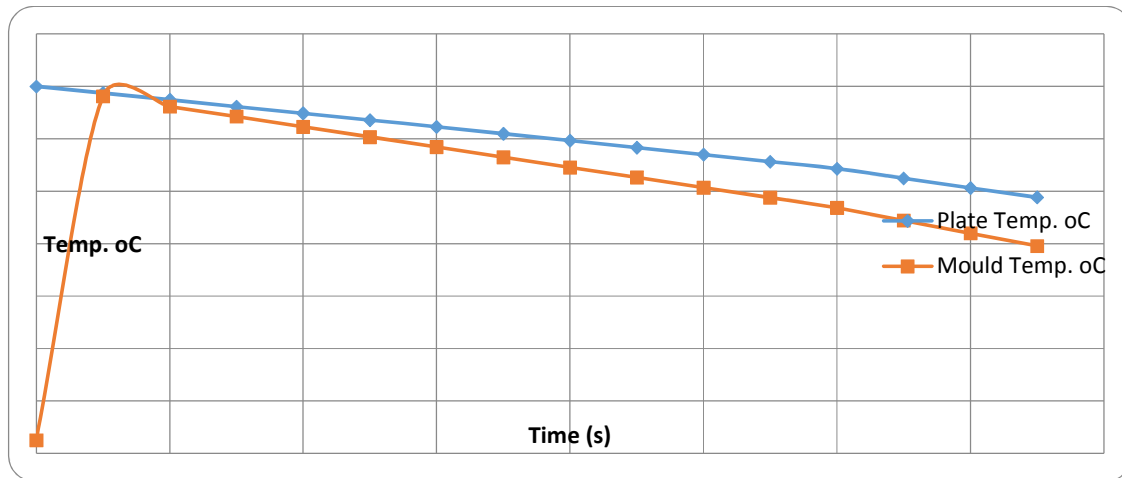

Figure 2: Temperature profile of rectangular plate

Table 4 presents heat transfer coefficient (HTC) of the alloy determined from the experimental result obtained for rectangular plate.

Table 4: HTC of rectangular plate.

Time (s)	T (^{o}C)	Ts(^{o}C)	T- Ts (^{o}C)	Ts - Tf (^{o}C)	HTC (W/m^{2}K)
10	687.2	680.7	6.00	655.4	6.2
20	674.3	661.4	12.9	636.1	13.8
30	661.4	642.1	19.3	616.8	21.3
40	648.6	622.8	25.8	597.5	29.4
50	635.7	603.5	32.2	578.2	37.9
60	622.9	584.1	38.8	558.8	47.2
70	609.6	564.8	44.8	539.5	56.5
80	596.3	545.5	50.8	520.2	66.4
90	583.0	526.2	56.8	500.9	156.9
100	569.7	506.9	62.8	481.6	180.9
110	556.4	487.6	68.8	462.3	206.0
120	543.0	468.2	74.8	442.9	233.7
130	524.7	444.0	80.7	418.7	266.8
140	506.4	419.7	86.7	394.4	304.2
150	488.2	395.5	92.7	370.2	346.6

The room/fluid temperature (T_f) used for the study was at 25.3 ^{o}C during the experiment. The length of cast plate was 0.125m (half of the cast length) and heat energy was expected to transfer across the cast for solidification to complete. The expected HTC of the cast rectangular plate after 90 seconds was 48.4 W/m^{2}K. It implies 48.4 W/m^{2}K was the HTC of molten stage of the plate. The liquid thermal conductivity of the plate was at 111.8 W/mK. The ASTM-liquid thermal conductivity of the alloy in Table 3.2 was at 85 W/mK therefore efficiency of obtained HTC was at 68.5 % in plate.
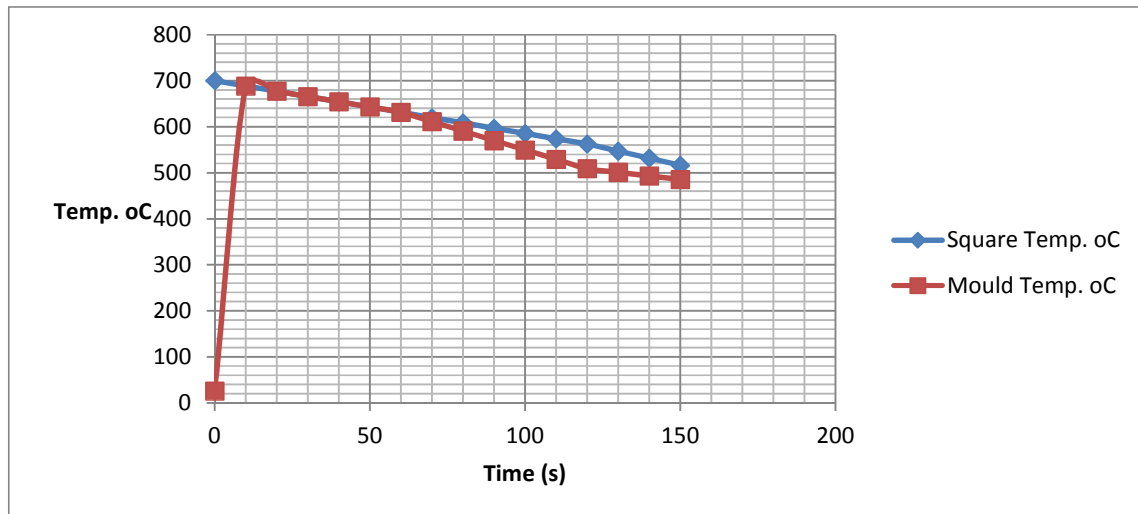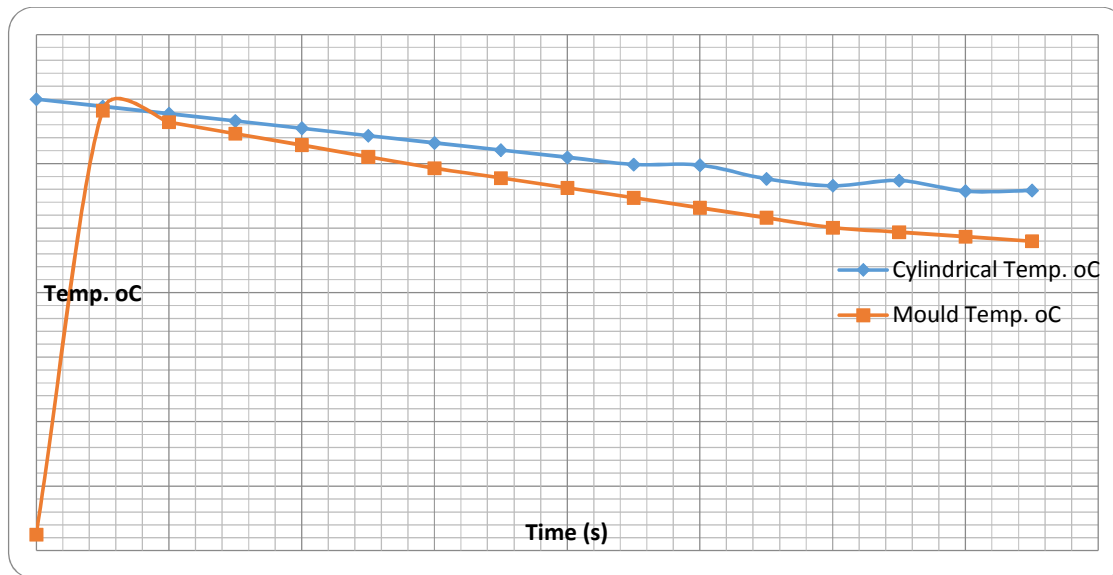
Figure 3: Temperature-profile of square bar

Figure 4: Temperature profile of cylindrical bar

Table 4.18 presents summary of HTC in aluminium alloy cast and therefore it was observed that plate has high value of HTC in the casting with 131.6 W/m^{2}K for the experiment. The HTC of cast square bar was at 73.6 W/m^{2}Kand HTC of cast cylindrical bar was at 98 W/m^{2}K after 150 seconds. Rectangular plate solidified faster than other cast object due high HTC across its surface

Table 5: HTC of the Aluminium Alloy

Time (s)	HTC-plate (W/m²K)	HTC-square (W/m²K)	HTC-cylindrical (axial) (W/m²K)
10	6.2	6.9	6.7
20	13.8	13.3	13.9
30	21.3	18.3	21.4
40	29.4	44.5	29.4
50	37.9	31.3	37.9
60	47.2	49.2	46.9
70	56.5	91.0	53.3
80	66.4	76.2	60.2
90	156.9	91.4	67.5
100	180.9	75.8	88.8
110	206.0	22.8	169.9
120	233.7	153.2	188.4
130	266.8	134.2	236.1
140	304.2	113.9	211.2
150	346.6	183.6	238.8
Average	131.6	73.7	98

Considering the average of HTC presented in Table 4.18 the HTC required for casting of aluminium alloy was at 101.1 W/m²K after 150 seconds. However, the liquid thermal conductivity (k) obtained of the material used was at 111.8, 90.1 and 105 W/mK for plate, square and cylindrical bar respectively. The average of liquid thermal conductivity was at 102.3 W/mK within the range of 85 to 173 W/mK of ASTM Table.

The following plates were the cast of rectangular plate, square bar and cylindrical bar obtained during the experiment.

Plate I: Cast Rectangular Plate.

Plate II: Cast Square Bar

Plate III: Cast Cylindrical Bar

4.0 CONCLUSSIONS

The aluminium alloys 6061 are cast-able using green sand mould. Heat transfer coefficient (HTC) in the cast objects was 101.1 W/m^{2}K. The study shows that plate has higher effective cooling surface in comparing to shapes such as square and cylindrical mode. However, it was observed that solidification process is faster in shape with lower modulus based on the use of same volume of material for casting of different shapes. However, the solidification process is obtained in higher rate with lower modulus in casting of different shapes due to high rate of heat transfer coefficient.

References

Ayoola, W. A., Adeosun, S. O., Oyetunji, A. and Oladoye, A. M. (2010). Suitability of Oshogbo Sand Deposit As Moulding Sand. Kenya Journal of Mechanical Engineering, 6(1), 1- 3, 33.

Ayoola, W. A., Adeosun, S. O., Sanni, O. S. and Oyetunji, A. (2012). Effect of Casting Mould on Mechanical Properties of 6063 Aluminium Alloy. Journal of Engineering Science and Technology, 7(1), 88-96.

Bala, K. C. and Khan, R. H. (2013). Experimental Determination of the Effect of Mould Thickness on the Solidification time of Aluminium Alloy (Al-Mn-Ni-Si) Casting in Rectangular Metallic Moulds. International Journal of Engineering Research and Technology (IJERT), (March), 2(3), 3.

Bylund, D., Cruz, R., Kalach, S. and Tsoi, M. (2008). Air Quenching of Aluminium: The effect of Quench Orientation and Air Velocity. Unpublished B.Sc Project, Worcester Polytechnic Institute, p.2.

Ilkhchy, A. F., Varahraam, N. and Davami, P. (2012). Evaluation of Pressure Effect on Heat Transfer Coefficient at The Metal- Mold Interface for Casting of A356 Al Alloy. Iranian Journal of Materials Science & Engineering, 9(1), 239.

Khan, R. H. (2005). Metal Casting Technology in Nigeria-Present Status and Future Prospects. Inaugural Lecture, Federal University of Technology, Minna (Dec. 29), Series 8, p. 10.

Machuta, J. and Nova, I. (2016). Analysis of Heat transfer conditions in sand and metal moulds and their effect on the solidifications of the casting. Journal for Science Research and Production. 16(2), 12-17.

Machuta, J. and Nova, I. (2015). Simulation of calculations of solidification and cooling of Copper alloys casts. . Journal Manufacturing Technology, 15(4), 591-596.

Mahesh, B. P., Pratihar, D. K. And Datta, G. L. (2008). Forward and reverse mapping in green sand mould system using neutral networks. Applied Soft Computing, 8(1), 239-260.

Singh, R. (2006). Introduction to Basic Manufacturing Processes and Workshop   Technology, (1st ed.). New Delhi: New Age International Ltd., pp.179-   250.

Santos, C. A., Quaresma, J. M. V. and Garcia, A. (2001). Determination of Transient Heat Transfer Coefficients in Chill Mold Castings. Journal of Alloys and Compounds,   139, 174-186.

Tiwani, S.K, Singh, R.K and Srivastawa, S.C.(2016). Optimisation of green Sand Casting process parameters for enhancing quality of mild steel Casting. International Journal of productivity and Quality Management. 17(2), 127-130.

A REVIEW ON FRACTURE PROPERTIES OF WELDED HIGH STRENGTH STEEL-(HSS) FOR LOW TEMPERATURE APPLICATION

By

[1,2]N. S. Akonyi, [1]O. A. Olugboji, [1]E. A. P. Egbe [a], O. [1]Adedipe.

[1]Department of Mechanical Engineering, Federal University of Technology, 920001 Minna, Nigeria.
[2]Scientific Equipment Development Institute Minna, National Agency for Science and Engineering Infrastructure, Idu Industrial Layout. Abuja FCT.
*Corresponding Author: E-mail: akonyi.pg612172@st.futminna.edu.ng, akonyi01@gmail.com, Tel: +2348054616400, +2348032548824.

Abstract

The technological evolution in structural steels are pointing towards high strength steel, especially in the offshore and marine applications. Therefore, there is need to have knowledge on the fracture behaviour of high-grade steel welded joints to improve and contribute to the potential upgrades of the design criteria. Lightweight structures (with reduced cost and weight) that guarantee high-quality/high-strength weld-able joints has become the trend in recent research. Natural gas and oil reservoir which have the potential to boost economic growth and play a vital role in the future energy requirements lie beneath the waters of the world's ocean. This water depths ranges from a few hundred to several thousand metres. Explorations and production activities in these offshore waters have revealed depths of 2000 metres and more. Generally, water depths of 1000m (known as mesopelagic zone) and above have low temperatures of about -2°C. At this temperature, seawater freezes and ductile materials are susceptible to brittle fracture. This has significant effects on installation of oil and gas pipelines at low temperature. This have become challenges, which calls for enhanced engineering techniques to cope with the risks of fatal failures. Due to inherent metallurgical phenomenon, mechanical properties heterogeneity, residual stresses and geometrical defects, cracks propagates easily especially at the welded joints. Studies have been conducted on the fracture properties of the HSS materials. This paper is aimed at reviewing the effects of chemical composition on the microstructural properties of HSS materials in low temperature applications. The concept of fracture mechanics as applied to fracture behaviour of welded joints with focus on the effects of low temperature on HSS materials is presented. The fracture toughness in deep water applications, where temperature at the depth of water is in semblance to the arctic region environment is briefly discussed. In conclusion, API X100 TMCP materials have been recommended as a types of high strength steels (HSS) for structural steel material applicable for low temperature because of the properties, chemical compositions and development methods or manufacturing processes. Also, modern welding techniques often used in the arctic region is suggested to be applied for the deep offshore materials for sustainability, effectiveness and fitness for service requirements.

Keywords: Low temperature, deep offshore, Fracture behaviour, Geometrical defects, Pipeline, Welded joints.

1. INTRODUCTION

The Federal Government of Nigeria, under the auspices of Nigeria National Petroleum Corporation-NNPC, had opened up a new frontier in Oil and Gas exploration, by allocating some offshore blocks in water depths reaching 2500metres [1]. These water depth and plans for even greater depths than 2500m will undoubtedly impact positively the country's production and reserve blueprint. Fig. 1 shows the Nigeria's deep offshore oil and gas exploration area. The deep and ultra-deep water operations are technically challenging for exploration. Water depths of 1000m and above have low temperatures as

seawater freezes at -2°C [2] and at this temperature, ductile materials are susceptible to brittle fracture and this has significant effects on the installation of oil and gas pipelines due to the low temperatures. Early researches revealed that deep offshore pipeline problems are caused by low temperature and high strain rate in the material that resulted to brittle fracture. [3]. For example, betweem 0°C and 5°C, offshore ships (vessels) have broken into two in harbours and bridges have collapsed, while gas storage tanks and pipelines have ripped open [4]. These are some of the common engineering challenges that come with the use of steel pipelines in low temperature region in deep offshores. Brittle failures of metals due to extreme cold, problems of corrosion, large deformation of pipelines as a result of reeling installation defects, microstructure heterogeneity and overloading of facilities due to some other factors in the seabed are examples of potential flaws that leads to pipeline failures.

Expectedly, since most of the deep water activity in Nigeria is in, so called, virgin territory, thereby lacking infrastructural support and services, there is the need to research the deep offshore environment for appropriate pipeline material and welding techniques to be adopted to prevent future structural problems in the Nigeria deep offshore region. This can be likened to the arctic region oil and gas exploration and production technologies. [5], opined that there is need to study the behaviour of newer materials applicable to certain areas, especially the fabrication techniques. The techniques involves welding process which affects the microstructure of the weld material and influence the crack growth behaviour, which occurs in both air and seawater environments. Other factors that affects the behaviour are the type of materials, level of induced residual stresses which depends on material thickness, welding input parameters, and level of expertise employed during welding.

Additionally, freezing temperatures, immense water pressure and pitch darkness all make producing oil and gas from deep water a major technical challenge. Substantial economic losses and negative environmental impacts are the consequential outcome. Therefore, safety and reliability becomes a source of concern to offshore engineering professionals.

Due to the challenges in production activities with oil and gas structures in deep offshore, an enhanced engineering techniques to cope with the risks of fatal failures is required [6].

Fig. 1. Oil and Gas Producing areas in Nigeria. [7]

1.1   Brief introduction to (low temperature) Deep offshores and similarity with arctic region environment

Arctic region is an environments within the globe that has enormous oil and gas resources, but with very harsh and hostile conditions. The similarity to deep offshore is the low temperature that is detrimental to steel materials used in the structural installations. The Arctic environment compared to deep offshore region are both hazardous to structural steels (metals) at low temperatures, because they have increased susceptibility to brittle fracture. Hence, materials with high toughness properties are required to ensure that adequate fracture-resistance at low temperatures are used to build the facilities [8]. Exploration to deep and ultra-deep offshores requires that construction of structures, platforms and many other facilities are capable of operating safely at very low temperature, say -70°C or lower down till -100°C. Fortunately, most of these structures, platforms and facilities were built with metals (mostly structural steels and HSS) and joined together by welding. The welded HSS steels used are due to some of the advantages in mechanical properties such as low cost (compared to high cost of titanium alloy materials), ease of fabrication (low carbon content), high strength, and availability of grades that are highly fracture-resistant at low temperatures. [8].

Therefore, the demands in properties of materials used for deep offshore and arctic structures are similar. These includes fatigue property, strength, corrosion resistance, impact resistance, toughness, and transition temperature. Other stringent demands are welding technologies which requires high efficiencies, high productivity, high qualities, for labour savings and low costs etc. [9]. As a result of these special conditions experienced with both Arctic environment and deep offshore, special and advanced welding technologies, with new grades of metallic materials (steels) are inevitable.

1.2 Materials Applicable for deep offshore (low temperature) Conditions

Researches into new and higher grades of steel that can satisfy the service conditions of deep offshore structures have become a challenge in recent times. Some of these new materials are steel grades of X80, X100, X120, titanium alloys (Grade 5, Ti-6Al-4V (Ti64)) and upgraded 9% Ni steels. Due to the entirely different environment from the usual moderate temperate region, lower grades of steel cannot be utilised. HSS structures with very high toughness property under extremely low temperature will suffice. In deep offshore region, the minimum ambient temperature recorded falls well below -40°C. This definitely, will account for the minimum design temperature to go down to -60°C. Hence, the need for special grade metals (materials) that can survive the extremely cold region without failing under service conditions.

There is need to investigate the welding technologies for joining the metal structures that can give a satisfactory weldments under low temperature service conditions too. The output quality of material is expected to be high among many other desired characteristics of the welded joints of X100 steel. The yield strengths minimum value should be 690 MPa and above which fall within the acceptable standard materials. The toughness of the material is rated high, as high as 150 J/cm^2 for CVN @ -40.

1.3 The Thermomechanical Controlled Process -TMCP

TMCP technology has enabled the production of excellent steel plate with high-strength and good low-temperature toughness. This process is divided into two, direct quenching and tempering process, and the Interrupted accelerated cooling process. The former involves high cooling rate of plate with water to barely room temperature. The tempering is required to obtain the appropriate ductility and toughness. In the later process, the plate is cooled with water at moderate cooling rate and then subjected to air cooling, only in the transformation temperature region. The self-tempering effect of

this process reveals excellent ductility and toughness. The processing conditions in TMCP have to be optimized in order to obtain high-strength and low toughness of the material, since they both depends on the process conditions.

2.0 Overview of High Strength Steels (HSS)

High-Strength Steels-HSS are complex, sophisticated materials with carefully selected chemical compositions and multiphase microstructure resulting from precisely controlled heating and cooling process, [10]. They contain ferrite and martensite in the microstructure. The 'high strength' is the major attribute, which enhances the use of thinner steel materials for weight consideration. HSS contains very low carbon content and small amounts of micro-alloying elements, such as Niobium, Vanadium, Titanium and Molybdenum [11-14]. They possess highly refined grain and cleanliness, characterized by the low sulphur content and reduced amount of detrimental second phases such as oxides inclusions and pearlite. They can be seen as advanced variant of HSLA steels. The evolution of HSS steel grades for line pipe in terms of strength and toughness over the last decades is shown in figure 2. The description of the main alloying elements and processing methods are briefly described [14-15].

The improvements in the mechanical properties of high-strength steels lies in the complex thermomechanical controlled processing (TMCP) routes and accelerated cooling (AcC) techniques. The advantages of the final products of higher strength micro alloyed steels and grain refinement is the reduced carbon content for excellent field weldability which are achieved through metallurgical tools of the rolling mills, [11-12].
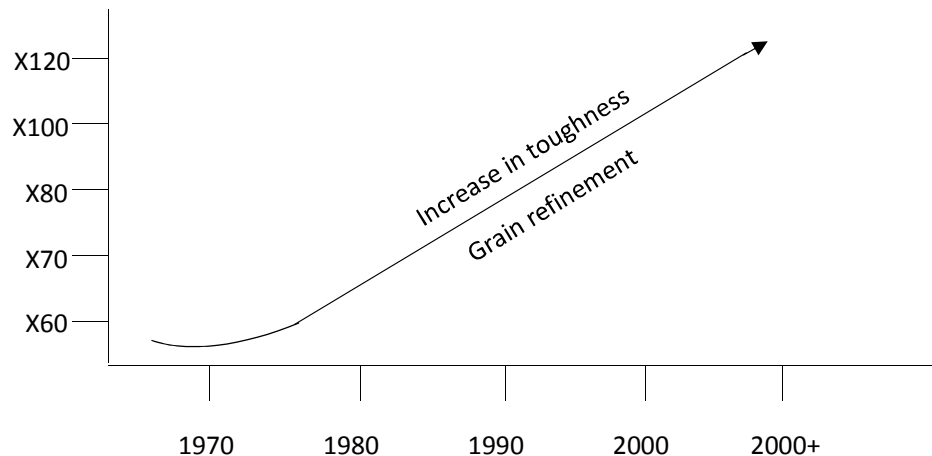

Fig. 2: Evolution of steel grades as an example of HSLA steel development. Grain refinement increases the strength and toughness.

2.1 Metallurgical Consideration of chemical composition.

The chemical composition of HSS steels may vary for different product for particular mechanical property requirements. This can be based on product specification levels 1 or 2 – (PSL1 or PSL2). Usually, Manganese-Mn (up to 2.0wt % in combination with very low Carbon-C of < 0.10 wt%) and minor additions of other alloying elements such as Niobium-Nb, Vanadium-V, Titanium-Ti, Molybdenum-Mo and Boron-B are the constituents [10]. The additions of the alloying elements serves mainly to strengthen the ferrite by:

- Grain refinement, which depends on the interaction between chemical composition,
- Solid solution hardening which is related to the contents of the alloying element and
- Precipitation hardening which depends on the TMCP process.

The type and volume fraction of the product formed under given conditions is determined by individual element and cooling rate applied [14, 16].

The increase in strength of steel is related to an increase of the following alloying elements: Molybdenum (Mo), Silicon (Si) and Nickel (Ni) [10]. However, CE and Pcm values are kept almost constant even for increasing steel grades. The alloying elements also exerts influence on transformation temperatures. For example reducing the temperature at which austenite begins to transform to ferrite and/or pearlite during cooling, results in a finer-grain microstructure [14, 16]. Over the years, some strategic alloying combinations have been pursued to meet the increasing demands on strength and toughness without compromising weldability, [17]. The following alloying combination suffices:

- V+Mo+Nb: to produce secondary hardening by forming carbides, nitrides and carbonitrides;
- Ni+Mo: effective addition of microstructure refinement by suppressing austenite recrystallization during controlled rolling and steel strengthening by precipitation hardening and enhancement of hardenability;
- Ni+B: synergistic improvement of hardenability;
- Nb+V: increase strength properties. However, steels based on this combination may require relatively high carbon equivalent design, which can compromise the capability for preheat-free field welding;
- Mo+Nb+Ti: More effective (compared to the formerly applied Nb+V steels) in achieving the strength requirements of X70 and X80 (high Mn steels) particularly in thicker pipe walls; A significantly finer ferrite grain size;

Table 1: Effects of alloying elements on HSS.

Element	wt % range	Effect
Carbon-C	0.03 – 0.10	Strengthens the matrix by precipitation
Manganese-Mn	1.6 - 2.0	Reduces DBTT, affects fine-grained lower bainite microstructure, substitutional strengthening.
Nickel-Ni	0.2 – 1.0	Improves the properties without effects on low temperature toughness and field weldability. Increases fracture toughness as it forms less hardened microstructural constituents that is detrimental to low temperature toughness.
Vanadium-V	0.03 – 0.08	Improves strength.
Molybdenum-Mo	0.2 - 0.6	Improves hardening
Niobium-Nb	0.03 – 0.06	Improves strength and toughness by grain refinement. Reduces temperature range between rolling passes.
Titanium-Ti	0.005 – 0.03	Strengthen the ferrite. Prevents detrimental effect of nickel on hardening. Grain refinement.
Silicon-Si	0.6	Improve in strength by solid solution

2.2 Microstructural Consideration

Material properties are finally determined by the microstructure. This must be a key variable in the design to ensure safe and optimal performance under operating conditions [13]. Modern HSS pipe have different and complex microstructural arrangements which depends on the chemical compositions and processing routes, i.e. the TMCP and Accelerated cooling-AcC.
For strain-based design applications, microstructures of different forms and combinations like bainite, martensite and ferrite are formed in order to achieve the target strength, toughness and ductility. These

qualities are based on a careful design of the steel chemistry and processing in order to control austenite phase transformations, such as lower bainite and lath martensite [19].

A bainitic microstructure is produced with precise chemical composition (micro-alloying) and low carbon content, aiming at a low Pcm value. The basic alloying system contains Cu, Ni, Cr and Mo and micro-alloying elements such as V, Nb, Ti and B [20]. Subsequently, the rolling and cooling procedures are very effective in achieving a grain structured (low angle boundaries) microstructure which hinders the dislocation mobility, resulting in a perfect combination of strength and toughness. This microstructure is also developed to ensure fully ductile failure behaviour and high crack arresting behaviour at temperatures as low as -40 °C (arctic conditions), [21, 22].

2.3 Steel processing
The development of thermo-mechanical controlled process (TMCP) was the real breakthrough to achieve grain refinement. This is the most effective metallurgical mechanism to improve both strength and toughness in high strength steels. According to [11, 14, and 18.] TMCP steels can be precisely controlled to obtain the desired microstructure for higher strain hardening capacity and ductility. In a separate work by [11, 21, 23], higher requirements for strain based design, with respect to strain hardenability, toughness and high strength, a particular cooling process (after rolling), known as accelerated cooling process (AcC) is performed. However, in some cases the steel plate is first hot rolled and soaked (held at a temperature until the desired microstructural changes takes place) and then submitted for inline quenching and tempering (QT) process. Such QT treatment is performed to produce a bainite-martensite microstructure without applying AcC process. By tempering, it is possible to reduce the brittleness of martensite and improve ductility and toughness [19, 24]. Different types of microstructures can be produced by these processing routes, such as: bainite single phase, ferrite-bainite dual phase and lower bainite-lath martensite [13, 19, and 23].

In 1998 a new concept of TMCP technology was developed in order to obtain not only high strength by transformation strengthening but also high toughness by refinement of transformed microstructure. This results to a combination of high strength/high toughness steel with reduced alloying elements. The microstructure consists of a bainitic matrix and finely dispersed martensite-austenite constituent (MA) as second phase with a volume fraction above 7%. The process consists of an advanced accelerated cooling device, with the purpose of reaching highest cooling rates and an induction heating equipment for online heat-treatment process (HOP), with high heating capacity to heat thick plates up to 40 mm [25]. This combination enables to reach a novel metallurgical controlling process that cannot be achieved by the 'conventional' TMCP. Some advantages of applying HOP process [23, 25]:

- Precipitation hardening by very fine carbide (reduction of diffusible free carbon content);
- Recovery of the dislocation density;
- Formation of MA constituents which enable the balance high strength / high deformability.

Table 2: Microstructure for different processing conditions (14)

S/No	API 5L	Process used	Microstructure
1	X120	TMCP + AcC	Ferrite + Martensite, Dual Phase, (19)
			Tempered Lath Martensite (19)
			Lower Bainite (19) (20)

2	X100	TMCP + AcC + HOP	Ferrite + Bainite, Dual Phase (23)
		TMCP	Ferrite + Bainite (20, 21, 26)
3	X80	TMCP + AcC + HOP	Bainite + Martensite-Austenite (23)
		TMCP + AcC	Ferrite + Bainite, Dual Phase (23)
			Lower Bainite (20)
			Lower Bainite + Lath Martensite, (27)
4	X70	TMCP	Bainite, (13)
			Polygonal Ferrite + Pearlite Band (28)
		TMCP + AcC + QT	Fine grain Bainite, (29)
		TMCP + QT	Bainite + Martensite + Ferrite (22)

3.0 The API X100 steel.

API X100 steel materials are types of high strength steels (HSS) used for structural steel material especially in the cold region because of the properties, chemical compositions and development methods or manufacturing processes. They are known for increased productivity due to efficiency in the reeling installation processes as a result of weight reduction. The excellent characteristics associated with X100 such as excellent field weldability, high toughness of base material and heat affected zone-HAZ at low temperature and microstructural properties, has made it to overcome the metallurgical problems associated with other forms of steels. The exhibition of these characteristics and the thermochemical controlled process-TMCP of API X100 steel during the development has made it an excellent material for use in the cold or low temperature region such as Arctic, deep and ultra-deep offshore region for energy explorations. The metallurgical problems associated with other forms of steel such as X52, X60 and X70 during development are overcome in the development of X100 steel because of its characteristics. Absolutely, an increase in strength increases the toughness, see figure 2. Figure 3 presents an overview of chemical compositions for typical API X100 TMCP steel. The same figure also shows the parameters that characterize good weldability, known as carbon equivalent (CE) and critical metal parameter for weld cracking (Pcm).
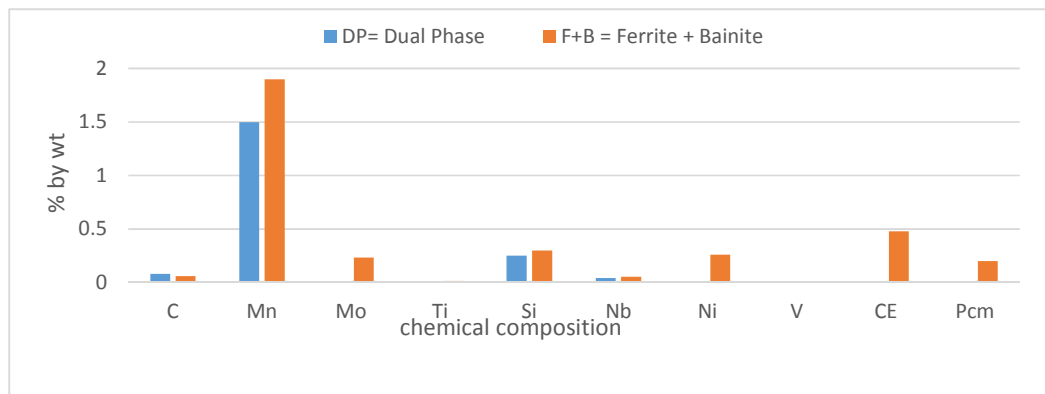

Fig. 3: Typical chemical composition of API X100 steel grades and weldability parameters.

3.1 Improving the strength of X100 steel for low-temperature toughness

Before the advent of X100, offshore structures are constructed with less strength thick plates such as X65 and X70 materials. The thickness ranges from 40 mm to 120 mm and even more. Due to the increased thickness, the tendency for brittle failure increases. The toughness of the welded joints are measured using Charpy V-notch test and CTOD, there is a minimum toughness value required for metal alloys or their welded joint to be suitable for low temperature use.

Toughness and Strength values have influence on weldability, improved by the TMCP process. The weld joints have well refined microstructures, high toughness and strength value, narrow HAZ and low distortion.

Precipitation hardening, Slid solution hardening and Transformation strengthening are the three major methods of strengthening steel. High and ultra-high strength steel such as X100 is often developed with the three methods. Transformation strengthening is the most important of the three and is normally achieved by micro-alloying and TMCP technology. Importantly, refining the austenitic structure by thermomechanical rolling and inhibiting the austenite grain coarsening during slab reheating by Titanium nitride (TiN) particles improves the low temperature toughness of the base material. Thermo-mechanical control process (TMCP) and cladding are part of the processes used to improve the properties for high strength materials. Increase in strength and toughness are aided by TMCP, while increased corrosion and wear resistance has been aided by Cladding.

The extremely low-temperature, water depth, and water pressure that renders the pipeline materials to failure risks needed an enhanced technology to overcome the challenges and bring them under control. One of the quality descriptions of any material is the design temperature. Generally, steels are prone to brittle fracture at low temperatures. Their ductility property changes to brittleness, often known as 'transition temperature'. Therefore, the design temperature of 20°C below the minimum expected service temperature and/or ambient temperature is often allowed in the design. In deep offshore region, the minimum ambient temperature recorded falls well below -40°C. This definitely, will account for the minimum design temperature to go down to -60°C. Hence, the need for special grade metals (materials) that can survive the extremely cold region without failing under service conditions.

3.2 Weldability

Welding of X100 steel material has become an essential part of developmental process to explore and develop materials for low temperature energy resources. However, there are several challenges with it and due to these challenges, an advanced welding technologies are applied to ensure a good weldment that can satisfy and survive the low temperature conditions.

Several welding methods have been used such as Narrow Gap Welding (NGW, or narrow groove welding), Laser welding, Laser-arc hybrid welding, Tandem, Metal Inert Gas/Metal Active Gas (MIG/MAG) welding and multi wire Submerged Arc welding (SAW). The welding method that will be recommended for this work shall be based on local factors.

4.0 Conclusions
The development within the field of Materials Technology is very vital to ensure success in reaching the aim of safe exploration, development and production of low-temperature region energy resources. A significant progress has been achieved during last years in the development of HSS line pipe steels, especially for strain-based design applications. Development of optimum microstructures (e.g. ferrite-bainite DP and/or bainite-martensite/austenite) which provides the required mechanical properties for

high strain capacity applications, such as higher strain hardening and uniform elongation are significant improvement for HSS development. High strength steel grades are showing improvements in mechanical properties. Increase in strength has been identified with proportions of basic chemical compositions such as Mo, Si and Ni contents. It can be observed that the characterizing parameters for good weldability (i.e. CE and Pcm) are maintained and practically unchanged. The TMCP processing routes are effective in order to produce steels with lower Y/T ratio and sufficient toughness.

The choice of API X100 TMCP steel materials needs further research to appropriately achieve the desired aim especially at the welded joints for low temperature applications. Narrow gap welding technique ensure good field weldability.

References

1. https://www.shell.com.sg/energy-and-innovation/deep-water.html.
2. V. V. Stolyarov and R. Z. Valiev, (2006). Enhanced low-temperature impact toughness of nanostructured Ti. Applied physics letters 88, 041905 2006.
3. Piyush K. Dutta, (1988). Behavior of Materials at Cold Regions Temperatures. Part 1: Program Rationale and Test Plan.
4. Parker, E.R. (1957). Brittle Behavior of Engineering Structures. New York: Wiley, pp. 253-301. (Parker, 1957).
5. Oyewole Adedipe, Feargal Brennan, Athanasios Kolios. (2016). Review of corrosion fatigue in offshore structures: Present status and challenges in the offshore wind sector. Renewable and Sustainable Energy Reviews 61 (2016) page 141–154
6. Van den Abeele F., and Vande Voorde J (2011). Stability of offshore structures in shallow water depth. Sustainable construction and design. OCAS N.V., J.F. Kennedylaan 3, 9060 Zelzate, Belgium.
7. https:/www.google.com.ng/searcg?
8. Anderson T.L. and McHenry H.I., 1982. Interim Progress Report: Fracture Toughness of Steel Weldments for Arctic Structures, NBSIR 83-16980, Fracture and Deformation Division National Measurement Laboratory, National Bureau of Standards, US. Department of Commerce, Boulder, Colorado 80303, December, 1982.
9. Shigeru O. and Hatsuhiko O., 2007. Latest Advances and Future Prospects of Welding Technologies, Nippon Steel Technical Report No. 95, January 2007.
10. E. Billur, and Prof. Dr-Ing T. Altan (2010), Challenges in Forming Advanced High Strength Steels, Engineering Research Center for Net Shape Manufacturing (ERC/NSM), 9, pp.2-7.
11. Hertelé, S., Coupled Experimental-Numerical Framework for the Assessment of Strain Capacity of Flawed Girth Welds in Pipelines, PhD Thesis, Ghent University, 2012.
12. Mouriño, N. S., Crystallographically controlled mechanical anisotropy of pipeline steel, PhD Thesis, Ghent University, 2010.
13. Stalheim, D. G., Muralidharan, G., The Role of Continuous Cooling Transformation Diagrams in Material Design for High Strength Oil And Gas Transmission Pipeline Steels, Proceedings of IPC 2006, IPC2006-10251, 2006.
14. Vervynckt, S., Control of the Non-recrystallization Temperature in High Strength Low Alloy (HSLA) Steels, PhD Thesis, Ghent University, 2010.
15. Liessem, A., Kalwa, C., Stallybrass, C., Mannesmann, S., & GmbH, Technological Solutions for High Strength, Europipe Technical Publications, 2008.
16. Tamehiro, H., Asahi, H., Hara, T., Terada, Y., Ultra-high Strength, Weldable Steels with Excellent Ultra-low Temperature Toughness, EXXON Production Research Company and NIPPON Steel, United States Patent 6264760, 1999.
17. Williams, J. G., Advances in Steels for High Strength ERW Pipeline Application in Australia, Materials Forum Volume 31, 1–10, 2007.

18. Liessem, A., Knauf, G., Zimmermann, S., Strain Based Design - What the Contribution of a Pipe Manufacturer Can Be, ISOPE 2007-SBD14, 1–8, 2007.
19. Koo, J. Y., Luton, M. J., Bangaru, N. V, Petkovic, R. A., et al. Metallurgical Design of Ultra-High Strength Steels for Gas Pipelines, Proceedings of IPC 2003 (5), 10–18, 2003.
20. Meimeth, S., Muelheim M., Ruhr M., Liessem, A., GmbH E. Development, Production and Application of Heavy Plates in Grades Up to X120, 1st International Conference Super-High Strength Steels, 1–10, 2005.
21. Grimpe, F., Meuser, H., Gerdemann, F., Muthmann, E., Mannesmann, S., & GmbH, G. (2010). Improvement of Mechanical Properties of Heavy Plates for High Strength Pipeline Application i.e. in Arctic Regions, 2nd International Conference on Super-High Strength Steels, 17–20, 2010.
22. Hukle, M. W., Hoyt, D. S., Dwyer, J. P., Horn, A. M., et al. Qualification of Welding Procedures for ExxonMobil High Strain Pipelines, Proceedings of OMAE 2006, 25th Edition , OMAE2006-92503, 1–9, 2006.
23. Ishikawa, N., Okatsu, M., Endo, S., Kondo, J., Design Concept and Production of High Deformability Pipeline, Proceedings of IPC 2006, IPC2006-10240, 1–8, 2006.
24. Murao, N., Hisamune, N., Osako, H., Kondo, K., High Strength Seamless Steel Pipe Excellent in Hydrogen-Induced Cracking Resistance and its Production Method, Sumitomo Metal Industries LTD., European Patent Specification 1546417B1, 1-15, 2012.
25. Okatsu, M., Shikanai, N., Kondo, J., Development of a High-Deformability Linepipe with Resistance to Strain-aged Hardening by HOP® (Heat-treatment On-line Process), JFE Technical Report, No.12, 2008.
26. Nonn, A., Kalwa, C., Modelling of Damage Behaviour of High Strength Pipeline, 18th European Conference on Fracture, 1–8, 2010.
27. Konrad, J., Stallybrass, C., Schneider, A., Meuser, H., et al. Characterization of the Microstructure of X80 Heavy Plate for Pipeline Applications using the EBSD Method, 3rd International Conference on Thermomechanical Processing of Steels, 10–12, 2008.
28. Zheng, L., Gao, S., Production and Application of High Strength and High Toughness Pipeline Steel with Acicular Ferrite, BAO Steel Corporate Publications, 2005.
29. Muthmann, E., Gjedrem, T., Stallybrass, C., Manufacturing of Large Steel Components for Nord Stream Project, 3R international Special-Edition, 26–31, 2010.

EXPERIMENTAL AND NUMERICAL SIMULATION ANALYSIS OF PERFORMANCE OF PARALLEL PLATE HEAT SINK FOR INVERTER MOSFET COOLING

Edeh. J. and Ayo S. A.

Department of Mechanical Engineering, Federal University of Technology, P.M.B 65 Minna, Niger State, Nigeria.

Abstracts

This paper takes a look at a locally produced inverter in order to forestall cases of frequent break down resulting from improper heat dissipation from one of the high power consuming component, the MOSFET. The MOSFETs are screwed on a flat plate heat sinks made from Aluminum alloy meant to draw the heat away and the heat subsequently blown away by a cooling fan. The heat transfer rate depends upon the velocity of the forced air from the fan, the surface area of the heat sink, fin geometry, the ambient temperature and the direction in which the heat sink are mounted relative to the cooling fan. Insufficient removal of heat from the inverter MOSFET will lead to high thermal stresses, lower efficiency and eventual thermal damage of the MOSFET. Therefore, the performance of the heat sink relative to its direction of mounting was carried out experimentally and by numerical simulation based on two other positions in addition to the present position being used by the manufacturer. The result showed that heat sink for direction perpendicular to the fan performance better, i.e have the higher cooling as against current position been used which is parallel and in the same direction as the fan, and also when in the opposite direction of the current position. The maximum temperature of the current heat sink position is 62.4°C, as against when the heat sink position was turned 90° which gave a 53.1°C

Key Words: MOSFT, heat sink, temperature, inverter, cooling, heat, simulation, experimental,

1.0   INTRODUCTION

Many engineering devices generate heat during their operation. If this generated heat is not dissipated rapidly to its surrounding atmosphere, this may cause rise in temperature of the system components. This cause over heating problems in device and may lead to the failure of component [3]. Fins or extended surfaces are known for enhancing the heat transfer in a system. Liquid-cooling system enhances better heat transfer than air-cooling system but the construction of air cooling system is very simpler. Therefore it is imperative for an air-cooled engine to make use of the fins effectively to obtain uniform temperature within the components [1]. The major heat transfer takes by two modes that is by conduction or by convection. Heat transfer through fin to the surface of the fin takes place through conduction where as from surface of the fin to the surroundings, it takes place by convection. Further heat transfer may be by radiation [2].

In an inverter, when AC voltage is converted to DC voltage heat is produced by some components of the inverter such as MOSFET, transformer, regulator especially when charging at high voltage or high fluctuation of the voltage supplied. Most electronic components inside the inverter cannot operate at high temperature. One of the most important components that generate a lots of heat is the MOSFET. MOSFET means metal-oxide-semiconductor field affected transistor. The MOSFET is a transistor that is used to switch or amplified signal and electrical power. It consist of three layers of semiconductor materials each capable of carrying current. Great amount of heat is being generated in performing this function and this heat have been found to reach close to 150°C. Heat sink or cooling fins are used to provide cooling when in operation.

1.1   Review of Related Literature

Barhatte et al [4] studied the fin flats which are modified by removing the central fin portion by cutting a triangular notch. This dissertation report presents an experimental analysis of the results obtained over a range of fin heights and heat dissipation rate. Attempts were made to establish a comparison between the experimental results and results obtained by using CFD software.
Mirapalli et al [5] provided rectangular and triangular fins on the periphery of engine cylinder. Heat transfer analysis was carried out by placing rectangular and then triangular fins. Analysis was carried out by varying temperatures on the surface of the cylinder from 200 °C to 600°C and
varying length from 6 cm to 14 cm. Input parameters such as density, heat transfer coefficient, thermal conductivity and thickness of fin were taken and output parameters such as rate of heat flow, heat flow per unit mass, efficiency and effectiveness are determined.

Jassem et al [6] investigated the heat transfer by natural convection in a rectangular perforated fin plates. Five fins used in this work first fin non-perforated and others fins perforated by different shapes these fins perforation by different shapes (circle, square, triangle, and hexagon) but these perforations have the same cross section area. These perforations distributed on 3 columns and 6 rows. Experiments produced through in an experimental facility that was specifically design and constructed for this purpose.

Daund et al [7] reviewed convection heat transfer through rectangular fins. Various experimental studies have been made to investigate effect of fin height, fin spacing, fin length and fin thickness over convective heat transfer. He also examined the experimental and numerical studies which are done in natural, mixed and forced convection. He found that sets of correlations to give relation between various parameters of heat sink were derived.

Shaikh et al [8] dealt with performance of various available fins profiles. Widely used fins profile viz. Rectangular, Triangular, Trapezoidal, Circular, Rhombic, and Elliptical Fins.

In addition to the normal configuration of fins, to new configurations were designed and created. This includes length of each fins its thickness at the base and number of fins on each model this provided a basis for proper comparison of different fin profiles.

2.0   Materials and Method

2.1   Materials

The following materials were used for this study;
i.   2.5KVA SLE Inverter that incorporates MOSFET IRF 150, Flat Plate Heat Sink and temperature Sensor
ii.   Wind Speed/Temperature Anemometer
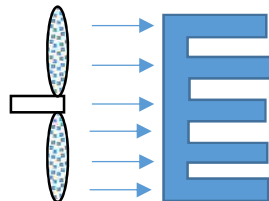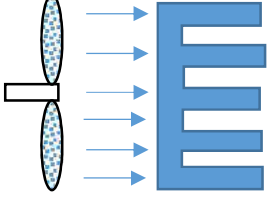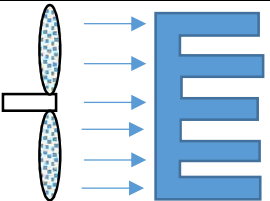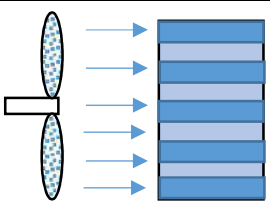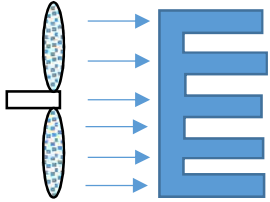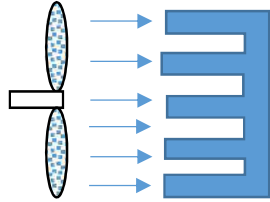
2.2 Method

2.2.1 Experimentation

The results of any experimentation depend to a large extent on the data collection methodology. The key reason of carrying out experiment is to measures the response (heat dissipation) of every possible combination of factors (for this case the flow direction) and factors levels (3 levels). This response was be analyzed so that the best heat configuration was identified. The heat sinks was mount on the inverter as presented in table 4.1. The inverter has a temperature sensor that is controlled by the

inverter circuit board and display its readings in a 6 x 4 LCD screen. As the inverter was switched on the time and temperature were recorded at an interval of five minute and the results recorded

Table 4.1: Current and proposed modification of the heat sink position relative to fan

S/No	Modification	Present	proposed
1	Plate Heat sink orientation relative to the fan – original (position 1)	D1 – from behind	D1- from behind
2	Plate Heat sink orientation relative to the fan – position 2	D1 – from behind	D2 – from the side
3	Plate Heat sink orientation relative to the fan – position 3	D1 – from behind	D3 – from the front

2.2.2 Modeling and Simulation

In this paper, computer modeling and simulation approach was used to investigate the heat dissipation of the existing plate heat sink and modified heat sink. The main task involved in the modeling and simulation are summarized in figure 1.

Geometric Modeling Material selection
↓
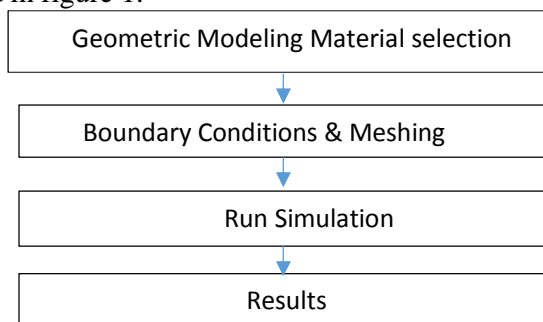Boundary Conditions & Meshing
↓
Run Simulation
↓
Results

Figure 1: Simulation steps

A typical parallel plate heat sink as shown in figure 4.2 was modelled and thermal simulation was carried out in the following steps:

i.   Geometric modeling – the 3D model of the heat sink and MOSFET are require for the numerical simulation and therefore, was created in SOlidworks software. First the 2D was create using the geometric parameters in table 4.2 and then the 3D model of the components. The important geometric variables considered are number of fins, fin length, fin height, and base height

Table 4.2 Geometric parameters

S/No	Dimension	Value
1	Width	48mm
2	Length	124mm
3	Fin thickness	3mm
4	Base thickness	4mm
5.	Number of fins	12
6.	Fin spacing	8mm

ii.   Material selection – the specific materials for each components were selected from the Solidworks material library. When material was specified the need properties for the FEA simulation are applied. Such thermal properties of the material.

iii. Mesh generation for the computational domain – the reliability of FEA analysis is a function of the quality of the mesh created. split line concept were used to generate the mesh for the heat sink and MOSFET. Both components have the same density of parabolic type. Each node in a solid element has three degrees of freedom that represent the translations in three orthogonal directions. The automatic mesher in the software generates were used to mesh based on a global element size, tolerance, and local mesh control specifications
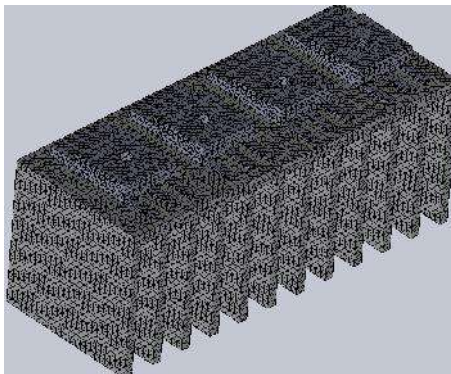

Figure 4.2: Meshed Heat Sink.

iv.   CFD modeling – thermal analysis of the inverter cooling system required already mesh geometry of the assembly. The solver engine in this package, uses a systems CFD solver for fluid flow and a full three dimensional (3D) thermal solver. The solver features include conservation of mass, conservation of momentum and conservation of energy.

Table 4.3: Simulation Parameters (Boundary Conditions)

S/No	Parameter	Value
1	Inlet lid velocity	10.1 m/s
2.	Environmental pressure (inlet and outlet)	101325Pa
3.	Inlet and outlet lids temperature	293.2K
4	MOSFET Temp	150ºC

3.0 Results and Discursion of Results

3.1 Results

The result of the experiment conducted and the simulation are shown in figure 5.1 and figure 5.2 respectively. The figures show the temperature recorded of the three position of the heat sink relative to the fan with position 2 in each case given a better heat dissipation.
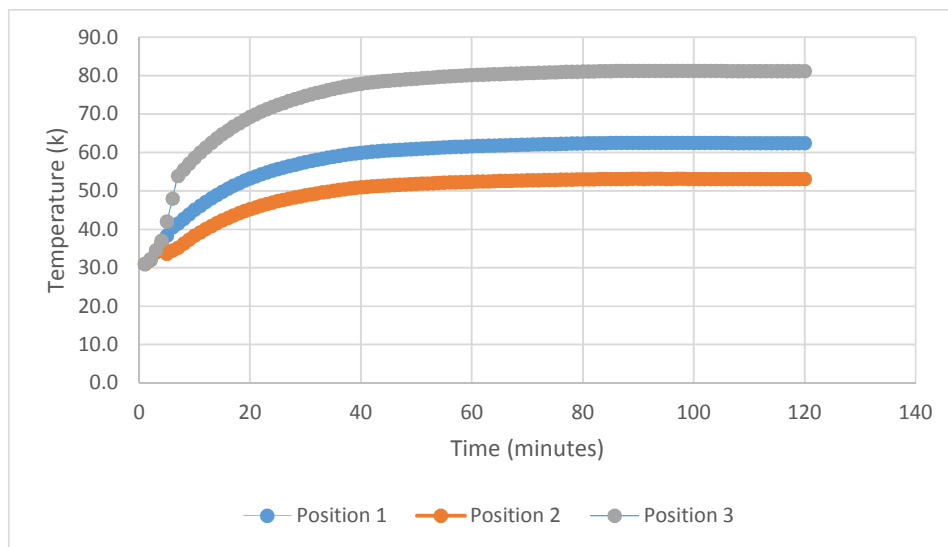

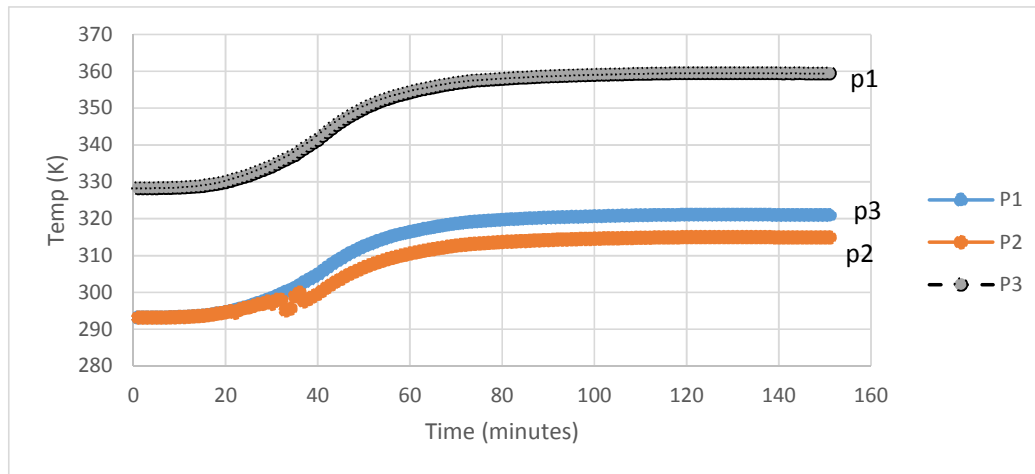Figure 5.1: Graph of the Heat Sink Temperature for experimental value.

Figure 5.2: Comparison of the Heat Sink temperature for the three directions for simulated result.

3.2. Discursion of Results

The simulation results shows the maximum temperature for positions 1, 2 and 3 are 48.1^{o}C, 42°C and 86.6^{o}C respectively. Also as indicated from the graph the position 2 has the best heat dissipation and a lower heat sink temperature of 42°C. the graph show that the inverter became stable of about 30 minutes of operations

4.0 Conclusion

The overall performance of flat plate heat sinks made from Al-alloy with three different heat sink position was studied using a fan velocity of 10 m/s. To find out best heat sink position the present position used was compared with two other different positions using experimental and numerical simulation method, and each case, position 2 was found to have better heat dissipation as compared to the positions 1 and 3.

References

[1]   Magarajan U, Thundil karuppa Raj R and Elango T, Numerical Study on Heat Transfer of Internal Combustion Engine Cooling by Extended Fins Using CFD , Research Journal of Recent Sciences, **2012**, 1(6), 32-37.

[2]   S.H. Barhatte, MR Chopade, Experimental and Computational Analysis and Optimization for Heat Transfer through Fins with Triangular Notch, International Journal of Emerging Technology and Advanced Engineering, **2012**, 2(7), 483-487.

[3]   V.S. Daund, A Walunj and DD Palande, Review of Natural Convective Heat Transfer from Rectangular Vertical Plate Fins , International Journal of Advanced Technology in Engineering and Science, **2014**, 2 (7), 294-304 .

[4]   S.H. Barhatte, MR Chopade, Experimental and Computational Analysis and Optimization for Heat Transferthrough Fins with Triangular Notch, International Journal of Emerging echnology and Advanced Engineering,**2012**, 2(7), 483-487.

[5]   Sandhya Mirapalli and Kishore PS, Heat Transfer Analysis on a Triangular Fin, International Journal ofEngineering Trends and Technology, **2015**, 19(5), 279-284.

[6]   Raaid R Jassem, Effect the Form of Perforation on the Heat Transfer in the Perforated Fins, Academic ResearchInternational, **2013**, 4(3), 198-207.

[7]   VS Daund, A Walunj and DD Palande, Review of Natural Convective Heat Transfer from Rectangular VerticalPlate Fins , International Journal of Advanced Technology in Engineering and Science, **2014**, 2 (7), 294-304 .

[8]   Rafeek Shaikh, SN Doijode and Geeta Lathkar, A Review on Experimental Study of Heat Transfer from PlateFin in Mixed Convection Mode (Square, Elliptical and Circular Fin), International Journal of Science and Research,**2015**, 4(2), 1091-1093.

[9]   Mehdi Nafar and Mohammad Tavassoli, An Analysis for Optimization of Heat Transfer for Various Heat Sink Cross-section and Length, Australian Journal of Basic and Applied Sciences, **2011**, 5(12), 1685-1682.

ASSESSMENT OF MOULDING PROPERTIES OF GBARA SAND DEPOSIT FOR CASTING PURPOSES

*Abdullahi Gana and Katsina Christopher Bala

Department of Mechanical Engineering, Federal University of Technology, P.M.B 65, Minna

*Corresponding author's email: abdulgana76@yahoo.com, 07030374544

Abstract

Assessment of moulding properties of Gbara sand deposit for casting purposes was carried out. Gbara sand sample was collected along the river bank and characterized to ascertain its suitability for use for casting purposes. Standard foundry laboratory testing equipment were used to carry out the tests and the results obtained were compared with American Foundry Men Society Standard (AFS). The samples of the sand were tested for Refractoriness, Sieve analysis, Clay content, Moisture content, Permeability, Shatter index, Dry and Green strength as well as Chemical analysis. The sand was divided into six specimens and tested with different percentages of Ant-hill as a binder which responded well. Casting was carried out using Gbara sand and Zungeru sand (used in SEDI Minna foundry) and the properties (Tensile, Hardness, Impact and Microstructure) of the cast specimens were compared. The result of the mechanical properties analysis was compared to existing foundry standard and it was found to be very suitable for all types of non-ferrous alloy casting. The result showed that Gbara river bank sand is alumina silicate with physio-chemical properties that are suitable for non-ferrous alloy casting.

Keywords: Gbara sand, Refractoriness, Clay content, Shatter index, Sieve analysis.

1.0 INTRODUCTION

Sand is a product of the disintegration of rocks over long periods of time. Most sand casting operation use silica sand (SiO_2). Sand is a major raw material used in constructions, industries and foundry. Sand casting operations are classified into green sand and dry sand. Sand moulds are designed to have good collapsibility and accommodate shrinkage of cast metal during solidification to avoid defects in the cast metal. Silica Sand is found in many natural deposits, and is suited for moulding purpose because of its ability to withstand high temperature without decomposition. Sand is resistant to high temperature, almost ancient, cheapest and most important especially in developing countries like Nigeria (Asuquo and Jama, 1991).

Most of the sand that used in foundry for moulds production or for casting must possess properties such as Permeability to gases, Cohesiveness or strength, and Refractoriness or ability to withstand high temperature (Udeh, 2017).

Casting involve molten metal being poured into the mould at a right temperature and is given time to solidify in the mould. The items produced in this foundries are household and machine parts (cooking pots, dishes, spoons, aluminum gates decoration, machine belt pulleys, fans etc) in production capacity of 200 tons of nonferrous metal per month (Umar and Samaila, 2014).

This study therefore assesses the mechanical and thermal properties of the locally available moulding sand deposits in Gbara, Niger State, Nigeria to ascertain its suitability for use in sand casting operations.

2.0 Materials and Method
2.1 Materials Used
Natural foundry sand was collected from deposits site in GBARA, River Gbara ward in Mokwa, Niger State, Nigeria and dried to room temperature. Other materials used include ant-hill binder collected within Bida, water, aluminium scrap.

2.2 Equipment Used

The equipment used include weighing Balance, EDXRF machine, Tensometer, Computer controlled hardness testing machine, Metallurgical microscope, Sieve shaker hand rammer, small hand foundry shovel, sand rammer, flowability meter, speedy moisture tester, Carbolite machine, anvil, strength testing machine and heat treatment furnace. The test samples were prepared in accordance with the standard specification for the preparation of moulding sand test samples using Ridsolate standard sand rammer conforming to imperial (51mm diameter x 51mm Height) or DIN (SCM diameter by 50mm height). The properties analyses include; Sieve analysis, Chemical composition analysis, Green compression strength, Dry compression strength, Permeability, Moisture content and Refractoriness.

2.3 Sand Mould Preparation
The sand additive and water mixture for each of the experiments 1 to 5 were thoroughly mixed using mixer. It was hand squeezed and the mixture was poured into a tube and rammed by impact with three blows of a 6.35kg weight to fall a distance of 5 cm one after another (Tokan et al., 2004).

2.4 Chemical Composition
The chemical composition of the sand sample was determined using the X-Ray Fluorescence (XRF) spectroscopy technique at the National Geoscience Research Laboratories Centre, Kaduna, Nigeria. This is a non-destructive analytical method in which X-ray tube is used to irradiate the sample with a primary beam of X-rays. Some of the impinging primary X-rays are absorbed by the sample elements in a process known as the photoelectric effect (Bala and Khan, 2013).

2.5 Clay Content
1kg of the control sand was first washed with raw water, in a 53 microns sieve to remove the clay content using AFS clay content determination. Particles which fail to settle were referred to as clay content and other additives. This process was repeated twenty times until the 1kg of the control sand was fully separated from clay and other undesirable impurities (Ayoola et al., 2010).

2.6 Sieve Analysis
100g of dried specimen was sieved using 150, 300, 600, 833 and 11167 μm. Equal amount of sands was placed on top of the sieves on a mechanical vibrator and then shaken for 30 minutes after which the content of each sieve was weighed. The mass of the specimen left at each compartment of the sieve, the percentage retained and the percentage passed was calculated.

GFN = Product/% weight retained

$$R = \left(\frac{M_1}{M_0}\right) \times 100\% \qquad\qquad 1$$

and $P = 100 - R$ $\qquad\qquad$ 2

Where;

GFN = Grain fines number

M_0 = Mass of each sample of sand (g)

M_1 = Mass of sand sample retained on the sieve (g)

R = % of sand sample retained

P = % of sand sample passing through the sieve (Ayuba et al., 2012).

2.7 Green Compression Strength Test

The green standard mould specimen of 50mm diameter by 50mm height was fixed on a strength testing machine using compression-holding device. A uniformly increasing load was applied on the specimen until the specimen crushed or squeezed. The point on the scale at which the specimen crushed or squeezed was recorded as the green compression strength (Tokan et al., 2004).

2.8 The Shatter Test

The specimen of 50mm height by 50mm diameter size was from its tabular mould by means a tripping post and allowed to fall through a height of 1800mm to a steel anvil. The fragments were collected in a 12.5 mm mesh sieve. The shatter index being that percentage of the total weight retain on the sieve was determined (Tokan et al., 2004).

2.9 Determination of Green Shear Strength

The Green Shear Strength (GSS) which is the measure of the shear strength of the prepared sample, when shear load is applied in its green state. The machine used for the GCS was also used for the determination of green shear strength (GSS), except that the compression head was replaced with shear head in the machine. The shear strength was recorded at the point of failures of the sample loaded.

2.10 Determination of Dry Compression Strength

Standard sample of 50mm diameter x 50mm height was prepared and dried in an oven at a temperature of 1100 ºC for a period of 30 minutes and then removed and allowed to cool in the air to ambient temperature. After cooling, the sample was fixed into the universal sand-testing machine with the compression head in place. The compressive load was applied and the samples failed at the ultimate compressive strength of the sample. The point at which the failure occurs was recorded at DCS (Abolarin et al., 2010).

2.11 Determination of Dry Shear Strength

The prepared standard sample of 50mm diameter x 50mm height was dried in an oven at a temperature of 1100 ºC for 30 minutes and then removed from the oven to cool in an air to ambient temperature. The same universal testing machine was used for dry compression strength. In this case, the shear head was replaced for the compression head. The shear strength was recorded at the point of failures of the standard test sample (Abolarin et al., 2012).

2.12 Determination of Permeability

The permeability test was carried out on the standard sample specimen of 50mm diameter x 50mm height. The specimen, while still in the tube, was mounted on permeability meter. The permeability meter is an electrical perimeter and it employed the orifice method for rapid determination of sand permeability. Air at a constant pressure was applied to the standard sample specimen, immediately after producing the sample and the drop in pressure was measured on the pressure gauge, which is calibrated directly in permeability numbers (Tokan et al., 2004).

2.13 Moisture Content

The speedy moisture tester was used for the test. Sand sample was weighed on a speedy moisture testers weighing balance. The sample and a small quantity of calcium carbide will be placed in a calibrated container and shaken for 2 minutes, and later for 1 minute. A measurable amount of acetylene gas proportional to the amount of sand moisture was produced. The moisture content was read directly from the calibrated scale on the instrument (Ayuba et al., 2012).

2.14 Refractoriness

The dried sand sample was fired to a temperature of 900 ℃ in a Muffler furnace. Pyrometric cones design to deform at 1300 ℃, 1400 ℃, 1500 ℃, 1700 ℃ was placed round the samples and the temperature was rise to above 1000 ℃ at 10 ℃/min. The heating was then discontinued when the test cone bend over and level with the base of the disc. The pyrometric cone equivalent (P.C.E) of the samples were recorded as the number of standard pyrometric cone corresponding in terms of softening to the test cone (Ayuba et al., 2012).

2.15 Experiment

During the experimentation bentonite and ant-hill were used as binder. Two mould were prepared for the casting. The first mould was prepared using 80% Zungeru sand (25kg), 13% bentonite (4.06kg) and 7% moisture (2.19kg) while the second mould was prepared using 50 % Gbara sand (15.63kg), 43% ant-hill (13.44kg) and 7% moisture (2.19kg). Mixing of various sand with additives was carried out using sand mixing machine.

2.16 Casting Process

Casting was carried out using the prepared sand samples and mechanical properties tests were carried out on the cast. The mechanical properties tests include: Hardness test, Tensile test, Impact test and Microstructural examination. Aluminium scrap was charge into a red-hot crucible pot on a charcoal-fired crucible furnace and allowed to melt at 660 ℃. The molten metal was then poured into a prepared cylindrical mould and allowed to cool. The cast sample was removed from the mould and machine to sample sizes for mechanical tests. The mechanical tests were carried out according to the Standard methods available in literature.

2.17 Microstructure Examination

Prior to the metallography and surface morphology examination, the surface of the samples was ground successively using grit papers of different grades of 120C, 180C, 320C, 400C, 600C, 800C and 1200C, with the application of lubricant intermittently to prevent overheating and provides a rinsing action that flushed away the particles been removed from the surface. They were subsequently polished with the aid of a polishing machine using Alumina to remove the scratches left during grinding. Etching was then carried out on the polished surface using "Keller's reagent (solution of 1ml distilled water, 5ml nitric acid and 2 ml hydrofluoric acid).

A computer control photographic visual metallurgical microscope MODEL NJF-120A, Rating- 230V-5V/60Hz was then used to view the microstructures of the polished samples.

2.18 Hardness Test

Hardness test was carried out on the samples according to ASTM E384-11 using standard computerized Vickers Hardness Testing Machine, Model MV1-PC serial No: 07/2012-1329, with a load of 0.3 kgf, max/min limit of 150/050 HV.

2.19 Tensile Test

The ultimate tensile strength test was conducted in accordance with ASTM E 8M using the Monsanto Tensometer, type W Serial No. 9875. The samples were gripped in the chucks of the Tensometer and load was applied by with the aid of load handle until the samples fracture.

2.20 Impact Test

The impact test was conducted in accordance with ASTM E 602-91 Standard Method and Definitions for Mechanical Testing of Steel Products. A V-notches of 0.5mm depth were made on the samples

each and the impact strength was carried out using Honsfield Balance Impact Machine, serial No: 3203.

3.0 RESULTS AND DISCUSSION
3.1 Chemical Composition
The chemical composition of the sand sample was determined using the X-Ray Fluorescence (XRF) spectroscopy technique and the result is presented in Table 3.1.

Table 3.1: Chemical Composition Analysis of Gbara sand

Elements	Si_2O	Al_2O_3	K_2O	CaO	TiO_2	V_2O_5	MnO	Fe_2O_3	CuO	AS_2O_3	SrO	CeO_2	PbO	L.I.O
Composition (%)	93.2	1.3	1.02	1.08	0.74	0	0.03	1.66	0.017	0.011	0.06	0.05	0.01	0.81

Table 3.2: Mechanical Sieve Analysis of Gbara sand

S/N	Sieve Aperture (mm)	BSS NO	Weight Retained (g)	Weight Retained (%)	Cumulative Weight Retained (%)	Multiplier	Product
1	1.18	10.00	0.30	0.35	0.30	6.00	2.10
2	0.83	22.00	1.03	1.03	1.33	9.00	9.27
3	0.60	2.00	6.95	6.95	8.28	15.00	104.25
4	0.30	30.00	12.10	12.13	20.38	25.00	303.25
5	0.15	44.00	24.90	24.90	45.28	35.00	871.50
	TOTAL			**99.99**			**4491.51**

Table 3.3: Mixing Composition and Properties Test Results of Gbara sand samples

Sample	Water (g)	Additive (g)	Sand (g)	GC (kN/m²)	GS (kN/m²)	DC (kN/m²)	DS (kN/m²)	P (No)	MC (%)	SI (No)
A	6.00	72.00	522.00	N.S	N.S	N.S	N.S	N.R	3.20	59.00
B	12.00	72.00	516.00	26.20	31.03	172.37	51.71	3.80	4.00	66.00
C	24.00	72.00	504.00	17.24	24.13	258.55	137.89	3.50	5.30	75.00
D	36.00	72.00	492.00	31.72	31.03	116.52	72.50	3.20	5.50	84.00
E	48.00	72.00	480.00	28.96	22.41	189.61	103.42	2.90	5.80	85.00
F	60.00	72.00	468.00	29.37	27.56	143.82	100.36	2.70	6.40	88.00
*Zungeru sand				24.00				0.28	15.40	36.06

*Bala and Olabisi, 2017. GC: Green Compression, GS: Green Strength, DC: Dry Compression, DS: Dry Strength, P: Permeability, MC: Moisture Content, SI: Shatter Index
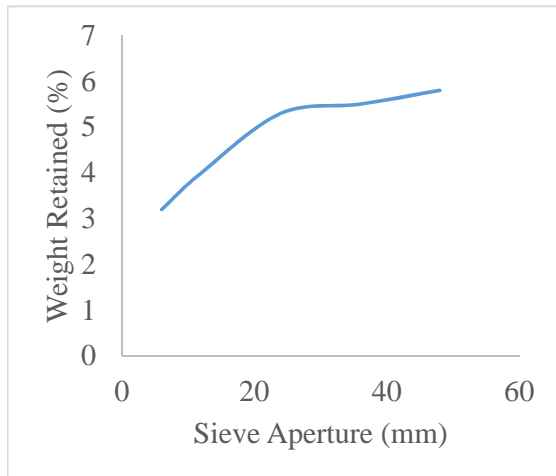
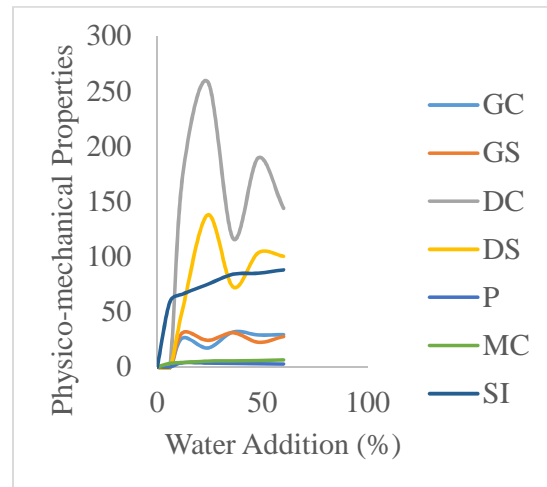**Figure 3.1: Grain size distribution**

Figure 3.2: Variation of Water Addition on Physico-mechanical Properties

3.2 Cast Samples

The cast cylindrical shaped (20mm diameter by 350mm length) were machine into standard test specimen for Tensile, Hardness and Impact tests.

3.3 Microstructure of the Cast Samples

The microstructure of the samples cast using Gbara sand and Zungeru sand viewed under metallurgical microscope are presented in Plate 4.4.
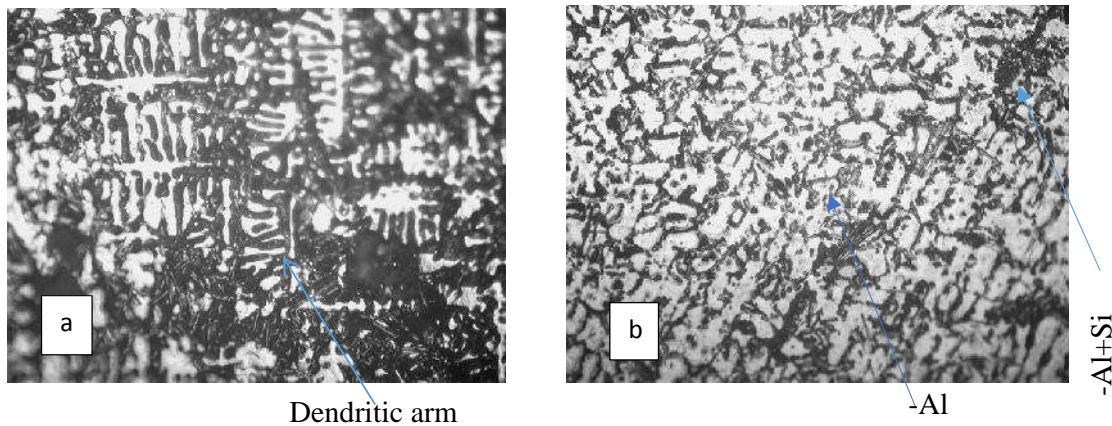

Plate 3.1: Optical micrograph of the cast samples using Gbara sand (a) and Zungeru sand (b). Mag x100.

3.4 Mechanical Properties

Figure 3.3 shows the results of the Hardness, Tensile and Impact tests of the samples cast using both Gbara and Zungeru sand respectively.
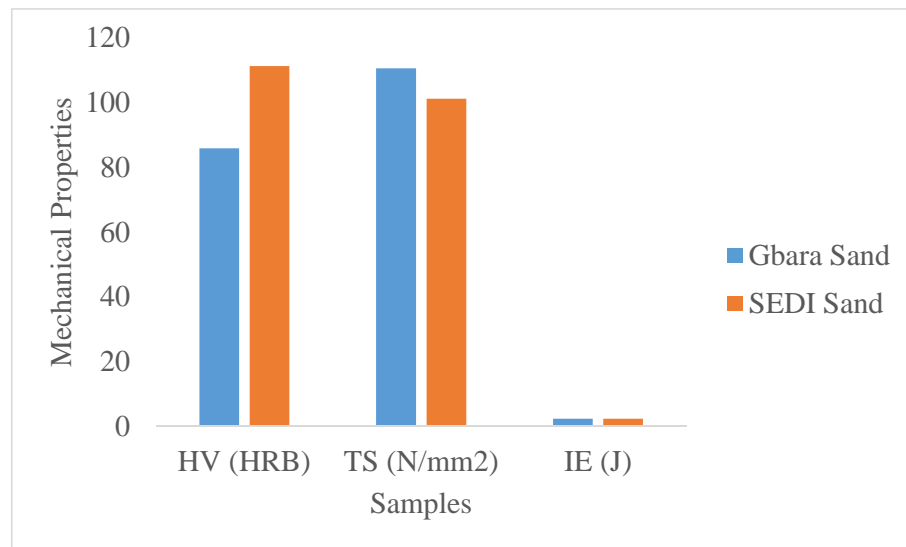
Figure 3.3: Variation of Mechanical Properties of the samples

3.5 Discussion
Chemical Composition
Table 3.1 shows the results of the chemical composition analysis of Gbara sand. The major constituents of the sample are silica (93.2%) and alumina (1.3%) with other substances such as oxides of iron, sodium, titanium, and calcium among others which are in small proportions. The values of the specimens' chemical constituents are in line with the recommended mould sand chemical compositions in literature (Bala, 2013). The sand can still be used as moulding with application of additive, such bentonite.

Sieve analysis
The AFS fineness number which is the standard for reporting the grain size and distribution of sand was used to assess the particles (Parkes, 1971). This was applied to the sieve result as in Table 3.2 to obtain the AFS number. From the table:

$$\text{Grain fineness} = \text{Total product} \div \% \text{ weight retained}$$
$$= 4491.51 \div 99.99 = 44.92$$

The sieve analysis of the samples gave AFS numbers 44.9. This value is in accordance with the grain fineness number used by most foundries, which is expected to be between 40 and 220 (Oke and Omidiji, 2016; Udeh et al., 2017).

Visual Inspection
Gbara sand is sub-angular in shape and light brown in colour. It is a very fine silica sand with very low clay content, this makes it suitable for use as core sand in addition to its suitability for use as a moulding sand (Mahmoud et al., 2016).

Clay Content
The clay content of Gbara sand sample which was found to be 6 %, indicate that the sand has good clay content and as such is good for foundry use, when compare with the standard which requires foundry sand to have 4-10% clay (PN RAO, 1998; Guma 2012).

Effect of Weight Retained on Grain Size Distribution

Figure 3.1 shows grain distribution curve of the various sample mixture. It can be seen from the figure that increase in sieve aperture increases the weight retained of the samples.

Effect of Water Addition on Physico-mechanical Properties

Figure 3.2 shows variation of water addition on some physico-mechanical properties for various prepared samples. It can be seen from the figure that increase in water addition increases the physico-mechanical properties of all the prepared sand samples, with the dry compression (DC) reaching the highest (258.55kN/m^2). As the water addition increases at a point, the physico-mechanical properties of the samples decreases. Permeability and moisture content samples exhibited lowest values of 2.7No and 6.4% respectively. This result agrees with the results put forward by several authors (Ayoola et al., 2013; Abolarin et al., 2010; Aweda and Jimoh, 2009).

Effect of Mechanical Properties of the Sand Samples

Figure 3.3 shows variation of the mechanical properties of the sand samples. Zungeru sand exibited the highest hardnes (111.33HRB) compared to Gbara sand. The enhanced hardness in Zungeru sand castings might be due to the presence of a fine-grained microstructure consisting of -Al dendrites and the hard and brittle eutectic phase (-Al+Si). It can also be seen that Gbara sand exibits highest tensile strength (110.61N/mm^2) compared to Zungeru sand, while there is no vissible variation of the impact energy of the two sand samples. This result is in agreement with the result put forward by Narasimha and Babu, 2017.

Effect of Microstructure of the Sand Samples

Plate 3.1 shows Optical micrograph of the cast samples using Gbara and Zungeru sand. Zungeru sand casting show refined microstructures than Gbara sand castings; this might be due to the presence of faster solidification rates in the moulds (Murthy et al., 2018). Zungeru sand products cools more quickly, resulting in microstructure with small size grains. The microstructure mainly consists of soft and ductile - aluminum dendrite phase containing hard and brittle eutectic phase (-Al+Si) in the inter-dendrite region, as shown in figures 3.1 (a-b).

The results of the study showed that the Gbara sand exhibit good properties for casting of non-ferrous metals such as aluminum. Based on the results presented, the following conclusions were made:

4.0 Conclusion

1. The chemical and physical analysis showed presence of elements such as Si, Al. XRF analysis confirmed that SiO_2 (93.2%), Al_2O_3 (1.3%) were found to be major constituents of the sand. Fe_2O_3 (1.66%), TiO_2 (0.743%) were also found to be present in traces.
2. Gbara sand have good green shear strength, green and dry compression strength, adequate permeability and shatter index as compared to Zungeru sand.
3. Mechanical properties of the cast samples produced showed high tensile strength of 110.61N/m^2 in the sample cast using Gbara sand compared to 101.28N/m^2 obtained for sample cast using Zungeru sand. Low hardness value of 85.93HRB was obtained from sample cast using Gbara sand compared to 111.33HRB obtained from sample cast using Zungeru sand. Equal value of impact energy (2.38J) was recorded for the both samples.

   Conclusively, Gbara silica sand is recommended for mould production and casting of non-ferrous metals.

References

Abolarin, M. S., Lawal, S. A., Salawu A. A. (2010). Effect of moisture content on the moulding properties of River Niger sand using Tudun-wada clay as a binder. AU J.T. 13 (3): 170-174.

Ajaokuta Steel Company Limited, Ajaokuta, Nigeria. American-Eurasian Journal of Scientific Research. 3 (1): 75-83, 2008 ISSN 1818-678.

Akinyele J. O. and Oyeyemi K. S. (2014). Strength Behaviour of Concrete using Foundry Sand as Aggregate. Journal of Natural Science, Engineering and Technology, Vol. 13: 99-108.

ASTM E384-11. (2012). Standard Test Method for Knoop and Vivkers Hardness of Materials. p6

ASTM E 8M: Standard Test Method for Tension Testing of Metallic Materials (Metric), Annual Book of ASTM Standards, Philadelphia; 1991.

ASTM E 602-91: Standard test method for sharp-notch impact testing with flat specimens. Philadelphia: American Society for Testing and Materials; 1992.

Asuquo and Jama B. (1991). Foundry technology. ABIC publishers, Enugu and Lagos, Nigeria Pp1-3

Ayoola W. A., Adeosun, S. O., Oyetunji A., Oladoye A. M. (2010). Suitability of Oshogbo sand as a moulding sand. The Kenya Journal of mechanical engineering. KJME 6, (1).

Aweda J. O, and Jimoh Y. A. (2009). Assessment of Properties of Natural Moulding Sands in Ilorin and Ilesha, Nigeria. USE: Journal of Research Information in Civil Engineering, l.6, (2).

Ayoola W. A., Adeosun S. O., Oyetunji A. (2013). Investigation into Foundry properties of Oshogbo and Saki silica sand deposits. Internal Journal of engineering. ISSN 1584-2673.

Katsina Christopher BALA and Balogun Abdulfatai OLABISI, (2017). Deterioration of Moulding Sand Properties with Number of Castings. Leonardo Electronic Journal of Practices and Technologies. ISSN 1583-1078 Issue 30, p. 209-220

Bala K. C. and Khan R. H. (2013). Characterization of Beach/River Sand for Foundry Application. Leonardo Journal of science Pp 77-83. Issue 23. ISSN 1583-0233

Bukar M., Aji I. S. and Mshelia Z. A. (2017). Grain Size Analysis of Biliri and Damaturu Moulding Sands for Foundry Application. University of Maiduguri Faculty of Engineering Seminar Series Volume 8.

Dietert H. W. (1966). Foundry core practice. 3ʳᵈ edition, American foundry men's society. Des Plaines, Inc., Pp2-154.

Fayomi O. S. I., Ojo O. I. and Popoola A. P. I. (2011). Investigating (Ochadamu) silica sand, clay and local oils for foundry core. International Journal of the Physical Sciences. 6(8), pp. 1894 -1904. ISSN 1992 – 1950, DOI: 10.5897/IJPS11.259 http://www.academicjournals.org/IJPS.

Guma (2012). Characteristic Foundry Properties of Kaduna River Sand. Research Invety: International Journal of Engineering and Science ISBN: 2319-6483, ISSN: 2278-4721, Vol. 1, Issue 11, PP 03-08 www.researchinventy.com

Higgins R. A. (1983). Engineering metallurgy part 1. Applied Physical Metallurgy, 6th edition. ELBS with Edward Arnold, U.K.

Joshua T. O., Fayomi O. S. I. and Olatuja F. H. (2016). Hybrid Effect of Selected Local Binders on the Moulding Properties of River Niger Silica Sand for Industrial Application. Journal of Nanoscience with Advanced Technology 1(4): 19-23. Doi: https://doi.org/10.24218/jnat.2016.19.

Mbimda Ali Mbishida and Seth Samuel AUDU. (2017). Investigation into the Suitability of Lere River Bank Sand for Green Sand Casting. American Journal of Engineering Research (AJER) e-ISSN: 2320-0847 p-ISSN: 2320-0936 6, (10), pp-01-05 www.ajer.org.

Mikhailov A. M. (1989). Metal Casting. Mir Publishers. Moscow, Pp 71-82.
Parkes, W. B. (1971). Clay Bonded Foundry sands. Applied Science Publishers Limited., pp: 3-9.

Mshelia Z. A., Abolarin M. S., Abubakre O. K. and Ademoh N. A. (2016). Characterisation of Natural Moulding Sands from Selected Deposits in Maiduguri-Nigeria for Casting Applications. Arid Zone Journal of Engineering, Technology and Environment. AZOJETE, 12:110-121. ISSN 1596-2490; e-ISSN 2545-5818, www.azojete.com.ng.

Oke A. O. and Omidiji B. V. (2016). Investigation of Some Moulding Properties of a Nigerian Clay-Bonded Sand. Archives of Foundry Engineering. 16, (3), 71 - 76

Tokan A., Adelemoni E. A. A., Datau, S. G. (2004). Mould characteristics of Azare foundry sand. JORMARI (1): 67-80. ISSN: 1597-3204.
Sand casting- The Designers and Buyers Guide. www.manufacturingnetwork.com. Retrieved 29-03-2016.

Shuaib-Babata Y. L., Yaru S. S., Abdulkareem S., Ajayi S., Busari Y. O., Ajao K. S., Ibrahim H. K., Ambali I. O. and Mohammed G. A. (2017). Suitability of some Selected Ado-Ekiti (Nigeria) Natural Moulding Sands Properties for Sand Casting. Covenant Journal of Engineering Technology (CJET) Vol.1 No. 2

Narasimha Murthy I. and Babu Rao J. (2017). Evaluation of the Microstructure, Secondary Dendrite Arm Spacing, and Mechanical Properties of Al–Si Alloy Castings made in Sand and Fe–Cr Slag Molds. International Journal of Minerals, Metallurgy and Materials. 24, (7), P 784 DOI: 10.1007/s12613-017-1462-x

Mahmoud L. U., Apeh F. I., Shuaibu S., Isheni Y. (2016). Application of Gwange Natural Sand as Foundry Moulding Material. American Scientific Research Journal for Engineering, Technology, and Sciences (ASRJETS) 20, (1), pp 148-156.

Murthy I. N., Babu N. A. and Rao, J. B. (2018). Microstructure and Mechanical Properties of A356 Alloy Castings made in Sand and Granulated Blast Furnace Slag Moulds. Materials Today: Proceedings 5 Pp161–167. www.materialstoday.com/proceedings

Stephens, H. A. and Waterworth (1968). British foundry men. Pp 61-202.

Umar L. and Samaila M. H, (2014), Foundry Operation Sand of Damaturu and Gombe Foundry Retrieved from www.myhome.Foundry.com

Udeh Jude Nnaemeka, Attama E. O., Engr. Ekere Jude Thaddeus, Ozioko C. C. (2017). Assessment and Characterization of Nkpologu Sand Deposit in Uzo-Uwani Local Government Area of Enugu State, Nigeria using Cassava Starch as a Binder for Mould Production. International Journal of Advanced Research in Science, Engineering and Technology, 4, (2), ISSN: 2350-0328.

Umar, A. A. (2001). An assessment of challawa river bed sand for casting purposes around Kano, Nigeria. Journal of General Studies. New series. 4, (1), 96, 104.